POLITECNICO DI TORINO

SCUOLA DI DOTTORATO

PhD Course in Physics – XXX cycle

PhD Dissertation

Magnetic Domain Wall Motion

Numerical Simulation and Collective Coordinate Modeling

S. Ali Nasseri
ID number: S219459

Supervisor	**Coordinator, PhD Course in Physics**
Dr. Gianfranco Durin	Arianna Montorsi

November 2017

Abstract

Manipulating magnetic domain walls in nanostructures has been linked with applications in spintronic logic, sensing and storage devices. Recent studies of domain wall motion have focused on perpendicular magnetic anisotropy heterostructures of ultrathin ferromagnets sandwiched between a heavy metal layer and an oxide, in which spin-orbit coupling and broken inversion symmetry can dominate domain wall motion.

Specifically, chiral domain walls are stabilized in these systems due to the Dzyaloshinskii-Moriya interaction, and current-driven domain wall motion is enhanced due to the spin Hall effect. The chirality of the domain walls in such systems may be partially influenced by the application of external in-plane magnetic fields. Such magnetic fields are used in bubble expansion experiments to assess the strength of the Dzyaloshinskii-Moriya interaction. In addition, bombarding the ferromagnetic layer with heavy metal ions can induce local changes in material properties such as magnetic anisotropy which could be used to manipulate local pinning properties.

While computational micromagnetic simulations can help elucidate the behavior of domain walls, their computational cost prohibits extensive studies. As such, assessing the strength of the Dzyaloshinskii-Moriya interaction, extracting material parameters and understanding the behavior of the domain wall to an extent depends on simpler models of domain wall motion based on collective characteristics of the domain wall, and derived from applying model reduction methods to the more complex micromagnetic model.

Several Lagrangian-based collective coordinate models exist to describe domain wall motion, namely the $q - \phi$, $q - \phi - \Delta$, and $q - \phi - \chi$ models. While these models can describe domain wall motion with acceptable accuracy, they fail to replicate results of micromagnetic simulations specially for domain wall motion under the application of in-plane fields in heterostructures of interest. Moreover, recent advances in domain wall motion such as pinning due to irradiation have not been included in these models.

In this work, we will first present the process for developing Lagrangian-based collective coordinate models, culminating in the derivation of a four collective coordinate model for domain wall motion (the $q - \phi - \chi - \Delta$ model). We show how this model can be extended for cases where in-plane magnetic fields are present to correctly account for the physics; this extension involved introducing the canting induced by the in-plane fields in the domains. We also extend these models to describe the dynamics of magnetic bubbles.

In-plane field cases are specifically studied to help identify specific conditions which could help measure properties of the magnetic material. We also compare the equations derived using our Lagrangian-based approach to another reduced model developed through the application of statistical methods to the LLG equation, shedding light on the shortcomings of our approach. The work culminates with a summary of how these models may be made more realistic, through the inclusion of pinning and thermal effects within the model.

Contents

List of Tables

List of Figures

Nomenclature

This list includes several symbols that will be used later in the Chapters to represent specific quantities.

α	Gilbert damping	$\vec{\mathrm{M}}$	Magnetization vector
α_{R}	Rashba strength	$\vec{\mathrm{m}}$	Normalized magnetization vector
β	Nonadiabaticity coefficient	Ω	Angle determining location on a magnetic bubble
$\mathcal{F}$	Rayleigh dissipation function		
$\mathcal{L}$	Lagrangian	ϕ	Magnetization angle at the center of the DW
$\mathcal{T}$	Kinetic energy of the system		
$\mathcal{V}$	Potential energy of the system	Φ_{av}	SW magnetization angle in the semi-analytical model
χ	Magnetic susceptibility of a material		
		θ, Φ	Euler angles of magnetization, defined in Figure 2.3
χ	Tilt angle of the DW		
Δ	DW width	θ_{SH}	Spin Hall angle
Δ_{av}	DW width in the semi-analytical model	$*$	Denotes a steady state value of a parameter
γ	Gyromagnetic ratio	A	Exchange constant
$\hat{\mathrm{N}}$	Demagnetizing tensor	B	Magnetic field due to current or in magnetic materials also knows as the B-field
$\hat{\mathrm{u}}_{\mathrm{SOT}}$	Direction of spin-orbit effects		
$\hbar$	Planck's constant		
λ	Landau-Lifshitz damping	D	DMI strength in systems with symmetru breaking at the z interface
μ	Magnetic permeability of a material		
μ_0	Magnetic permeability of free space, also known as the magnetic constant or the permeability constant	E	Energy of the magnetic system
		e	Electron charge
		$\mathrm{E}_{\mathrm{dens,anis}}$	Anisotropy energy density
		$\mathrm{E}_{\mathrm{dens}}$	Total energy density of the system
μ_{B}	Bohr magneton		
$\vec{\tau}_{\mathrm{SOT}}$	Spin-orbit torques (SOTs)	g	Dimensionless magnetic moment
$\vec{\tau}_{\mathrm{STT}}$	Spin transfer torques (STTs)	H	Magnetic field in vaccum also known as H-field
$\vec{\mathrm{D}}$	DMI vector	H_{d}	Demagnetizing field

h_i	The i field normalized by the Walker breakdown field	t	Layer thickness
H_{anis}	Anisotropy field	u	Electron velocity
H_{eff}	Effective field	u_{Zeeman}	Zeeman energy density
H_{ext}	External magnetic field	X_{av}	DW geometric tilting in the semi-analytical model
H_{FL}	Field-like field due to spin-orbit effects	$\mathcal{H}$	Hamiltonian
H_{SL}	Slonczewski-like field due to spin-orbit effects	H_{anis}	Anisotropy field
H_{STT}	Effective field due to the Spin Transfer Torque (STT)	H_{exch}	Exchange field
		H_{ext}	External magnetic field
J	Current density	H_{ms}	Magnetostatic field
K_0, K_1, K_2	Anisotropy constants	H_R	Rashba field
K_U	Uniaxial anisotropy constant	H_{SHE}	Spin Hall effect field
K_{eff}	Effective anisotropy taking into account both uniaxial anisotropy and demagnetizing effects	DMI	Dzyaloshinski-Moriya interaction
		DW	Domain wall
M_s	Saturation Magnetization	MRAM	Magnetoresistive random access memory
N_a, N_b, N_c	Demagnetizing factors along ellipsoidal axes a, b, andc	Q	DW position in the semi-analytical model
P	Current polarization		
q	DW position	SHE	Spin Hall effect
		STT	Spin transfer torque

List of Dissemination Activities as Part of this PhD Thesis

Journal Publications

1. S. Ali Nasseri, Eduardo Martinez, Gianfranco Durin, "Collective coordinate descriptions of magnetic domain wall motion in perpendicularly magnetized nanostructures under the application of in-plane fields", Journal of Magnetism and Magnetic Materials (under review), arxiv: 1804.00569 [1].

2. Bhaskarjyoti Sarma, Felipe Garcia-Sanchez, S. Ali Nasseri, Arianna Casiraghi, Gianfranco Durin, "Dynamics and morphology of chiral magnetic bubbles in perpendicularly magnetized ultra-thin films with the Dzyaloshinskii-Moriya Interaction", Journal of Magnetism and Magnetic Materials, vol. 456, pp. 433-438, 2018, doi: 10.1016/j.jmmm.2018.01.075 [2].

3. Jasper Vandermeulen, S. Ali Nasseri, Ben Van de Wiele, Gianfranco Durin, Bartel Van Waeyenberge, and Luc Dupre, "Comparison between collective coordinate models for domain wall motion in PMA nanostrips in the presence of the Dzyaloshinskii-Moriya interaction", Journal of Magnetism and Magnetic Materials, vol. 449, pp. 337-352, 2018, doi: 10.1016/j.jmmm.2017.10.008 [Joint First Author] [3].

4. S. Ali Nasseri, Simone Moretti, Eduardo Martinez, Gianfranco Durin, Claudio Serpico, "Collective coordinate models of domain wall dynamics in PMA materials under spin Hall effect and longitudinal in-plane fields", Journal of Magnetism and Magnetic Materials, vol. 426, pp. 195-201, 2017, doi: 10.1016/j.jmmm.2016.11.081 [4].

5. Jasper Vandermeulen, S. Ali Nasseri, Ben Van de Wiele, Gianfranco Durin, Bartel Van Waeyenberge and Luc Dupre, "The effect of the Dzyaloshinskii-Moriya interaction on field-driven domain wall dynamics analysed by a semi-analytical approach", Journal of Physics D: Applied Physics, vol. 49 (46) no. 465003, 2016, doi: 10.1088/0022-3727/49/46/465003 [5].

Conference Proceedings

1. S. A. Nasseri, B. Sarma, G. Durin, C. Serpico, "Analytical modeling of magnetic domain wall motion under applied fields and currents", Physics Procedia (proceedings of the 20th International Conference in Magnetism, Barcelona), vol. 75, pp. 974-985, 2015, doi: 10.1016/j.phpro.2015.12.133 [6].

Conference Digests

1. S. A. Nasseri, E. Martinez, G. Durin, "Effect of canting on magnetic domain wall motion", IEEE International Magnetics Conference (INTERMAG), Dublin, April 2017, doi: 10.1109/INTMAG.2017.8007942 [7].

2. S. Ali Nasseri, S. Moretti, E. Martinez, G. Durin, C. Serpico, "Analytical modeling of domain wall dynamics in PMA materials under spin Hall effect and in-plane fields", Proceedings of the 1st IEEE Conference Advances in Magnetics (AIM), Bormio, Italy, March 2016 [8].

Oral Presentations and Talks

1. S. A. Nasseri*, G. Durin, "Spins in Space: Spintronics Enabling Future Space Exploration Endeavours", 68th International Astronautical congress (IAC), Adelaide, Australia, September 2017.

2. S. A. Nasseri*, E. Martinez, G. Durin, "Domain Wall Dynamics Under the Application of In-plane Fields: Wires vs. Films", 5th Italian Conference on Magnetism (MAGNET), Assisi, Italy, September 2017.

3. S. A. Nasseri*, E. Martinez, G. Durin, "Effect of Canting on Magnetic Domain Wall Motion", IEEE International Magnetics Conference (INTERMAG), Dublin, Ireland, April 2017.

4. S. A. Nasseri, "Spintronics in Space", Grid Talk, SpaceUp Milan, November 2016.

5. S. A. Nasseri, E. Martinez, G. Durin*, "Spin-Hall Effect Driven Magnetic Domain Wall Motion under the Application of In-plane Fields in PMA Nanowires", 61st Annual Conference on Magnetism and Magnetic Materials (MMM), New Orleans, USA, October 2016.

6. S. A. Nasseri*, G. Durin, "Collective Coordinate Models for Magnetic Domain Wall Motion", 7th Young Researcher Meeting (YRM), Torino, Italy, October 2016 [video].

7. S. A. Nasseri*, G. Durin, "Applications of Spintronics in Future Space Exploration Endeavours", 67th International Astronautical congress (IAC), Guadalajara, Mexico, September 2016.

8. S. A. Nasseri*, E. Martinez, G. Durin, "Analytical Modeling of Domain Wall Dynamics in PMA Materials under Spin Hall Effect and in-Plane Fields", 2nd Marie Curie School on Domain Walls and Spintronics, Spetses, Greece, September 2016.

9. S. A. Nasseri*, G. Durin, "Analytical Modeling of Magnetic Domain Wall Motion", 8th Joint European Magnetics Symposia (JEMS), Glasgow, UK, August 2016 [won second place for best early career presentation].

10. S. A. Nasseri*, E. Martinez, G. Durin, "Analytical Modeling of Domain Wall Dynamics in PMA Materials under Spin Hall Effect and in-Plane Fields", 8th Joint European Magnetics Symposia (JEMS), Glasgow, August 2016.

11. S. A. Nasseri*, E. Martinez, G. Durin, "Analytical Modeling of Domain Wall Dynamics in PMA Materials under Spin Hall Effect and in-Plane Fields", VI Euro-Asian Symposium Trends in Magnetism (EASTMAG), Krasnoyarsk, Russia, August 2016.

12. S. A. Nasseri*, S. Moretti, E. Martinez, G. Durin, C. Serpico, "Analytical Modeling of Domain Wall Dynamics in PMA Materials under Spin Hall Effect and in-Plane Fields", 1st IEEE Conference Advances in Magnetics (AIM), Bormio, Italy, March 2016.

13. S. A. Nasseri, "Limitations of the 1-D Model for DW Motion", Spinicur Summer School, Braga, Portugal, September 2015.

Poster Presentations

1. S. A. Nasseri*, R. Allenspach, G. Durin, "Analytical Description of Intermediate Domain Walls with semi-Neel Structure", 5th Italian Conference on Magnetism (MAGNET), Assisi, Italy, September 2017.

2. S. A. Nasseri*, G. Durin, "ITN-WALL: Controlling domain wall dynamics for functional devices", 2nd Science Communication School, Castiglione del Lago, Italy, March 2017.

3. B. Sarma*, Y. Liu, X. Zhang, N. Vernier, M. Voto, A. Magni, S. A. Nasseri, L. Lopez-Diaz, J. Langer, B. Ocker, G. Durin, L. H. Diez, and D. Ravelosona, "Tailoring the domain wall pinning in CoFeB/MgO films with perpendicular magnetic anisotropy", 61st Annual Conference on Magnetism and Magnetic Materials (MMM), New Orleans, USA, October 2016.

4. S. A. Nasseri*, G. Durin, "Analytical study of field-driven bubble expansion in PMA materials under the application of in-plane fields", 61st Annual Conference on Magnetism and Magnetic Materials (MMM), New Orleans, USA, October 2016.

5. J. Vandermeulen*, S. A. Nasseri, B. Van de Wiele, G. Durin, B. Van Waeyenberge and L. Dupr, "An averaging collective coordinate approach to interpret field-driven domain wall dynamics in magnetic nanostrips with Dzyaloshinskii-Moriya interaction", 2nd Marie Curie School on Domain Walls and Spintronics, Spetses, Greece, September 2016.

6. B. Sarma*, S. A. Nasseri, F. Garcia-Sanchez, B. Van de Wiele, G. Durin, "Evolution of bubble domain wall in the presence of Dzyaloshinskii-Moriya interaction", 2nd Marie Curie School on Domain Walls and Spintronics, Spetses, Greece, September 2016.

7. J. Vandermeulen*, S. A. Nasseri, B. Van de Wiele, G. Durin, B. Van Waeyenberge and L. Dupr, "An averaging collective coordinate approach to interpret field-driven domain wall dynamics in magnetic nanostrips with Dzyaloshinskii-Moriya interaction", 8th Joint European Magnetics Symposia (JEMS), Glasgow, UK, August 2016.

8. B. Sarma*, S. A. Nasseri, F. Garcia-Sanchez, B. Van de Wiele, G. Durin, "Evolution of bubble domain wall in the presence of Dzyaloshinskii-Moriya interaction", 8th Joint European Magnetics Symposia (JEMS), Glasgow, UK, August 2016.

9. S. A. Nasseri*, E. Martinez, G. Durin, "Analytical Modeling of Domain Wall Pinning in PMA Materials", 8th Joint European Magnetics Symposia (JEMS), Glasgow, August 2016.

10. S. A. Nasseri*, G. Durin, "ITN-WALL: Controlling domain wall dynamics for functional devices", Marie Curie Alumni Association Annual Conference, Venice, Italy, March 2016.

11. B. Sarma*, K. Shahbazi, A. Hrabec, S. A. Nasseri, B. Van de Wiele, C. Marrows, G. Durin, "Bubble Domain Wall Dynamics in the Presence of Dzyaloshinskii- Moriya Interaction", Micromagnetics: Analysis, Numerics, Applications (MANA), Vienna, Austria, February 2016.

12. S. A. Nasseri*, J. Vandermeulen, G. Durin, B. Van de Wiele, C. Serpico, "Magnetic DW motion: Comparison of analytical and statistical approaches", Micromagnetics: Analysis, Numerics, Applications (MANA), Vienna, Austria, February 2016.

13. S. A. Nasseri*, G. Durin, C. Serpico, "Analytical Modeling of Magnetic DW Motion", Newspin4: Transport beyond electrons conference, Utrecht, the Netherlands, December 2015.

14. B. Sarma*, S. A. Nasseri, J. Vandermeulen, B. V. Wiele, G. Durin, "Dynamics of the Magnetic Bubble-domains in a Perpendicular Magnetic Anisotropy (PMA) Thin Film with Dzyaloshinskii-Moriya Interaction", Spinicur Summer School, Braga, Portugal, September 2015.

15. S. A. Nasseri*, B. Sarma, G. Durin, C. Scerpico, "Analytical Modeling of Magnetic Domain Wall Motion under Applied Fields and Currents", 20th International Conference in Magnetism (ICM), Barcelona, Spain, July 2015.

Honors and Awards

1. IAF Young Space Leader Award, International Astronautical Federation, June 2018.

2. IAF Liugi G. Napolitano Finalist, International Astronautical Federation, September 2017.

3. Best Early Career presentation, 8th Joint European Magnetics Symposia (JEMS 2016) and Institute of Physics (IOP), August 2016.

Acknowledgments

Like any journey, the road to a PhD degree is filled with ups and downs; navigating through this path is not possible without the help and support of colleagues and mentors. While I will do my best to note all of those that contributed directly or indirectly to my journey, I apologize in advance if I miss anybody.

I would like to start by thanking Dr. Gianfranco Durin, my supervisor and scientific coordinator of the ITN WALL project, for offering me the position on the project and through that giving me the opportunity to enter the field of nanomagnetism and spintronics. I am so grateful for his support throughout my training, and his encouragement and acceptance of my other endeavors which helped me grow significantly in my professional life during the project.

The ITN WALL project was an international collaboration, and as such this work reports on the outcome of such collaboration with various researchers, as evident by the multiple coauthors on most of the publications resulting from this work. I would like to specially thank Professor Eduardo Martinez for supervising my month long research stay at the University of Salamanca, helping form the foundation of my studies on domain wall motion under in-plane magnetic fields. I also wish to thank Professor Rolf Allenspach for hosting me at IBM Research Zurich, where we studied anomalous domain walls with structures we are still trying to understand. A big thank you to all other WALL principal investigators, specially Professor Claudio Serpico, Professor Dafine Ravelosona, Dr. Liza Herera Diez, Professor Luis Lopez Diaz, Professor Thomas Moore, and Professor Mathias Kläui for continuous discussion and feedback throughout the project.

During this work we organized multiple meeting among the Early Stage Researcher's of ITN WALL and a summer school in Greece. These could not have been possible without the help of the ITN WALL Early Stage Researchers Benjamin Borie, Samridh Jaswal, Michele Voto, Simone Moretti, Risalat Khan, Kowsar Shahbazi, Bhaskarjyoti Sarma, Yuting Liu, Fabienne Musseau, and Gurucharan V. Karnad. Their feedback throughout the project definitely helped me better understand some of the scientific concepts, and at the same time helped me cope through some of the issues we faced together within the project and our PhD programs. I also wish to thank Jasper Vandermeulen, and his supervisors Ben Van de Wiele and Bartel Van Waeyenberge, with whom we collaborated on studying the semi-analytical collective coordinate models.

Finally, there were so many others who discussed ideas with me at INRiM, or as part of different discussions whom I wish to thank. Special thanks to Dr. Felipe Garcia-Sanchez and Dr. Arianna Casiraghi, our postdocs during the last year of ITN WALL, who provided a lot of insights on the research directions we took. Having conducted my work at ISI Foundation, I would like to thank the foundation for providing the facilities and helping me navigate the Italian red tape.

Chapter 1

Introduction

One of the promising fields of technological advancement is the area of *spintronics*, which exploits both the charge and the spin degrees of freedom of electrons in the design of devices [9, 10]. Fueled by the limitations of current technologies in areas such as storage media, physicists and material scientists have focused on developing a fundamental understanding of spintronic phenomena along with possible applications for these new discoveries in data processing, storage and transfer [11–20].

Advances in manufacturing have led to the miniaturization of electronic components towards nanoscale devices. Manipulating magnetic domain walls (DWs) in nanostructures has been linked with applications in spintronic logic [21–25], storage/memory [26–34] and sensing [35, 36]. Potential advantages of devices which use magnetic moments to carry information include low power dissipation, nonvolatile data retention, radiation tolerance, faster manipulation of data, high areal densities and lack of mechanical parts. Such applications have led to increased interest within the scientific community in developing models which can qualitatively or quantitatively describe the dynamics of magnetic moments.

1.1   Spintronics and Domain Wall Devices

Spintronic devices have been in industrial use for many years. Since the 1988 discovery of giant magnetoresistance [37, 38] which led to the 2007 Noble prize in physics for the scientists involved, there has been an increasing interest in the control of charge transport through magnetism, and use of new fundamental effects which emerge at the nanoscale in functional devices. Further studies in this area led to the creation of spin valve sensors and the first applications of spintronics in hard drive read-heads, helping increase hard drive capacities [26].

The next important application came with the *magnetoresistive random access memory (MRAM)*; this device combines nonvolatility, endurance and fast random access to the data, making it a likely candidate for universal memory [39]. A *universal memory* is one which combines data retention (seen in Flash and Read Only Memory - ROM), fast execution (seen in Dynamic and Static RAMs) with high density (seen in Hard Disk Drives). While MRAMs use the reading and writing principle previously used in magnetic core memories of the 1950s [40–42], they use new advances in nanofabrication and fundamental physics to improve storage capacity. In 2006, the first commercial MRAM was released by Freescale and in 2007 a space and military qualified version was introduced, meeting relevant thermal limits and using the intrinsic radiation resistance of magnetic storage to its advantage. MRAMs are limited by the *superparamagnetic threshold* which limits the size of the cells; below the size determined by this threshold, the magnetization of the cells can spontaneously reverse as a result of thermal fluctuations [30].

Magnetic Domain Walls (DWs) are interfaces that separate *magnetic domains*, areas in a magnetic material where the direction of magnetism is homogeneous. The next generation of magnetic mass storage devices could rely on moving DWs. This approach, which is closely related to the Bubble Magnetic Memories of the 1970s [43, 44], relies on the fact that file architectures for mass storage do not require random access to single bits; instead they need random access to sectors of sequential binary information, which could be represented by a chain of DWs in a strip of material. In a series of papers [28, 29], Parkin and his team presented the *racetrack memory*, which uses this principle in different architectures and relies on oscillating magnetic fields or electric currents to move the data. The racetrack memory promises mass storage without any mechanical moving parts along with the possibility of achieving 3-D memory units which could help with increasing storage capacity. Other concepts proposed in the area of magnetic memories include the use of structural features in nanowires to increase the number of memory states achievable [30], or using oscillating fields to move magnetic bubble domains as part of the *bubblecade memory* concept [34].

Up until 2002, most work on spintronics focused on data storage, and specifically MRAM applications. Logic devices became another possibility when Allwood et al. demonstrated an all-metallic submicrometer device able to perform NOT operations on magnetic signals [21]. This approach was later extended to other logic elements such as AND, Fan-out, Cross-over, and more complex logic circuits [22]. The main motivation of these attempts were to improve scaling by not using semiconductor materials [21].

Many other applications have been demonstrated for DW devices. For instance, nanomagnetic systems of DWs in in-plane magnetic materials have been used to manipulate ultracold atoms, which could find application in quantum information technology [45], and domain wall assisted transport of nanoparticles [46–48]. Spintronics has also been seen as an enabler of other novel technologies such as bioinspired computational architectures [49].

While all these applications are important and fuel further fundamental research, as noted by Dyakonov [50], these applications might never be realized or might be outperformed by other new technologies (as happened to the bubble memory); the hype should not overshadow scientific understanding.

1.2   Magnetic Domain Walls and Their Motion

Engineering any device that relies on magnetic domains or domain walls to code information will inadvertently require proper understanding of the motion of domain walls.

As depicted in Figure 1.1, domain wall motion has been generally broken down into three regimes depending on the strength of the driving interaction [51]:

1. The *creep regime*, where the driving interaction is low enough for the motion of the DW to be dominated by thermal activation and the disorder within the system.

2. The *depinning regime*, where the drive interaction is high enough for thermal activation to have minimal effect, but pinning still exerts a strong effect on the dynamics.

3. The *flow regime* where the drive interaction is much higher than pinning or thermal fluctuations, with minimal effect from the latter two contributions.

In the flow regime, it is well established that a steady state condition can be reached if the excitation is lower than the *Walker excitation* (H_w) [53]. In this condition the DW speed changes almost linearly with the drive interaction, a fact that could also be verified using micromagnetic simulations. Below the Walker breakdown, the precession of magnetization and evolution of other DW parameters halt after a specific amount of time has passed. Above the Walker breakdown field

(a) Low drive interaction.

(b) Flow regime.
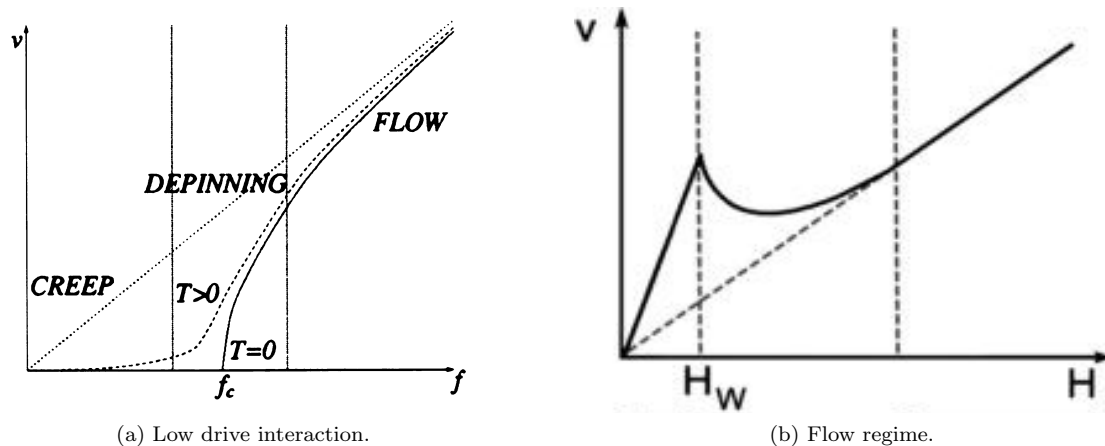
Figure 1.1: The main regimes of domain wall motion [51,52]. (a) In the absence of thermal effects, no creep is observed; however, a threshold drive force exists after which the interface moves. This threshold is the depinning force. Presence of thermal effects means that the interface can move at lower force strengths due to the extra energy contribution from the temperature. In the flow regime, effects of temperature and pinning are negligible. (b) Below a threshold field called the Walker breakdown field (H_W), the motion has a linear relationship with the field applied. Above this field, we see a reduction in speed due to energy dissipation from the precession of magnetization. At very high fields a linear regime can be observed with a different slope.

the domain wall moves back and forth (due to magnetization precession) with a general motion forward. At fields much higher than the Walker breakdown, the precession of magnetization becomes so fast that it leads to a linear increase of velocity with applied excitation; however, the slope is different compared to excitations lower thna the Walker breakdown.

It is notable that the motion of the domain wall has to be modeled differently in different regimes. Stochastic effects are dominant in the creep and depinning regimes, due to the effect of thermal fluctuations and disorder within the system. As such, modeling these regimes relies heavily on statistical physics. In the flow regime, the motion of the domain wall is more deterministic and acceptable results may be obtained without taking into account the stochastic nature of the physics.

1.3   Modeling DW Motion

The *Landau-Lifshitz-Gilbert (LLG)* equation has been used extensively to study magnetization dynamics in ferromagnetic systems. Micromagnetic simulation tools based on the LLG equation are flexible (may be applied to different problems in magnetism with new interactions introduced based on the set-up of the system) and help better understand the underlying physics; however, their use is computationally costly and might be hard to interpret at times.

Alternatively, simpler models may be extracted from the LLG equation to analyze the motion of specific spin textures of interest, such as vortices and DWs. In 1972, Slonczewski used a Lagrangian approach to propose the first widely used *collective coordinate model (CCM)* for DW motion in perpendicularly magnetized materials (the $q - \phi$ model) which takes into account the change in the position (q) and magnetization angle (ϕ) of the DW [54, 55]. Meanwhile, Thiele used a different approach to derive the equations of motion for magnetic bubbles based on a force description which some find easier to interpret [56, 57]. Both descriptions rely on an assumption for how the

3

perpendicular component of the magnetization changes within the system. In a series of papers, Sobolev et al. extended these models to systems under in-plane fields [58–61].

Thiaville and Nakatani later extended the Slonczewski model to in-plane systems, adding the DW width parameter (Δ) as an additional coordinate in the $q - \phi - \Delta$ model, and revisited the use of the Thiele model for in-plane systems [62]. They later added the spin transfer torque (STT) stemming from use of electric currents in their models as well [63, 64]. These collective coordinate models were later made more realistic by the inclusion of thermal fluctuations and pinning [65–68].

Recent studies on DW motion have focused on heterostructures of ultrathin ferromagnets sandwiched between a heavy metal layer and an oxide. In these systems, spin-orbit coupling (SOC) and broken inversion symmetry at the interfaces stabilizes Néel-like chiral DWs [69–71] through the interfacial Dzyaloshinski-Moriya interaction (DMI) [72, 73]. Transition to the Bloch DW structure is not favored in systems with DMI, and this delays the Walker Breakdown [53], allowing for larger DW velocities to be reached compared to systems without DMI [74]. SOC also leads to enhanced current induced DW motion, attributed to the spin Hall effect (SHE) [75, 76] or Rashba SOC [77, 78]. The main torques stemming from SOC may be added to the LLG equation as a field-like and a damping-like torque [79–81].

In the case of DW motion in perpendicular magnetic anisotropy (PMA) nanowires with DMI, the DWs were observed to tilt in the plane of the sample (Figure 1.2). This led to the development of the most recent collective coordinate model for DW motion, namely the $q - \phi - \chi$ model which takes into account the effect of rigid tilting of the DW through the parameter χ and assuming a fixed DW width [82, 83].
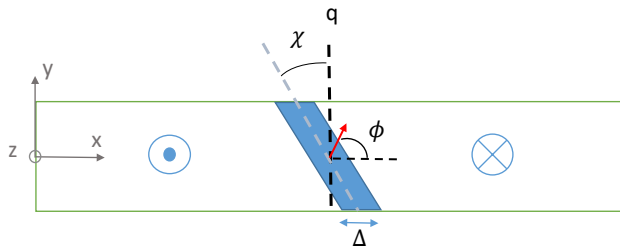
Figure 1.2: Visual depiction of the collective coordinates used to describe a DW in different models. The red arrow shows the magnetization inside the DW, which we assume is homogeneous at every point inside the DW.

While these collective coordinate models have been successfully applied to many problems, there have been several cases in which their use was unsatisfactory. One of the problems of interest is the study of DW motion in PMA systems with DMI under the application of applied fields in the plane of the sample [82–87]. While micromagnetic simulations of this problem are in agreement with experiments, conventional collective coordinate models ($q - \phi$ and $q - \phi - \chi$) fail to reproduce the micromagnetic results [82, 85]. The failure of CCMs is a major issue, as the main method for measuring DMI strength is bubble expansion under in-plane fields which relies on equations derived using the collective coordinate approach [88–90].

In addition, characterizing pinning based on material properties is key in modeling DW pinning due to ion irradiation [91–94], but this has not been achieved in analytical models. All these limitations call for improvements in collective coordinate modeling of DW motion.

1.4   Aims and Objectives

The aim of this work is to improve the accuracy of collective coordinate models used to describe the motion of magnetic domain walls (DWs) under applied fields and currents in perpendicular magnetic anisotropy (PMA) systems with the Dzyaloshinskii-Moriya interaction (DMI). The Euler-Lagrange equation with the Lagrangian and dissipation functions presented in reference [82] are used as a starting point to reduce the LLG equation from a spatio-temporal description to one based on temporal evolution of collective coordinates describing the DW. In order to study the heterostructures of interest, along with the traditional interactions (exchange, anisotropy and magnetostatics) and the Zeeman energy, we include the DMI [74,95,96], spin-orbit torques [80,81], and the STT mechanism [64,97].

Specific objectives of this work include:

- extension of the method of collective variables to derive simplified models for DW dynamics in PMA materials, under applied fields and currents (including spin-transfer and spin-orbit torque effects);

- description of the propagating DW state by a finite set of state variables, such as position and width, taking into account local spin structure features; and

- use of a Lagrangian approach, based on micromagnetic theory, to describe the dynamics of the state variables.

1.5   Approach

Based on micromagnetic simulations, experimental observations and previous studies in this area [54,62,82], the following time dependent collective coordinates were used to describe the collective behavior of the DW as depicted in Figure 1.2:

- The position of the center of the DW (q);

- The magnetization angle at the center of the DW (ϕ);

- The DW width parameter (Δ); and

- The geometric tilting of the DW (χ).

Using these coordinates, the DW is modeled as a thin line with four degrees of freedom as depicted in Figure 1.2. An ansatz is used to link the collective coordinates with the components of the magnetization, basically defining the structure of the object under study. For DWs, one such ansatz is the tilted Bloch profile [82], while another option is an inherently canted ansatz [58–61] proposed for cases when strong in-plane fields are applied. Irrespective of the ansatz used, we also assume that magnetization is homogeneous along the DW, hence $\phi(r,t) = \phi(t)$.

Armed with these assumptions for the profile of the DW, one can write the Lagrangian and dissipation density functions (describing the energy landscape of the system) in terms of the collective coordinates. This description of the energy landscape needs to be integrated along the dimensions of the system to characterize the total energy of the system. The total energy of the system may then be plugged into the Euler-Lagrange equation to derive the equations of motion. Depending on the ansatz used and the integration approach, different collective coordinate models may be developed which will be detailed in this thesis.

1.6   Structure of This Dissertation

This thesis has been prepared in 9 Chapters. The current Chapter highlighted the aims of the project, along with some of the background information regarding the field.

Chapter 2 introduces micromagnetic theory and the LLG equation in detail, highlighting the framework used in this work. In addition, a summary of material properties for typical materials currently under investigation are provided.

Chapter 3 focuses on the use of the collective coordinate approach to predict the static structure of domain walls.

Chapter 4 introduces the Euler-Lagrange approach for developing collective coordinate models in detail, and present four collective coordinate models for DW motion. The accuracy of these models are compared to micromagnetic simulations.

In Chapter 5, models from Chapter 4 are extended to include canting in the domains, which is an effect playing an important role in domain wall motion under in-plane fields. We apply the models to two cases of nanowires under in-plane fields, identifying critical points in domain wall motion.

Chapter 6 applies the models developed to magnetic bubbles in thin films, providing a toy model and showcasing the importance of using models with canting in measuring DMI.

Chapter 7 showcases a comparison between the models developed using the approach above with another model, called the "semi-analytical collective coordinate model" based on spatial averages of the LLG equation outputs.

Chapter 8 introduces effects of DW pinning and thermal activation on DW motion, and some of the approaches these effects may be added to collective coordinate models.

In Chapter 9, a summary of the findings of this work is presented, along with perspectives on future work.

Chapter 2

Magnetic Materials: Properties and Interactions

In this Chapter, we review some of the basic properties of magnetic materials, and the fundamental interactions that give rise to these properties. A list of typical material stacks currently under investigation by different groups will also be presented.

For conciseness, only the properties relevant to the studies in this thesis will be discussed. For more information about magnetic materials, readers may refer to references [98–100]. For more information about magnetic domain walls and their properties, the reader is referred to [101, 102].

2.1 Spins and Magnetic Moments

Subatomic particles such as protons, neutrons and electrons have *spins*. According to the Heisenberg uncertainty principle, particles at the same energy level need to have different spins. In the case of even numbers of particles, usually the spins cancel out; however, with an odd number of particles are present, or energy levels are not full, a net moment may exist. This is why 3d elements such as iron, cobalt, and nickel (the most commonly used magnetic elements) are ferromagnetic, showcasing specific behaviors under magnetic fields.

While atoms can have a net spin, *atomistic modeling* of systems based on quantum mechanics is resource intensive. *Continuum theories* of magnetism are not based on atomic spins, but based on *magnetization*, which is the summation of all spins within a specific volume of the system, or the density of magnetic spins within the system, with the units A/m. The *saturation magnetization* (M_s) is the maximum magnetization that a system can reach which coincides with a condition when all spins within the system are parallel.

The most distinctive features of ferromagnetism are the existence of the *Curie point* and the observation of a *hysteresis loop* [98]. At temperatures near the Curie point, the material loses its permanent magnetic properties. The hysteresis loop is a curve depicting the magnetization versus the applied field (H) measured in A/m or magnetic induction (B) measured in Teslas.

2.2 Energy Description of Magnetic Materials and Micromagnetics

Micromagnetics is the formulation of equations describing the microscopic arrangement of magnetization within a material. The term was coined by Brown [103, 104] who studied the total

magnetic energy of the material using a phenomenological description. In micromagnetics, the aim is to minimize the total free energy of the system with respect to the magnetization in order to find a relaxed state and describe system behavior.

Micromagnetics relies on the description of the system based magnetic moments $\vec{M} = M_s \vec{m}$, vectors which describe the properties of the spins in a macroscale volume in the system. In this equation $\tilde{m}$ is the normalized magnetization, describing the direction of magnetization while the saturation magnetization M_s describes the value of the magnetization. M_s can vary in space and time, but has an almost fixed value for temperatures far below the Curie temperature.

Different interactions contribute to the internal energy of the system. In most systems, these include the exchange interaction, magnetocrystalline anisotropy, magnetostatics, and the Zeeman energy.

The *exchange interaction* stems from electrostatic coupling between electron orbitals while satisfying the Pauli exclusion principle [98]. It favors long-range ordering of magnetization (electron spins), and prefers the magnetization vectors to be parallel with each other. Mathematically, the exchange interaction energy density is written as:

$$E_{dens,\,exchange} = A \sum_{i=1}^{3} |\nabla m_i| \tag{2.1}$$

Magnetocrystalline anisotropy stems from the interaction of electron orbitals with the potential from the hosting lattice which breaks the symmetry of isotropic exchange interactions [98]. In essence, anisotropy effects make specific spatial orientations of magnetization more favorable than others. This leads to the formation of *easy magnetization axes*, directions which are favored by anisotropy or along which anisotropy energy is minimum. On the other hand, unfavored directions are also formed, called *hard magnetization axes*, along which the anisotropy energy reaches a maximum. Johnson et al. performed an extensive review of magnetic anisotropy of metallic multilayers, with specific focus on Iron, Cobalt and Nickel [105]. They list theories and numerous experimental results for these materials.

Anisotropy can have various forms based on the complexity of the easy and hard axes. The simplest case is *uniaxial anisotropy* in which case anisotropy energy only depends on the orientation of magnetization with respect to a single axis. Most magnetic materials of interest have this form of anisotropy and are characterized by their anisotropy axis, with in-plane magnetized systems and perpendicular magnetized systems being the two commonly used.

The energy density due to uniaxial anisotropy may be formulated as:

$$E_{dens,\,anis}(\vec{m}) = K_0 + K_1 \sin^2 \theta + K_2 \sin^4 \theta + K_3 \sin^6 \theta + ... \tag{2.2}$$

in which K_0, K_1, K_2 and K_3 are anisotropy constants and θ is the angle the magnetization $\tilde{m}$ makes with respect to the anisotropy axis. In most cases, only the lowest degree term with respect to θ is considered, in which case K_1 is denoted as K_U.

Based on the anisotropy energy, the anisotropy field can be defined as:

$$H_{anis} = \frac{2K_1}{\mu_0 M_s} \tag{2.3}$$

The *magnetostatic energy* represents the mechanical work needed to build up the magnetic body by bringing its magnetic moments together, or in a sense the magnetic field sensed due to the finite nature of the system and the fact that flux lines need to close. Magnetostatics focuses on magnetic properties of steady state stationary currents and may be analyzed using a simplified form of the Maxwell equations of electromagnetism. In the context of magnetostatics, a helpful concept is the concept of magnetic charges. Despite not existing physically, these abstractions can help visualize a magnetic phenomena using analogy with electric charges.

Magnetized matter produces a magnetic field in space as a consequence of its atomic structure due to the electron's spin angular momentum. In the phenomenological description ,the magnetic matter is described as an assembly of elementary moments of atomic origin, with the magnetic field

$$\vec{B} = \mu_0(\vec{H} + \vec{M}) \tag{2.4}$$

Solving this equation requires a constitutive law for the medium, relating B or H to the magnetization. Such laws take the form:

$$\vec{B} = \mu\vec{H}$$
$$\vec{M} = \chi_m\vec{H} \tag{2.5}$$

in which μ and χ_m are the magnetic permeability and susceptibility of the medium, and related to each other through:

$$\mu = \mu_0(1 + \chi_m) \tag{2.6}$$

with $\chi_m \geq -1$ and $\mu > 0$ for thermodynamic stability. In a ferromagnetic body, the dependence of $\vec{M}$ on $\vec{H}$ is usually anisotropic, nonlinear, and hysteretic. Hence, this model is only an approximation used for simplicity.

Magnetostatic effects are usually summarized using the demagnetizing field, which opposes the magnetization:

$$\vec{H}_d = -\hat{N} \cdot \vec{M} \tag{2.7}$$

where N is the tensor of *demagnetizing factors.*

If the object under study has an ellipsoidal shape, N will be diagonally matrix defined along the ellipsoidal axes of the system, and we have three demagnetizing factors, N_a, N_b, N_c associated with each of the three ellipsoid principal axes, a, b, and c. These demagnetizing factors obey the general constraint $N_a + N_b + N_c = 1$. The demagnetizing field is small when the body has an elongated shape and the magnetization points along the long axis. The magnetostatic energy density of an ellipsoidal magnetic body can simply be written as [98]:

$$E_{dens, magnetostatic} = \frac{\mu_0}{2}\vec{H}_d \cdot \vec{m} = \frac{\mu_0}{2}(N_aM_a^2 + N_bM_b^2 + N_cM_c^2) \tag{2.8}$$

The demagnetizing factors of a generalized ellipsoid (assuming ellipsoidal semiaxes a,b, and c with $a \leq b \leq c \leq 0$) may be calculated using the following formulae [106]:

$$N_a = \frac{\cos\psi\cos\nu}{\sin^3\nu\sin^2\alpha}\left[F(k,\nu) - E(k,\nu)\right] \tag{2.9}$$

$$N_c = \frac{\cos\psi\cos\nu}{\sin^3\nu\cos^2\alpha}\left[\frac{\sin\nu\cos\psi}{\cos\nu} - E(k,\nu)\right] \tag{2.10}$$

$$N_b = 1 - N_a - N_c \tag{2.11}$$

with $\cos\nu = \frac{c}{a}$, $\cos\psi = \frac{b}{a}$ and $k = \sin\alpha = \frac{\sin\psi}{\sin\nu}$. F is the elliptical integral of the first kind:

$$F(k,\nu) = \int_0^k \frac{d\theta}{\sqrt{1 - \nu^2\sin^2\theta}} \tag{2.12}$$

9

and E is the elliptical integral of the second kind:

$$E(k,\nu) = \int_0^k \sqrt{1 - \nu^2 \sin^2 \theta} d\theta \tag{2.13}$$

Different authors have provided simpler descriptions for these factors based on mathematical simplification [107–110].

Finally, the *Zeeman energy* characterizes the energy added to the system due to the application of an external magnetic field. The energy density due to the external field has the form:

$$E_{dens,\,Zeeman} = \mu_0 \vec{M} \cdot \vec{H_{ext}} \tag{2.14}$$

2.3   Modeling Magnetization Dynamics: The LLG Equation

The *Landau-Lifshitz-Gilbert (LLG) equation* is a phenomenological relationship used in the continuum limit to describe magnetization dynamics through a series of torques on the magnetization. This equation, developed from energy minimization, has the form [111]:

$$\frac{d\vec{m}}{dt} = -\gamma \vec{m} \times \vec{H}_{effective} + \alpha \vec{m} \times \frac{d\vec{m}}{dt} \tag{2.15}$$

in which $\gamma = 1.79 \times 10^{11}$ is the gyromagnetic ratio, m⃗ is the normalized magnetization vector, $\vec{H}_{\text{effective}} = \frac{\delta E}{\delta \vec{m}}$ is the effective magnetic field acting on the magnetization and α is the phenomenological Gilbert damping, formulated based on the Lagrangian approach [111]. The LLG equation constitutes two torques as depicted in Figure 2.1: a torque by the effective field trying to precess the magnetization, and a damping torque perpendicular to the former which relaxes the magnetization towards the effective field direction.
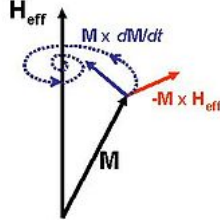
Figure 2.1: The torques due to the effective field and damping. The torque in red is due to the effective field and aims to precess the magnetization around the effective field direction, while the damping torque shown in blue eventually relaxes the magnetization towards the direction of the effective field. Most torques from other origins are usually studied in the field-like and damping-like directions defined in this figure.

The LLG equation can also be written as the *Landau-Lifshitz equation* with a different form of damping [112]:

$$\frac{d\vec{m}}{dt} = -\gamma_{LL} \vec{m} \times \vec{H}_{effective} - \lambda \vec{m} \times (\vec{m} \times \vec{H}_{effective}) \tag{2.16}$$

in which λ is the Landau-Lifshitz form of damping. The two equations can be transformed into one another using algebraic manipulation. The Landau-Lifshitz form of damping encounters problems

for large damping, which was the main reason behind developing the Gilbert form of damping [111]. As such, we will base all further discussion in this work on the LLG equation.

Due to our specific interest in current-induced magnetization dynamics, we will separate terms due to currents and add them as separate torques to the LLG equation, leading to the extended LLG equation:

$$\frac{d\vec{m}}{dt} = -\gamma\vec{m} \times \vec{H}_{effective} + \alpha\vec{m} \times \frac{d\vec{m}}{dt} + \vec{\tau}_{STT} + \vec{\tau}_{SOT} \tag{2.17}$$

where $\vec{\tau}_{\text{STT}}$ are the torques due to spin transfer and $\vec{\tau}_{\text{SOT}}$ are torques due to spin-orbit interactions. These torques will be outlined in the next sections.

2.3.1 The Effective Field

The *effective field* in the LLG equation is key to understanding magnetization dynamics. This field includes internal interactions within the magnetic material, and may include external stimulation of the system due to fields and currents. The effective field is related to the energy of the different interactions through $\tilde{H}_{\text{eff}} = -\frac{1}{\mu_0 M_s}\frac{\delta E}{\delta \tilde{m}}$. The major energy terms inherent to a ferromagnetic sample are exchange, magnetic anisotropy, and magnetostatic energies. Any applied external field will also contribute to the effective field through an associated Zeeman energy term.

In the presence of an applied field, the total energy density of a system with DMI and uniaxial anisotropy may be written as:

$$E_{dens} = \overbrace{A\sum_{i=1}^{3}|\nabla m_i|^2}^{Exchange} + \overbrace{K_U\sin^2\theta}^{Anisotropy} - \overbrace{\frac{\mu_0 M_s}{2}\vec{H}_d \cdot \vec{m}}^{Magnetostatics} - \overbrace{\mu_0 M_s\vec{H}_{ext} \cdot \vec{m}}^{Zeeman} \tag{2.18}$$

where A is the *exchange constant*, K_U is the uniaxial anisotropy constant, M_s is the saturation magnetization, H_d is the demagnetizing field, H_{ext} is the externally applied field and θ is the angle between the easy axis of magnetization and the magnetization. The demagnetizing field may be calculated as $H_d = -\hat{N}.\vec{m}$ where $\hat{N}$ is the demagnetizing tensor. It is also notable that the magnetostatic energy can be included in anisotropy energy as shape anisotropy. In a system with perpendicular magnetic anisotropy and ellipsoidal conditions, the effective anisotropy will be defined as:

$$K_{eff,0} = \frac{1}{2}\mu_0 M_s^2 N_z \tag{2.19}$$

$$K_{eff,U} = K_U + \frac{1}{2}\mu_0 M_s^2\left(N_x\cos^2\phi + N_y\sin^2\phi - N_z\right) \tag{2.20}$$

2.3.2 Spin Transfer Torques

When a spin polarized current is injected in a ferromagnetic material, it gives rise to *spin transfer torques (STTs)* which can induce magnetization dynamics and move a DW [113,114]. Sloncwezski and Berger were the first to predict this phenomenon [115,116], which was later experimentally demonstrated [117,118]. Spin polarization of current may be achieved by various methods, including injection of the current in a ferromagnet [19]; most nanowires are sufficiently long enough to assume spin polarization of the current to an extent as it traverses the ferromagnetic layer [64].

Two underlying mechanisms contribute to DW motion through STT:

1. Linear momentum transfer and electron reflection:In theory, the electron can be assumed to reflect completely after hitting the DW. The reflected electrons will have opposite spin compared to the incoming electrons. This requires linear momentum transfer to the wall, leading to DW motion. This mechanism is the most important for thin DWs due to electron scattering.

2. Electron transmission and angular momentum transfer: Theoretically, the electron can also traverse the wall. During this process, the electron changes its spin direction, which requires angular momentum transfer between the transmitting electron and the DW, to comply with conservation of angular momentum. This process is most important in thick DWs where strong exchange interaction prevents electron scattering.

Of course, in reality we have a combination of the two happening in any system.

Several authors developed theories to describe STT and its effects on magnetization dynamics [97, 119, 120]. These two processes can be modeled by adding two terms in the LLG equation: An adiabatic term taking into account electron transmission and angular momentum transfer, and a non-adiabatic term which stems from linear momentum transfer and spin relaxation. The torques on the magnetization due to these terms may be written as [64, 97]:

$$\vec{\tau}_{STT} = \underbrace{-\left(\vec{u} \cdot \vec{\nabla}\right)\vec{m}}_{adiabatic} + \overbrace{\beta\vec{m} \times \left(\left(\vec{u} \cdot \nabla\right)\vec{m}\right)}^{non-adiabatic} \tag{2.21}$$

in which β is the *nonadiabaticity coefficient* and $\vec{u} = \frac{\vec{J}Pg\mu_b}{2eM_s}$ is the velocity of the electrons, with J denoting current density and P denoting the polarization rate of the current. The adiabatic torque is also known as the in-plane or Slonczewski-like torque (the torque being in the same direction as the damping torque), while the non-adiabatic term is also called the field-like torque, perpendicular torque or β term (the torque being in the same direction as the torque due to the effective field). The direction of DW motion in STT is the same as that of electron motion or opposite current flow. Note that the non-adiabatic torque is the driving force in DW motion, while the adiabatic torque competes with damping and prevents precession to end.

These torques may also be included as an equivalent effective field using the following formulation:

$$H_{STT} = \underbrace{\vec{m} \times \left(\left(\vec{u}.\vec{\nabla}\right)\vec{m}\right)}_{adiabatic} + \overbrace{\beta\left(\vec{u}.\vec{\nabla}\right)\vec{m}}^{non-adiabatic} \tag{2.22}$$

Some authors describe this as the in-plane STT, as it is only valid when the current is going within the ferromagnetic layer. The out-of-plane spin transfer torque happens when the current is traversing the ferromagnetic layer perpendicular to the system (in magnetic tunnel junctions for example), and has a form similar to the Sloncwezski-like spin orbit torques presented in the next section (with u_{SOT} replaced with the current polarization vector) and $H_{SL} = \frac{-|g|}{2}\frac{\mu_B}{M_s}\frac{1}{t}\frac{J}{|e|}$ [116].

2.4   Spin Orbit Interactions

Recent studies on heterostructures of ultrathin ferromagnets sandwiched between a heavy metal layer and an oxide have highlighted the importance of *spin-orbit coupling (SOC)* and *broken inversion symmetry (BIS)* in domain wall (DW) motion. In these structures, interfacial effects contribute to DW motion as predicted theoretically [121–123] and later observed in experiments [75, 124].

Current-dependent spin-orbit interactions are observed in systems with a ferromagnetic layer sandwiched between two heavy metal layers, or a heavy metal layer and an oxide layer. Such effects stem from the fact that the flow of electric current in a crystalline structure lacking inversion symmetry can transfer orbital angular momentum from the lattice to the spins, giving rise to effects which can enhance the STT or act on their own to move DWs. Enhancement of current-driven DW motion in these systems was attributed to mechanisms such as the *Rashba spin-orbit effect* [77] and the *spin Hall effect* (SHE) [125].

In SHE, first predicted in 1971 [126, 127], spin dependent scattering in the heavy metal layer leads to spin accumulation at lateral boundaries of the heavy metal layer with opposite spins accumulating on opposite boundaries [50]. This leads to a spin current perpendicular to the charge current and interface normal, which may interact with the magnetization in the magnetic layer. The Rashba effect arises from spin dependent scattering at the interface of the heavy metal layer and the ferromagnet [78].

The main torques stemming from current dependent spin-orbit interactions may be modeled as [81]:

$$\tau_{SOT} = \underbrace{\gamma H_{FL}\left(\vec{m} \times \hat{u}_{SOT}\right)}_{field-like} - \overbrace{\gamma H_{SL}\vec{m} \times \left(\vec{m} \times \hat{u}_{SOT}\right)}^{Slonczewski-like} \tag{2.23}$$

in which $\hat{u}_{SOT} = \hat{J} \times \hat{n}$ is the direction of spin current when $\hat{J}$ is the direction of current flow in the heavy metal layer and $\hat{n}$ is the interface normal. These two torques are called the homogeneous torques, as higher order torques are not included in the above model [79, 80].

While both the SHE and Rashba effect contribute to these torques, it has been suggested [80, 81, 128] that, effectively $H_{FL}^{SHE} << H_{SL}^{SHE} = \frac{\hbar\theta_{SH}J}{2eM_st}$ in which θ_{SH} is the spin Hall angle which signifies the strength of the spin Hall effect and t is the layer thickness. It has also been suggested that $H_{SL}^{Rashba} << H_{FL}^{Rashba} = \frac{\alpha_R JP}{\mu_B M_s}$ in which α_R is a parameter outlining the strength of the Rashba effect. The strength of the field-like and damping-like components of the torque arising from SHE and Rashba effect are of course affected by the thickness of the layers [129].

It should be noted that some authors have argued that the above torques have a complex vector dependence on the direction of the magnetization, and that Rashba and SHE alone are not enough to explain such dynamics [80]. Other authors have noted that under specific circumstances (such as thin wires), one mechanism can give rise to considerable torques in both directions [130].

The torques mentioned above could also be included as an equivalent effective field [131]:

$$H_{SOT} = \underbrace{H_{FL}\hat{u}_{SOT}}_{field-like} + \overbrace{\frac{H_{SL}}{M_s}(\vec{m} \times \hat{u}_{SOT})}^{Slonczweski-like} \tag{2.24}$$

An example of current independent spin-orbit interaction is the interfacial *Dzyaloshinski-Moriya interaction (DMI)* also known as the antisymmetric exchange interaction which stems from interfacial spin-orbit coupling [72, 73]. This effect has the following Hamiltonian form:

$$\mathcal{H}_{DMI} = -\vec{D} \cdot (\vec{S_1} \times \vec{S_2}) \tag{2.25}$$

where $\tilde{D}$ is the DMI vector. This clearly shows that the DMI prefers the spins to lie perpendicular to each other. The energy density associated with the DMI for a sample isotropic in the plane, where the Dzyaloshinskii vector originated from symmetry breaking at the z surface, may be calculated as [74, 95, 96]:

$$E_{dens, DMI} = D(m_z\vec{\nabla}.\vec{m} - (\vec{m}.\nabla)m_z) \tag{2.26}$$

13

where D is a uniform constant signifying the strength of the DMI.

The DMI favors DW structures of specific chirality [69,70] and stabilizes Néel-like DW structures over the Bloch DW structure, with the final structure depending on the competition between DMI and anisotropy [71]. Thiaville et al. later suggested that this has consequences for DW motion, as it makes transition to the Bloch DW structure unfavorable and may increase the Walker breakdown field, allowing larger DW velocities [74]. Experiments have found that depending on the chirality of the DW and the stacking of the materials in the heterostructure, the DW might move along or against the direction of electron flow in systems with spin-orbit interactions [75,132]. As such, many recent studies have focused on tailoring the DMI interaction [89,133] to achieve more efficient DW motion.

2.4.1 Other Interactions

Other effects may also be included in the LLG equation. Electric fields [134–136] and mechanical stress [137] can also be used to manipulate DW motion. Pinning due to disorder in the system is usually modeled using a quadratic [138] or harmonic [139] pinning potential added to the energy landscape of the system. Thermal effects and wire roughness may also be modeled as stochastic processes changing the energy landscape of the system [140, 141]. The effect of defects may be included using a nonlinear dry friction dissipation model [67].

2.5 Micromagnetic Simulations

The LLG equation can be numerically solved within a system to understand the response of the system to different stimuli. Several tools for numerical solution of the LLG exist, most notably OOMMF [142], and Mumax^3 [143]. Both of these tools rely on finite difference solutions, with the former solving the equations using CPUs, and the latter relying on CUDA-enabled GPUs to do so. In this thesis, all simulations were performed with Mumax^3, unless otherwise stated in the text. The color code used to present the results from micromagnetic simulations is depicted in the color wheel of Figure 2.2. Outputs of Mumax^3 include the magnetic moment at each simulation cell. Details of post-processing the images to extract information of relevance to this work are presented in Chapter 4.
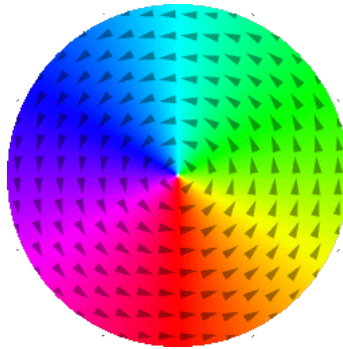
Figure 2.2: The color code used in micromagnetic snapshots presented in this work. The arrows show the direction of the magnetization and the color is the corresponding color used to denote that direction of magnetization. Magnetization out of the plane of the sample is shown as white or black.

As these tools rely on discretization of the solution space, it is important to understand their

limits. Cell sizes used in studies should be smaller than the exchange length, $l_{ex} = \sqrt{\frac{A}{K_{eff}}}$. At the same time, these cells cannot be too close to atomistic limits, where the continuum theory is no longer valid. All simulations in this work were done with a cell size of 1 nm $\times$ 1 nm unless otherwise stated.

An additional limitation of the micromagnetic approach based on the LLG is the assumption that the temperature is zero. Based on statistical mechanics [65, 141], approaches have been developed for approximating finite temperature effects on magnetization dynamics. Such approaches are only valid far below the Curie temperature, as the LLG equation also assumes a fixed saturation magnetization.

2.6 LLG in Spherical Coordinates

It seems simpler to use a set of spherical coordinates to describe magnetization, as they could be more intuitive. The spherical coordinates used to describe magnetization are depicted in Figure 2.3. The normalized magnetization vector in this case (assuming a constant saturation magnetization, M_s) is:

$$\vec{m} = (\cos \Phi \sin \theta, \sin \Phi \sin \theta, \cos \theta) \tag{2.27}$$

This helps describe magnetization as a spinning top, aiding in the development of the Lagrangian description of magnetization dynamics [103]. Note that, while the coordinates θ and Φ are useful for calculations, they only posses physical meaning for magnetization (or spins), and not the DW as a collective entity.
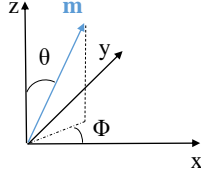
Figure 2.3: Spherical coordinates used in this work to describe magnetization.

The LLG equation in spherical coordinates (neglecting spin transfer and spin orbit torques) may be written as:

$$\dot{\theta} - \alpha \sin \theta \dot{\Phi} = \mu_0 \gamma H_\Phi \tag{2.28}$$

$$\alpha \dot{\theta} - \sin \theta \dot{\Phi} = \mu_0 \gamma H_\theta \tag{2.29}$$

where:

$$H_\theta = -\frac{1}{\mu_0 M_s} \frac{\delta E}{\delta \theta} = -\frac{1}{\mu_0 M_s} \frac{\delta E}{\delta m_i} \frac{\delta m_i}{\delta \theta} \tag{2.30}$$

$$H_\Phi = -\frac{1}{\mu_0 M_s \sin \theta} \frac{\delta E}{\delta \Phi} = -\frac{1}{\mu_0 M_s} \frac{\delta E}{\delta m_i} \frac{\delta m_i}{\delta \Phi} \tag{2.31}$$

Based on this description, it can be shown that the following Lagrangian and Dissipation functions could be used in the context of the Euler Lagrange equation to derive the LLG equation equivalent above:

$$\mathcal{L} = E + \frac{M_s}{\gamma} \dot{\Phi} \cos \theta \tag{2.32}$$

$$\mathcal{F} = \frac{\alpha M_s}{\gamma} \dot{m}^2 = \frac{\alpha M_s}{\gamma} \left(\dot{\theta}^2 + \dot{\Phi}^2 \sin^2 \theta \right) \tag{2.33}$$

Additional terms need to be added to the equations above to take into account the effect of STT and SOTs. A more complex form of this equation will be presented in Chapter 4.

2.7   Materials of Interest

In recent years, studies have focused on multilayers made of a ferromagnetic layer sandwiched between a heavy metal layer and an oxide. The composition of the sandwiching layers affect the magnetic properties of the ferromagnetic layer [144]. Initial interest in forming multilayers stemmed from the fact that the addition of the underlayers helped increase anisotropy due to interfacial effects. Later on, finding large DW velocities in systems with DMI led to further studies in these materials.

Table 2.1 summarizes some of the material stacks studied in the literature, some of which will be used in this work. Most properties of these stacks were determined experimentally, or through fitting the experimental results using models. In general, the stacks can be broken down into symmetric stacks (with the top and bottom layers being the same material and of the same thickness) and non-symmetric stacks. The heavy metal layer (in particular its spin-orbit coupling) and lack of symmetry in the stacks play major roles in the presence of the DMI in these systems.

Table 2.1: Properties of recent PMA material stacks used in the literature to study magnetic domain walls. HM denotes heavy metal, FM ferromagnet and Ox oxide.

Material	length (μm)	width (nm)	thickness (nm)	Msat (MA/m)	Aex (pJ/m)	Ku (MJ/m³)	α (-)	D (mJ/m²)	β (-)	θ_{SH} (rad)	Ref.
Pt/Co/Pt	20	1500	FM: 0.5 / HM: 4 .2	1.4	16	1.5	0.1	0.02	-	0.068	[75]
Pt/CoFe/MgO	40	500	FM: 0.6 / HM: 3 / Ox: 1.8	0.7	10	0.48	0.3	-1.2	-	0.07	[85,86]
Ta/CoFe/MgO	40	500	FM: 0.6 / HM: 5 / Ox: 1.8	0.7	10	0.48	0.3	-0.05	-	-0.11	[85,86]
Pt/CoSiB/Pt	50	150 300 500	FM: 0.6 / HM: 1.4	0.35	10	0.15	0.5	0.43	-	0.06 [145]	[146]
Pt/Co/AlOx	10	500	FM: 0.6 / HM: 3 / Ox: 2	0.796	10	1.19	0.5	-2.2 [147]	-	0.07 [85]	[77]
Pt/Co/AlOx	-	-	0.6	1.09	10	1.25	0.5	-2.2 [147]	1.7	0.07 [85]	[82] [148]
Pt/Co/AlOx	-	-	FM: 0.8 / HM: 4 / Ox: 3	1.18	16	0.41	0.39	1.63	-	-	[149]
Pt/Co/Gd	-	-	FM: 1 / HM: 4 / Ox: 3	0.64	16	0.26	0.3	1.78	-	0.07 [85]	[149]
Pt/Co/Ni/Co/Pt	50	2000	FM: 0.3, 0.7, 0.15 / HM: 1.5 / N: 5	0.6	16	0.72	0.1			0.1	[76]
Pt/Co/Ni/Co/Pt	-	57-300	FM: 0.4, 0.8, 0.4, 0.8, 0.4, 0.8, 0.55 / HM: 3, 1.5	0.570	12	0.28	-	0	-	-	[150]
Pt/Co/Ni/Co/Pt	50	1000	FM: 0.3, 0.6, 0.3 / HM: 2	0.837	10	0.9	0.15	0.038	-	0.07 [85]	[151]
Pt/Co/Ni/Co/MgO/Pt	50	1000	FM: 0.3, 0.6, 0.3 / HM: 2 / Ox: 1	0.837	10	1.31	0.15	0.6	-	0.07 [85]	[151]
Ir/Co/Ni/TaN	50	2000	FM: 0.3, 0.7, 0.15 / HM : 5 - / N: 5	0.52	16	0.3	0.07	0.037	0	0.008	[152]
Pd/Co/Ni/TaN	50	2000	FM: 0.3, 0.7, 0.15 / HM : 5 / N: 5	0.54	10	0.25	0.04	0.0261	0	0.045	[152]
Pt/Co/Ni/TaN	50	2000	FM: 0.3, 0.7, 0.15 / HM : 2 / N: 5	0.59	16	0.54	0.1	0.2642	0	0.098	[152]
Au/Co/Ni/TaN	50	2000	FM: 0.3, 0.7, 0.15 / HM : 5 / N: 5	0.514	16	0.19	0.1	0	0.08	0	[152]

Chapter 3

Domain Wall Structures

Using a theoretical approach based on energy minimization, different static stable structures within the magnetic material can be derived [55, 101, 102, 153]. Magnetic domains walls are formed to minimize the energy in the system mainly owing to the effects from magnetostatics. They are interfaces through which magnetization rotates from a specific direction in the first domain, to another direction in the second domain; this rotation is typically 90 or 180 degrees. In recent years, the energy minimization method has been extended to systems with DMI, showcasing a difference in the type of DWs formed [153].

In this Chapter, we study the structure of magnetic domain walls in the materials of interest. We will present the theoretical predictions of magnetic domain wall structures, and compare them to micromagnetic simulations. These static structures are key to the models which will be developed in future Chapters to describe DW dynamics.

3.1 DW Structure without DMI

In perpendicularly magnetized thin films, the main interactions playing a role in magnetic texture of the material are exchange, anisotropy, and the dipolar interactions. Using spherical coordinates (Figure 3.1), the total internal energy density (E_{dens}) for a material with uniaxial crystalline anisotropy in the absence of any external excitation may be written as:

$$
E_{dens} = \overbrace{A \left[\left(\frac{\partial \theta}{\partial x} \right)^2 + \left(\frac{\partial \theta}{\partial y} \right)^2 + \left(\frac{\partial \theta}{\partial z} \right)^2 + sin^2\theta \left(\left(\frac{\partial \Phi}{\partial x} \right)^2 + \left(\frac{\partial \Phi}{\partial y} \right)^2 + \left(\frac{\partial \Phi}{\partial z} \right)^2 \right) \right]}^{Exchange}
$$
$$
+ \overbrace{K_U \sin^2 \theta}^{Anisotropy} + \overbrace{\frac{\mu_0}{2} M_s^2 \left(N_x \sin^2 \theta \cos^2 \Phi + N_y \sin^2 \theta \sin^2 \Phi + N_z \cos^2 \theta \right)}^{Magnetostatics}
$$

(3.1)

In the above equation, the demagnetizing factors may be calculated based on the geometry of the system and ellipsoidal approximations as highlighted in Chapter 2.

3.1.1 Variation of the Perpendicular Component of Magnetization θ: The Bloch Profile

Assuming an infinitely long wire with a flat domain wall, neglecting edge effects (or assuming a large width), and assuming a homogeneous in-plane magnetization along the DW, we can model

(a) Spherical coordinates.   (b) Collective coordinates.
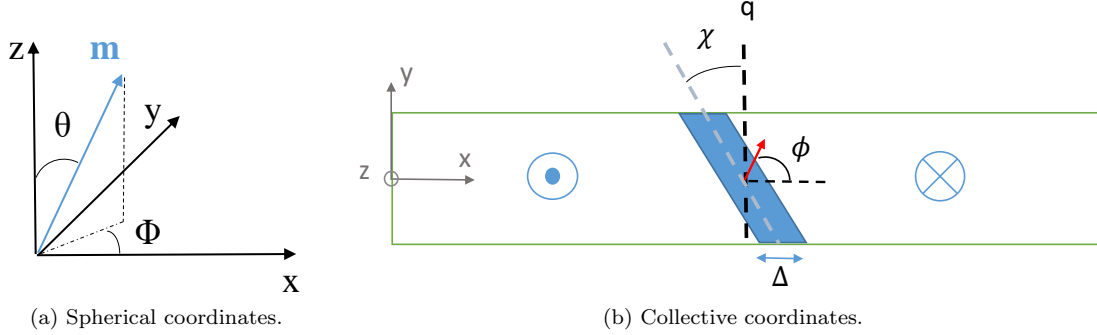
Figure 3.1: The coordinate systems used in this work. The collective coordinates of interest here are the DW width parameter Δ, the DW magnetization angle ϕ and the geometric tilting of the DW χ.

this system as a one dimensional system where all changes happen along the length of the wire. The energy density in this case simplifies to:

$$E_{dens} = A \left(\frac{\partial \theta}{\partial x} \right)^2 + \left(K_u + \frac{\mu_0 M_s^2}{2} \left(N_x \cos^2 \Phi + N_y \sin^2 \Phi - N_z \right) \right) \sin^2 \theta + \frac{\mu_0 M_s^2}{2} N_z \quad (3.2)$$

The total energy density of the static system should be constant as no external excitation is applied to the system. Hence, we need to solve the differential equation:

$$A \left(\frac{\partial \theta}{\partial x} \right)^2 + \left(K_u + \frac{\mu_0 M_s^2}{2} \left(N_x \cos^2 \Phi + N_y \sin^2 \Phi - N_z \right) \right) \sin^2 \theta = constant \quad (3.3)$$

A particular solution of this equation is what has been dubbed the *Bloch profile*:

$$\tan \left(\frac{\theta}{2} \right) = \exp \left(\pm \frac{x - q}{\Delta} \right) \equiv \sin \theta = \frac{1}{\cosh \left(\pm \frac{x-q}{\Delta} \right)} \quad (3.4)$$

with Δ defined as:

$$\Delta = \sqrt{\frac{A}{K_u + \frac{\mu_0 M_s^2}{2} \left(N_x \cos^2 \phi + N_y \sin^2 \phi - N_z \right)}} \quad (3.5)$$

and ϕ being a temporal measure of the spatio-temporal variable Φ.

The range for θ using this function is $[0, \pi]$, which makes sense based on what is observed in experiments on perpendicular systems and in micromagnetic simulations. Note that this description of the domain wall is valid in any system (in-plane or perpendicular); only the coordinate system should be adjusted for in-plane systems.

3.1.2   Variation of the In-plane component of Magnetization ϕ

To find the ϕ degree of freedom (or in-plane component of magnetization inside the DW), we first need to plug in the DW profile derived in the previous section into the equations and integrate along the length of the wire. The energy density integrated over the wire length of the wire E_x

will be:

$$E_x = \frac{-2A}{\Delta} - 2\Delta \left(K_u + \frac{\mu_0 M_s^2}{2} \left(N_x \cos^2 \phi + N_y \sin^2 \phi - N_z \right) \right) + \frac{\mu_0 M_s^2}{2} N_z l$$

$$= -4\sqrt{A \left[K_u + \frac{\mu_0 M_s^2}{2} \left(N_x \cos^2 \phi + N_y \sin^2 \phi - N_z \right) \right]} + \frac{\mu_0 M_s^2}{2} N_z l \qquad (3.6)$$

$$= -4\sqrt{A \left[K_u + \frac{\mu_0 M_s^2}{2} \left(N_x - N_z + (N_y - N_x) \sin^2 \phi \right) \right]} + \frac{\mu_0 M_s^2}{2} N_z l$$

where l is the length of the nanowire, which coincides with the direction along which the DW profile changes based on the assumptions. Using energy minimization $\partial E_x / \partial \phi = 0$, we get:

$$-\Delta \mu_0 M_s^2 \left(N_y - N_x \right) \sin 2\phi = 0 \Rightarrow \phi = 0, \frac{\pi}{2}, \pi \frac{3\pi}{2} \qquad (3.7)$$

which predicts two classes of domain walls based on the rigid model presented here. The cases $\phi = 0$ or π are called Néel DWs, while the case with $\phi = \frac{\pi}{2}$ or $\frac{3\pi}{2}$ characterizes Bloch DWs. In the Néel DW, the magnetization rotates along the direction parallel to the DW and in the plane of the thin film, while for Bloch DWs the magnetization rotates about an axis perpendicular to the DW and out of the plane of a thin film sample. Figure 3.2 shows these two type of DWs. Clearly, this theoretical approach does not predict an intermediate state between Bloch and Néel. To determine whether the Bloch structure or Néel structure is present, one should compare the energy for the two cases; the structure with the lowest energy is the stable structure predicted by the theory.
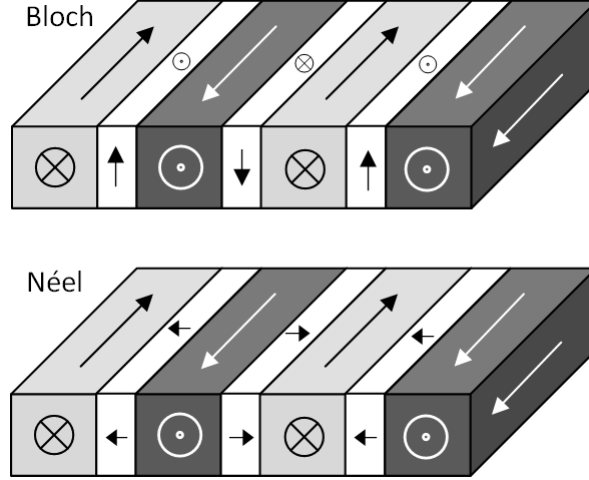
Figure 3.2: The structure of Bloch and Néel domain walls. The domains are marked with different shades of gray and the domain walls in white.

3.1.3 Validation of Theory

To validate the theory above, we compared the DW structure predicted from micromagnetics to that predicted by the theory for Pt/Co/Ni/Co/Pt [150, 151] and Au/Co/Ni/TaN [152] which are systems without DMI as listed in Chapter 2. We observed that in all cases the θ component of magnetization followed the Bloch profile. Figure 3.3 shows the results of this comparison for the

magnetization angle ϕ and the DW width parameter Δ; the lines in this figure are a result of numerically simulating the energy for different magnetization angles using the one-dimensional model of DW structure presented here, and then finding the magnetization corresponding to minimum energy. The squares showcase the results from micromagnetic simulations.

From Figure 3.3.b, it is clear that the model fails to reproduce micromagnetic results as the DW becomes wider. This is understandable as a wider wall is more 2-D and has higher degrees of freedom while the model assume all changes happening along the DW. Moreover, the assumption of a homogeneous ϕ along the wall is not fully valid for a wide DW.

Figure 3.3.a shows two cases where intermediate DWs are predicted from micromagnetics while the analytical description in one case does not predict a transition from Bloch to Néel and in the other case predicts an abrupt one. Figure 3.3.b shows a case in which the transition takes part over a wider range of wire widths, with an intermediate DW being stable from $200-300$nm. Comparing the width of the DWs as shows in Figure 3.3.c, we see that the gold sample has a much wider DW with potential for potential for more local minimums where the micromagnetic simulation can stop at. In addition, the gold sample DWs are the least 1-D, as owing to the low anisotropy and wider DWs.

These transitory domain wall structures are in contradiction with our model and other analytical [154] and micromagnetic [154, 155] studies. This partially arises as in most micromagnetic studies, the authors assumed that the DWs can only have Bloch or Néel structure, and only compared the energy of these two cases.

To better understand the reason for the differences seen in Figure 3.3, we initially looked at the changes in the energy density of the different interactions in the system with DW width as depicted in Figure 3.4. Clearly, the source of the presence of intermediate DWs with structure between Bloch and Néel is the change in the dipolar interaction whose energy density varies with the DW width the most.

Looking at the variation of the demagnetizing field of the system with DW width as depicted in Figure 3.4, we see that during transition from Bloch to Néel, the demagnetizing field along the y and z direction dramatically changes. We also see that in the Au/Co/Ni/Co/TaN system, the changes in the demagnetizing field take place over a longer width similar to changes in ϕ. While the general behavior of the different components of the demagnetizing field is the same in all three cases, the changes happen over a different range of wire width values as the DW gets wider.

As depicted in Figure 3.6, an increase in saturation magnetization will shift the transition towards higher widths, while increasing the uniaxial anisotropy shifts the transition to lower widths. This is understandable, as the major interactions playing a role in these systems are the anisotropy and the demagnetizing field, with the demagnetizing field being directly related to M_s.

Figure 3.5 shows how the ellipsoidal approximation of the demagnetizing factors vary with the nanowire width. Clearly, as the system gets wider, the perpendicular (N_z) and transverse (N_y) component of demagnetizing factors increase with the longitudinal component (N_x) decreasing until they reach a somewhat fixed value. We also see that the system with the lowest K_u has the highest N_z (anisotropy exerts this effect by changing the domain wall width Δ). These changes in demagnetizing factors are important, but clearly do not fit the changes in the demagnetizing fields seen in Figure 3.4 (note that the demagnetizing field is $B_i = -M_s N_i m_i$ for an ellipsoid where i is the axis under consideration; as such, we verified that the demagnetizing factors and field follow almost the same trend). While the ellipsoidal demagnetizing factors vary smoothly, the demagnetizing fields in Figure 3.4 vary much differently; specifically B_z initially becomes negative before moving to positive values, and B_y initially drops and then increases. These complex changes in the dipolar fields seem to be the source of the inaccuracy of the one dimensional model.

To better understand the profile of the DW along the width of the wire), we plotted the changes of the magnetization angle at the center of the DW (ϕ) along the width of the Pt/Co/Ni/Co/Pt

(a) Magnetization angle (ϕ) in Pt based systems.

(b) Magnetization angle (ϕ) in a Au based system.

(c) Variation of DW width (Δ).
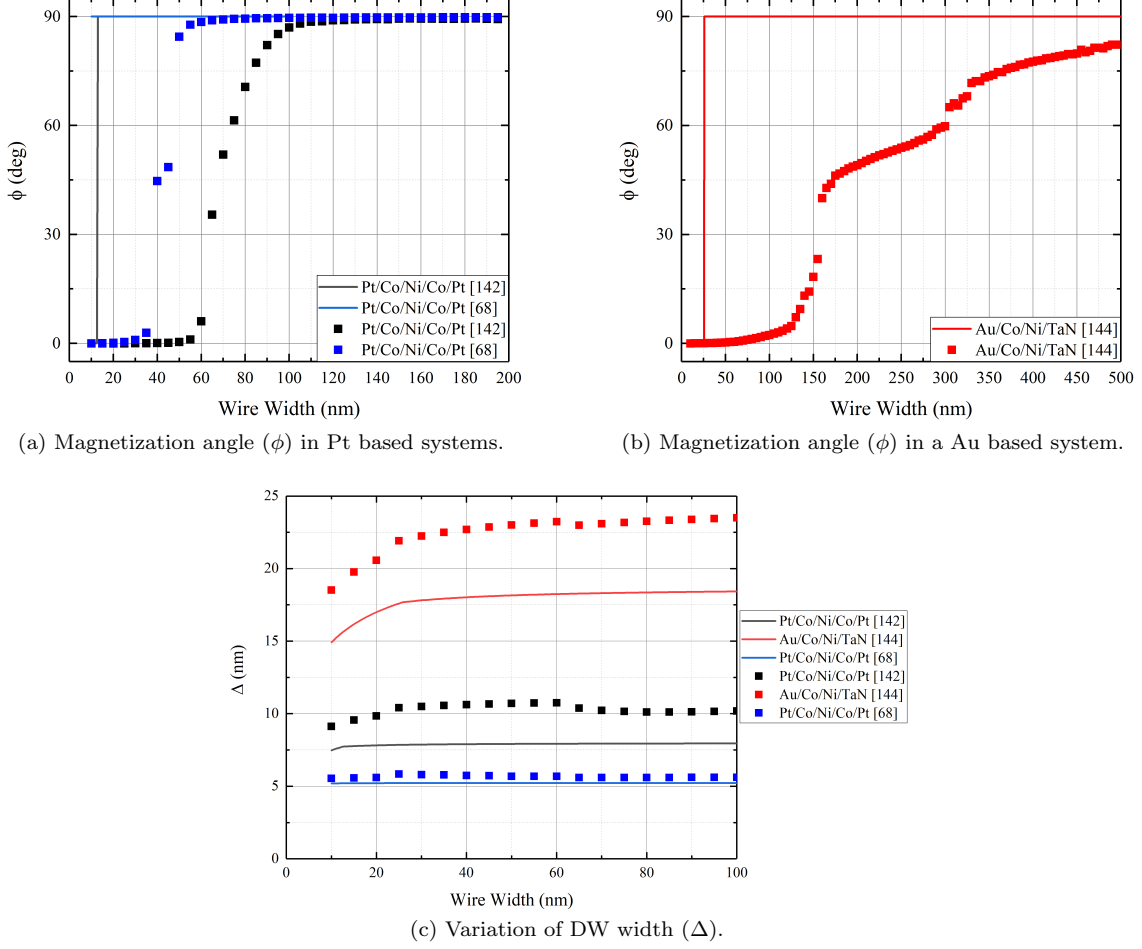
Figure 3.3: The variation of magnetization angle and domain wall width parameter with wire width in three different systems without DMI. The lines showcase one-dimensional predictions, while the squares are results of micromagnetic simulation. (a) shows two cases where intermediate DWs are predicted from micromagnetics while the analytical description in one case does not predict a transition from Bloch to Néel and in the other case predicts an abrupt one. (b) shows a case in which the transition takes part over a wider range of wire widths. From (c) it is clear that the model fails as the DW becomes wider. We did not show the change in DW width for wire widths more than 200 nm as the DW width changed negligibly for higher wire widths.

nanowire [150] in Figure 3.7. We see that at widths lower than 40nm, the DW has a Néel structure overall, with the in-plane magnetization slightly changing along the DW in an almost linear manner. Above 40nm width, these changes become more profound, and the profile of the in-plane magnetization changes from somewhat linear to a parabolic shape along the width (as shown in Figure 3.7.b and c). In these intermediate DWs, the structure near the edge may have a magnetization angle up to 5 degrees different from the middle of the wire. As the width increases, the DW changes to a fully Bloch structure, with a profile showing magnetization being about 90 degrees at a large part of the center of the DW, and slightly above or below that value at the two edges (Figure 3.7.d).
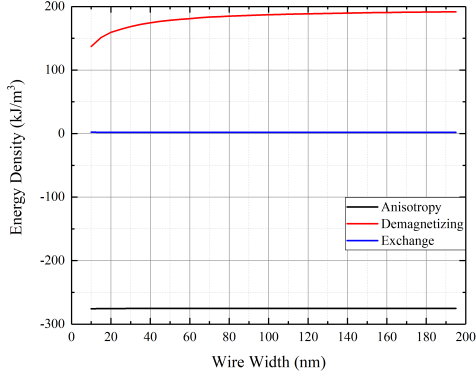
(a) Energy density variation with nanowire width for the Pt/Co/Ni/Co/Pt sample [150].
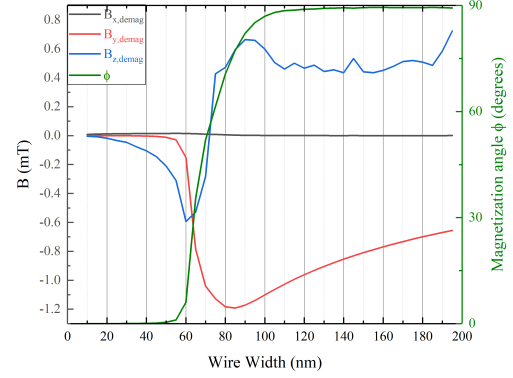
(b) Demagnetizing field and magnetization angle variation with nanowire width for the Pt/Co/Ni/Co/Pt sample [150].
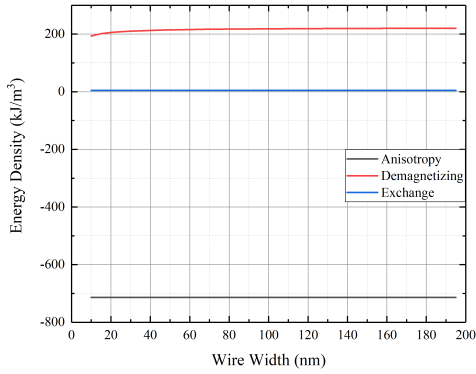
(c) Energy density variation with nanowire width for the Pt/Co/Ni/Co/Pt sample [76].
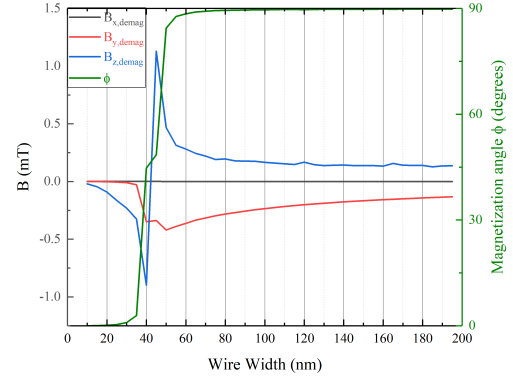
(d) Demagnetizing field and magnetization angle variation with nanowire width for the Pt/Co/Ni/Co/Pt sample [76].
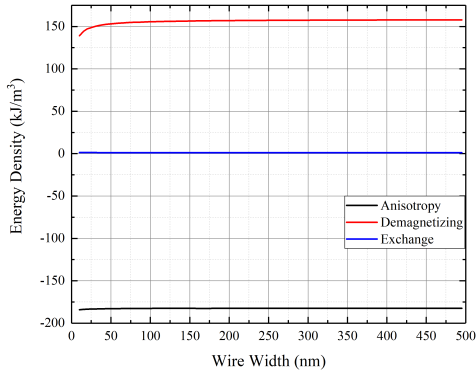
(e) Energy density variation with nanowire width for the Au/Co/Ni/TaN sample [152].
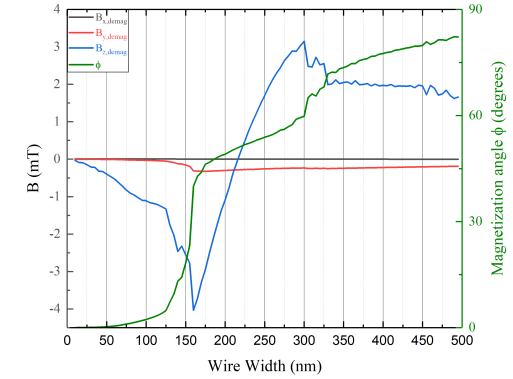
(f) Demagnetizing field and magnetization angle variation with nanowire width for the Au/Co/Ni/TaN sample [152].

Figure 3.4: The variation of DW energy density and demagnetizing fields with the width of the wire in three different systems without DMI from micromagnetic simulations. (a), (c), and (e) show that the main source of difference is the demagnetizing energy. In (b), (d), and (f) we see that in fact the changes in the demagnetizing field in the x and z direction gives rise to the transition from Bloch to Néel DWs.

23
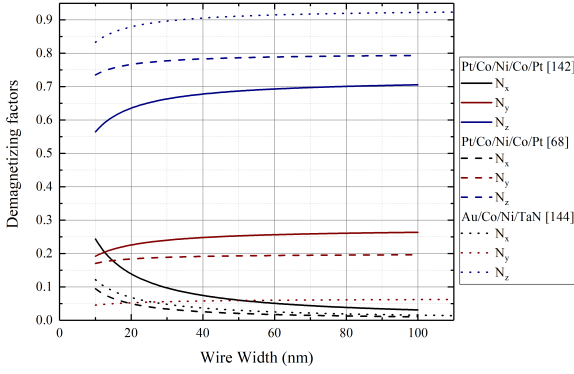
Figure 3.5: The variation of the demagnetizing factors in the one-dimensional model with nanowire width.
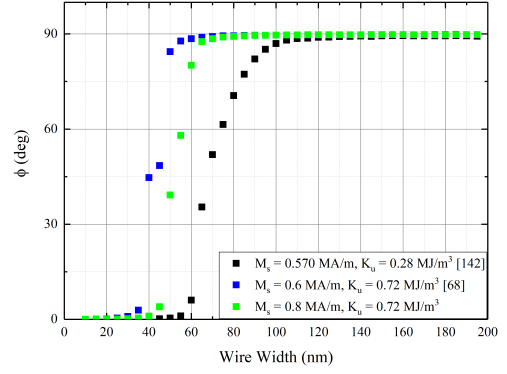
Figure 3.6: Change in DW structure with width for different material parameters based on micromagnetic simulations.

(a) w = 10 − 50 nm

(b) w = 60 nm

(c) w = 90 − 95 nm

(d) w = 120 and 190 nm
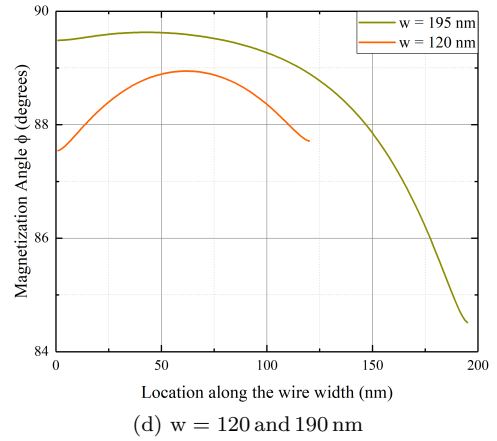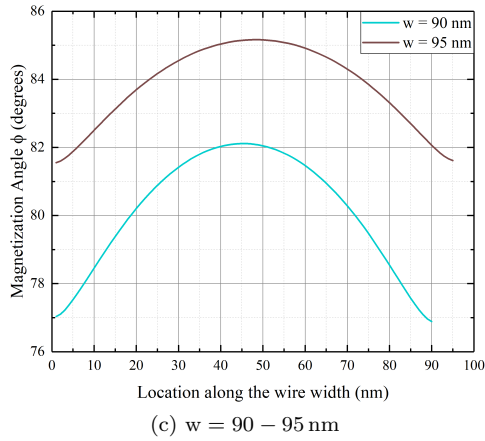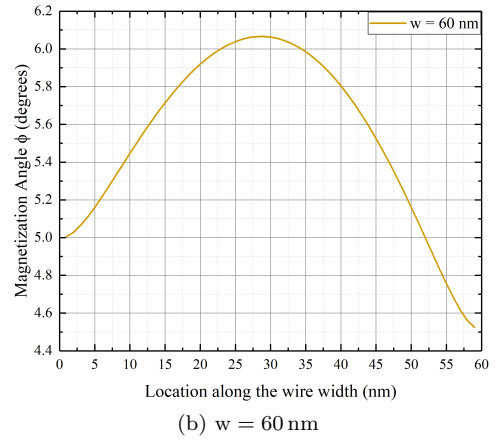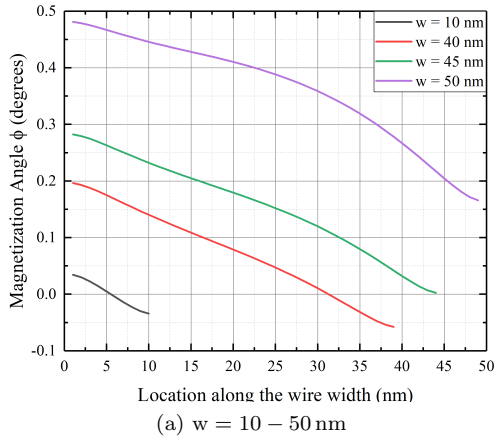
Figure 3.7: Variation of the in-plane magnetization ϕ along the width of the Pt/Co/Ni/Co/Pt wire [150]. (a) For Néel DWs, this variation is almost linear. (b) and (c) during the transition this variation becomes non-linear. (d) For the cases close to a Bloch DW the variation stays nonlinear but a less quadratic form.

3.2   DW Structure with DMI

We now focus on systems with spin-orbit coupling and broken inversion symmetry which give rise to the interfacial Dzyaloshinskii-Moriya interaction. In these systems, an additional term due to the DMI needs to be added to the one-dimensional energy of Equation 3.2:

$$E_{dens} = A \left(\frac{\partial \theta}{\partial x} \right)^2 + \left(K_u + \frac{\mu_0 M_s^2}{2} \left(N_x \cos^2 \Phi + N_y \sin^2 \Phi - N_z \right) \right) \sin^2 \theta + D \cos \Phi \frac{\partial \theta}{\partial x} + \frac{\mu_0 M_s^2}{2} N_z$$

(3.8)

3.2.1   DW Profile: Variation of θ

For a small enough DMI strength, the spin texture will not rotate, and the solution to the system is a DW with the same Bloch profile as before. However, in the presence of high DMI there are other solutions possible which are beyond the scope of this work [153].

If the domain wall tilts rigidly (which is seen in systems with DMI when the DW moves as discussed in the next Chapter), this will simply change the terms inside the profile to:

$$\tan \left(\frac{\theta}{2} \right) = \exp \left(\pm \frac{(x - q) \cos \chi + y \sin \chi}{\Delta} \right)$$

(3.9)

where χ is the geometric tilting angle, and the DW is assumed to tilt as a rigid line as depicted in Figure 3.1.

Figure 3.8 highlights the effect of changing the ansatz parameters. Clearly, the DW width defined through the ansatz is much more rigid than a real DW (with no internal degree of freedom). This means there should be a limit for the width, after which the profile is no longer valid. A similar effect is seen for tilting, where the wall seems to deform for $\chi > \frac{\pi}{4}$. In general, the profile seems to work for moderate tilting and DW width.

3.2.2   In-plane Magnetization of the DW ϕ

Assuming no tilting for now ($\chi = 0$ which is valid for static DWs), the integrated energy density along the length of the wire has the form:

$$E_x = -4\sqrt{A \left[K_u + \frac{\mu_0 M_s^2}{2} \left(N_x - N_z + (N_y - N_x) \sin^2 \phi \right) \right]}$$
$$+ \pi D \cos \phi + \frac{\mu_0 M_s^2}{2} N_z l$$

(3.10)

and energy minimization ($\frac{\partial E_x}{\partial \phi} = 0$) results in:

$$-2\Delta \frac{\mu_0 M_s^2}{2} \left(N_y - N_x \right) \sin 2\phi - \pi D \sin \phi = 0 \Rightarrow$$

$$\cos \phi = -\frac{\pi}{2} \frac{D}{\mu_0 M_s^2 \Delta \left(N_y - N_x \right)} = -\frac{\pi}{2} \frac{H_{DMI}}{H_K}$$

$$= -\frac{\pi}{2} \frac{D}{\sqrt{A}} \frac{\sqrt{K_u + \mu_0 M_s^2 \left(N_x \cos^2 \phi + N_y \sin^2 \phi - N_z \right)}}{\mu_0 M_s^2 \left(N_y - N_x \right)}$$

(3.11)
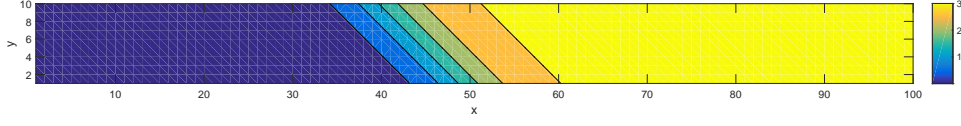
(a) Variation of θ in radians along the width and length for $\Delta = 3$ and $\chi = 45°$. The DW tilting angle can clearly be seen in this figure.
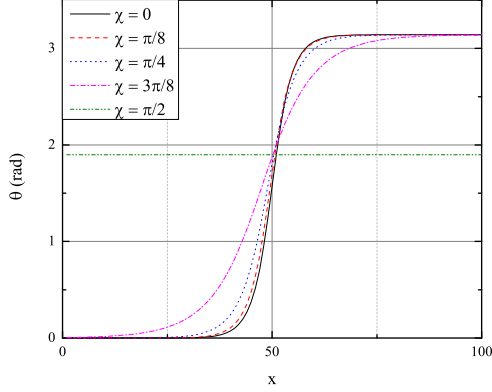
(b) Variation of θ with the DW tilt angle (χ) for $\Delta = 3$ and $y = 0$. It is clear that incleasing χ increases the area of the system affected by the profile.
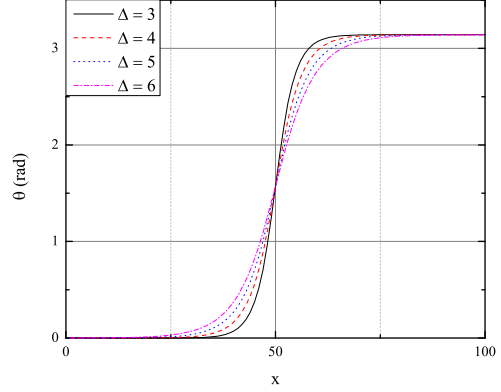
(c) Variation of θ with DW width (Δ) for $\chi = 45°$ and $y = 0$.

Figure 3.8: Variation of the θ calculated from the tilted Bloch profile with different parameters. (a) clearly shows that the wall tilts along the width of the material. (b) shows the effect of changing χ and (c) highlights that changing Δ changes the width of the wall. It is clear that the profile becomes invalid at high values of χ and Δ, as the DW can no longer be distinguished from the surrounding.

where $H_{DMI} = \frac{D}{\mu_0 M_s \Delta}$ is the DMI field, and $H_K = M_s (N_y - N_x)$ is the shape anisotropy field [53].

Figure 3.9 visually presents this equation, showcasing that when the DMI field us about 0.65 times the shape anisotropy field, the DWs will be fully Néel. According to this equation and the figure, for small values of the DMI, the DW will have a near Bloch structure ($\phi \sim \frac{\pi}{2}$) while for higher values you reach a near Néel DW. After a threshold $D_{crit} = \frac{2}{\pi} \mu_0 M_s^2 \Delta (N_y - N_x)$, the DW will always be of Néel structure.

Predictions for the critical DMI strength are shown in Figure 3.10 (assuming a length of 1μm and thickness of 0.6nm for the ferromagnetic layer). We should first note that in the large yellow area at the right of each figure (with high M_s and low K_u), the DW is Néel without the need for DMI (or the system turns in-plane). We see that at high K_u and low M_s ($K_u >> M_s$), a low critical DMI exists which is almost independent of the values of K_u and M_s, while for a small range of K_u and M_s really high DMI is needed to maintain a Neel DW. Increasing the exchange constant generally increases the range of critical DMI values achieved, while increasing the width reduced these values. there is a set of M_s and K_u values for which really high critical DMIs are predicted (shown similar to a line in the graphs).
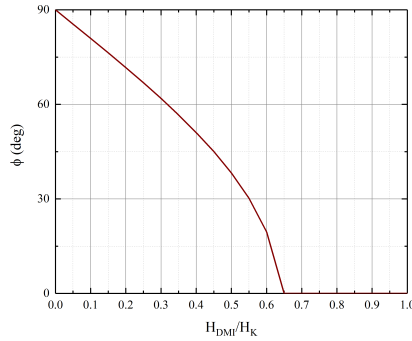
Figure 3.9: Variation of DW structure with the relative strength of DMI to the shape anisotropy fields.

3.3 Validation of Theory

For each of the material stacks presented in Chapter 2 with DMI, we performed micromagnetic simulations on a 1200nm long sample, with different widths. While the out-of-plane component of magnetization followed the Bloch profile in all cases, intermediate DWs with structures in between Bloch and Néel could be observed. In Pt/Co/AlOx [82], Pt/CoFe/MgO [85], Ta/CoFe/MgO [85], Pt/CoSBi/Pt [146], Pt/Co/Gd [149], Pt/Co/Ni/Co/MgO/Pt [151], Ir/Co/Ni/TaN [152], and Pt/Co/Ni/TaN [152] our micromagnetic results revealed only Néel DWs for w = 10 − 200nm. This observation can be connected to the high DMI in these systems. One special case was Pt/Co/Gd [149] in which the DMI was so high that single domain walls could not be stabilized for w > 50nm.

The theoretical studies also revealed fully Néel DWs for Pt/Co/AlOx [82], Pt/Co/AlOx [77], Ta/CoFe/MgO [85], Pt/CoSBi/Pt [146], Pt/Co/Gd [149], Pt/Co/Ni/Co/MgO/Pt [151], and Pt/Co/Ni/TaN [152]. This is not fully in agreement with our micromagnetic results, as in some cases the one-dimensional prediction does not match micromagnetics.

Figure 3.11 illustrates the structures predicted in systems with DMI using micromagnetic simulations and our one-dimensional model. We only illustrated cases in which intermediate structures were present (cases with only Néel DWs are not shown). The three cases where micromagnetic simulations show intermediate DWs do not follow the smooth transition from Bloch to Néel we saw in the systems without DMI. Instead, in these systems as the width of the wire increases the DW seems to transition to a Néel or Néel-like structure of opposite chirality before moving towards a Bloch-like structure. Our one-dimensional model does not predict such effects, likely as they arise from dipolar effects which are not properly modeled in the on-dimensional approach.

3.4 DW Structure Under In-plane Fields in a system with DMI

In recent years, several studies of magnetic DWs have focused on the behavior of DWs under in-plane fields. For example, bubble expansion under in-plane magnetic fields is used to assess the strength of the DMI interaction [88, 89].

In this section, we study the static structure of a magnetic DW in systems with DMI under the applications magnetic in-plane fields. This work will later connect with Chapters 6 and 7, where the dynamics of DWs under similar conditions are being studied.

In the presence of an in-plane fields, a Zeeman term will be added to the energy equation of

(a) A = 1pJ/m and w = 150nm.

(b) A = 2pJ/m and w = 150nm.

(c) A = 1pJ/m and w = 300nm.

(d) A = 2pJ/m and w = 300nm.
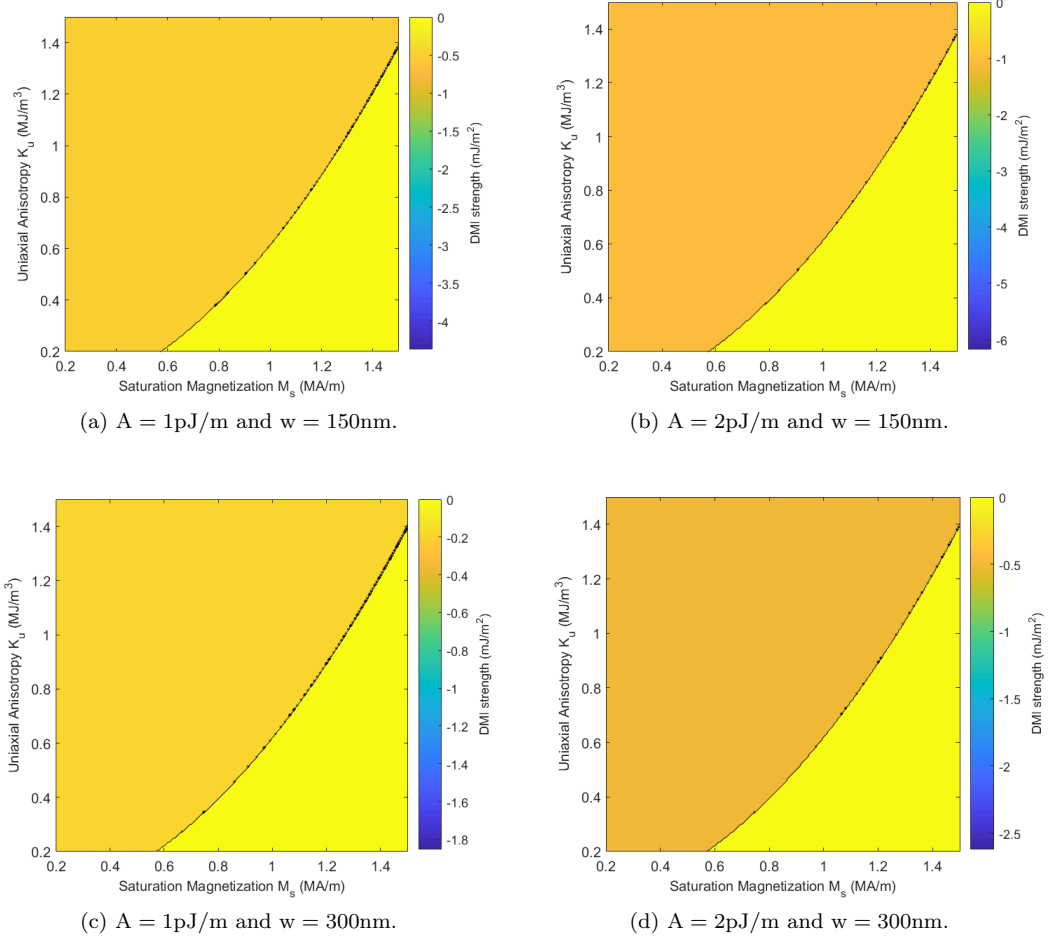
Figure 3.10: Variation of critical DMI values with material parameters. We see that for each width, when $M_s >> K_u$ or $K_u >> M_s$ the critical DMI reaches fixed values, while there is a set of M_s and K_u values for which really high critical DMIs are predicted (shown similar to a line in the graphs).

the DW as written in Equation 3.8 leading to:

$$
\begin{aligned}
E_{dens} =& A \left(\frac{\partial \theta}{\partial x} \right)^2 + \left(K_u + \frac{\mu_0 M_s^2}{2} \left(N_x \cos^2 \Phi + N_y \sin^2 \Phi - N_z \right) \right) \sin^2 \theta \\
&+ D \cos \Phi \frac{\partial \theta}{\partial x} + \mu_0 M_s \left(H_x \cos \Phi + H_y \sin \Phi \right) \sin \theta + \frac{\mu_0 M_s^2}{2} N_z
\end{aligned}
\tag{3.12}
$$

For small enough in-plane fields and DMI, the Bloch profile presented in the past (Equation 3.9) is still valid but the DW width parameter will adjust to:

$$
\Delta = \sqrt{\frac{A}{K_u + \frac{\mu_0 M_s^2}{2} \left(N_x \cos^2 \phi + N_y \sin^2 \phi - N_z \right) + \mu_0 M_s \left(H_x \cos \phi + H_y \sin \phi \right)}}
\tag{3.13}
$$

(a) Micromagnetic simulations.

(b) One dimensional model.
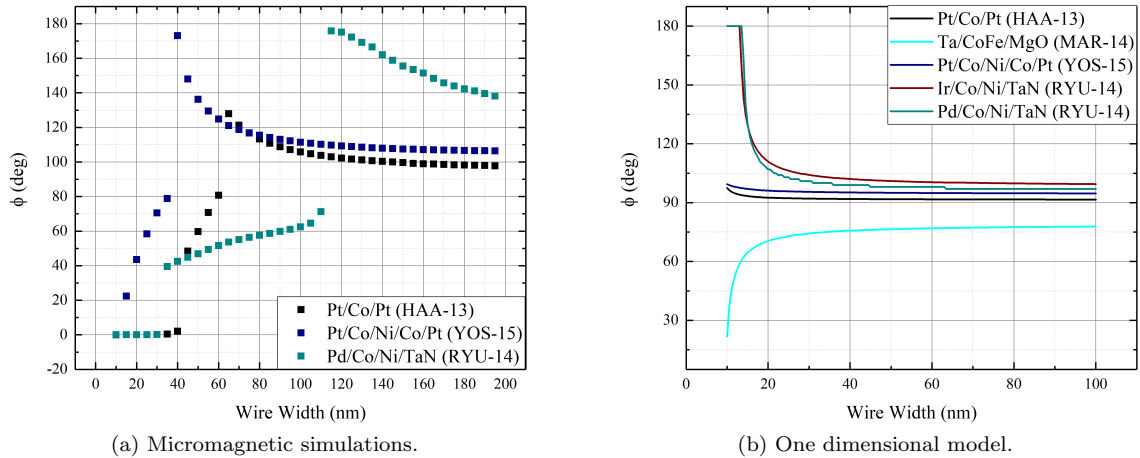
Figure 3.11: Micromagnetic and collective coordinate study of DW structure in systems with DMI. We have only included results for systems which showed intermediate structures.

3.4.1   Micromagnetic Study

To understand the effect of in-plane fields on the DW structure, micromagnetic simulations were conducted under static conditions on a Pt/CoFe/MgO nanowire with the dimensions $2.8\mu m \times$ 160nm $\times$ 0.6nm.

Figure 3.12 shows the results of such simulations for two values of longitudinal fields (B_x), compared to the case where no external field is applied. The application of B_x tilts the magnetization in the domains into the plane, reducing the m_z component (or θ). This changes the θ component of magnetization in the domains from the neutral zero and π values, *canting* the magnetization in the domains. The effect of canting does not fit the traditional Bloch profile.

It can be seen that, in the absence of in-plane fields, the Bloch profile describes the change in θ acceptably. The Bloch profile can fit the transition from one domain to the next under longitudinal fields, if the value of the DW width is adjusted or a prefactor is added to the profile.

It can be seen from the snapshots in Figure 3.13 that, when the DMI and B_x are supporting each other within the DW ($B_x > 0$) in Figure 3.13.c-d), the DW width increases and the DW is further stabilized. In cases where the DMI and B_x are competing ($B_x < 0$ in Figure 3.13.a, e, f), a sufficiently large longitudinal field can change the chirality of the DW; as the magnetization of the DW aligns with this field, the DW tilts in its plane (Figure 3.13.a).

Figure 3.14 shows the static DW profile under four values of transverse field (B_y) compared to the Bloch profile. It is clear that the effect of transverse fields on the DW are symmetric (do not depend of the direction of the field). The deformation of the DW at high field ($|B_y| > 100$mT) creates large deviations from the Bloch profile. For smaller transverse fields, the Bloch profile seems to suitability describe the DW profile. The effect of canting in the domains can also be seen in these cases as well.

Figure 3.15 shows snapshots of DW structure under transverse fields. The elastic behavior of the wall for $|B_y| > 100$mT could clearly be seen (with the wall curving and increasing length), which gives rise to the well rounded profile in Figure 3.14.b. Such a DW could not be modeled as a tilted line. However, the DW at smaller values of B_y could be modeled as a line. More importantly, transverse fields seem to affect the DW tilting more prominently, changing the direction of tilting of the DW.

Simulations under dynamic conditions revealed that the Bloch profile is not an exact predictor

29

(a) Average θ around the DW position.

(b) θ at the middle of the wire around the DW position.
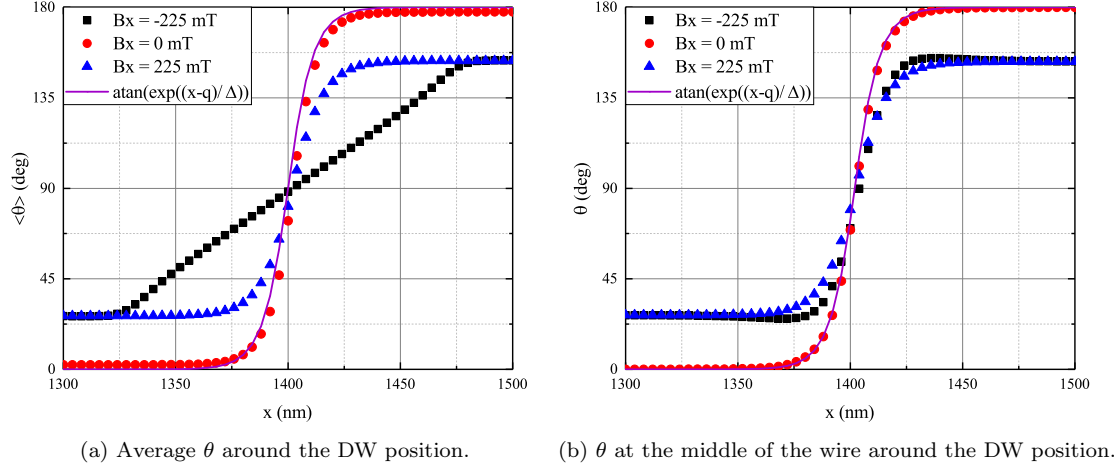
Figure 3.12: Comparison of the static DW profile under different longitudinal fields as determined by micromagnetic simulations to the Bloch Profile.

(a) Static DW structure for $B_x = -225\,\text{mT}$.

(b) Static DW structure for $B_x = -100\,\text{mT}$.

(c) Static DW structure for $B_x = 0\,\text{mT}$.

(d) Static DW structure for $B_x = 325\,\text{mT}$.

Figure 3.13: Snapshots of DW static structure determined by micromagnetic simulations under longitudinal fields.

of DW structure under dynamic conditions. Figure 3.16 illustrates the DW structure after 10ns under the application of a current density of 0.1TA/m and two different values of longitudinal fields. In each case, it is clear that the Bloch profile can fit the transition between the two domains, if the right parameters are selected. Note that, in the case of Bx = 325mT, while the profile fits the transition, there is a misfit due to the canting angle (as mentioned before) and the DW width tends to increase dramatically to 3-4 times its value when no fields are applied. As such, it seems better profiles might be needed to study DW motion under in-plane fields.

In conclusion, under both longitudinal and transverse fields, the transition region of the wall somewhat follows the Bloch profile (the fit can be improved by tuning Δ or adding a prefactor to the profile), albeit not exactly. However, the Bloch profile does not describe the magnetization in the domains correctly under in-plane fields.

3.4.2 Analytic Characterization of the Canting in the Domains

As we mentioned in the previous section, under the application of in-plane magnetic fields the magnetization in the domains cants into the plane. This effect could be characterized using energy minimization. As mentioned in the previous Chapter, the micromagnetic internal energy at any

(a) Average θ around the DW position.

(b) θ in the middle of the wire around the DW position.
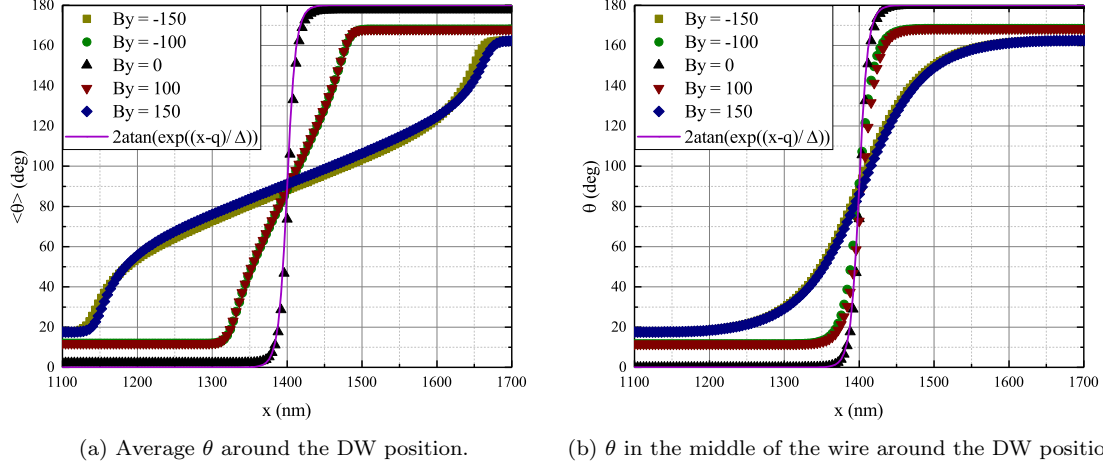
Figure 3.14: Comparison of the static DW profile to the Bloch profile for four different transverse fields.

(a) Static DW structure for $B_y = -150\,\mathrm{mT}$.

(b) Static DW structure for $B_y = 150\,\mathrm{mT}$.

(c) Static DW structure for $B_y = -100\,\mathrm{mT}$.

(d) Static DW structure for $B_y = 100\,\mathrm{mT}$.

Figure 3.15: Snapshots of DW static structure determined by micromagnetic simulations under static conditions.

location within the system may be written as:

$$
\begin{aligned}
E = {} & \overbrace{A\left[\left(\frac{\partial\theta}{\partial x}\right)^2 + \left(\frac{\partial\theta}{\partial y}\right)^2 + \left(\frac{\partial\theta}{\partial z}\right)^2 + \sin^2\theta\left((\frac{\partial\phi}{\partial x})^2 + (\frac{\partial\phi}{\partial y})^2 + (\frac{\partial\phi}{\partial z})^2\right)\right]}^{Exchange} + \overbrace{K_U\sin^2\theta}^{Anisotropy} \\
& + \overbrace{\frac{\mu_0}{2}M_s^2\left(N_x\sin^2\theta\cos^2\phi + N_y\sin^2\theta\sin^2\phi + N_z\cos^2\theta\right)}^{Magnetostatics} \\
& + \overbrace{D\left[\cos\phi\frac{\partial\theta}{\partial x} + \sin\phi\frac{\partial\theta}{\partial y} - \sin\theta\left(\sin\phi\frac{\partial\phi}{\partial x} - \cos\phi\frac{\partial\phi}{\partial y}\right)\right]}^{DMI} \overbrace{-\mu_0 M_s\left[(H_x\cos\phi + H_y\sin\phi)\sin\theta\right]}^{Zeeman}
\end{aligned}
$$

(3.14)

Assuming a long wide wire to reduce the effects of the wire edges on the domains, the local gradients of ϕ and θ will be negligible (in reality the magnetization at the edges of the system

(a) $B_x = 0$.   (b) $B_x = -225$mT.   (c) $B_x = 325$mT.
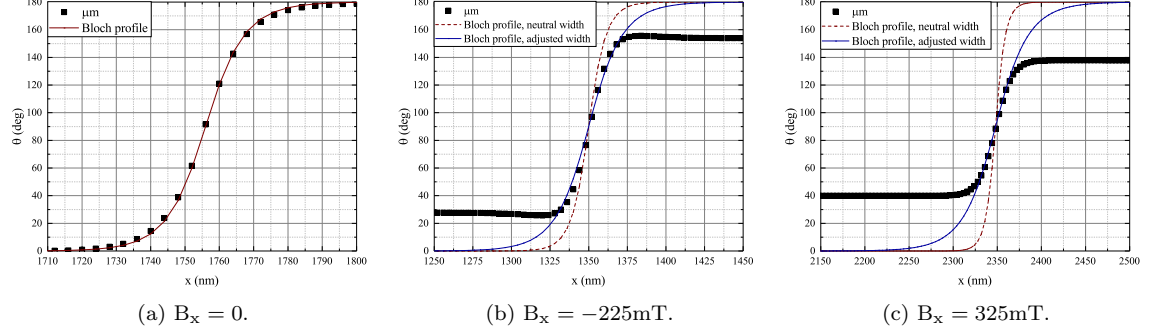
Figure 3.16: Comparison of the moving DW structure to the Bloch profile (Equation 3.4) in SHE-driven DW motion in Pt/CoFe/MgO under a current density of $1TA/m^2$.

are also canted into the plane). As a result, exchange and DM interactions will not play a role in the domains. It should be emphasized that this assumption is not valid for nanowires with small widths. The energy description may be simplified as:

$$E = \overbrace{K_U \sin^2 \theta}^{Anisotropy} + \overbrace{\frac{\mu_0}{2} M_s^2 \left(N_x \sin^2 \theta \cos^2 \phi + N_y \sin^2 \theta \sin^2 \phi + N_z \cos^2 \theta \right)}^{Magnetostatic} \\ \underbrace{-\mu_0 M_s \left[(H_x \cos \phi + H_y \sin \phi) \sin \theta \right]}_{Zeeman} \tag{3.15}$$

ϕ is only dependent on the in-plane fields being applied: in the absence of in-plane fields $\phi = 0$ while in the presence of these fields $\tan \phi = \frac{H_y}{H_x}$.

Minimization of energy means $\frac{\partial E}{\partial \theta} = 0$ (not $\nabla E = 0$ since the ϕ degree of freedom is only determined by applied fields) which yields:

$$\sin \theta_c = \frac{\mu_0 M_s \left(H_x \cos \phi + H_y \sin \phi \right)}{2K_u + \mu_0 M_s^2 \left(N_x \cos^2 \phi + N_y \sin^2 \phi - N_z \right)} \tag{3.16}$$

The equation above may be used to calculate the canting angle in the domains. Figure 3.17 illustrates predictions from equation 3.16 when compared to micromagnetic simulations for the Pt/CoFe/MgO sample studied in the previous section. While the analytical approach accurately predicts the canting angle under longitudinal fields, it fails to do so for transverse fields unless demagnetizing effects (estimated using ellipsoidal approximations) are neglected. The inaccuracy in the case of transverse fields could be attributed to the geometry of the system, as edge effects become important when a field is applied along the width due to the small width of the wire.

(a) Longitudinal fields.

(b) Transverse fields.
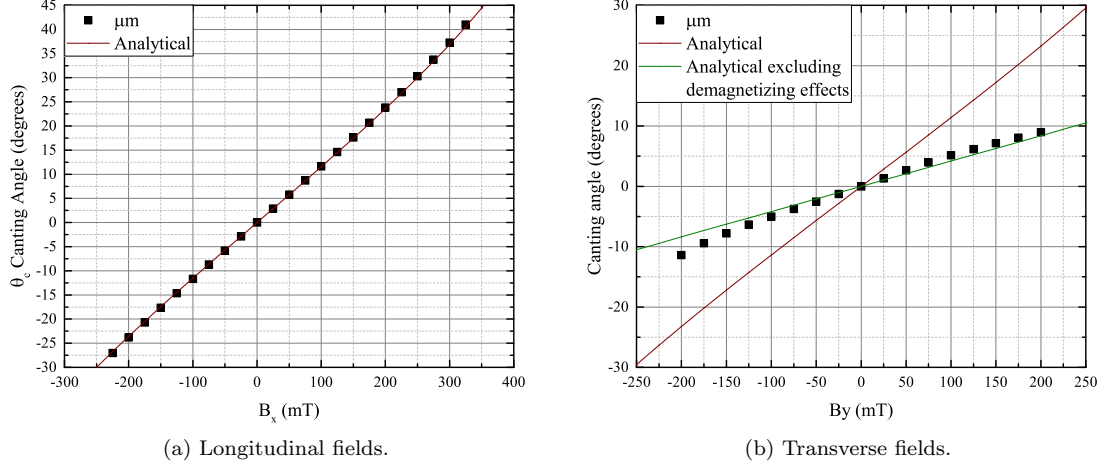
Figure 3.17: Comparison of the canting angle predicted analytically to that predicted through micromagnetic simulations.

3.4.3 A Canted Domain Wall Profile

Boulle et al. included canting in the domains as an alternative angle affecting θ [156]. However, we take a different approach.

An alternative DW profile for systems with canted domains was proposed by Hubert [101], and used extensively by Sobolev et al. [58–61]. This profile takes the form:

$$
\begin{cases}
\sin\theta - \sin\theta_c = \frac{\cos^2\theta_c}{\cosh(\frac{(x-q)\cos\chi + y\sin\chi}{\Delta}) + \sin\theta_0}, & \text{if } x \le q(\theta_c \le \theta \le \pi/2) \\
\sin(\pi - \theta) - \sin\theta_c = \frac{\cos^2\theta_c}{\cosh(\frac{(x-q)\cos\chi + y\sin\chi}{\Delta}) + \sin\theta_0}, & \text{if } x > q(\pi/2 \le \theta \le \theta_x)
\end{cases}
\tag{3.17}
$$

Through mathematical manipulation, we were able to show that this ansatz may be alternatively written as:

$$
\tan\frac{\theta + \theta_c}{2} = \frac{[\exp(u) + \sin\theta_c]}{\cos\theta_c}
\tag{3.18}
$$

where $u = \frac{(x-q)\cos\chi + y\sin\chi}{\Delta}$. For $\theta_c = 0$ this equation is equivalent to the extended Bloch profile (equation 3.9). As depicted in Figure 3.18, this profile is a much better fit to the DW structure when in-plane fields are applied.

3.5 In-Plane Magnetization Angle ϕ

Integrating the energy along the length of the wire, and minimizing it with respect to the magnetization angle ϕ, we find the static in-plane field component of magnetization in the DW.

Taking into account canting, the Bloch profile yields:

$$
\cos\phi = (\pi - 2\theta_c)\frac{\frac{D}{\mu_0 M_s \Delta} - H_x + H_y \cot\phi}{2\cos\theta_c M_s(N_y - N_x)} = \frac{\left(\frac{\pi}{2} - \theta_c\right)}{cos\theta_c}\frac{H_{DMI} + (H_y \cot\phi - H_x)}{H_K}
\tag{3.19}
$$

(a) $B_x = 325mT$.

(b) $B_x = -225mT$
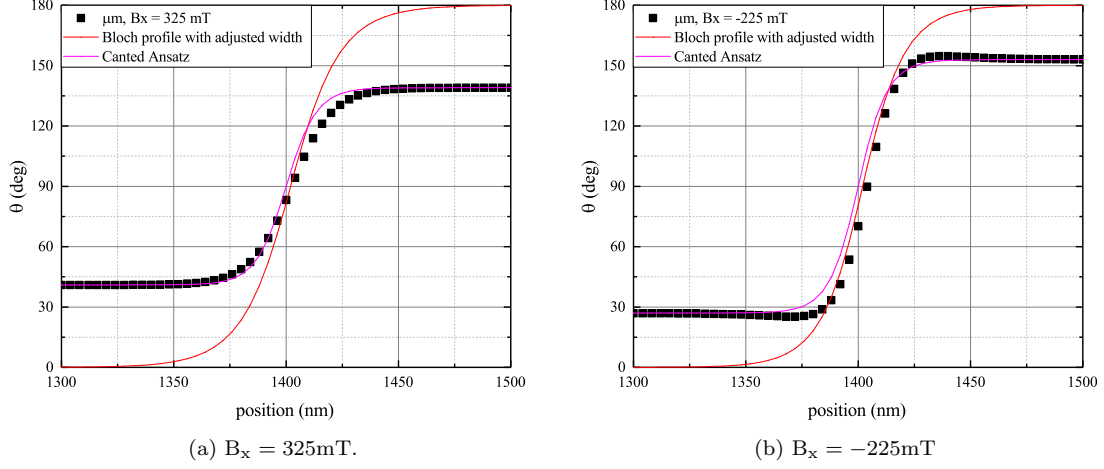
Figure 3.18: Comparison of the static DW structure to the Bloch profile and the inherently canted profile. It is clear that the inherently canted profile is a better fit to the actual DW structure.

while for the inherently canted profile we have:

$$
\begin{aligned}
\cos \phi &= (\pi - 2\theta_c) \frac{\frac{D}{\mu_0 M_s \Delta} - H_x + H_y \cot \phi}{2 \left(\cos^2 \theta_c + \left(\frac{\pi}{2} - \theta_c \right) \sin \theta_c \cos \theta_c \right) M_s (N_y - N_x)} \\
&= \frac{\frac{\pi}{2} - \theta_c}{\cos^2 \theta_c + \left(\frac{\pi}{2} - \theta_c \right) \sin \theta_c \cos \theta_c} \frac{H_{DMI} + (H_y \cot \phi - H_x)}{H_K}
\end{aligned}
\tag{3.20}
$$

Both equations are similar in form to Equation 3.11 with additional terms due to the in-plane fields and canting. Interestingly, the H_x and H_{DMI} field have similar effects on the DW (hence longitudinal fields in the opposite direction as the DMI field can stabilize the DW), while transverse fields have a nonlinear effect.

Clearly, the difference between the output of the ansatz does not stem from the fields, but from the prefactor. Dividing Equation 3.19 by 3.20 we have:

$$
\frac{\cos \phi_{Bloch}}{\cos \phi_{inherently\ canted}} = \cos \theta_c + \left(\frac{\pi}{2} - \theta_c \right) \sin \theta_c
\tag{3.21}
$$

Which clearly shows that the difference between predictions from the two models increases with increasing canting (or increasing the in-plane field applied). Figure 3.19 shows how this ration changes with canting angle. It is clear that higher in-plane fields lead to further difference, with positive canting angles have more effect on the ratio than negative canting angles.

3.6 Conclusion

In this chapter we presented the static structure of DWs for systems with and without DMI. In the absence of DMI, the Bloch profile was extracted to describe the variation of the θ component of magnetization which we found to be valid for cases with DMI as well. Under in-plane fields, canting in the domains also affects the DW structure, and an alternative canted profile was presented to take these effects into account.
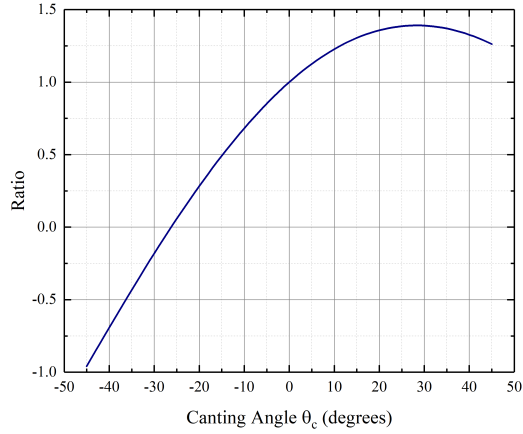
Figure 3.19: Comparison of the ratio between $\cos \phi$ predicted from a Bloch profile with canting assumption to that predicted from the inherently canted profile ($\frac{\cos \phi_{\text{Bloch}}}{\cos \phi_{\text{inherently canted}}}$) for different canting angles.

The in-plane component of magnetization was harder to elucidate. While in systems without DMI our 1-D description predicted only Bloch or Néel DWs, we observed that micromagnetic simulations and experiments also showcase Dws with intermediate structures between Bloch and Néel. This was attributed to the limitations of the on-dimensional model in predicting dipolar effects. We found similar issues under the DMI, although for systems with high DMI the predicted structure from the on–dimensional model matched micromagnetics.

Overall, it seems that the on-dimensional prediction is valid for narrow domain walls, and in systems with high DMI or systems under strong longitudinal in-plane fields.

Chapter 4

Towards an Analytical Model: A Collective Coordinates Approach to DW Motion

While the LLG equation could be used to describe magnetization dynamics involving magnetic domain walls, such an approach is computationally costly due to the need for discretization of the systems and use of numerical techniques at each discrete cell.

This Chapter attempts to introduce a method to derived reduced models of magnetization dynamics from the LLG equation. These models are based on collective physical coordinates which are characteristic of the DW being studies. To achieve such models, one approach is to develop a Lagrangian description of magnetization dynamics, so coordinate changes could be properly applied. The Euler-Lagrange formulation has the added benefit of incorporating dissipative functions relating to position and velocity, which stem from damping and Slonczewski-like torques.

With the Euler-Lagrange equations, the first step is to solve the inverse problem of finding the Lagrangian ($\mathcal{L}$) and Rayleigh dissipation function ($\mathcal{F}$) that can regenerate the LLG equation if put in the Euler-Lagrange-Rayleigh equation:

$$\frac{\partial \mathcal{L}}{\partial q_i} - \frac{d}{dt}\left(\frac{\partial \mathcal{L}}{\partial \dot{q}_i}\right) + \frac{\partial \mathcal{F}}{\partial \dot{q}_i} = 0 \tag{4.1}$$

Note that the Lagrangian is related to the energy of the system through $\mathcal{L} = \mathcal{T} - \mathcal{V}$ where $\mathcal{V}$ is the potential energy and $\mathcal{T}$ is the kinetic energy of the system.

Acknowledgment: Parts of the content in this Chapter were published in following publications:

Please use those papers in any citations.

4.1 The Lagrangian Formulation

We are interested in magnetic DW dynamics under fields and currents in perpendicularly magnetized systems described in Chapter 2. It can be shown that the following Lagrangian density function can be used in the Euler-Lagrange equation to derive the LLG [82, 103]:

$$\frac{d^3\mathcal{L}}{dr^3} = \mathcal{L}_{dens} = E_{dens} + \overbrace{\frac{M_s}{\gamma}\dot{\phi}\cos\theta}^{Precessional\,Term} \overbrace{-\frac{M_s}{\gamma}((\vec{u}.\vec{\nabla})\vec{m})}^{STT} \overbrace{-\mu_0 M_s H_{FL}\vec{m}\cdot\hat{u}_{SOT}}^{SOT_{FL}} \tag{4.2}$$

where E_{dens} takes into account the energy density of exchange, anisotropy, demagnetizing, DM interactions and external fields.

As our interest is in systems with STT along the length of the wire, we may simplify the STT term assuming small angle approximation to $-\frac{uM_s}{\gamma}\phi\frac{d(\cos\theta)}{dx}$ where u is the electron velocity along the length of the wire. Other forms of STT may be included as a field-like term or using the full description.

The dissipation density function may be written as:

$$\frac{d^3\mathcal{F}}{dr^3} = \mathcal{F}_{dens} = \frac{\alpha M_s}{2\gamma}\left[\frac{d\vec{m}}{dt} + \frac{\beta}{\alpha}(\vec{u}\cdot\nabla)\vec{m} - \frac{\mu_0\gamma H_{SL}}{\alpha}\vec{m}\times\hat{u}_{SOT}\right]^2 \tag{4.3}$$

Clearly, the Lagrangian includes the internal energy of the system (the derivative of which with respect to m̃ gives the effective field) plus a precession term to model the precessional motion of magnetization. The dissipation function is made up of the torques acting in the damping direction (which show up as the cross product of fields with m̃ in the LLG equation). The LLG may be retrieved from this Lagrangian and dissipation description of the system, by forming the cross product of the Euler-Lagrange equation with the magnetization.

The Lagrangian relies on a description for the internal energy density of the system. Using spherical coordinates, the total internal energy density (E_{dens}) for a material with uniaxial crystalline anisotropy and DMI may be written as:

$$E_{dens} = A\overbrace{\left[\left(\frac{\partial\theta}{\partial x}\right)^2 + \left(\frac{\partial\theta}{\partial y}\right)^2 + \left(\frac{\partial\theta}{\partial z}\right)^2 + \sin^2\theta\left(\left(\frac{\partial\phi}{\partial x}\right)^2 + \left(\frac{\partial\phi}{\partial y}\right)^2 + \left(\frac{\partial\phi}{\partial z}\right)^2\right)\right]}^{Exchange}$$

$$+ \overbrace{K_U\sin^2\theta}^{Anisotropy} + \overbrace{\frac{\mu_0}{2}M_s^2\left(N_x\sin^2\theta\cos^2\phi + N_y\sin^2\theta\sin^2\phi + N_z\cos^2\theta\right)}^{Magnetostatics}$$

$$+ \overbrace{D\left[\cos\phi\frac{\partial\theta}{\partial x} + \sin\phi\frac{\partial\theta}{\partial y} - \sin\theta\left(\sin\phi\frac{\partial\phi}{\partial x} - \cos\phi\frac{\partial\phi}{\partial y}\right)\right]}^{DMI}$$

$$\overbrace{-\mu_0 M_s\left[(H_x\cos\phi + H_y\sin\phi)\sin\theta + H_z\cos\theta\right]}^{Zeeman\,and\,Field-like\,SOT} \tag{4.4}$$

In the above equation, the demagnetizing factors may be calculated based on the geometry of the system and ellipsoidal approximations [106–110]. Note that this assumption is only valid in a coordinate system along the DW (Figure 4.1.b). The Zeeman energy term includes both effects of applied fields and field-like spin-orbit torques with $H_i = H_{a,i} + H_{FL}u_{SOT,i}$ is the effective field like excitation in the i direction and $u_{SOT,i}$ is equal to 1 when there are field-like spin orbit effects in direction i and zero, otherwise.

The dissipation density function will have the following form in spherical coordinates (keeping in mind the assumption of STT along the wire length):

$$
\mathcal{F}_{dens} = \frac{\alpha M_s}{2\gamma} \Bigg[\left(\dot{\theta}\cos\theta\cos\phi - \dot{\phi}\sin\theta\sin\phi - \frac{\mu_0\gamma H_{SL}}{\alpha} \left[\sin\theta\sin\phi u_z - \cos\theta u_y\right] + \frac{\beta u}{\alpha}\frac{\partial(\sin\theta\cos\phi)}{\partial x} \right)^2
$$
$$
+ \left(\dot{\theta}\cos\theta\sin\phi + \dot{\phi}\sin\theta\cos\phi - \frac{\mu_0\gamma H_{SL}}{\alpha} \left[\cos\theta u_x - \sin\theta\cos\phi u_z\right] + \frac{\beta u}{\alpha}\frac{\partial(\sin\theta\sin\phi)}{\partial x} \right)^2
$$
$$
+ \left(-\dot{\theta}\sin\theta - \frac{\mu_0\gamma H_{SL}}{\alpha} \left[\sin\theta\cos\phi u_y - \sin\theta\sin\phi u_x\right] + \frac{\beta u}{\alpha}\frac{\partial(\cos\theta)}{\partial x} \right)^2 \Bigg]
$$

$$(4.5)$$

which may be further simplified to the following:

$$
\mathcal{F}_{dens} = \frac{\alpha M_s}{2\gamma} \Bigg[\dot{\theta}^2 + \dot{\phi}^2\sin^2\theta + (\frac{\beta u}{\alpha})^2 \left[\left(\frac{\partial\theta}{\partial x}\right)^2 + \sin^2\theta\left(\frac{\partial\phi}{\partial x}\right)^2 \right]
$$
$$
+ (\frac{\mu_0\gamma H_{SL}}{\alpha})^2 [\left(\cos^2\theta + \sin^2\theta\sin^2\phi\right)u_x^2 + \left(\cos^2\theta + \sin^2\theta\cos^2\phi\right)u_y^2 + \sin^2\theta u_z
$$
$$
- 2\sin\theta\cos\theta\left(\cos\phi u_x + \sin\phi u_y\right)u_z - \sin^2\theta\sin 2\phi u_x u_y]
$$
$$
+ 2\frac{\beta u}{\alpha}\left(\frac{\partial\theta}{\partial t}\frac{\partial\theta}{\partial x} + \sin^2\theta\frac{\partial\phi}{\partial t}\frac{\partial\phi}{\partial x}\right)
$$
$$
- 2\frac{\mu_\gamma H_{SL}}{\alpha}\left[\left(\sin\phi u_x - \cos\phi u_y\right)\frac{\partial\theta}{\partial t} - \left(\sin 2\theta u_z + \sin\theta\cos\theta\left(\cos\phi u_x + \sin\phi u_y\right)\right)\frac{\partial\phi}{\partial t}\right]
$$
$$
- 2\frac{\beta u}{\alpha}\frac{\mu_0\gamma H_{SL}}{\alpha}\left[\left(\sin\phi u_x - \cos\phi u_y\right)\frac{\partial\theta}{\partial x} - \left(\sin\theta\cos\theta\left(\cos\phi u_x - \sin\phi u_y\right) + \sin^2\theta u_z\right)\frac{\partial\phi}{\partial x}\right] \Bigg]
$$

$$(4.6)$$

4.2 A Collective Coordinates Approach to Magnetic DW Motion

Our aim is to develop a description of the collective motion of the DW; a description which does not rely on the properties of single magnetic moments in the system, but the DW as a collection of magnetic moments. To do so, we need to introduce assumptions in the system in order to connect the spatial change of magnetization with the collective properties of the DW which only change temporally.

As previously mentioned, the system of interest in this work is a multilayer perpendicularly magnetized nanostrip containing a magnetic DW. Based on micromagnetic simulations and experimental observations [54, 62, 82], the following time dependent collective coordinates were selected to describe DW motion in such systems:

1. The position of the center of the DW (q);

2. Magnetization angle at the center of the DW (ϕ);

3. The domain wall width parameter (Δ);

4. The tilt angle of the wall as a whole (χ).

Using these coordinates, the DW is modeled as a thin line with four degrees of freedom. The coordinates above are depicted in Figure 4.1.b.

The coordinate q was included as a measure of DW motion, ϕ was included to provide a measure of the magnetization state which is how the DW interacts with its environment, and Δ was included as physically any DW has a width. The coordinate χ was added in order to model the effects of the DMI on a moving DW, which tends to tilt the DW in its plane [82], as depicted in Figure 4.1.d and e. This tilting has also been observed in systems without DMI under in-plane fields [156], and is a way for the DW to adjust its internal magnetization while keeping multiple energy terms to a minimum. Under high in-plane fields or high DMI, the DW no longer tilts rigidly and, a rigid description based on a tilting line might no longer be suitable.

(a) Collective coordinates.

(b) Ellipsoidal coordinates of the DW.

(c) t = 0, D = 1 mJ/m^2.

(d) t = 100 ps, D = 1 mJ/m^2.

(e) t = 0, D = 2 mJ/m^2.

(f) t = 100 ps, D = 2 mJ/m^2.
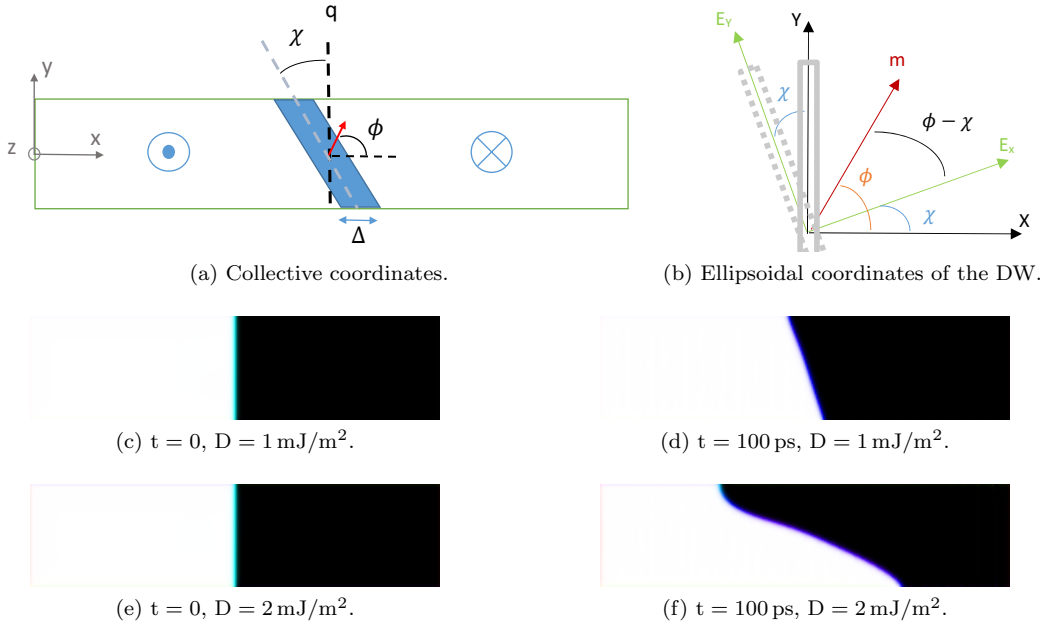
Figure 4.1: The selected collective coordinates and snapshots from micromagnetic simulations with an applied field of 10mT. (b) Relevant ellipsoidal coordinates.The rectangle in solid gray shows the initial state of the Dw and the one in dotted gray rectangle shows the DW in motion with a tilting angle χ. Clearly, during motion the ellipsoidal axes (E$_x$ and E$_y$) of the DW tilt by χ as well. (d) and (f) clearly show the tilting of the DW, when compared to the initial DWs illustrated in (c) and (e) respectively. Note that (f) also shows the partial deformation of the DW at high DMI.

In order to introduce a DW as an object within the system, and move from a description based on spherical coordinates to collective coordinates, the two coordinate systems need to be linked. To relate the spherical coordinates with the collective coordinates, we may use the profile of a tilted Bloch or Néel wall derived in Chapter 2 (Equation 3.9) as an ansatz:

$$\tan\frac{\theta}{2} = \exp\left(\pm\frac{(x-q)\cos\chi + y\sin\chi}{\Delta}\right) \tag{4.7}$$

The ansatz above (Eq. 4.7) is a generalization of the original ansatz used by Slonczewski [54,157] (and derived in Chapter 2) with the additional parameter χ added to account for the tilting of the

wall. Note that by introducing the parameter χ, the diagonal axes of the DW change, as depicted in Figure 4.1.b.

By introducing this ansatz, magnetization dynamics is now constrained. This means that the degrees of freedom such as as θ man no longer follow any direction they want and need to obey this ansatz, moving them slightly away from the exact LLG equation towards a form of the LLG with additional torques which constrain the dynamics of the magnetic moments. These constraints are the main reason why micromagnetic simulations do not exactly match 1-D model predictions in some cases.

The ansatz (Equation 4.7) has the following properties

$$\frac{\partial \theta}{\partial x} = \frac{\sin \theta}{\Delta} \cos \chi \tag{4.8}$$

$$\frac{\partial \theta}{\partial y} = \frac{\sin \theta}{\Delta} \sin \chi \tag{4.9}$$

$$\begin{aligned}\frac{\partial \theta}{\partial t} &= \left(-\dot{q}\frac{\cos \chi}{\Delta} + \dot{\chi}\frac{(q-x)\sin \chi + y\cos \chi}{\Delta} - \frac{\dot{\Delta}}{\Delta}\frac{(x-q)\cos \chi + y\sin \chi}{\Delta} \right) \sin \theta \\ &= \left(-\dot{q}\cos \chi + \frac{\dot{\chi}}{\cos \chi}\left(y - \Delta \sin \chi \ln\left(\tan\left(\theta/2\right)\right)\right) - \frac{\dot{\Delta}}{\Delta}\left((x-q)\cos \chi + y\sin \chi\right) \right) \frac{\sin \theta}{\Delta}\end{aligned} \tag{4.10}$$

which shows all derivatives of θ somehow relating to $\sin \theta / \Delta$, simplifying spatial and temporal integration of the energy (Lagrangian and dissipation) functions. For the DW to maintain its shape, we must also have [59, 61]:

$$|\dot{\Delta}| \ll |\dot{q}|, \ |\dot{\phi}| \gg |\frac{\dot{\Delta}}{\Delta}|, \ |\nabla \phi| < \frac{1}{\Delta_0}, \ |\nabla q| \ll 1 \tag{4.11}$$

which are equivalent to the DW internal degrees of freedom changing slower than its collective motion, and ϕ and q being almost spatially homogeneous.

To evaluate DW dynamics using the collective coordinates, we need to rewrite the energy terms using these coordinates and the properties of the ansatz. The Lagrangian density will take the form:

$$\frac{d^3\mathcal{L}}{dr^3} = \mathcal{L}_{dens} = \overbrace{\frac{A}{\Delta}\sin^2 \theta}^{Exchange} + \overbrace{\frac{D}{\Delta^2}\cos(\phi - \chi)\sin \theta}^{DMI} + \overbrace{K_U \sin^2 \theta}^{Anisotropy}$$
$$+ \overbrace{\frac{\mu_0}{2}M_s^2\left(N_x \sin^2 \theta \cos^2(\phi - \chi) + N_y \sin^2 \theta \sin^2(\phi - \chi) + N_z \cos^2 \theta\right)}^{Magnetostatic}$$
$$\overbrace{-\mu_0 M_s\left[(H_x \cos \phi + H_y \sin \phi)\sin \theta + H_z \cos \theta\right]}^{Zeeman} + \overbrace{\frac{M_s}{\gamma}\dot{\phi}\cos \theta}^{PrecessionalTerm} \tag{4.12}$$
$$\overbrace{-\frac{uM_s}{\gamma}\phi\frac{d(\cos \theta)}{dx}}^{STT}\overbrace{-\mu_0 M_s H_{FL}\vec{m}\cdot\hat{u}_{SOT}}^{SOT_{FL}}$$

Note the change in the Magnetostatic terms from equations based on ϕ only, to equations based on $\phi - \chi$. This is due to the local nature of the demagnetizing field, which acts on magnetization

at each point within the system. In order to maintain the ellipsoidal assumption (or diagonality of the demagnetizing factors tensor), a change of axes is required (as depicted in 4.1.b) which leads to these new equations. The dissipation density can be written as:

$$
\begin{aligned}
\mathcal{F}_{dens} = \frac{\alpha M_s}{2\gamma} \Bigg[&\left(-\dot{q}\frac{\cos\chi}{\Delta} + \dot{\chi}\frac{y - \Delta\sin\chi\ln\left(\tan\left(\theta/2\right)\right)}{\Delta\cos\chi} - \frac{\dot{\Delta}}{\Delta}\frac{(x-q)\cos\chi + y\sin\chi}{\Delta} \right)^2 \sin^2\theta \\
&+ \left[\dot{\phi}^2 + \left(\beta u\frac{\cos\chi}{\alpha\Delta}\right)^2 \right]\sin^2\theta - 2\frac{\beta u}{\alpha}\frac{\mu_0\gamma H_{SL}}{\alpha}\left(\sin\phi u_x - \cos\phi u_y\right)\frac{\cos\chi}{\Delta}\sin\theta \\
&+ 2\frac{\beta u}{\alpha}\left(-\dot{q}\frac{\cos\chi}{\Delta} + \dot{\chi}\frac{y - \Delta\sin\chi\ln\left(\tan\left(\theta/2\right)\right)}{\Delta\cos\chi} - \frac{\dot{\Delta}}{\Delta}\frac{(x-q)\cos\chi + y\sin\chi}{\Delta} \right)\frac{\cos\chi}{\Delta}\sin^2\theta \\
&+ (\frac{\mu_0\gamma H_{SL}}{\alpha})^2\Big[\left(\cos^2\theta + \sin^2\theta\sin^2\phi\right)u_x^2 + \left(\cos^2\theta + \sin^2\theta\cos^2\phi\right)u_y^2 + \sin^2\theta u_z \\
&\qquad - 2\sin\theta\cos\theta\left(\cos\phi u_x + \sin\phi u_y\right)u_z - \sin^2\theta\sin 2\phi u_x u_y \Big] \\
&- 2\frac{\mu_0\gamma H_{SL}}{\alpha}\left(\sin\phi u_x - \cos\phi u_y\right)\sin\theta \\
&\qquad \left(-\dot{q}\frac{\cos\chi}{\Delta} + \dot{\chi}\frac{y - \Delta\sin\chi\ln\left(\tan\left(\theta/2\right)\right)}{\Delta\cos\chi} - \frac{\dot{\Delta}}{\Delta}\frac{(x-q)\cos\chi + y\sin\chi}{\Delta} \right) \Bigg]
\end{aligned}
\tag{4.13}
$$

Next, the Lagrangian and dissipation density function need to be integrated over the length of the wire. The properties of the ansatz help simplify the integration process. This integration will remove the dependence of terms on θ, leading to an equation based only on the collective coordinates and material properties. We have:

$$
\begin{aligned}
\frac{d^2\mathcal{L}}{dydz} = \mathcal{L}_x = &\frac{2A}{\Delta^2}\cos\chi + \pi\frac{D}{\Delta^2}\cos\left(\phi - \chi\right) + 2\frac{M_s}{\gamma}\dot{\phi}\left(q - y\tan\chi\right) - \pi\frac{uM_s}{\gamma}\phi \\
&+ \frac{2\Delta}{\cos\chi}\left[K_U + \frac{\mu_0}{2}M_s^2\left(N_x\cos^2\left(\phi - \chi\right) + N_y\sin^2\left(\phi - \chi\right) - N_z\right) \right] \\
&- \pi\mu_0 M_s\left[H_x\cos\phi + H_y\sin\phi + 2H_z\left(q - ytan\chi\right) \right]
\end{aligned}
\tag{4.14}
$$

$$
\begin{aligned}
\mathcal{F}_x = \frac{\alpha M_s}{\gamma} \Bigg[&\frac{\dot{q}^2}{\Delta}\cos\chi + \frac{\pi^2}{12}\frac{\dot{\Delta}^2}{\Delta\cos\chi} + \frac{\dot{\chi}^2\Delta}{\cos\chi}\left(\left(\frac{y}{\Delta\cos\chi}\right)^2 + \frac{\pi^2}{12}\tan^2\chi \right) \\
&+ \dot{\phi}^2\frac{\Delta}{\cos\chi} - 2y\frac{\dot{q}}{\Delta}\frac{\dot{\chi}}{\cos\chi} + \frac{\pi^2}{6}\dot{\Delta}\frac{\dot{\chi}}{\cos\chi}\tan\chi + 2\dot{\phi}\frac{\mu_0\gamma H_{SL}}{\alpha}\frac{\Delta}{\cos\chi}u_z \\
&+ (\frac{\beta u}{\alpha})^2\frac{\cos\chi}{\Delta} + \left[\pi\frac{\gamma H_{SL}}{\alpha}\left(\sin\phi u_x - \cos\phi u_y\right) - 2\frac{\beta}{\alpha}\frac{u}{\Delta}\cos\chi \right]\left[\dot{q} - y\frac{\dot{\chi}}{\cos^2\chi} \right] \\
&- \pi\frac{\beta u}{\alpha}\frac{\gamma H_{SL}}{\alpha}\left(\sin\phi u_x - \cos\phi u_y\right) \\
&- (\frac{\gamma H_{SL}}{\alpha})^2\frac{\Delta}{\cos\chi}\left(u_z^2 + u_y^2\cos^2\phi + u_x^2\sin^2\phi - 2u_x u_z\sin 2\phi + constants \right) \Bigg]
\end{aligned}
\tag{4.15}
$$

The constant terms are not all written down here to save space, specially since only terms with a derivative of a collective coordinate play a role in the dynamics.

The above equations still need to be integrated along the width and thickness of the wire. Considering the DW tilts along the center of the wire, integration from $-w/2$ to $w/2$ is reasonable along the width (if other coordinate systems are used, as they will not be inertial, inertial terms will show up in the equations). After integration, the Lagrangian and dissipation function may be used to derive the equations of motion using the Euler-Lagrange equation. Four models may be developed, which will be outlined below.

4.2.1 Models without DW Tilting

The q − ϕ Model

The simplest model that can be derived using the approach above is the q − ϕ model which is most similar to the original model proposed by Sloncweski [54]. This model assumes that the DW width parameter Δ is fixed and derived using the equation presented in Chapter 3. It also neglects tilting in the DW. It consists of the following two equations describing the evolution of the collective coordinates q and ϕ:

$$\alpha \frac{\dot{q}}{\Delta} + \dot{\phi} = \mu_0 \gamma \left(H_z - \frac{\pi}{2} H_{SL} \left[\sin \phi \, u_{SOT,x} - \cos \phi \, u_{SOT,y} \right] \right) + \beta \frac{u}{\Delta} \tag{4.16}$$

$$\begin{aligned}
\frac{\dot{q}}{\Delta} - \alpha \dot{\phi} &= \frac{1}{2} \mu_0 \gamma M_s \left(N_y - N_x \right) \sin 2\phi - \frac{\pi}{2} \frac{\gamma D}{M_s \Delta} \sin \phi \\
&\quad + \frac{u}{\Delta} + \frac{\pi}{2} \mu_0 \gamma \left[H_x \sin \phi - H_y \cos \phi \right] + \mu_0 \gamma H_{SL} u_{SOT,z}
\end{aligned} \tag{4.17}$$

In the equations above, Equation 4.16 includes the effect of external interactions that drive the DW, while equation 4.17 includes all interactions that change the internal structure of the DW. Equations 4.16 and 4.17 may be rewritten in explicit form as:

$$\begin{aligned}
(1 + \alpha^2) \frac{\dot{q}}{\Delta} &= \mu_0 \gamma \left(\alpha H_z + H_{SL} u_{SOT,z} \right) + (1 + \alpha\beta) \frac{u}{\Delta} + \frac{1}{2} \mu_0 \gamma M_s \left(N_y - N_x \right) \sin 2\phi \\
&\quad + \frac{\pi}{2} \mu_0 \gamma \left[\left(H_x - \frac{D}{\mu_0 M_s \Delta} - \alpha H_{SL} u_{SOT,x} \right) \sin \phi - \left(H_y - \alpha H_{SL} u_{SOT,y} \right) \cos \phi \right]
\end{aligned} \tag{4.18}$$

$$\begin{aligned}
(1 + \alpha^2) \dot{\phi} &= \mu_0 \gamma \left(H_z - \alpha H_{SL} u_{SOT,z} \right) + (\beta - \alpha) \frac{u}{\Delta} - \alpha \frac{1}{2} \mu_0 \gamma M_s \left(N_y - N_x \right) \sin 2\phi \\
&\quad - \frac{\pi}{2} \mu_0 \gamma \left[\left(\alpha \left(H_x - \frac{D}{\mu_0 M_s \Delta} \right) + H_{SL} u_{SOT,x} \right) \sin \phi - \left(\alpha H_y + H_{SL} u_{SOT,y} \right) \cos \phi \right]
\end{aligned} \tag{4.19}$$

The q − ϕ − Δ Model

Another somewhat simple models is the q − ϕ − Δ model (similar to the model proposed by Thiaville [62]) which extends the q − ϕ model by adding an additional equation outlining the evolution of the DW width parameter. While the first two equations of the q − ϕ − Δ model are 4.16 and 4.17, an additional equation is added with the form:

$$\begin{aligned}
\frac{\pi^2}{12} \alpha \frac{\dot{\Delta}}{\Delta} &= \frac{\gamma}{M_s} \left[\frac{A}{\Delta^2} - K_u - \frac{\mu_0 M_s^2}{2} \left[N_x \cos^2 \phi + N_y \sin^2 \phi - N_z \right] \right] \\
&\quad + \frac{\pi}{2} \mu_0 \gamma \left(H_x \cos \phi + H_y \sin \phi \right)
\end{aligned} \tag{4.20}$$

The q $- \phi$ and q $- \phi - \Delta$ models show the same dynamic behavior, since Δ relaxes towards a steady state value rather fast and is independent of the driving excitation.The steady state value of the DW width parameter may be calculated at $\dot{\Delta} = 0$ as:

$$\Delta^* = \sqrt{\frac{A}{K_u + \frac{\mu_0 M_s^2}{2} \left[N_x \cos^2 \phi + N_y \sin^2 \phi - N_z \right] + \frac{\pi}{2} \mu_0 \gamma \left(H_x \cos \phi + H_y \sin \phi \right)}} \tag{4.21}$$

Clearly the DW width depends directly on exchange, anisotropy, dipolar interaction and in-plane fields, while the DMI exerts an effect on the DW width indirectly by affecting ϕ which is also affected by the other interactions as well.

Due to the fast relaxation of the DW width parameter towards a steady state value, an analytical analysis of the q $- \phi - \Delta$ is valid for the q $- \phi$ model. These models are valid in the absence of DMI (or presence of very low DMI), when negligible tilting is observed on the DW. Several observation can be made regarding the mathematical form of the q $- \phi - \Delta$ and the q $- \phi$ models:

1. Considering the relatively small changes in Δ, the dynamics is entirely determined by ϕ.

2. The uniaxial anisotropy only affects the dynamics of the DW width directly. As the DW width is relatively stable when no in-plane fields are applied, the uniaxial anisotropy plays a minimal role in DW dynamics.

3. The DMI and external excitations directly play a role in the dynamics of ϕ and velocity.

4. The dipolar interaction and in-plane fields are involved in all three equations.

5. The ϕ angle predicted by these equations is equivalent to $\phi - \chi$ in models with tilting of the DW as we will show later on in this chapter.

Closed-Form and Analytical Solutions

Steady State Condition In the case of a thin film in the absence of in-plane fields and neglecting the smaller demagnetizing effects, the steady state DW width parameter (Equation 4.21) can be approximated by:

$$\Delta^* \simeq \sqrt{\frac{A}{K_u - \frac{\mu_0 M_s^2}{2} N_z}} \tag{4.22}$$

This approximation of the DW width parameter may be used in the q $- \phi$ with negligible errors compared to the full q $- \phi - \Delta$ model.

It is well established that a steady state condition can be reached if the excitation is lower than the Walker excitation, with the DW moving at a constant speed [53]. Based on our equations, and considering Δ relaxes really fast, a steady state motion is equivalent to the magnetization stopping its precession ($\dot{\phi} \sim 0$). We have:

$$\dot{\phi} = 0 \Rightarrow \alpha \frac{1}{2} M_s \left(N_y - N_x \right) \sin 2\phi^* = \left(H_z - \alpha H_{SL} u_{SOT,z} \right) + (\beta - \alpha) \frac{u}{\mu_0 \gamma \Delta^*}$$
$$- \frac{\pi}{2} \left[\left(\alpha \left(H_x - \frac{D}{\mu_0 M_s \Delta^*} \right) + H_{SL} u_{SOT,x} \right) \sin \phi^* - \left(\alpha H_y + H_{SL} u_{SOT,y} \right) \cos \phi^* \right] \tag{4.23}$$

The equation above shows that the excitations need to balance out with the dipolar and DM interactions in order to reach a steady state. Otherwise, the precession will continue. Note that the DM field may be defined here as $H_{DMI} = \frac{D}{\mu_0 M_s \Delta^*}$, and the STT field as $H_{STT} = \frac{u}{\mu_0 M_s \Delta^*}$.

In the simplest case of field-driven DW motion without any DMI, we have:

$$\sin 2\phi^* = \frac{2H_z}{\alpha M_s(N_y - N_x)} = \frac{H_z}{H_W} \tag{4.24}$$

$$\dot{q}^* = \frac{\mu_0 \gamma}{\alpha} H_z \Delta^* \tag{4.25}$$

In such a case, the threshold field $H_W = \frac{\alpha}{2}M_s(N_y - N_x) = \frac{\alpha}{2}H_K$ exists, above which no steady state solution can be achieved. This field is called the Walker Breakdown field [53]. A similar approach could be used to define the Walker breakdown current for the STT driven DW motion or Sloncweski-like SOTs in the z direction.

With the definition of the Walker Breakdown field, the general equation for the stead state ϕ may be written as:

$$\begin{aligned}
\sin 2\phi^* &= \frac{H_z}{H_W} - \frac{\alpha H_{SL} u_{SOT,z}}{H_w} + (\beta - \alpha)\frac{H_{STT}}{H_w} \\
&\quad - \frac{\pi}{2}\left[\left(\alpha\frac{H_x}{H_w} - \alpha\frac{H_{DMI}}{H_w} + \frac{H_{SL}}{H_w}u_{SOT,x}\right)\sin\phi - \left(\alpha\frac{H_y}{H_w} + \frac{H_{SL}}{H_w}u_{SOT,y}\right)\cos\phi\right] \\
&= h_z - \alpha h_{SL}u_{SOT,z} + (\beta - \alpha)h_{STT} \\
&\quad - \frac{\pi}{2}\left[(\alpha h_x - \alpha h_{DMI} + h_{SL}u_{SOT,x})\sin\phi - (\alpha h_y + h_{SL}u_{SOT,y})\cos\phi\right]
\end{aligned} \tag{4.26}$$

where h_is are each field term normalized by the Walker breakdown field ($h_z = \frac{H_z}{H_w}$, $h_{sl} = \frac{H_{SL}}{H_w}$, $h_{STT} = \frac{H_u}{H_w} = \frac{u}{\mu_0\gamma H_w \Delta}$, and $h_D = \frac{H_{DMI}}{H_w} = \frac{D}{\mu_0 M_s \Delta H_w}$). This equation clearly shows that the relative strength of each field compared to the Walker Breakdown is the dominating factor in DW motion.

Using this equation, the velocity of the DW may be simplified to:

$$\dot{q}^* = \frac{\mu_0\gamma\Delta^*}{\alpha}\left[H_z + \beta\frac{u}{\mu_0\gamma\Delta^*} + \frac{\pi}{2}H_{SL}\left(u_{SOT,y}\cos\phi^* - u_{SOT,x}\sin\phi^*\right)\right] \tag{4.27}$$

This equation clearly shows that (assuming a fixed DW width) in field- and STT-driven DW motion, the DW velocity should vary linearly with the applied interaction, while in SOT-driven DW motion we expect a nonlinearity in DW velocity. Moreover, SOT fields in the y direction cannot move Bloch DWs ($\phi^* = \frac{\pi}{2}$), while SOT fields in the x-direction cannot move Néel DWs ($\phi^* = 0$). Note that the field-like component of the SOTs do not contribute to the velocity directly, while they do have an effect on ϕ^*.

Linearized Solution Using a Taylor series expansion of the steady state equation 4.26, we have:

$$\begin{aligned}
\left(2\phi^* - \frac{8\phi^{*3}}{6} + \frac{32\phi^{*5}}{120} + ...\right) &= h_z - \alpha h_{SL}u_{SOT,z} + (\beta - \alpha)h_STT \\
&\quad - \frac{\pi}{2}[(\alpha h_x - \alpha h_{DMI} + h_{SL}u_{SOT,x})\left(\phi^* - \frac{\phi^{*3}}{6} + \frac{\phi^{*5}}{120} + ...\right) \\
&\quad - (\alpha h_y + h_{SL}u_{SOT,y})\left(1 - \frac{\phi^{*2}}{2} + \frac{\phi^{*4}}{24} + ...\right)]
\end{aligned} \tag{4.28}$$

44

From these expansions we can extract a linear solution to the equation. Using only the first term of each expansion, we have:

$$\phi^* = \frac{h_z - \alpha h_{SL} u_{SOT,z} + (\beta - \alpha) h_{STT} + \frac{\pi}{2} (\alpha h_y + h_{SL} u_{SOT,y})}{2 + \frac{\pi}{2} (\alpha h_x - \alpha h_{DMI} + h_{SL} u_{SOT,x})}$$
$$= \frac{H_z - \alpha H_{SL} u_{SOT,z} + (\beta - \alpha) H_{STT} + \frac{\pi}{2} (\alpha H_y + H_{SL} u_{SOT,y})}{\alpha H_K + \frac{\pi}{2} (\alpha H_x - \alpha H_{DMI} + H_{SL} u_{SOT,x})} \tag{4.29}$$

The intriguing feature of this equation is that it shows that the internal structure of the DW is Dependant on the ratio of interactions in the y and z directions to those interactoins acting along the length of the DW.

Force Description   During steady state motion (after the relaxation of Δ and ϕ), it can be shown that the dynamics of the system follows the equation below:

$$m_{DW} \ddot{q} + \alpha \dot{q} = -\mu_0 \gamma \Delta \left(H_z - \frac{\pi}{2} H_{SL} \left[\sin \phi u_{SOT,x} - \cos \phi u_{SOT,y} \right] \right) + \beta u \tag{4.30}$$

This equation shows that the DW in these two models is acting as a particle with the time dependent mass:

$$m_{DW} = \frac{1 + \alpha^2}{\mu_0 \gamma \left[H_K \cos 2\phi + \frac{\pi}{2} \left[(H_x - H_{DMI} - \alpha H_{SL} u_{SOT,x}) \cos \phi + (H_y - \alpha H_{SL} u_{SOT,y}) \sin \phi \right] \right]} \tag{4.31}$$

Note that while in the case of field, field-like SOT and STT driven DW motion the mass does not depend on excitation strength, in the case of Sloncweski-like driven DW motion, the mass depends on the strength of the excitation. The mass, and hence inertial effects and relaxation time, are dependant on the coordinate ϕ.

This is related to the Doring mass [62, 158]:

$$m_{Doring} = 2M_s \frac{1 + \alpha^2}{\mu_0 \gamma^2 \Delta H_K} \tag{4.32}$$

Frequency Domain Solution   As the evolution of Δ has minimal effect on the dynamics, the dynamics in this model is driven by ϕ. Equations 4.19 for the evolution of ϕ may be reqritten as:

$$\frac{1 + \alpha^2}{\mu_0 \gamma H_w} \dot{\phi} = \left(\frac{1}{\alpha} \frac{H_z}{H_w} - \frac{H_{SL}}{H_w} u_{SOT,z} \right) + (\frac{\beta}{\alpha} - 1) \frac{H_{STT}}{H_w} - \sin 2\phi$$
$$- \frac{\pi}{2} \left[\left(\left(\frac{H_x}{H_w} - \frac{H_{DMI}}{H_w} \right) + \frac{1}{\alpha} \frac{H_{SL}}{H_w} u_{SOT,x} \right) \sin \phi - \left(\frac{H_y}{H_w} + \frac{1}{\alpha} \frac{H_{SL}}{H_w} u_{SOT,y} \right) \cos \phi \right] \tag{4.33}$$

Introducing the the time constant $\omega_\phi = \frac{1}{\tau_\phi} = \frac{\mu_0 \gamma H_w}{1 + \alpha^2}$, and using the notation for normalized fields, we have:

$$\frac{1}{\omega_\phi} \dot{\phi} = \left(\frac{1}{\alpha} h_z - h_{SL} u_{SOT,z} \right) + (\frac{\beta}{\alpha} - 1) h_{STT} - \sin 2\phi$$
$$- \frac{\pi}{2} \left[\left(h_x - h_{DMI} + \frac{1}{\alpha} h_{SL} u_{SOT,x} \right) \sin \phi - \left(h_y + \frac{1}{\alpha} h_{SL} u_{SOT,y} \right) \cos \phi \right] \tag{4.34}$$

45

In the simplest case (absence of in-plane fields, DMI and spin-orbit torques), this simplifies to:

$$\frac{1}{\omega_\phi}\dot{\phi} = \frac{1}{\alpha}h_z + (\frac{\beta}{\alpha} - 1)h_{STT} - \sin 2\phi \tag{4.35}$$

which can be analytically solved:

$$\omega_\phi t = \frac{1}{\sqrt{1-h^2}} \log\left|\frac{h\tan\phi - 1 - \sqrt{1-h^2}}{h\tan\phi - 1 + \sqrt{1-h^2}}\frac{h\tan\phi_0 - 1 + \sqrt{1-h^2}}{h\tan\phi_0 - 1 - \sqrt{1-h^2}}\right| \tag{4.36}$$

with h $= \frac{1}{\alpha}$h$_z$ $+ (\frac{\beta}{\alpha} - 1)h_{STT}$ and noting $1 \geq$ h. This equation can further be simplified to:

$$\left|\frac{h\tan\phi - 1 + \sqrt{1-h^2}}{h\tan\phi - 1 - \sqrt{1-h^2}}\right| = \frac{h\tan\phi_0 - 1 + \sqrt{1-h^2}}{h\tan\phi_0 - 1 - \sqrt{1-h^2}} \exp(-\sqrt{1-h^2}\omega_\phi t) = \eta \exp(-w_0 t) \tag{4.37}$$

Note that $\eta > 1$. To get to an analytical description three cases can be solved. When $\tan\phi \leq \frac{1-\sqrt{1-h^2}}{h}$ or $\tan\phi \geq \frac{1+\sqrt{1-h^2}}{h}$, we have:

$$\tan\phi = \frac{1}{h} - \frac{\sqrt{1-h^2}}{h}\frac{1 + \eta\exp(-\omega_0 t)}{1 - \eta\exp(-\omega_0 t)} \tag{4.38}$$

Otherwise:

$$\tan\phi = \frac{1}{h} - \frac{\sqrt{1-h^2}}{h}\frac{1 - \eta\exp(-\omega_0 t)}{1 + \eta\exp(-\omega_0 t)} \tag{4.39}$$

In both cases, the steady state solution (when $t|\infty$) is:

$$\tan\phi^* = \frac{1}{h} - \frac{\sqrt{1-h^2}}{h} \tag{4.40}$$

4.2.2 Tilted Models

The q $- \phi - \chi$ **Model**

Another model which may be derived assuming a fixed DW width parameter (Δ) is the q $- \phi - \chi$ model which takes into account the tilting of the DW during its motions (similar to the model proposed by Boulle [82]). In this model, the DW is seen as a rigid tilted line moving through the system which may be described using the following three equations:

$$\alpha\frac{\dot{q}}{\Delta}\cos\chi + \dot{\phi} = \mu_0\gamma\left(H_z - \frac{\pi}{2}H_{SL}\left[\sin\phi u_{SOT,x} - \cos\phi u_{SOT,y}\right]\right) + \beta\frac{u}{\Delta}\cos\chi \tag{4.41}$$

$$\begin{aligned}\frac{\dot{q}}{\Delta}\cos\chi - \alpha\dot{\phi} &= \frac{1}{2}\mu_0\gamma M_s\left(N_y - N_x\right)\sin(\phi - \chi) - \frac{\pi}{2}\frac{\gamma D}{M_s\Delta}\sin(\phi - \chi)\\ &+ \frac{u}{\Delta}\cos\chi + \frac{\pi}{2}\mu_0\gamma\left[H_x\sin\phi - H_y\cos\phi\right] + \mu_0\gamma H_{SL}u_{SOT,z}\end{aligned} \tag{4.42}$$

$$\begin{aligned}-\alpha\frac{\pi^2}{12}\frac{\dot{\chi}}{\cos\chi}&\left[\left(\frac{w}{\pi\Delta}\right)^2 + \sin^2\chi\right] = \frac{1}{2}\gamma\mu_0 M_s\cos\chi(N_x - N_y)\sin 2\left(\phi - \chi\right) + \frac{\pi}{2}\frac{\gamma D}{M_s\Delta}\sin\phi\\ +\frac{\gamma}{M_s}\sin\chi&\left[\frac{A}{\Delta^2} + \left(K_u + \frac{\mu_0 M_s^2}{2}\left[N_x\cos^2(\phi - \chi) + N_y\sin^2(\phi - \chi) - N_z\right]\right)\right]\\ -\frac{\pi}{2}\mu_0\gamma&\left(H_x\cos\phi + H_y\sin\phi\right)\sin\chi\end{aligned} \tag{4.43}$$

Note that the first two equations are the same as Equations 4.16 and 4.17 with the effect of tilting on each term added in.

The equations for the evolution of each coordinate may be derived explicitly as:

$$
\begin{aligned}
\frac{(1+\alpha^2)}{\mu_0\gamma}\frac{\dot{q}}{\Delta}\cos\chi =\ &\alpha H_z + H_{SL}u_{SOT,z} + (1+\alpha\beta)\frac{u}{\mu_0\gamma\Delta}\cos\chi \\
&+ \frac{\pi}{2}\left[(H_x - \alpha H_{SL})\sin\phi - (H_y - \alpha H_{SL})\cos\phi\right] \\
&+ \frac{1}{2}M_s\left(N_y - N_x\right)\sin 2(\phi-\chi) - \frac{\pi}{2}\frac{D}{\mu_0 M_s\Delta}\sin(\phi-\chi)
\end{aligned}
\tag{4.44}
$$

$$
\begin{aligned}
\frac{(1+\alpha^2)}{\mu_0\gamma}\dot{\phi} =\ &H_z - \alpha H_{SL}u_{SOT,z} + \frac{\beta-\alpha}{\mu_0\gamma}\frac{u}{\Delta}cos\chi \\
&- \frac{\pi}{2}\left[(\alpha H_x + H_{SL}u_{SOT,x})\sin\phi - (\alpha H_y + H_{SL}u_{SOT,y})\cos\phi\right] \\
&- \alpha\left[\frac{1}{2}M_s\left(N_y - N_x\right)\sin 2(\phi-\chi) - \frac{\pi}{2}\frac{D}{\mu_0 M_s\Delta}\sin(\phi-\chi)\right]
\end{aligned}
\tag{4.45}
$$

$$
\begin{aligned}
&-\frac{\alpha}{\mu_0\gamma}\frac{\pi^2}{12}\left[\frac{\dot{\chi}}{\cos\chi}\left[\left(\frac{w}{\pi\Delta}\right)^2 + \sin^2\chi\right]\right] = \frac{1}{2}M_s\cos\chi(N_x - N_y)\sin 2\left(\phi-\chi\right) \\
&+ \frac{\sin\chi}{\mu_0 M_s}\left[\frac{A}{\Delta^2} + \left(K_u + \frac{\mu_0 M_s^2}{2}\left[N_x\cos^2\left(\phi-\chi\right) + N_y\sin^2\left(\phi-\chi\right) - N_z\right]\right)\right] \\
&+ \frac{\pi}{2}\frac{D}{\mu_0 M_s\Delta}\sin\phi - \frac{\pi}{2}\left(H_x\cos\phi + H_y\sin\phi\right)\sin\chi
\end{aligned}
\tag{4.46}
$$

From the equations, it can be observed that:

1. Applied field in the z direction and Slonczewski-like torques directly affect $\dot{\phi}$ and velocity.

2. The DMI, dipolar interaction and in-plane fields affect all three coordinates.

3. Exchange and uniaxial anisotropy only affect the evolution of the tilting angle directly.

4. In-plane fields can be used to enhance the effect of Sloncweski-like torques.

Note that our simulations of this case show that in the steady state condition non of $\dot{\phi}$, $\dot{\chi}$ or $\dot{\phi} - \dot{chi}$ are necessarily equal to zero although a steady state condition can usually be observed.

The $q - \phi - \Delta - \chi$ **Model**

If all four coordinates are used, the collective coordinate model will take the following form:

$$
\alpha\frac{\dot{q}}{\Delta}\cos\chi + \dot{\phi} = \mu_0\gamma\left(H_z - \frac{\pi}{2}H_{SL}\left[\sin\phi u_{SOT,x} - \cos\phi u_{SOT,y}\right]\right) + \beta\frac{u}{\Delta}\cos\chi
\tag{4.47}
$$

$$
\begin{aligned}
\frac{\dot{q}}{\Delta}\cos\chi - \alpha\dot{\phi} =\ &\frac{1}{2}\mu_0\gamma M_s\left(N_y - N_x\right)\sin 2(\phi-\chi) - \frac{\pi}{2}\frac{\gamma D}{M_s\Delta}\sin(\phi-\chi) \\
&+ \frac{u}{\Delta}\cos\chi + \frac{\pi}{2}\mu_0\gamma\left[H_x\sin\phi - H_y\cos\phi\right] + \mu_0\gamma H_{SL}u_{SOT,z}
\end{aligned}
\tag{4.48}
$$

$$\frac{\pi^2}{12}\alpha\left[\frac{\dot{\Delta}}{\Delta} + \frac{\dot{\chi}}{\cos\chi}\sin\chi\right] = \frac{\gamma}{M_s}\left[\frac{A}{\Delta^2} - K_u - \frac{\mu_0 M_s^2}{2}\left[N_x\cos^2(\phi-\chi) + N_y\sin^2(\phi-\chi) - N_z\right]\right]$$
$$+ \frac{\pi}{2}\mu_0\gamma\left(H_x\cos\phi + H_y\sin\phi\right)$$

$$(4.49)$$

$$-\alpha\frac{\pi^2}{12}\left[\frac{\dot{\Delta}}{\Delta}\sin\chi + \frac{\dot{\chi}}{\cos\chi}\left[\left(\frac{w}{\pi\Delta}\right)^2 + \sin^2\chi\right]\right] = \frac{\gamma}{M_s}\sin\chi\left[\frac{A}{\Delta^2}\right.$$
$$+ \left(K_u + \frac{\mu_0 M_s^2}{2}\left[N_x\cos^2(\phi-\chi) + N_y\sin^2(\phi-\chi) - N_z\right]\right)\right]$$
$$+ \frac{1}{2}\gamma\mu_0 M_s\cos\chi(N_x - N_y)\sin 2(\phi-\chi)$$
$$+ \frac{\pi}{2}\frac{\gamma D}{M_s\Delta}\sin\phi - \frac{\pi}{2}\mu_0\gamma\left(H_x\cos\phi + H_y\sin\phi\right)\sin\chi$$

$$(4.50)$$

Here the first two equations are the same as the $q - \phi - \chi$ model, while the latter two equations are completely different from those seen in the $q - \phi - \Delta$ and $q - \phi - \chi$ models.

The equations for the evolution of each collective coordinate may explicitly be written as:

$$\frac{(1+\alpha^2)}{\mu_0\gamma}\frac{\dot{q}}{\Delta}\cos\chi = \alpha H_z + H_{SL}u_{SOT,z} + (1+\alpha\beta)\frac{u}{\mu_0\gamma\Delta}\cos\chi$$
$$+ \frac{\pi}{2}\left[(H_x - \alpha H_{SL})\sin\phi - (H_y - \alpha H_{SL})\cos\phi\right]$$
$$+ \frac{1}{2}M_s(N_y - N_x)\sin 2(\phi-\chi) - \frac{\pi}{2}\frac{D}{\mu_0 M_s\Delta}\sin(\phi-\chi)$$

$$(4.51)$$

$$\frac{(1+\alpha^2)}{\mu_0\gamma}\dot{\phi} = H_z - \alpha H_{SL}u_{SOT,z} + \frac{\beta-\alpha}{\mu_0\gamma}\frac{u}{\Delta}\cos\chi$$
$$- \frac{\pi}{2}\left[(\alpha H_x + H_{SL}u_{SOT,x})\sin\phi - (\alpha H_y + H_{SL}u_{SOT,y})\cos\phi\right]$$
$$- \alpha\left[\frac{1}{2}M_s(N_y - N_x)\sin 2(\phi-\chi) - \frac{\pi}{2}\frac{D}{\mu_0 M_s\Delta}\sin(\phi-\chi)\right]$$

$$(4.52)$$

$$\frac{\pi^2}{12}\alpha\frac{\dot{\Delta}}{\Delta}\left(\frac{w}{\pi\Delta}\right)^2 = \frac{\gamma}{M_s}\frac{A}{\Delta^2}\left(\left(\frac{w}{\pi\Delta}\right)^2 + 2\sin^2\chi\right)$$
$$- \frac{\gamma}{M_s}\left(\frac{w}{\pi\Delta}\right)^2\left(K_u + \frac{\mu_0 M_s^2}{2}\left[N_x\cos^2(\phi-\chi) + N_y\sin^2(\phi-\chi) - N_z\right]\right)$$
$$+ \frac{\pi}{2}\left(\frac{w}{\pi\Delta}\right)^2\mu_0\gamma\left(H_x\cos\phi + H_y\sin\phi\right)$$
$$+ \frac{1}{4}\gamma\mu_0 M_s\sin 2\chi(N_x - N_y)\sin 2(\phi-\chi) + \frac{\pi}{2}\frac{\gamma D}{M_s\Delta}\sin\phi\sin\chi$$

$$(4.53)$$

$$-\frac{\alpha}{\mu_0\gamma}\frac{\pi^2}{12}\frac{\dot{\chi}}{\cos\chi}\left(\frac{w}{\pi\Delta}\right)^2 = 2\frac{A}{\mu_0 M_s\Delta^2}\sin\chi + \frac{\pi}{2}\frac{D}{\mu_0 M_s\Delta}\sin\phi$$
$$+ \frac{1}{2}M_s(N_x - N_y)\sin 2(\phi-\chi)\cos\chi$$

$$(4.54)$$

These equations show that:

1. Only the evolution of the DW width depends on the magnetocrystalline anisotropy.

2. Exchange interaction affects both tilting and the DW width directly.

3. The DMI and dipolar interaction show up in all equations.

4. Out-of-plane fields and Sloncweskii torques affect the evolution of $\dot{\phi}$ and velocity directly.

5. In-plane fields do not directly affect the evolution of tilting.

Note that our simulations of this case show that in the steady state condition only $\dot{\Delta}$ necessarily equals zero.

Closed-Form and Analytical Solutions

Steady State Conditions   In simulations and using the model, we observed the rapid relaxation of the DW width parameter. The steady state DW width parameter can be calculated:

$$
\begin{aligned}
\dot{\Delta} = 0 \Rightarrow & \\
0 = \frac{\gamma}{M_s} & \left[\frac{A}{\Delta^2} - \left(K_u + \frac{\mu_0 M_s^2}{2} \left[N_x \cos^2\left(\phi - \chi\right) + N_y \sin^2\left(\phi - \chi\right) - N_z \right] \right) \right] \\
& + \frac{\pi}{2} \mu_0 \gamma \left(H_x \cos\phi + H_y \sin\phi \right) \\
& + \frac{\gamma}{M_s} \left(\frac{w}{\pi\Delta} \right)^2 \left[2\frac{A}{\Delta^2} \sin^2\chi + \frac{\pi}{2}\frac{D}{\Delta} \sin\phi \sin\chi + \frac{1}{4}\mu_0 M_s^2 \sin 2\chi (N_x - N_y) \sin 2\left(\phi - \chi\right) \right]
\end{aligned}
\tag{4.55}
$$

Assuming a small tilting angle of the DW $\chi \sim 0$, the steady state DW width may be estimated as:

$$
\Delta^* = \sqrt{\frac{A}{K_u + \frac{\mu_0 M_s^2}{2} \left[N_x \cos^2\phi + N_y \sin^2\phi - N_z \right] + \frac{\pi}{2}\mu_0\gamma \left(H_x \cos\phi + H_y \sin\phi \right)}}
\tag{4.56}
$$

which is the same as Equation 4.21. This approximation of the DW width may be used in the q $-$ ϕ and q $-$ ϕ $-$ χ models with negligible errors compared to the models that take into account the evolution of Δ.

While we did observe the relaxation of ϕ and χ in micromagnetic simulations, we did not necessarily observe them when using the CCMs. Yet, using the assumptions $\dot{\phi} = \dot{\chi} = 0$, an approximation of steady state velocity may be extracted as:

$$
\dot{q}^* = \frac{\mu_0 \gamma \Delta^*}{\alpha \cos\chi^*} \left[H_z + \beta\frac{u}{\mu_0\gamma\Delta^*} + \frac{\pi}{2} H_{SL} \left(u_{SOT,y} \cos\phi^* - u_{SOT,x} \sin\phi^* \right) \right]
\tag{4.57}
$$

Determining the steady state value of the ϕ and χ angles is somewhat more complex. Based on our assumption, a steady state condition is equivalent to:

$$
\begin{aligned}
\dot{\phi} = 0 \Rightarrow \alpha\frac{1}{2} M_s \left(N_y - N_x \right) \sin 2(\phi^* - \chi^*) = & \left(H_z - \alpha H_{SL} u_{SOT,z} \right) + \frac{\beta - \alpha}{\mu_0\gamma}\frac{u}{\Delta^*} \\
& - \frac{\pi}{2} \left[(\alpha H_x + H_{SL} u_{SOT,x}) \sin\phi^* - (\alpha H_y + H_{SL} u_{SOT,y}) \cos\phi^* \right] \\
& + \alpha\frac{\pi}{2}\frac{D}{\mu_0 M_s \Delta^*} \sin(\phi^* - \chi^*)
\end{aligned}
\tag{4.58}
$$

$$\dot{\chi} = 0 \Rightarrow \frac{1}{2} M_s (N_y - N_x) \sin 2(\phi^* - \chi^*) \cos \chi^* = \frac{2A}{\mu_0 M_s \Delta^{*2}} \sin \chi^* + \frac{\pi}{2} \frac{D}{\mu_0 M_s \Delta^*} \sin \phi^* \quad (4.59)$$

Equation 4.58 clearly shows that the excitations need to balance out with the dipolar and DM interactions in order to reach a steady state condition. Otherwise, the precession of magnetization will continue. Equations 4.58 and 4.59 may only be analytically solved in the simplest cases.

The presence of DMI changes the dynamics by adjusting the applied field or current at which Walker Breakdown happens. For simplicity, we will use H_W defined in the previous section as Walker breakdown to help visualize the effect of DMI.

Assuming a case field driven DW motion with a small angle assumption for $\phi - \chi$, equation 4.58 yields:

$$\phi^* - \chi^* = \frac{H_z}{\alpha \left(M_s (N_y - N_x) - \frac{\pi}{2} \frac{D}{\mu_0 M_s \Delta^*} \right)} = \frac{H_z}{2H_w - \alpha H_{DMI}} \quad (4.60)$$

where H_{DMI} denotes the effective DMI field. It is clear that, depending on its sign, the DMI field can extend the range of fields over which a steady state condition may be reached. The DW width can be estimated using $\dot{q} = \frac{\mu_0 \gamma \Delta}{\alpha} H_z$.

A similar approach could be used to define the Walker breakdown current for the STT driven DW motion or Sloncweski-like SOTs in the z direction. However, these cases will not be presented here as in most heterostructures with SOC, the SOTs are in the y direction and STT has negligible effect due to the low thickness of the system [75, 85, 86].

Another case which could be analytically solved is the case of Sloncweski-like driven DW motion, with SOTs in the x-direction. Assuming a small tilting angle ($\chi \sim 0$) we have:

$$cos\phi^* = \frac{\pi}{2} \frac{\alpha H_{DMI} - H_{SL} u_{SOT,x}}{\alpha M_s (N_y - N_x)} = \frac{\pi}{2} \frac{\alpha H_{DMI} - H_{SL} u_{SOT,x}}{2H_w} \quad (4.61)$$

Note that in the case above, DMI changes the effective field at which Walker breakdown is reached. However, this case effectively does not lead to the motion of Néel walls as shown in [81] ad also in our simulations.

Small SOT excitations in the y direction may also be analytically written under the $\chi \sim 0$ approximation, yielding:

$$\alpha \frac{1}{2} M_s (N_y - N_x) \sin 2\phi^* - \frac{\pi}{2} H_{SL} \cos \phi^* - \alpha \frac{\pi}{2} \frac{D}{\mu_0 M_s \Delta^*} \sin \phi^* = 0 \quad (4.62)$$

This equation can only be analytically solved under the assumption of small ϕ:

$$\phi^* = \frac{\pi}{2} \frac{H_{SL}}{\alpha (M_s (N_y - N_x) - \frac{\pi}{2} \frac{D}{\mu_0 M_s \Delta^*})} = \frac{\pi}{2} \frac{H_{SL}}{2H_w - \frac{\pi}{2} H_{DMI}} \quad (4.63)$$

Note that in this case, the DMI may reduce or increase the effective Walker breakdown field depending on the sign of the DMI strength. The steady state velocity with small ϕ and the $\chi \sim 0$ approximation may simply be written as:

$$\dot{q} = \frac{\pi}{2} \frac{\mu_0 \gamma}{\alpha} H_{SL} \Delta^* u_{SOT,y} \quad (4.64)$$

4.3   Comparison to Micromagnetic Simulations

To assess the accuracy of the models developed in this Chapter, simulations were preformed on nanowires made of Pt/CoFe/MgO. In all cases, a nanowire was simulated with the dimensions 2.8μm $\times$ 160nm $\times$ 0.6nm with the material parameters outlined in Chapter 2 and reference [85].

Different methods of extracting the collective coordinates were assessed to find the most effective way of extracting the relevant coordinates from micromagnetic simulations. These included the Porter definition for DW width and velocity [159], the Thiele definition for DW width [62], the fingerprinting method [160], local definitions of spherical coordinates and fitting of the data to the Bloch profile. The most accurate description was found to be:

- DW velocity extracted following the methods in [159]: $v = \frac{L_x}{2}\frac{d\langle m_x(t)\rangle}{dt}$ where L_x is the length of the nanowire. Other methods provided results with negligible difference.

- ϕ extracted from the local values of the x and y component of magnetization at the center of the DW (position q and y = w/2).

- The tilting angle extracted by finding the center of the DW at the edges of the nanowire and computing the angle of the line connecting the two points with respect to the width of the wire through the center of the DW (q).

- DW width extracted following the Thiele definition of DW width [62]: $\Delta = \frac{2A_{tw}}{\int(\frac{\partial \hat{m}}{\partial x})^2}$ with A_{tw} denoting the cross sectional area of the wire.

Figure 4.2 compares the different coordinates as predicted by different CCMs to micromagnetic simulations for the case of field-driven DW motion below the Walker breakdown. Clearly, the models which include tilting of the DW predicts the DW velocity with better accuracy. The DW width parameter was found to vary negligibly, and seems to have minimal effect on the dynamics based on the fact that models with a varying DW width and with a fixed DW width behave similarly. All collective coordinate models clearly predict similar values for $\phi - \chi$ and the differences could be attributed to the effect of χ as a degree of freedom.

Figure 4.2.(a) clearly shows that the collective coordinate models deviate from the trend in the micromagnetic simulations for applied fields above 40mT. To better understand these deviations, we calculated the goodness of fit (R^2) and root mean square error (RMSE) normalized by the average value of each parameter; the results of which are summarized in Table 4.1. Clearly, the four coordinate model improves the accuracy in predicting DW velocity and DW magnetization angle, while maintaining similar accuracy compared to other models in predicting the DW width and tilting angle.

Figure 4.3 depicts the predictions of the collective coordinate models compared to micromagnetic simulations for the case of SHE-driven DW motion below the Walker breakdown. We assumed that the SHE-mechanism only gives rise to Slonczewski-like torques, and that contributions from the STT mechanism are negligible. Clearly, the $q - \phi - \chi$ and $q - \phi - \chi - \Delta$ models accurately reproduce the DW velocity curve, while predicting the difference between tilting and magnetization to an acceptable degree. In terms of the angle $\phi - \chi$, the predictions of $q - \phi - \chi$ and $q - \phi - \chi - \Delta$ are only similar at high currents. This difference could be attributed to the effect of changes in the DW width. In fact, reviewing the DW width curves (not shown here) shows that the DW width adjusts itself for low fields in the case of SHE-driven DW motion, until it reaches a fixed value for high fields. Normalized root mean square error (NRMSE) and goodness of fit computed for the different models in Table 4.2 clearly show the higher accuracy of the $q - \phi - \chi - \Delta$ model. Specifically, this model improves the accuracy in predicting the DW magnetization angle and the DW width.

(a) DW velocity ($\dot{q}$).

(b) DW width (Δ).

(c) DW tilting angle (χ).

(d) $\phi - \chi$.

Figure 4.2: Comparison of the 1-D model predictions to micromagnetic simulations for field driven DW motion below Walker breakdown.

The inability of the $q - \phi$ and $q - \phi - \Delta$ models in reproducing the micromagnetic results in this case could be attributed to the more complex coupling between the interactions and the angles. The Slonczewski-like field in the y-direction is directly multiplied by $\cos\phi$ (Eqs. 4.51 and 4.52), while the other interactions simulated here relate to $\phi - \chi$.

Based on the relative errors in Tables 4.1 and 4.2, it can be concluded that the collective coordinate model developed in this work with four coordinates ($q - \phi - \chi - \Delta$) can reproduce micromagnetic simulations with acceptable accuracy, and is particularly suited for current-driven studies. Specifically, this model improves the accuracy in predicting the DW magnetization angle, while maintaining the accuracy in predicting other DW properties. However, for most purposes the $q - \phi - \chi$ model also has acceptable accuracy, with errors less than 10%.

A study using this model was also performed on STT-driven DW motion, highlighting the high accuracy of the Lagrangian models in replicating STT-driven DW motion, with errors lower than 1% in predicting velocity and DW tilting, and less than 10% fo other collective coordinates [3].

Table 4.1: R^2 and normalized root mean square error (NRMSE) for field driven DW motion. The small angle approximations are (Eqs. 4.57, and 4.60). The bold values show the lowest NRMSE achieved (if significant).

Model/ NRMSE [R^2]	Velocity	ϕ	χ	$\phi - \chi$	Δ
q $-\phi$	23.38% [99.92%]	54.65% [93.31%]	-	7.06% [99.87%]	-
q $-\phi-\Delta$	23.73% [99.92%]	12.16% [93.45%]	-	6.89% [99.88%]	3.12% [71.35%]
q $-\phi-\chi$	12.93% [99.98%]	54.86% [98.78%]	12.58% [99.94%]	7.06% [99.87%]	-
q $-\phi-\chi-\Delta$	**12.49%** [99.98%]	**11.86%** [98.81%]	12.59% [99.95%]	6.89% [99.88%]	3.12% [71.35%]
Small angle approximation	19.31% [99.92%]	-	-	10.01% [99.68%]	-

Table 4.2: R^2 and normalized root mean square error (NRMSE) for field driven DW motion. The small angle approximations are Eqs. 4.57, and 4.63. The bold values show the lowest NRMSE achieved (if significant).

Model/ NMRSE [R^2]	Velocity	ϕ	χ	$\phi - \chi$	Δ
q $-\phi$	24.98% [99.57%]	29.94% [96.26%]	-	106.15% [90.43%]	-
q $-\phi-\Delta$	24.78% [99.58%]	30.08% [96.45%]	-	105.70% [90.42%]	15.98% [95.73%]
q $-\phi-\chi$	2.61% [99.93%]	6.83% [90.63%]	6.67% [97.03%]	23.77% [57.94%]	-
q $-\phi-\chi-\Delta$	2.6% [99.93%]	**1.79%** [99.85%]	6.67% [97.04%]	**12.97%** [94.11%]	**15.75%** [97.09%]
Small angle approximation	161.39% [95.82%]	4.87% [88.56%]	-	99.61% [78.20%]	-

4.4 Conclusion

In this Chapter we presented the Euler-Lagrange approach to developing collective coordinate models. This approach was used to develop four collective coordinate models to describe DW motion. We found that in systems with DMI use of three collective coordinates (q, ϕ and χ) leads to acceptable results while a four coordinate model with the addition of Δ only slightly improves the accuracy of the models compared to micromagnetic simulations. We also showed some of the closed-form results of these models which may be useful for back-of-the-envelope calculations or extracting material parameters from experiments.

(a) DW velocity ($\dot{q}$).

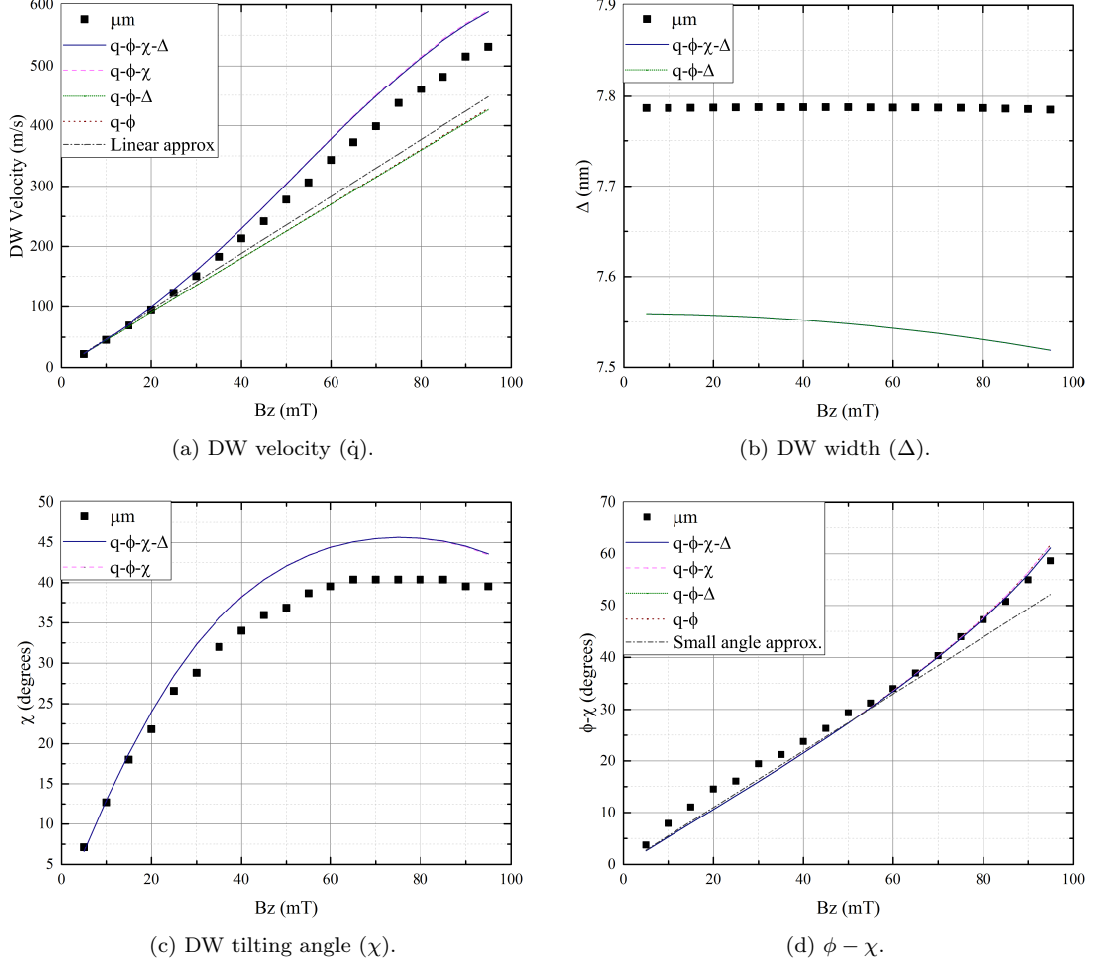(b) DW width (Δ).

(c) DW tilting angle (χ).

(d) $\phi - \chi$.
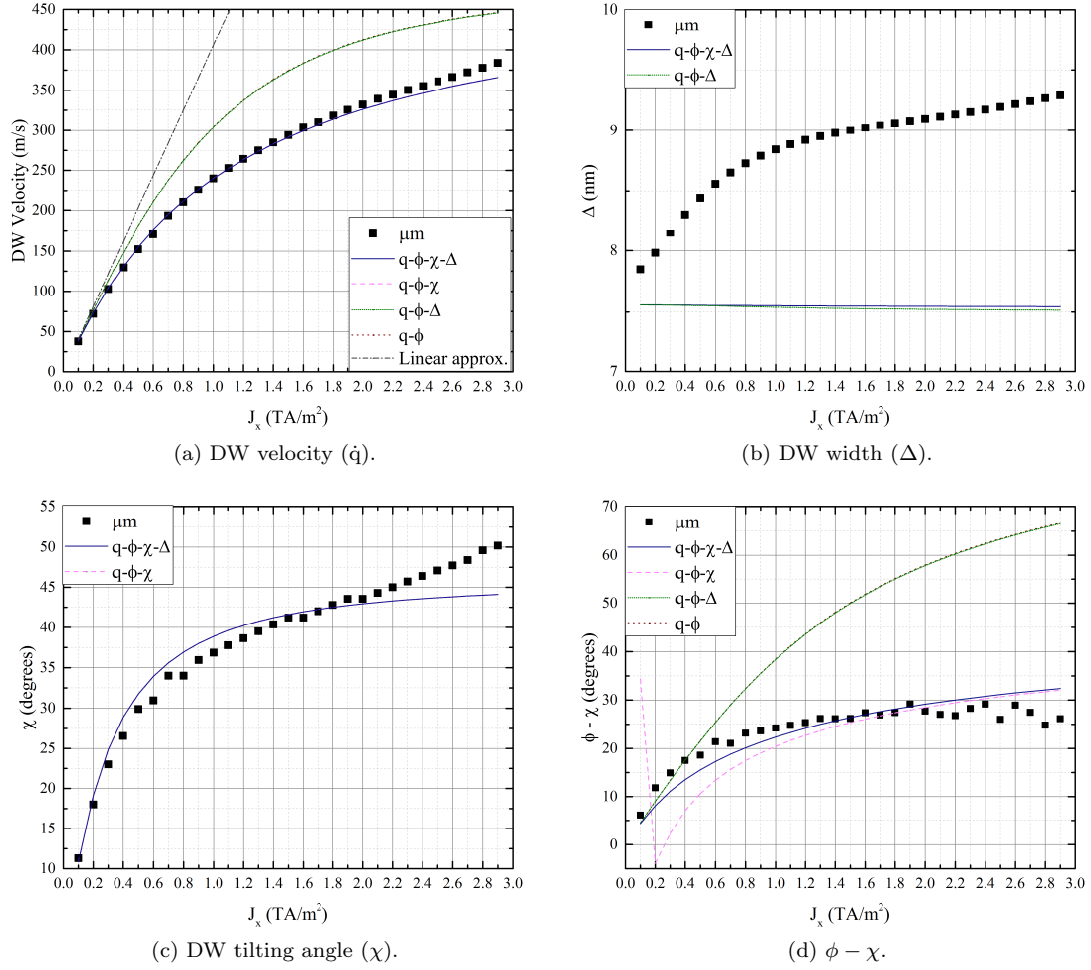
Figure 4.3: Comparison of the 1-D model predictions to micromagnetic simulations for SHE driven DW motion below the Walker breakdown.

Chapter 5

DW Motion in Nanowires Under the Application of In-plane Fields

As outlined in Chapters 1 and 2, recent studies on DW motion have focused on perpendicular magnetic anisotropy (PMA) heterostructures of ultrathin ferromagnets sandwiched between a heavy metal layer and an oxide. In these structures, spin-orbit coupling (SOC) and broken inversion symmetry (BIC) contribute to DW motion [75, 121–124]. Specifically, the Dzyloshinskii-Moriya interaction (DMI) present in these systems stabilizes Néel DW structures of specific chirality. SOC has also been linked with enhanced current induced DW motion, with the spin Hall effect (SHE) suggested as the dominant mechanism for this observation [75].

In perpendicularly magnetized heterostructures with DMI, applied fields in-plane of the sample could be used to control DW chirality and the behavior of the DW [82–87, 156]. Micromagnetic simulations of such systems are in agreement with experiments [85], showing an increase in DW velocity with fields parallel to the internal magnetization of the DW. However,conventional CCMs (q $- \phi$ [54] and q $- \phi - \chi$ [82]) fail to reproduce these results [82, 85].

Despite this shortcoming of collective coordinate models, two of the most prominent methods of assessing the strength of the DMI rely on DW motion under in-plane fields. The method used by most investigators to measure DMI strength is studying the expansion of magnetic bubbles under the application of in-plane and out-of-plane fields [88, 89]. This method assumes that the points with significant Néel character are located on the axis of the in-plane field applied, and the DMI field is assumed to be equal to the in-plane field which reverses the chirality of the DW. In an alternative method, a critical longitudinal field in current-driven DW motion in systems with DMI is used at which the DW is locked in place, and does not move irrespective of applied current [4].

Most experimentalists rely on the q $- \phi - \chi$ model in such measurements for determining the DMI strength; however, as mentioned previously, this model cannot reproduce the micromagnetic results. This calls for improvements in collective coordinate modeling of DW motion, both to reproduce micromagnetic results and to help in the assessment of DMI strength in material stacks.

We initially applied the models developed in Chapter 4 to a case of current-driven DW motion in a Pt/CoFe/MgO sample under longitudinal in-plane fields [4]. As depicted in Figure 5.1, none of our models were able to accurately predict DW behavior under in-plane fields, while the q$-\phi-\chi-\Delta$ model seems to be the most close in replicating the qualitative behavior of the DW. This is partially due to changes in the DW structure under in-plane fields, as presented in Chapter 3.

In this Chapter, we look at the impact of in-plane fields on field- and current-driven DW motion, presenting two extended collective coordinate models that take into account canting in the domains as an additional parameter. We compare these model to other CCMs for DW motion [4, 54, 62, 82], showcasing its improved accuracy. Critical points in the behavior of the DW under in-plane

magnetic fields are also identified, along with closed form solutions for these critical points which could be used to estimate different material properties based on experimental measurements.

Acknowledgment: Parts of the content in this Chapter were published in the following publications:

- S. Ali Nasseri, Eduardo Martinez, Gianfranco Durin, "Collective Coordinate Descriptions of Magnetic Domain Wall Motion in Perpendicularly Magnetized Nanostructures under the Application of In-plane Fields", Journal of Magnetism and Magnetic Materials (under review), arxiv: 1804.00569 [1].

- S. Ali Nasseri, Simone Moretti, Eduardo Martinez, Gianfranco Durin, Claudio Serpico, "Collective Coordinate Models of Domain Wall Dynamics in PMA Materials under Spin Hall Effect and Longitudinal in-Plane Fields", Journal of Magnetism and Magnetic Materials, vol. 426, pp. 195-201, 2017, doi: 10.1016/j.jmmm.2016.11.081 [4].

Please use these papers in any citations.

5.1 Materials under study

We study two $2.8\mu m$ long, 160nm wide nanowires with the magnetic properties listed in Table 5.1 and a 0.6nm thickness for the ferromagnetic layer. These samples were selected as they both have DMI and PMA; however, the DMI strength of the Pt/CoFe/MgO sample is twice that of the Pt/Co/Ni/Co/MgO/Pt sample, while its PMA constant is 1/3 that of the later sample. This helps us better understand the effects of these two parameters on the structure and dynamics of DWs.

Table 5.1: Material parameters of the two systems studied in this work. The DMI strength of the Pt/CoFe/MgO sample is twice that of the Pt/Co/Ni/Co/MgO/Pt sample, while its PMA constant is 1/3 that of the later sample. This difference in material properties helps better understand their effects on DW dynamics.

	Pt/CoFe/MgO [86]	Pt/Co/Ni/Co/MgO/Pt [151]
Saturation magnetization M_s (kA/m)	700	837
Exchange constant A (pJ/m)	10	10
Uniaxial perpendicular anisotropy constant K_u (MJ/m^3)	**0.48**	**1.310**
DW width parameter (nm) $\Delta \sim \sqrt{\frac{A}{K_u - \mu_0 M_s^2/2}}$	7.2	3.39
Gilbert damping α	0.3	0.15
SHE angle θ_{SH}	0.07	0.07 (assumed)
DMI strength D (mJ/m^2)	**-1.2**	**0.6**

5.2 Extended Collective coordinate Models

In this section we will present two approaches to improve the accuracy of the CCMs for cases in which in-plane fields are applied. We will rely on the same collective coordinates presented in Chapter 4 to model the DW under in-plane fields.
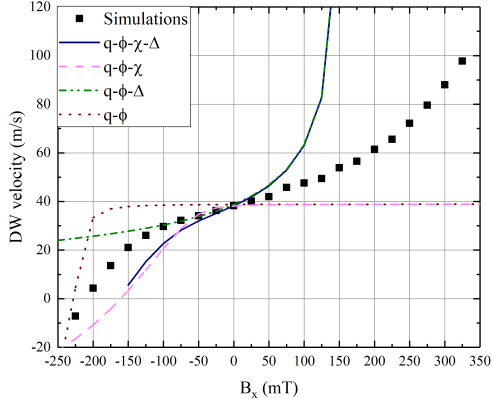
(a) DW velocity ($\dot{q}$).
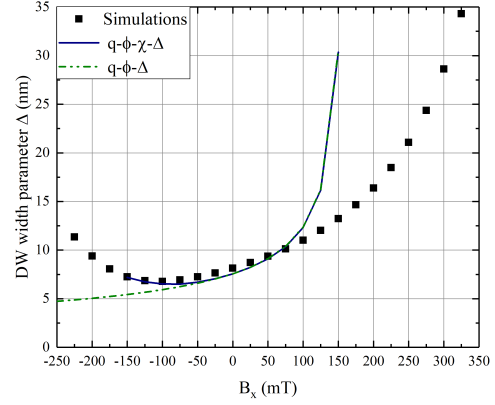
(b) DW width (Δ).
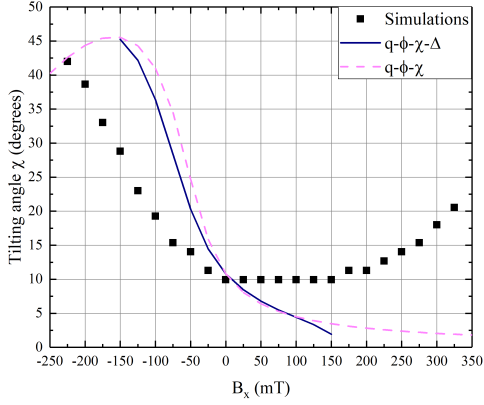
(c) DW tilting angle (χ).
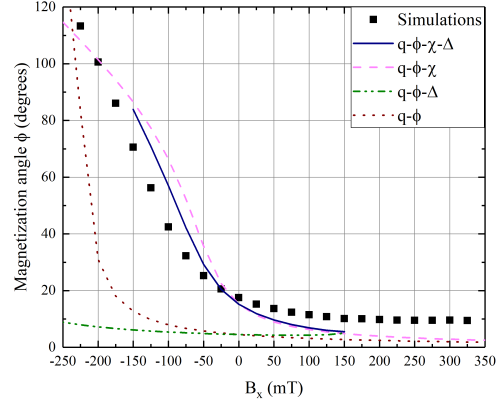
(d) DW in-plane angle (ϕ).
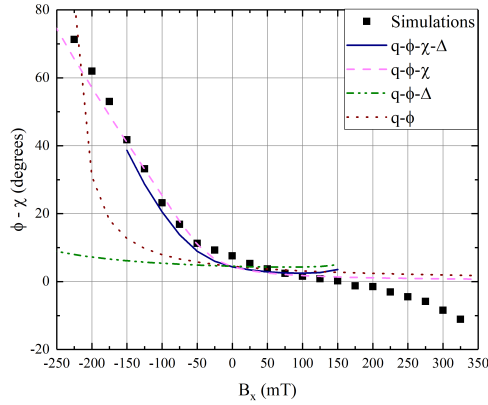
(e) $\phi - \chi$.

Figure 5.1: Comparison of results from the collective coordinate models presented in Chapter four to micromagnetic simulations for SHE-driven DW motion under the application of longitudinal in-plane fields. Clearly, non of the models can reproduce the micromagnetic results fully. Only the four coordinate $q - \phi - \chi - \Delta$ model qualitatively matches the results of micromagnetics with a point of inflection predicted in the velocity curve.

As mentioned in the previous Chapter, an ansatz is needed to link the collective coordinates with the spherical coordinates for the magnetization in order to write the Lagrangian and dissipation functions in terms of these coordinates. As highlighted in Chapter 3, the structure of the DW under in-plane fields is affected as the domains will be canted into the plan of the sample. In the presence of an applied in-plane field in the domains, the magnetization in the domains may be described in spherical coordinates as $\phi = \mathrm{atan}\left(\frac{H_y}{H_x}\right)$ and $\sin\theta_c = \mathrm{sgn}(H_x, H_y)\frac{\mu_0 M_s (H_x \cos\phi + H_y \sin\phi)}{2K_u + \mu_0 M_s^2 (N_x \cos^2\phi + N_y \sin^2\phi - N_z)}$ where θ_c is the canting angle. Note that, as we are projecting the 3-D magnetization angle onto a plane, a sign for the canting angle θ_c also needs to be included in the model; we defined the angle to be negative for negative in-plane fields and positive for positive in-plane fields (which is equivalent to clock-wise/counter clockwise convention for the sign of angles in 2-D); comparison to cases where this sign was not taken into account later revealed the importance of this convention to improve model accuracy.

As such, in addition to the models presented in Chapter 3, we can derive two additional groups of models in this Chapter:

1. Integrating the tilted Bloch profile [82] $\tan\frac{\theta}{2} = \exp(u)$ from θ_c to $\pi - \theta_c$: This model approximates the effect of the canting in the domains and was the first model we developed to take into account this effect.

2. Integrating the inherently canted profile $\tan\left(\frac{\theta+\theta_c}{2}\right) = \frac{\exp(u)+\sin\theta_c}{\cos\theta_c}$ from θ_c to $\pi - \theta_c$: We expected this model to be the most accurate, as it takes into account the effect of canting not just in the domains but on the DW structure.

In both profiles $u = \frac{(x-q)\cos\chi + y\sin\chi}{p_w \Delta}$. The parameter p_w can take the value of ± 1 to adjust for top-down vs bottom-up DWs. In both cases, we also assume that magnetization is homogeneous within the DW, hence $\phi(r,t) = \phi(t)$. The two profiles were already presented in Chapter 3 and compared to the static structure of the DW.

In order to evaluate DW dynamics using the collective coordinates, we need to rewrite the energy terms using these coordinates and the properties of the ansatz. The energy and dissipation function then need to be integrated along the length and width of the wire, and plugged into the Euler-Lagrange equation. This process will result in four equations:

$$\alpha I_1 \frac{\dot{q}}{p_w \Delta}\cos\chi + I_2 \dot{\phi} = \mu_0 \gamma \left(I_2 H_z - I_3 H_{SL}\left[\sin\phi u_{SOT,x} - \cos\phi u_{SOT,y}\right]\right) + \beta I_1 \frac{u}{p_w \Delta}\cos\chi \quad (5.1)$$

$$I_2 \frac{\dot{q}}{p_w \Delta}\cos\chi - \alpha I_4 \dot{\phi} = I_4 \frac{\mu_0 \gamma M_s}{2}\left(N_y - N_x\right)\sin 2(\phi - \chi) + I_5 \frac{u}{p_w \Delta}\cos\chi$$
$$+ I_6 \mu_0 \gamma \left[H_x \sin\phi - H_y \cos\phi\right] - I_3 \frac{\gamma D}{M_s p_w \Delta}\sin(\phi - \chi) \quad (5.2)$$

$$\alpha I_7 \left[\frac{\dot{\Delta}}{p_w \Delta} + \dot{\chi}\tan\chi\right] = \frac{\gamma}{M_s}\left[I_1 \frac{A}{(p_w \Delta)^2} - I_4 p_w K\right] + I_6 \mu_0 \gamma p_w \left(H_x \cos\phi + H_y \sin\phi\right) \quad (5.3)$$

$$-\alpha I_7 \left[\frac{\dot{\Delta}}{p_w \Delta}\sin\chi + \frac{\dot{\chi}}{\cos\chi}\left[\frac{I_1}{6I_7}\left(\frac{w}{P_w \Delta}\right)^2 + \sin^2\chi\right]\right] = I_3 \frac{\gamma D}{M_s p_w \Delta}\sin\phi$$
$$+ I_4 \frac{\mu_0 \gamma M_s}{2}\cos\chi(N_x - N_y)\sin 2(\phi - \chi)$$
$$+ \frac{\gamma}{M_s}\sin\chi\left[I_1 \frac{A}{(p_w \Delta)^2} + I_4 K - I_6 \mu_0 M_s \left(H_x \cos\phi + H_y \sin\phi\right)\right] \quad (5.4)$$

where $K = K_u + \frac{\mu_0 M_s^2}{2} \left[N_x \cos^2 (\phi - \chi) + N_y \sin^2 (\phi - \chi) - N_z \right]$.

Note that the equations 5.1-5.4 above may be further simplified into two coordinate models (assuming $\chi = 0$ and a fixed Δ leads to a model similar to the $q - \phi$ model [54]), or three coordinate models ($\chi = 0$ leads to a model similar to the $q - \phi - \Delta$ [62] model, while assuming a fixed Δ leads to a model similar to the $q - \phi - \chi$ [82] model).

In the equations above, I_is are integration constants which depend on the ansatz used and relate to the amount of canting in the domains. Three classes of models were derived based on the ansatz used and how they were integrated:

1. Integrating ansatz 1 from 0 to π: This model does not take into account the canting in the domains, and was presented in one of our previous works [3].

2. Integrating ansatz 1 from θ_c to $\pi - \theta_c$: This model approximates the effect of the canting in the domains and was presented in our past work [4].

3. Integrating ansatz 2 from θ_c to $\pi - \theta_c$: We expect this model to be the most accurate, as it takes into account the effect of canting not just in the domains but on the DW structure.

Equations 5.1-5.4 are rather interesting as they show that the ansatz used does not affect the functionality in terms of the collective coordinates. Instead, the effect of the ansatz (including canting) is taken into account in the I_i parameters.

Table 5.2: Summary of model parameters derived from integration for the three different models. Model 1 is the model based on the Bloch profile without canting, model 2 is also based on the Bloch profile but takes into account canting in the domains through the canting angle in the domains (θ_c), and model 3 is based on an inherently canted ansatz. The column labeled Model 3/ Model 2 shows the ratio of the parameter in model 3 to the one in model 2.

	Model 1	Model 2	Model 3	Model 3 / Model 2
I_1	1	$\cos \theta_c$	$1 - \left(\frac{\pi}{2} - \theta_c \right) \tan \theta_c$	$\sec \theta_c \left(1 - \left(\frac{\pi}{2} - \theta_c \right) \tan \theta_c \right)$
I_2	1	1	$\cos \theta_c$	$\sec \theta_c$
I_3	$\frac{\pi}{2}$	$\frac{\pi}{2} - \theta_c$	$\frac{\pi}{2} - \theta_c$	1
I_4	1	$\cos \theta_c$	$\cos^2 \theta_c + \left(\frac{\pi}{2} - \theta_c \right) \sin \theta_c \cos \theta_c$	$\cos \theta_c + \left(\frac{\pi}{2} - \theta_c \right) \sin \theta_c$
I_5	1	$\cos \theta_c$	$\cos \theta_c$	1
I_6	$\frac{\pi}{2}$	$\frac{\pi}{2} - \theta_c$	$\frac{\pi}{2} - \theta_c$	1
I_7	$\frac{\pi^2}{6}$	Equation 5.5	Equation 5.6	-

Table 5.2 summarizes the value of the I_is for the three different groups of models, which are parameters included in th model to account for the effect of the ansatz and the canting in the domains. For model 2, the closed form of the I_7 constant is:

$$
\begin{aligned}
I_7 = &\left[Li_2 \left(-\cos \frac{\theta_c}{2} \right) - \text{Li}_2 \left(-\sin \frac{\theta_c}{2} \right) - \text{Li}_2 \left(1 - \cos \frac{\theta_c}{2} \right) + Li_2 \left(1 - \sin \frac{\theta_c}{2} \right) \right] \\
&- \cos^2 \frac{\theta_c}{2} \left[1 - log(\cos \frac{\theta_c}{2}) \right] + \sin^2 \frac{\theta_c}{2} \left[1 - \log(\sin \frac{\theta_c}{2}) \right] \\
&- \cos^2 \frac{\theta_c}{2} \log(\sin^2 \frac{\theta_c}{2}) \left[\log(\cos \frac{\theta_c}{2}) - \frac{1}{2} \right] + \sin^2 \frac{\theta_c}{2} \log(\cos^2 \frac{\theta_c}{2}) \left[\log(\sin \frac{\theta_c}{2}) - \frac{1}{2} \right] \\
&- \frac{1}{2} \log(\sin^2 \frac{\theta_c}{2}) + \frac{1}{2} \log(\cos^2 \frac{\theta_c}{2}) + \log(\cos \frac{\theta_c}{2}) \log(1 + \cos \frac{\theta_c}{2}) \\
&- \log(\sin \frac{\theta_c}{2}) \log(1 + \sin \frac{\theta_c}{2}) + \cos \theta_c + (\cos \theta_c + 1) \ln^2(\cos \frac{\theta_c}{2}) + (\cos \theta_c - 1) \ln^2(\sin \frac{\theta_c}{2})
\end{aligned}
$$

(5.5)

where Li_2 is the polylogarithm function of order 2.

A closed form for I_7 could not be derived for model 3. Instead, the integral was numerically solved and fitted to the following polynomial function ($R^2 = 1$, RMSE $= 3.82 \times 10^{-4}$):

$$I_7 = 0.568\theta_c^3 - 0.4232\theta_c^2 - 1.47\theta_c + 1.649 \tag{5.6}$$

The mathematical form of the I_is reveal the differences between the model families. Figure 5.2 visually depicts the differences between these constants. While both model families 2 and 3 reproduce the constants for model 1 in the limit $\theta_c = 0$, there is considerable difference between the models for the behavior of constants I_1, I_2, I_4, and I_7 for non-zero canting angles. Not only these parameters for model 2 and 3 do not predict the same value for the same amount of canting, but also their behavior as a function of the canting angle is considerably different for negative canting angles. As I_1 and I_2 directly multiply $\dot{q}$ and $\dot{\phi}$ in the equations, and I_4 affects the demagnetizing field, there should be a dramatic difference between the predictions from the two models.

It should also be noted that with ansatz 2, several divergent terms were neglected in the integration of some of these factors. Specifically, parameter I_4 had the additional term $-\frac{\sin^2\theta_c}{2}\ln(-\sin\theta_c\cos\theta_c)$, and parameter I_6 had the additional term $+\frac{\tan\theta_c}{2}\ln(-\sin\theta_c\cos\theta_c)$. These terms will likely affect the accuracy of the models, specially when canting is not playing a role in the dynamics.

The models may also be written in explicit form as well, leading to equations for the evolution of the 4 collective coordinates:

$$
\left(I_2 + \alpha^2 \frac{I_1 I_4}{I_2}\right) I_1 \frac{\cos\chi}{\mu_0 \gamma p_w \Delta} \dot{q} = \alpha \left(I_4 H_z - \frac{I_3 I_4}{I_2} H_{SL} \left[\sin\phi u_{SOT,x} - \cos\phi u_{SOT,y}\right]\right)
$$
$$
+ \left(\alpha\beta \frac{I_1 I_4}{I_2} + I_5\right) \frac{u}{p_w \Delta} \cos\chi + \frac{1}{2} I_4 M_s (N_y - N_x) \sin 2(\phi - \chi) \tag{5.7}
$$
$$
- I_3 \frac{D}{\mu_0 M_s p_w \Delta} \sin(\phi - \chi) + I_6 \left[H_x \sin\phi - H_y \cos\phi\right]
$$

$$
\frac{\left(I_2 + \frac{I_1 I_4}{I_2}\right)}{\mu_0 \gamma} \dot{\phi} = (I_2 H_z - I_3 H_{SL} \left[\sin\phi u_{SOT,x} - \cos\phi u_{SOT,y}\right]) + \left(\beta I_1 - \alpha \frac{I_4 I_5}{I_2}\right) \frac{u}{p_w \Delta} \cos\chi
$$
$$
- \alpha \frac{I_4^2}{I_2} \frac{M_s}{2} (N_y - N_x) \sin 2(\phi - \chi) + \alpha \frac{I_3 I_4}{I_2} \frac{D}{\mu_0 M_s p_w \Delta} \sin(\phi - \chi) \tag{5.8}
$$
$$
- \alpha \frac{I_4 I_6}{I_2} \left[H_x \sin\phi - H_y \cos\phi\right]
$$

$$
\frac{\alpha}{\mu_0 \gamma} \frac{I_1}{6} \left(\frac{w}{p_w \Delta}\right)^2 \frac{\dot{\Delta}}{p_w \Delta} = I_1 \frac{A}{\mu_0 M_s (p_w \Delta)^2} \left[\frac{I_1}{6 I_7} \left(\frac{w}{p_w \Delta}\right)^2 + 2\sin^2\chi\right]
$$
$$
+ I_4 \frac{K}{\mu_0 M_s} \left((1 - p_w)\sin^2\chi - p_w \frac{I_1}{6 I_7} \left(\frac{w}{p_w \Delta}\right)^2\right)
$$
$$
+ \frac{1}{2} I_4 M_s \sin\chi \cos\chi (N_x - N_y) \sin 2(\phi - \chi) \tag{5.9}
$$
$$
+ I_3 \frac{D}{\mu_0 M_s p_w \Delta} \sin\phi \sin\chi + p_w (H_x \cos\phi + H_y \sin\phi) I_6
$$

$$
-\frac{\alpha}{\mu_0 \gamma} \frac{I_1}{6} \frac{\dot{\chi}}{\cos\chi} = 2 I_1 \frac{A}{\mu_0 M_s (p_w \Delta)^2} \sin\chi + I_4 \frac{K}{\mu_0 M_s} (1 - p_w)\sin\chi
$$
$$
+ \frac{1}{2} I_4 M_s \cos\chi (N_x - N_y) \sin 2(\phi - \chi) + I_3 \frac{D}{\mu_0 M_s p_w \Delta} \sin\phi \tag{5.10}
$$
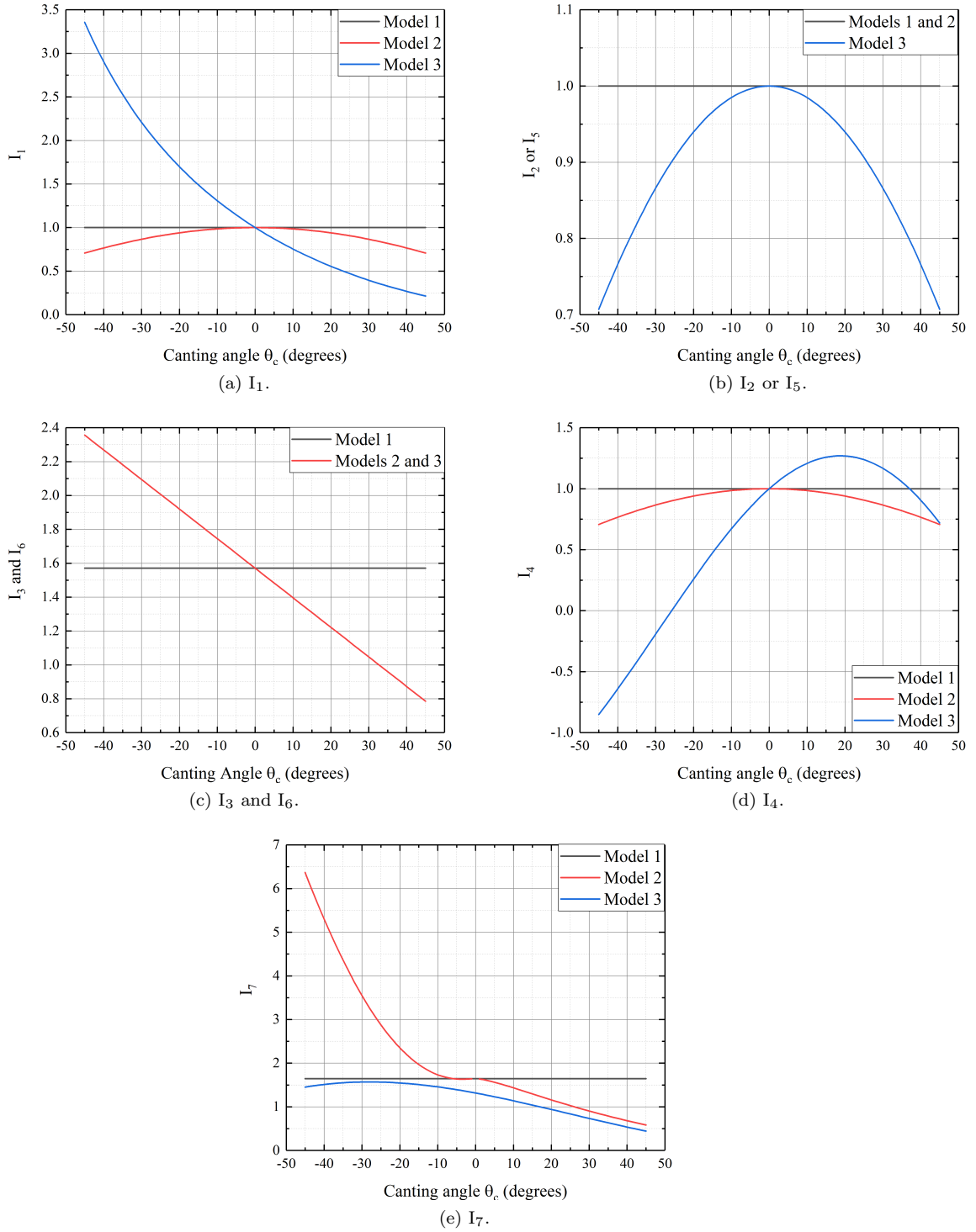
Figure 5.2: Variation of the I_i parameters of the collective coordinate models with canting angle. The equations corresponding to each parameter may be found in Table 5.2.

5.3   Collective Coordinate Models: Differences and Accuracy

5.3.1   Current-driven DW Motion in $\mathrm{Pt/CoFe/MgO}$

To compare all the models to each other, we analyzed the case of current-driven DW motion in Pt/CoFe/MgO sample using the extended models.

Figure 5.3 illustrates predictions of model 2 compared to micromagnetic simulations. Including an approximation of canting improves the accuracy of the $q - \phi - \chi - \Delta$ model to an extent, while other models still fail. This shows that canting in the domains is playing an important role in DW motion.

Figure 5.4 illustrates predictions of model 3 (model with canted ansatz) compared to micromagnetic simulations on the Pt/CoFe/MgO sample. Interestingly, the $q - \phi$ form of model 3 has the largest range of applicability, and predicts the right trend in DW velocity. The four coordinate form of this model also shows acceptable accuracy for $-75\mathrm{mT} < B_x < 100\mathrm{mT}$. This shows that the profile used for the DW is much more important than the additional degrees of freedom.

Finally, in Figure 5.5 we compare the best models from each model set together in predicting DW behavior. Clearly, models with inherent canting show superior capability in replicating the micromagnetic results, and require a lower number of degrees of freedom for accurate predictions (only q and ϕ). This shows the important effect of canting on the DW motion.

The application of the in-plane field does not just add a new term in the equations, but also affects the relative strength of the other interactions in the system. The Lagrangian density of the system and the Dissipation function describe the energy landscape of the system. Figure 5.5.(f) illustrates the energy landscape of the Pt/CoFe/MgO system for a current density of $1\mathrm{PA/m^2}$ under the application of longitudinal in-plane fields using the Lagrangian description with four collective coordinates. We can see that with increasing B_x, the role of anisotropy and demagnetization energy increase, while the exchange and DMI energy decrease in magnitude. These changes are modulated by changes in DW width, DW tilting angle and the canting protractors (which affect all energy terms above), along with changes in the magnetization angle (which effects the DMI and demagnetizing energies). The effect of other energy terms on the energy landscape is minimal. Moreover, there seems to be a correlation between increase in the proportion of exchange interaction and DMI, and the speed of the DW, with the speed increasing as the proportion of these two interactions decreases.

(a) DW velocity.

(b) DW width parameter Δ.

(c) DW tilting angle χ.

(d) DW magnetization angle ϕ.

(e) $\phi - \chi$.
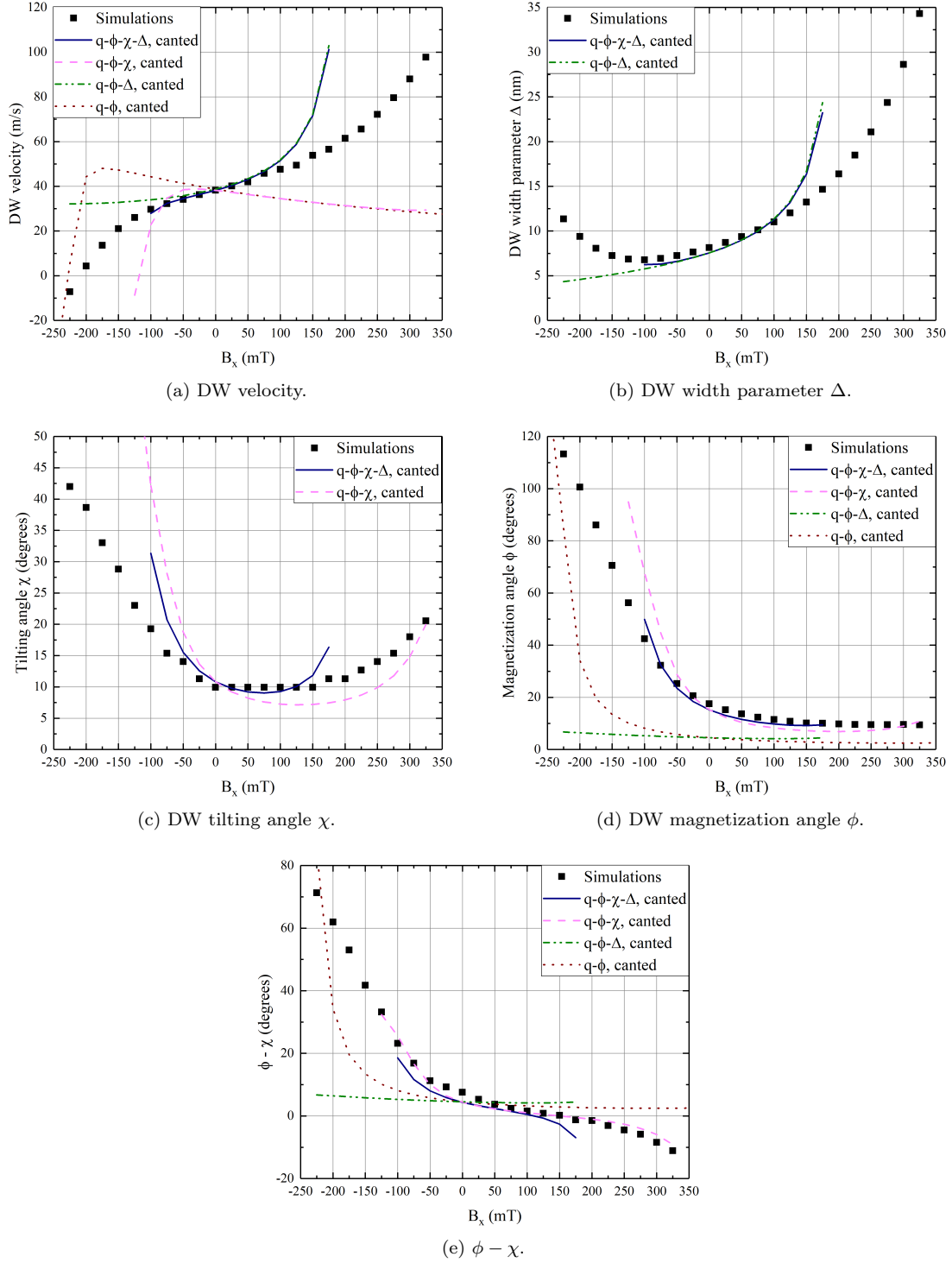
Figure 5.3: Predictions of different forms of model 2 compared to micromagnetic simulations in the case of current-driven DW motion with a current density of $J_x = 0.1 \mathrm{TA/m^2}$.

(a) DW velocity.

(b) DW width parameter Δ.

(c) DW tilting angle χ.

(d) Magnetization angle ϕ.

(e) $\phi - \chi$.
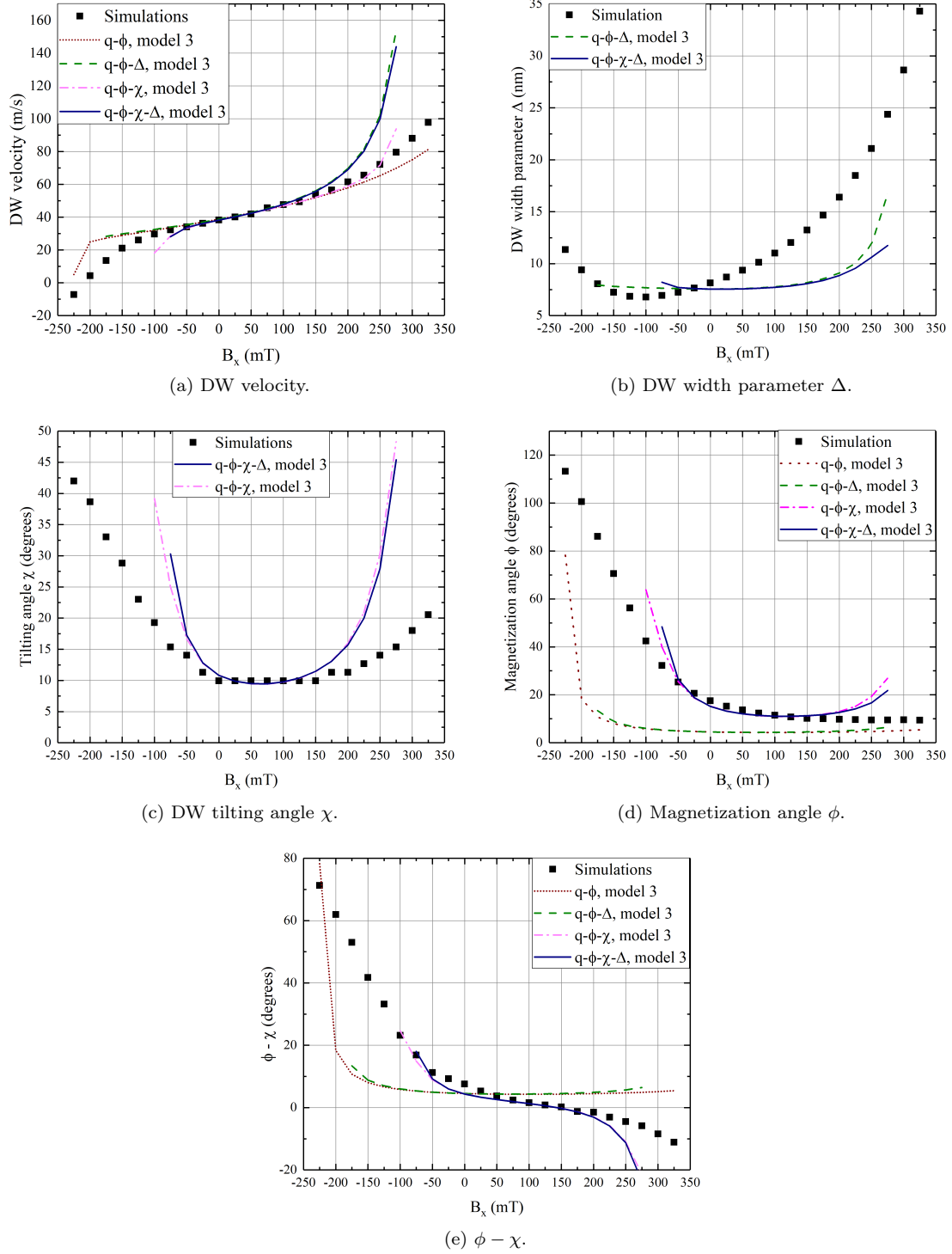
Figure 5.4: Predictions of different forms of model 3 compared to micromagnetic simulations in the case of current-driven DW motion with a current density of $J_x = 0.1 TA/m^2$.

(a) DW velocity in m/s.

(b) DW width parameter Δ in degrees.

(c) DW tilting angle χ in degrees.

(d) DW tilting angle χ in degrees.

(e) $\phi - \chi$ in degrees.

(f) Contributions of different energy terms.
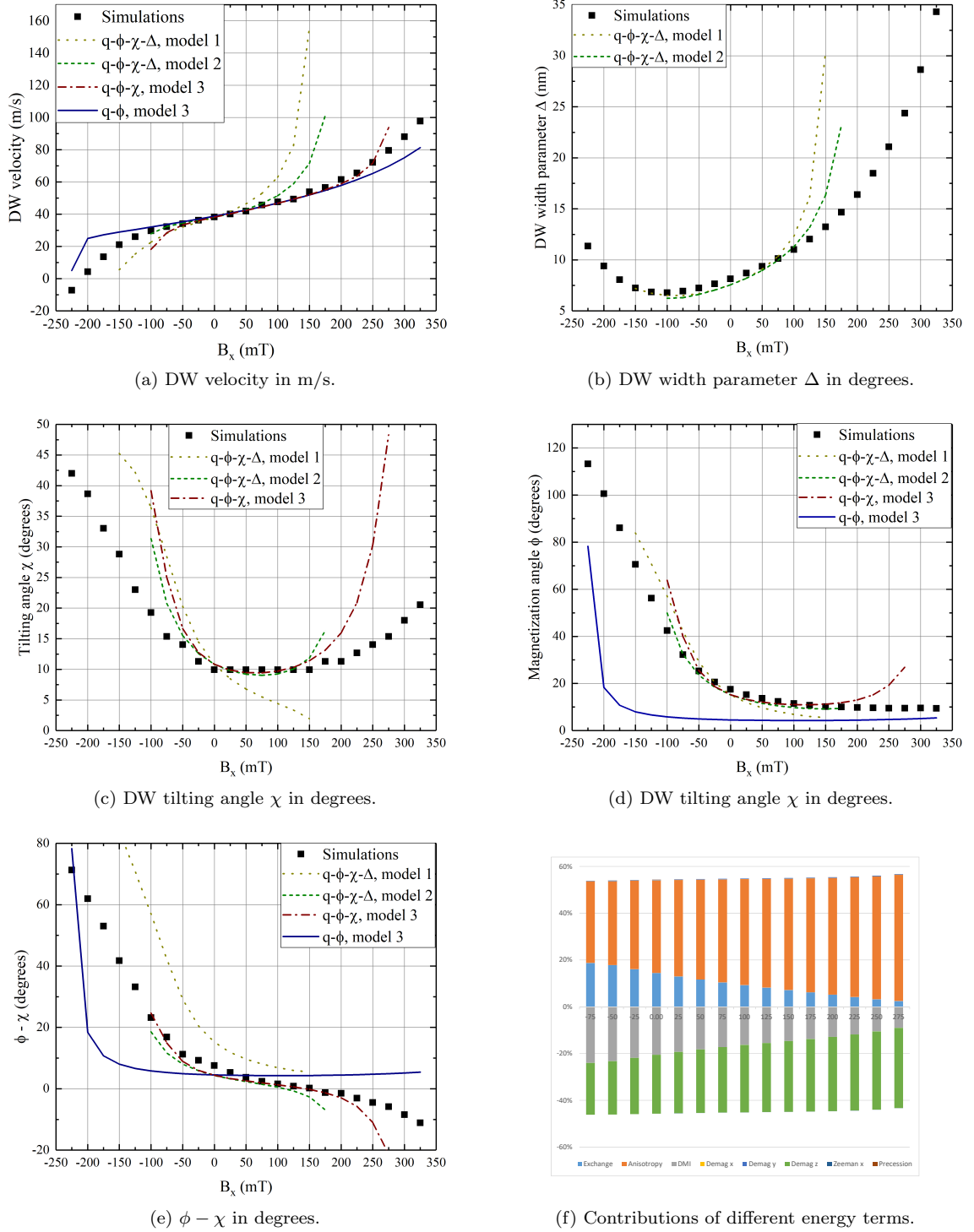
Figure 5.5: Predictions of the best collective coordinate models of each group compared to micromagnetic simulations in the case of current-driven DW motion with a current density of $J_x = 0.1 TA/m^2$.

5.3.2   Other Cases

We also performed simulations for field-driven DW motion under longitudinal fields in the Pt/Co/Ni/Co/MgO/Pt sample, and current-driven DW motion under transverse fields in the Pt/CoFe/MgO, the results of which are presented in Figure 5.6.

In the Pt/Co/Ni/Co/MgO/Pt sample (which has stronger anisotropy and lower DMI which lead to smaller canting and tilting), according to Figure 5.6. (a) we see that the DW tilting has minimal effect on accuracy of the models, while DW width plays an important role in these narrower DWs. We verified this in other models as well, observing that in this case models without canting are better suited to reproduce micromagnetic results likely due to the smaller value of the canting and the fact that ansatz three had some divergent terms. We also observe that the models are able to predict the Walker Breakdown initiation and cessation properly, and showcase the right qualitative trends.

In summary, it seems that narrower DWs are better modeled by CCMs that include DW width while for wider DWs this parameter plays a minor role. In addition, in systems with high anisotropy canting effects can be neglected. In the next section, we provide a more detailed analysis of different cases of DW motion under in-plane field using the models verified here.

Applications of the models in the case of transverse fields as shown in Figure 5.6. (b) highlighted that in those cases more rigid models are better able to reproduce micromagnetic simulations. This is likely due to the strong interaction between tilting and DW width when transverse fields are applied, with the DW adjusting these two parameters in concert to reduce energy. The models did predict the magnetization angle of the DW (ϕ), and $\phi - \chi$ well as highlighted in Figure 5.6, specially for the critical case $\phi - \chi \sim 0$.
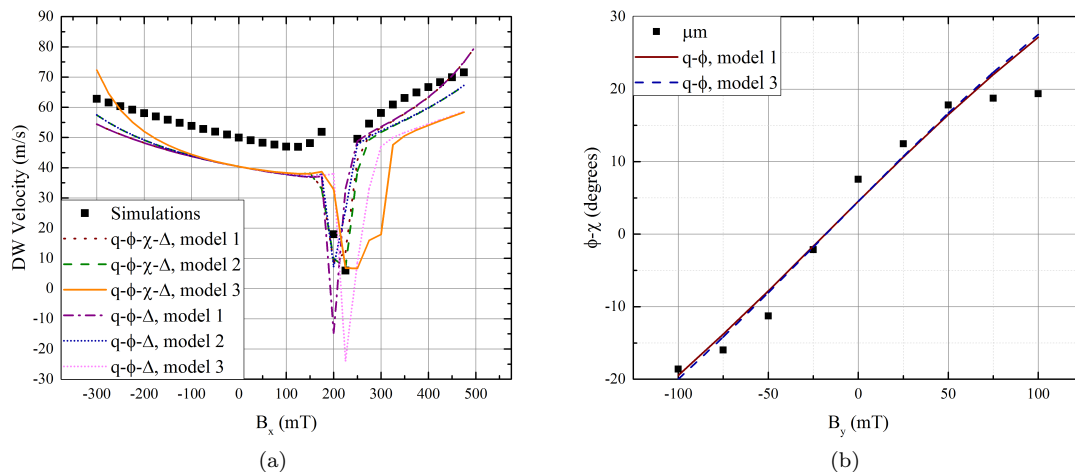
Figure 5.6: Comparison of the DW velocity among the most accurate CCMs of each class. (a) instantanuous velocity predictions for PtCoNiCoMgOPt under an applied field of $B_z = 10mT$, and (b) prediction of tilting in Pt/CoFe/MgO under a current density of $J_x = 0.1TA/m^2$.

5.4   Characteristics of Domain Wall Motion Under in-plane Fields in Nanowires

Micromagnetic simulations were performed on the two nanowires outlined in Table 5.1 with DWs driven by fields or Slonczewski-like spin-orbit torques under the applications of longitudinal (B_x) and transverse (B_y) magnetic fields. To interpret the results of the micromagnetic simulations, we used the four time dependent collective coordinates identified earlier.

It is well-known from micromagnetic studies that the motion of the DW reaches steady state conditions after a period of transient behavior, which we also verified for our systems. In our simulations, steady state conditions were reached after about 2.5ns in most cases, with $\dot{\phi} \sim \dot{\chi} \sim \dot{\Delta} \sim 0$. While we found the evolution of the micromagnetic model to not exactly match the CCMs, a steady state condition was identified in the CCMs as well. In CCMs without the tilting of the DW, a steady state condition was observed with $\dot{\phi} \sim \dot{\Delta} \sim 0$, while in tilted models we found only $\dot{\Delta} \sim 0$ (although in many cases $\dot{\phi} \sim \dot{\chi} < 1$). In steady state conditions, the collective coordinate models may be simplified to better understand the critical points which can be identified in the micromagnetic simulations. In this section we use a * to denote steady state values of the collective coordinate.

In the next subsections, we will show which CCMs were able to better predict the micromagnetic results for different combinations of in-plane fields and drive interactions, and use these models to highlight features or critical points in the dynamics of the DW. By better predicting the micromagnetic results, we mean reproducing the results with the lowest error over a wider range of fields. Note that the range of in-plane field values over which different collective coordinate models can be solved with a convergent solution is different for different materials and drive-conditions; we only show cases where a solution could be calculated.

5.4.1   General Observations

We identified several general features in the simulations. First, as outlined in our previous work [4], one notes that domains under large in-plane fields can no longer be assumed to be fully perpendicularly magnetized, but clearly show some canting of the magnetization into the plane of the sample. This effect was much smaller in Pt/Co/Ni/Co/MgO/Pt compared to Pt/CoFe/MgO, due mainly to the difference in the uniaxial magnetic anisotropy of the two samples.

Second, in the Pt/Co/Ni/Co/MgO/Pt sample we observed limited tilting of the DW (only up to 10 degrees in many cases) which likely is due to the much lower DMI compared to the Pt/CoFe/MgO sample. As a result, we expect the χ coordinate to play a small role in modeling this system.

Third, we found that DW shape and rigidity (lack of elasticity) are affected by in-plane fields. As depicted in Figure 5.7, depending on the combination of drive interaction and in-plane fields, the DW might have a rigid line shape, or a curved shape (either S-shaped or an arch of a circle). With large in-plane fields (longitudinal and transverse), the DW might lose its rigidity, and instead extend elastically through the system. In Pt/CoFe/MgO system, we found both longitudinal and transverse fields where the DW starts to elongate instead of moving rigidly. Thess fields were dependent on the material properties, and also the driving interaction applied to the system. In the Pt/Co/Ni/Co/MgO/Pt system, these effects were not observed, likely due to the high uniaxial anisotropy of the system which helps maintain the DW shape. However, in this material the DW shape was disrupted due to other features which will be discussed later.

(a) $B_x = -200\text{mT}$ (b) $B_x = 300\text{mT}$ (c) $B_y = -100\text{mT}$ (d) $B_y = 100\text{mT}$
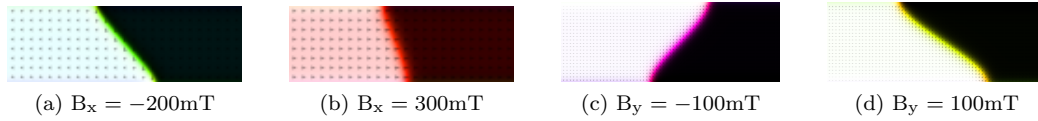
Figure 5.7: Snapshots of different shapes of the DWs observed under a current density of 0.1TA/m in Pt/CoFe/MgO after 5ns. (a) and (b) show a rigidly moving linear DW, while the DW in (c) and (d) is rather S-shaped.

5.4.2 Domain Wall Motion Under Longitudinal in-plane Fields

Field-Driven Case

The two samples were studied under drive fields of $B_z = 5\text{mT}$, 30mT. Longitudinal in-plane fields in the range $B_x = -225\text{mT}$ to 325mT were used for Pt/CoFe/MgO, while a range of $B_x = -500\text{mT}$ to 500mT was used for Pt/Co/Ni/Co/MgO/Pt. The results of these micromagnetic simulations are presented in Figures 5.9 and 5.10, and compared to the most accurate collective coordinate models.

Comparing the variation of velocity for the two samples, as depicted in Figure 5.9.a and 5.10.a, we see that in both cases the general trend with the drive field is the same; the velocity and nonlinearity of the curve increases with increasing drive field (B_z), while changing B_x tunes the velocity to an extent (with the curve having a minimum with respect to the longitudinal field). The DW velocity predictions are qualitatively in agreement the behavior observed in experiments [161, 162]. However, the Pt/Co/Ni/Co/MgO/Pt sample shows the additional effect of a sudden drop in DW velocity for a range of in-plane fields applied. This Walker Breakdown (WB) like behavior [53] was verified by looking at the snapshots of the moving DW (depicted in Figure 5.8), where we can see local precession of the magnetization and formation of vertical Bloch lines arising from the edge that modify the DW structure [151]. This behavior could be attributed to the higher anisotropy of this material, which reduces the local field needed to reach WB. Note that this behavior is local; the DW does not oscillate back and forth as a single object (unlike an actual WB behaviour during which the DW moves back and fourth rapidly), but the overall effect of the local precession of magnetization over time is equivalent to the DW moving back and forth rigidly and slowing down, which is why the collective coordinate model can replicate this effect to an extent.

In terms of the CCMs, we found models without canting to better reproduce the results for Pt/Co/Ni/Co/MgO/Pt (where canting and DW tilting are small). However, in this material the DW width parameter Δ was important in predicting the DW behavior properly. In Pt/CoFe/MgO with its higher canting and tilting of the DW, we found that $q - \phi$ form of model 3 (with inherent canting) is better suited in predicting the DW behavior.

Looking closely at Figures 5.9.b and 5.10.b, we find a serious flaw in model set 3; this model set seems to not be able to predict the DW width correctly, which in turn can affect its outputs. As such, when a two coordinate form of this model is used, it is able to better predict the DW motion. This also shows why this model set is not suitable for the Pt/Co/Ni/Co/MgO/Pt sample where lack of canting and tilting mean Δ is one of the main variables affecting the DW. Overall, this observation suggests that the $q - \phi$ form of model 3 is the most suitable for studying DW motion in these systems.

A major difference between the two cases can be observed in the DW's tilting behavior; while Pt/CoFe/MgO DWs always maintain a positive tilting, in the case of Pt/Co/Ni/Co/MgO/Pt negative tilting can be observed which is likely due to the lower DMI strengths and the higher applied fields used (see Figures 5.9.e and 5.10.e). Another notable feature of the DW behavior

could be seen in Figure 5.9.c where at a specific field $\phi - \chi \sim 0$ independent of the drive field, while in Figure 5.10.c a point could be observed for which $\phi - \chi \sim \frac{\pi}{2}$. We label these points as critical in-plane fields which will be discussed in details in later sections.

(a) $B_z = 10\,\text{mT}$, $B_x = 225\,\text{mT}$.   (b) $B_z = 30\,\text{mT}$, $B_x = 225\,\text{mT}$.   (c) $B_z = 30\,\text{mT}$, $B_x = 100\,\text{mT}$.
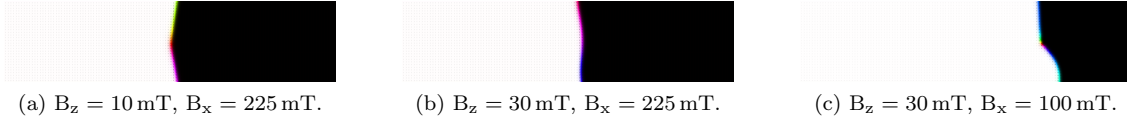
Figure 5.8: Snapshots of the moving DW under different conditions in the Pt/Co/Ni/Co/MgO/Pt sample. The rapid change of magnetization along the DW owing to the Walker Breakdown can be observed.

Current-Driven Case

Figures 5.11 and 5.12 illustrate the results of micromagnetic simulations for current-driven DW motion under longitudinal fields. The trends observed in the velocity of current-driven DW motion (Figures 5.11.a and 5.12.a) are in general agreement with published experimental results [76, 86, 87, 152]. A somewhat linear behavior is observed for low longitudinal fields, which becomes non-linear as the in-plane field increases. The non-linearity in behavior also seems to increase with increasing current. In terms of the CCMs, we saw results similar to the field-driven case, with models without canting being more suitable for the high anisotropy system and those with canting more suitable for the low anisotropy high DMI system.

We also observe a point where the DW velocity is zero in both cases; the in-plane field at which this happens is another critical point of interest. For the system with lower DMI the nonlinearity in the DW velocity seems to be observable mainly around this point, while in the system with larger DMI this nonlinear behavior is observed over all in-plane fields studied. Interestingly, this in-plane field seems to have an additional feature: the DW will have the same tilting angle χ for different drive interactions ((Figures 5.11.e and 5.12.e)). In the system with the higher anisotropy and lower DMI (namely Pt/Co/Ni/Co/MgO/Pt), we also observe that at this point $\phi - \chi \sim 90°$ (a fully Bloch DW).

One unexpected result was the presence of Walker Breakdown in our initial current-driven simulations of Pt/Co/Ni/Co/MgO/Pt; however, in these cases while a vertical Bloch line is nucleated, it is short-lived and simulating for longer durations shows that this is just a transitory effect. One point with such an effect can be observed in Figure 5.12.a as an outlier at $B_x = 250\text{mT}$.

In terms of angles, an in-plane field exists for which $\phi - \chi \sim 0$ (Figures 5.11.c and 5.12.c); in the Pt/CoFe/MgO sample we also see a case of $\phi = 0$ (Figures 5.11.d) which is absent in the Pt/Co/Ni/Co/MgO/Pt sample. These could be points of interest for further analytical studies.

(a) DW velocity.

(b) DW width parameter (Δ).

(c) $\phi - \chi$

(d) DW magnetization angle (ϕ).

(e) DW tilting angle (χ).
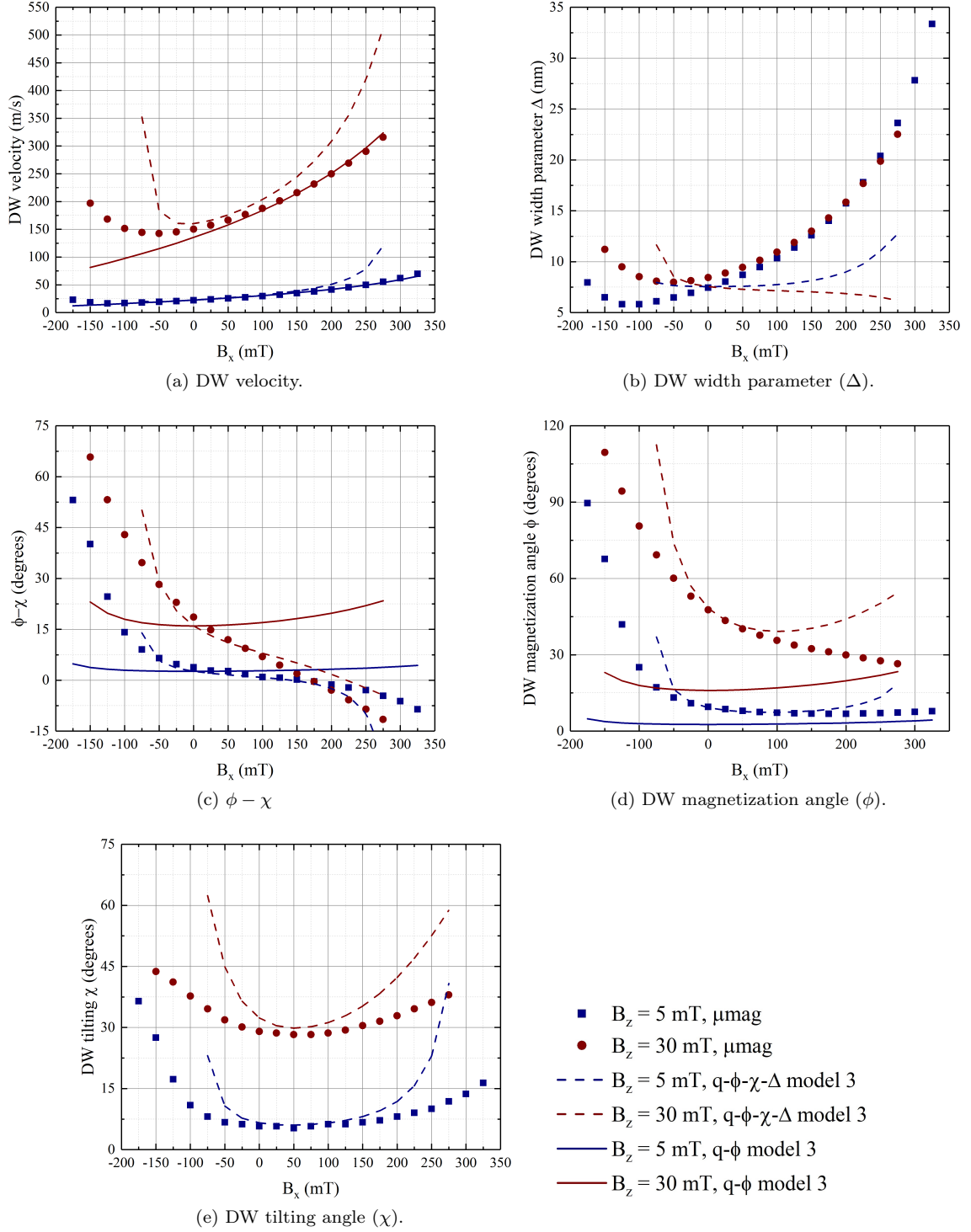
Figure 5.9: Instantaneous steady state DW characteristics for field-driven DW motion in Pt/CoFe/MgO with different out of plane and longitudinal fields applied. Only the collective coordinate models with highest accuracy in predicting the DW velocity are shown.

(a) DW average speed.

(b) Instantaneous DW width parameter (Δ).

(c) Instantaneous $\phi - \chi$

(d) Instantaneous DW magnetization angle (ϕ).

(e) Instantaneous DW tilting angle (χ).

Figure 5.10: DW characteristics for field-driven DW motion in Pt/Co/Ni/Co/MgO/Pt with different out of plane and longitudinal fields applied. Only the collective coordinate models with highest accuracy in predicting the DW velocity are shown. We decided to show the average DW speed in place of the instantaneous velocity of the DW, due to the walker breakdown behavior; this behavior is observed in panels (b)-(e) for $50\,\mathrm{mT} < B_x < 300\,\mathrm{mT}$.

(a) DW velocity.

(b) DW width parameter (Δ).

(c) $\phi - \chi$

(d) DW magnetization angle (ϕ).

(e) DW tilting angle (χ).
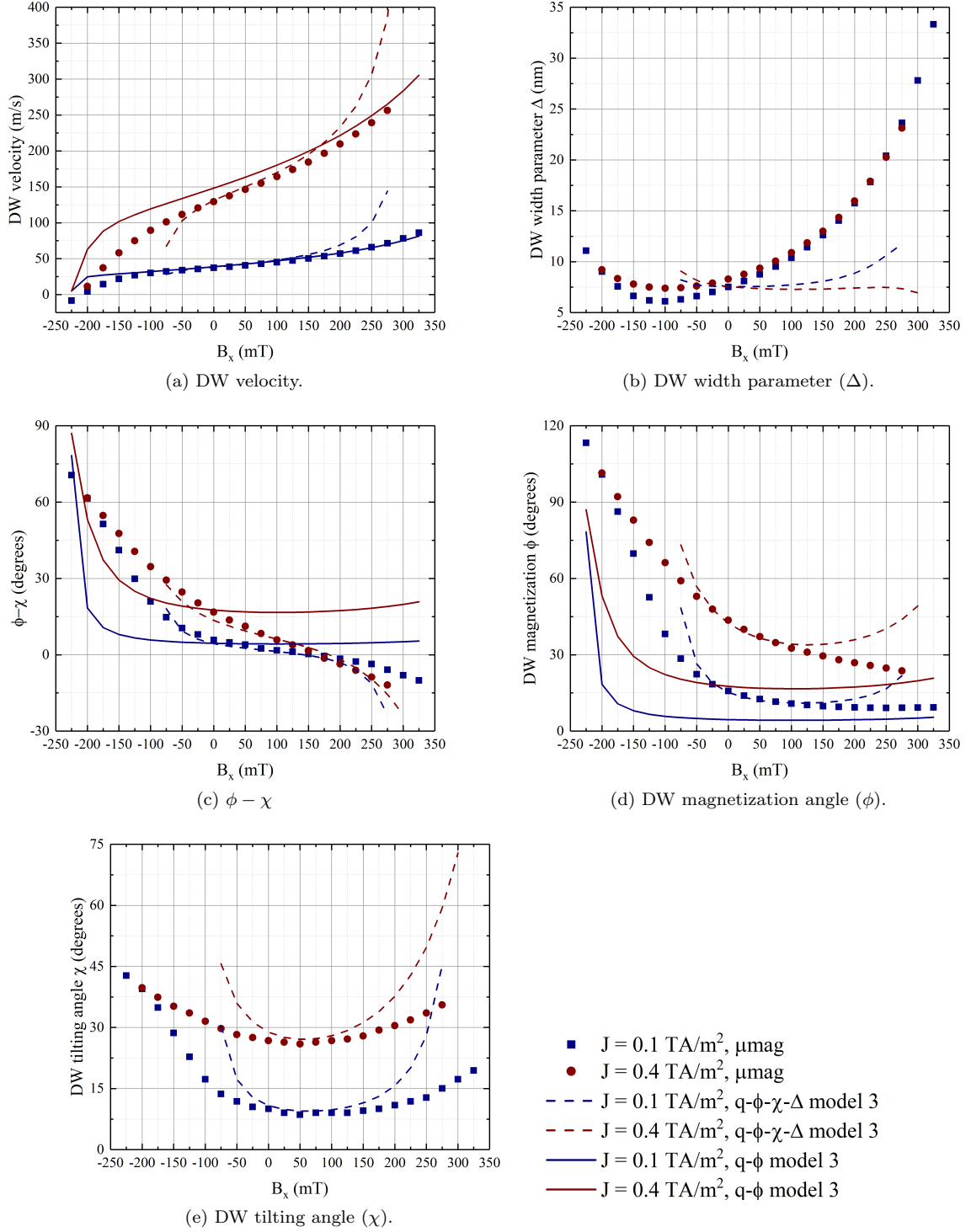
Figure 5.11: Instantaneous steady state DW characteristics for SHE-driven DW motion in Pt/CoFe/MgO with different currents and longitudinal fields applied. Only the collective coordinate models with highest accuracy in predicting the DW velocity are shown.

(a) DW velocity.

(b) DW width parameter (Δ).

(c) $\phi - \chi$

(d) DW magnetization angle (ϕ).

(e) DW tilting angle (χ).
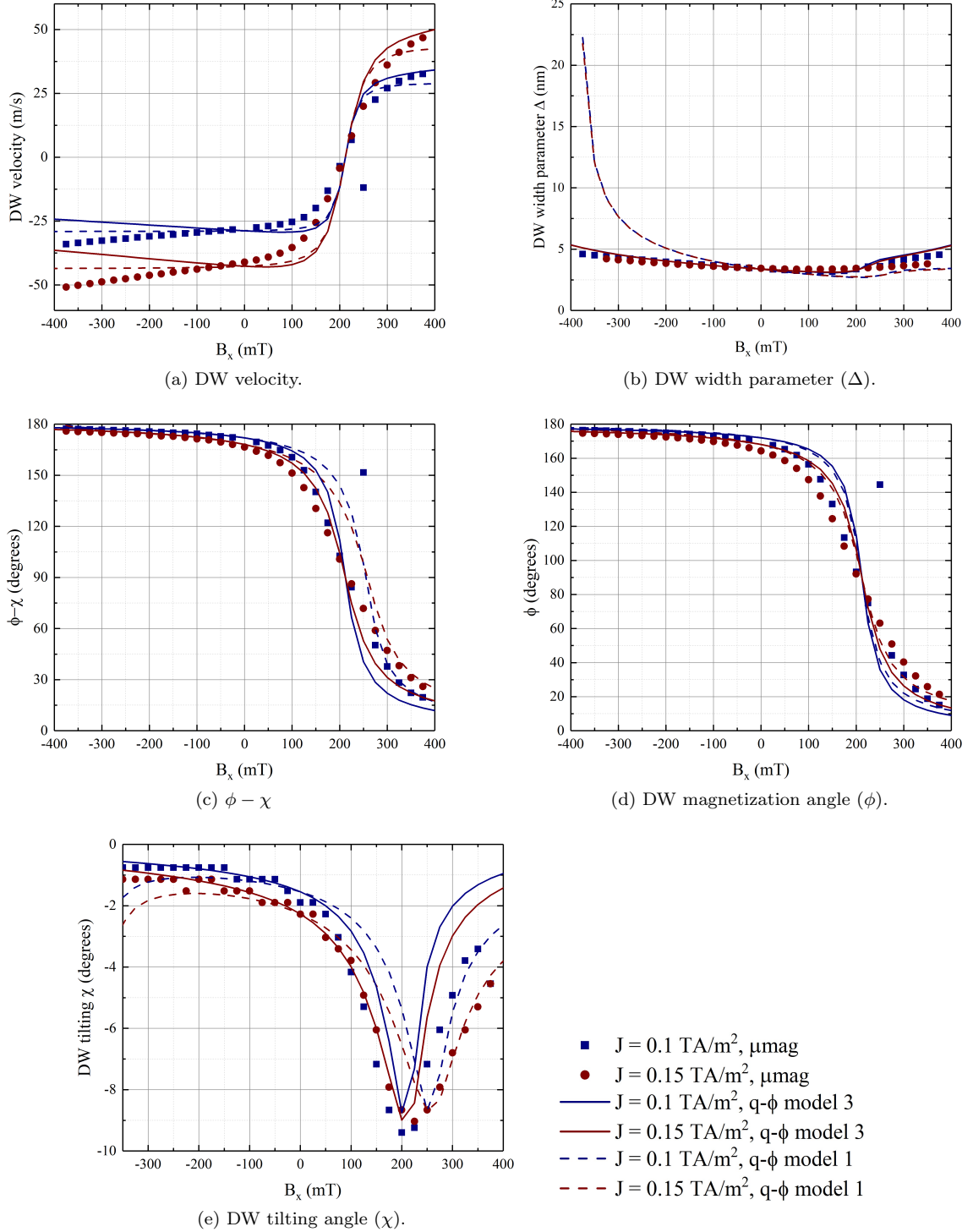
Figure 5.12: Instantaneous steady state DW characteristics for SHE-driven DW motion in Pt/Co/Ni/Co/MgO/Pt with different currents and longitudinal fields applied. We found that the best models in these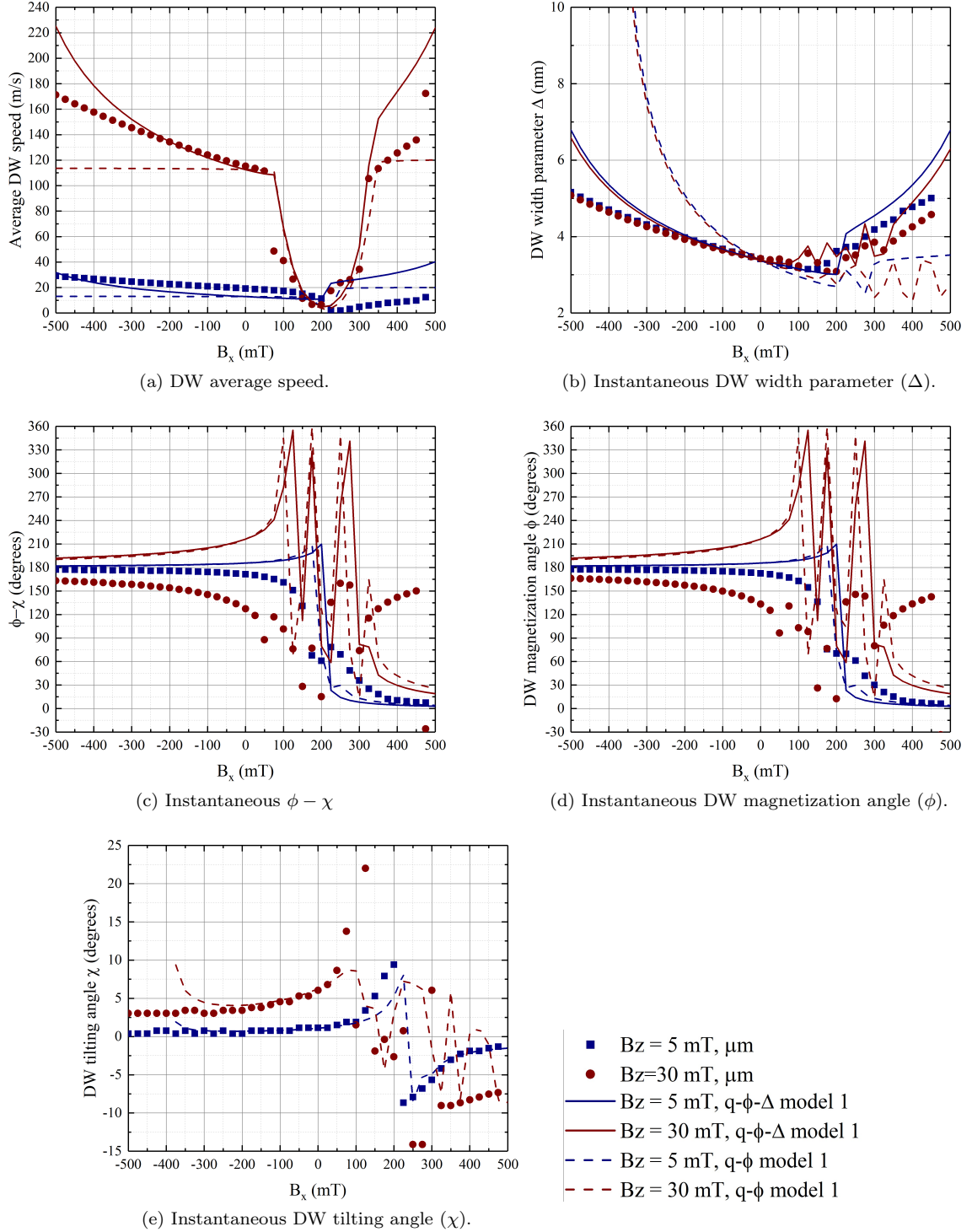 cases were two coordinate models. Canting has a minimal effect on the outputs. We also observed Walker Breakdown in these cases. Only the collective coordinate models with highest accuracy in predicting the DW velocity are shown.

5.4.3   Domain Wall Motion Under Transverse Fields

Figures 5.13 and 5.14 show the results of field-driven DW motion under the application of transverse fields in the materials under study, while figures 5.15 and 5.16 show the results of current-driven DW motion under transverse fields.

As observed from Figures 5.13.e, 5.14.e, 5.15.e, and 5.16.e, the DW tilting angle changes dramatically under transverse fields with a behavior different compared to what was observed under longitudinal fields. While under longitudinal fields we only observed positive or negative tilting for a specific material, under transverse fields we can observe both types of angles; in a sense the transverse fields could be used to control the tilting of the DW. Obviously, under these conditions the tilting of the DW is an important coordinate. Yet we see that the collective coordinate models are accurate in predicting the behavior of the DW, with and without the tilting included in the models.

In the Pt/CoFe/MgO sample (Figures 5.13.c, and 5.15.c) , we can identify a critical transverse fields at which $\phi \sim \chi \sim 0$. In the Pt/Co/Ni/Co/MgO/Pt system (Figures 5.14, and 5.16 panels c, d, and e), we instead have a point where $\chi = 0$ and $\phi = 180$. These points coincide with when the DW is fully Néel, with the difference in magnetization being due to the different chirality of the DW in the two systems.

5.4.4   Analysis of the critical points

In the micromagnetic simulations and collective coordinate results of Figures 5.9-5.16, we were able to identify several points where the DW behavior showed features that could be reproduced irrespective of material properties. These points could be used to derive simplified forms of the DW dynamic equations.

We observed that in several cases (field- and current-driven DW motion under longitudinal and transverse fields in Pt/CoFe/MgO, and field-driven case under transverse fields and field- and current-driven cases under transverse field for Pt/Co/Ni/Co/MgO/Pt), an in-plane field exists for which $\phi - \chi \sim 0$ or $180°$. In addition, under longitudinal fields this point is independent of the drive interaction. We observed in Figures 5.9-5.16 that the CCMs can accurately predict the DW behavior at this point. From a CCM perspective, this is the point where the DW has a fully Néel like structure. This means the contributions from the DMI and magnetostatic terms become zero, and we have:

$$
\left(I_2 + \alpha^2 \frac{I_1 I_4}{I_2}\right) I_1 \frac{\dot{q}}{\mu_0 \gamma p_w \Delta} =
\begin{cases}
\alpha \left(I_4 \frac{H_z}{\cos \chi} - \frac{I_3 I_4}{I_2} H_{SL} \left[\tan \chi u_{SOT,x} - u_{SOT,y}\right]\right) \\
+ \left(\alpha \beta \frac{I_1 I_4}{I_2} + I_5\right) \frac{u}{p_w \Delta} + I_6 \left[H_x \tan \chi - H_y\right] \quad \text{for } \phi - \chi \equiv 0 \\[2ex]
\alpha \left(I_4 \frac{H_z}{\cos \chi} + \frac{I_3 I_4}{I_2} H_{SL} \left[\tan \chi u_{SOT,x} - u_{SOT,y}\right]\right) \\
+ \left(\alpha \beta \frac{I_1 I_4}{I_2} + I_5\right) \frac{u}{p_w \Delta} - I_6 \left[H_x \tan \chi - H_y\right] \quad \text{for } \phi - \chi \equiv 180°
\end{cases}
$$

$$(5.11)$$

Under the application of transverse fields, the equations become slightly more simplified, as at

the same time $\chi = 0$, which yields:

$$\left(I_2 + \alpha^2 \frac{I_1 I_4}{I_2}\right) \frac{I_1}{\mu_0 \gamma p_w \Delta} \dot{q} = \begin{cases} \alpha\left(I_4 H_z + \frac{I_3 I_4}{I_2} H_{SL} u_{SOT,y}\right) \\ + \left(\alpha\beta \frac{I_1 I_4}{I_2} + I_5\right) \frac{u}{p_w \Delta} - I_6 H_y & \text{if } \phi - \chi \equiv 0 \, (D < 0) \\ \\ \alpha\left(I_4 H_z - \frac{I_3 I_4}{I_2} H_{SL} u_{SOT,y}\right) \\ + \left(\alpha\beta \frac{I_1 I_4}{I_2} + I_5\right) \frac{u}{p_w \Delta} + I_6 H_y & \text{if } \phi - \chi \equiv 180° \, (D > 0) \end{cases} \quad (5.12)$$

Equations 5.11 and 5.12 are thought-provoking, as they connect measured properties of the DW (DW velocity and tilting) to parameters arising from material properties such as the DW width parameter. These equations can be used to measure specific properties of the DW. Recent experiments have shown the visualization of DW tilting under experimental conditions [163]. In an experimental setting, first a transverse field should be identified at which the DW tilting is negligible; in this condition one may assume based on our results that $\phi \sim \chi \sim 0$. Using field-driven DW motion measurements, equation 5.12 may be used to measure the DW width parameter, which can in turn help estimate the exchange constant through $\Delta = \sqrt{\frac{A}{K}}$. In a current-driven case, the same equation could be used to estimate the SHE angle.

In current-driven DW motion, we identified a longitudinal field for which DW velocity is zero. In Pt/CoFe/MgO, this field was about $B_x \sim -200\,\text{mT}$, while in Pt/CoFe/MgO it was $B_x \sim 200\,\text{mT}$. We had shown in our previous work that this field is related to the DMI strength [4]. Under these conditions, the DW velocity equation simplifies to:

$$\alpha \frac{I_3 I_4}{I_2} H_{SL} \left[\cos\phi \, u_{SOT,y} - \sin\phi \, u_{SOT,x}\right] + \left(\alpha\beta \frac{I_1 I_4}{I_2} + I_5\right) \frac{u}{p_w \Delta} \cos\chi = \frac{1}{2} I_4 M_s \left(N_x - N_y\right) \sin 2(\phi - \chi)$$
$$+ I_3 \frac{D}{\mu_0 M_s p_w \Delta} \sin(\phi - \chi)$$
$$- I_6 \left[H_x \sin\phi - H_y \cos\phi\right]$$
$$(5.13)$$

Looking at Figures 5.11 and 5.12, we also observe that at this in-plane field ϕ and χ seem to be independent of the drive interaction, and $\phi \sim 90°$. Using this assumption, we have:

$$-\alpha \frac{I_3 I_4}{I_2} H_{SL} u_{SOT,x} + \left(\alpha\beta \frac{I_1 I_4}{I_2} + I_5\right) \frac{u}{p_w \Delta} \cos\chi = \frac{1}{2} I_4 M_s \left(N_x - N_y\right) \sin 2\chi + I_3 \frac{D}{\mu_0 M_s p_w \Delta} \cos\chi - I_6 H_x$$
$$(5.14)$$

Equation 5.14 could be used to measure DMI under conditions which the DW is stationary under applied currents. Plugging observations from the micromagnetic simulations into a two coordinate form of model 3 (and assuming $J = 0.1\,\text{TA/m}^2$), we predict a DMI strength of $D = -1.1\,\text{mJ/m}^2$ for Pt/CoFe/MgO and $D = 0.57\,\text{mJ/m}^2$ for Pt/Co/Ni/Co/MgO/Pt, which are very close to the values used in the micromagnetic simulations.

In the Pt/Co/Ni/Co/MgO/Pt sample, in field-driven DW motion ($B_z = 30\,\text{mT}$), we observed initiation of Walker Breakdown at $B_x = 50\,\text{mT}$ and cessation of this behavior at $B_x = 325\,\text{mT}$. This scenario could be studied using our CCMs. Assuming small tilting for the DW (which is valid

in this case), we can simplify the steady state equation as:

$$\cos\phi = \frac{I_2 H_z + I_3 H_{SL}\cos\phi}{\alpha\frac{I_4^2}{I_2}M_s\left(N_y - N_x\right)\sin\phi} + \alpha\frac{\frac{I_3 I_4}{I_2}\frac{D}{\mu_0 M_s p_w \Delta} + \frac{I_4 I_6}{I_2}\left(H_y\cot\phi - H_x\right)}{\alpha\frac{I_4^2}{I_2}M_s\left(N_y - N_x\right)}$$

$$= \frac{1}{2}\left[\left(\frac{I_2}{I_4}\right)^2\frac{H_z}{H_w\sin\phi} + \frac{I_2 I_3}{I_4^2}\frac{H_{SL}}{H_w}\cot\phi + \alpha\frac{I_3}{I_4}\frac{H_{DMI}}{H_w} - \alpha\frac{I_6}{I_4}\frac{H_x}{H_w} + \alpha\frac{I_6}{I_4}\frac{H_y}{H_w}\cot\phi\right]$$

<div align="right">(5.15)</div>

where H_w is the conventional Walker Breakdown field [53], and H_{DMI} is the DMI field. Walker Breakdown happens when the right side of the equation above is larger than 1 or smaller than -1. While in systems without DMI, only the drive interaction and the demagnetizing field played a role in this solution, in a system with DMI and in-plane fields additional terms are introduced; the relevant strength of these terms compared to each other determined whether Walker breakdown will take place or not. Note that magnetocrystalline anisotropy plays a role in this through the I_i values, as these values depend on θ_c which in turn depends on K_u.

Finally, we also observed in-plane fields that led to switching of the system through the elastic extension of the DW. The threshold for this switching field seems to relate to the canting angle reaching $\theta_c = 45°$ at which point the DW does not maintain a rigid structure as the domains try to fully align with the external magnetic field. This leads to $H_{x,s} = \frac{\sqrt{2}}{2}\left[\frac{2K_u}{\mu_0 M_s} + M_s(N_x - N_z)\right]$ for the longitudinal switching field and $H_{y,s} = \frac{\sqrt{2}}{2}\left[\frac{2K_u}{\mu_0 M_s} + M_s(N_y - N_z)\right]$ for transverse fields. These equations are expected to over-predict the switching field, as they do not take into account edge effects in the system and the effect of the drive interaction.

For the Pt/CoFe/MgO system, $B_{x,s} \approx \pm 354\text{mT}$ which is only $25 - 50\text{mT}$ higher than the field at which the system switched in micromagnetic simulations for positive longitudinal fields. For negative longitudinal fields, switching could not be observed due to the nucleation of a new DW. The transverse switching field was found to be $B_{y,s} \approx \pm 359\text{mT}$ depending on the width of the system; however, we observed elongations in the DW prior to reaching such high fields, albeit these elongations were seen in conjunction with translational motion of the DW. The nature of these elongations and their modeling is beyond the scope of this work, as our CCMs assume the DW is a rigid object. We did not observe any of these effects for the Pt/Co/Ni/Co/MgO/Pt cases; we verified that the switching field for this sample under both longitudinal and transverse fields is about $\pm 1.48\text{T}$, well above the in-plane field values studied.

(a) DW velocity.

(b) DW width parameter (Δ).

(c) $\phi - \chi$

(d) DW magnetization angle (ϕ).

(e) DW tilting angle (χ).

- $B_z = 5$ mT, μmag
- $B_z = 30$ mT, μmag
- $B_z = 5$ mT, q-ϕ-χ-Δ model 3
- $B_z = 30$ mT, q-ϕ-χ-Δ model 3
- $B_z = 5$ mT, q-ϕ model 3
- $B_z = 30$ mT, q-ϕ model 3

Figure 5.13: Instantaneous steady state DW characteristics for field-driven DW motion in Pt/CoFe/MgO with different out of plane and transverse fields applied. Only the collective coordinate models with highest accuracy in predicting the DW velocity are shown.

77

(a) DW velocity.

(b) DW width parameter (Δ).

(c) $\phi - \chi$

(d) DW magnetization angle (ϕ).

(e) DW tilting angle (χ).

■ Bz=5 mT, μmag
● Bz=30 mT, μmag
- - - Bz=5 mT, q-ϕ-χ-Δ model 3
- - - Bz=30 mT, q-ϕ-χ-Δ model 3
— Bz=5 mT, q-ϕ-χ-Δ model 1
— Bz=30 mT, q-ϕ-χ-Δ model 1
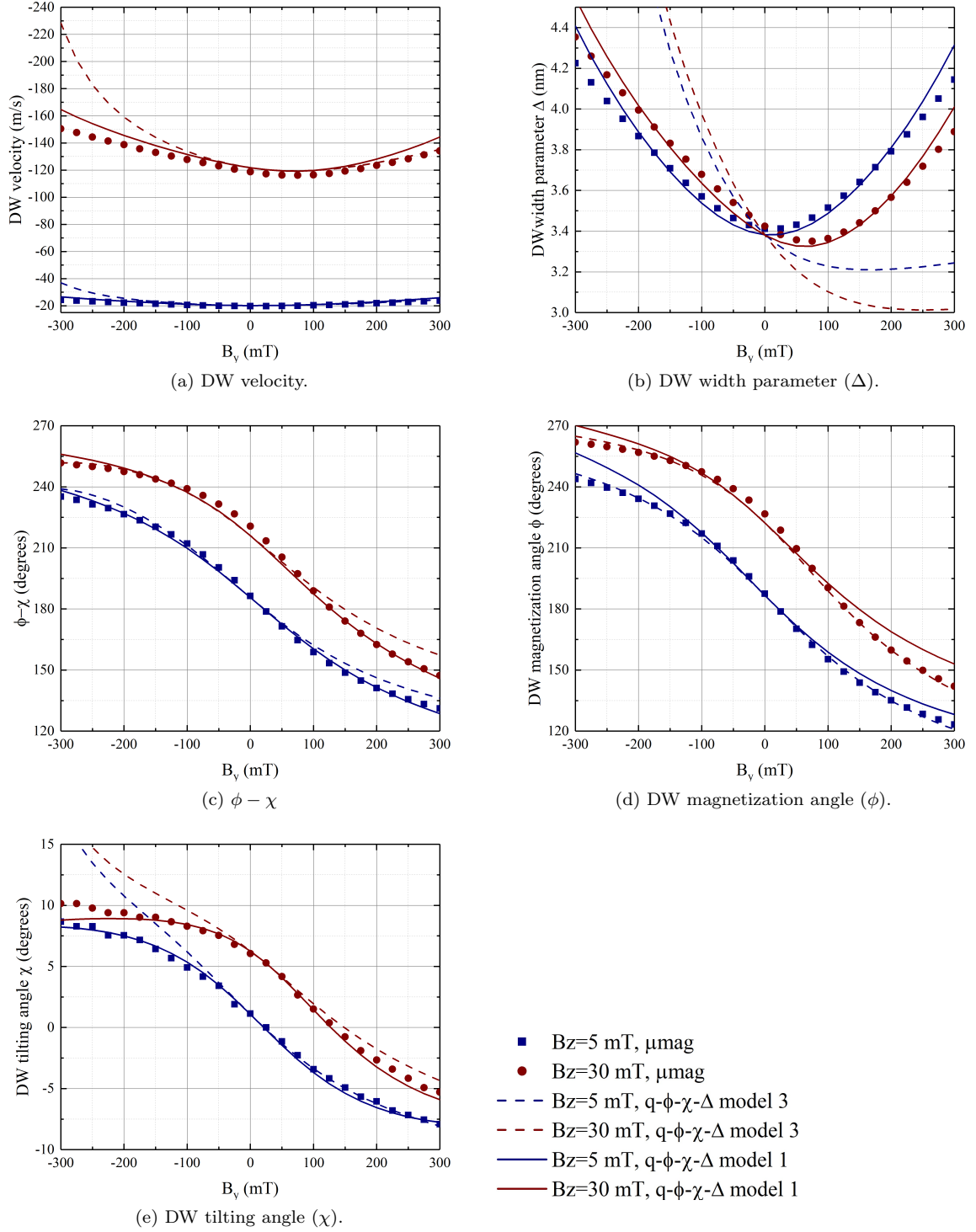
Figure 5.14: Instantaneous steady state DW characteristics for field-driven DW motion in Pt/Co/Ni/Co/MgO/Pt with different out of plane and transverse fields applied. Only the collective coordinate models with highest accuracy in predicting the DW velocity are shown.

78

(a) DW velocity.

(b) DW width parameter (Δ).

(c) $\phi - \chi$

(d) DW magnetization angle (ϕ).

(e) DW tilting angle (χ).

- ■ J = 0.1 TA/m^2, μmag
- ● J = 0.4 TA/m^2, μmag
- - - - J = 0.1 TA/m^2, q-ϕ-χ-Δ model 3
- - - - J = 0.4 TA/m^2, q-ϕ-χ-Δ model 3
- —— J = 0.1 TA/m^2, q-ϕ model 3
- —— J = 0.4 TA/m^2, q-ϕ model 3
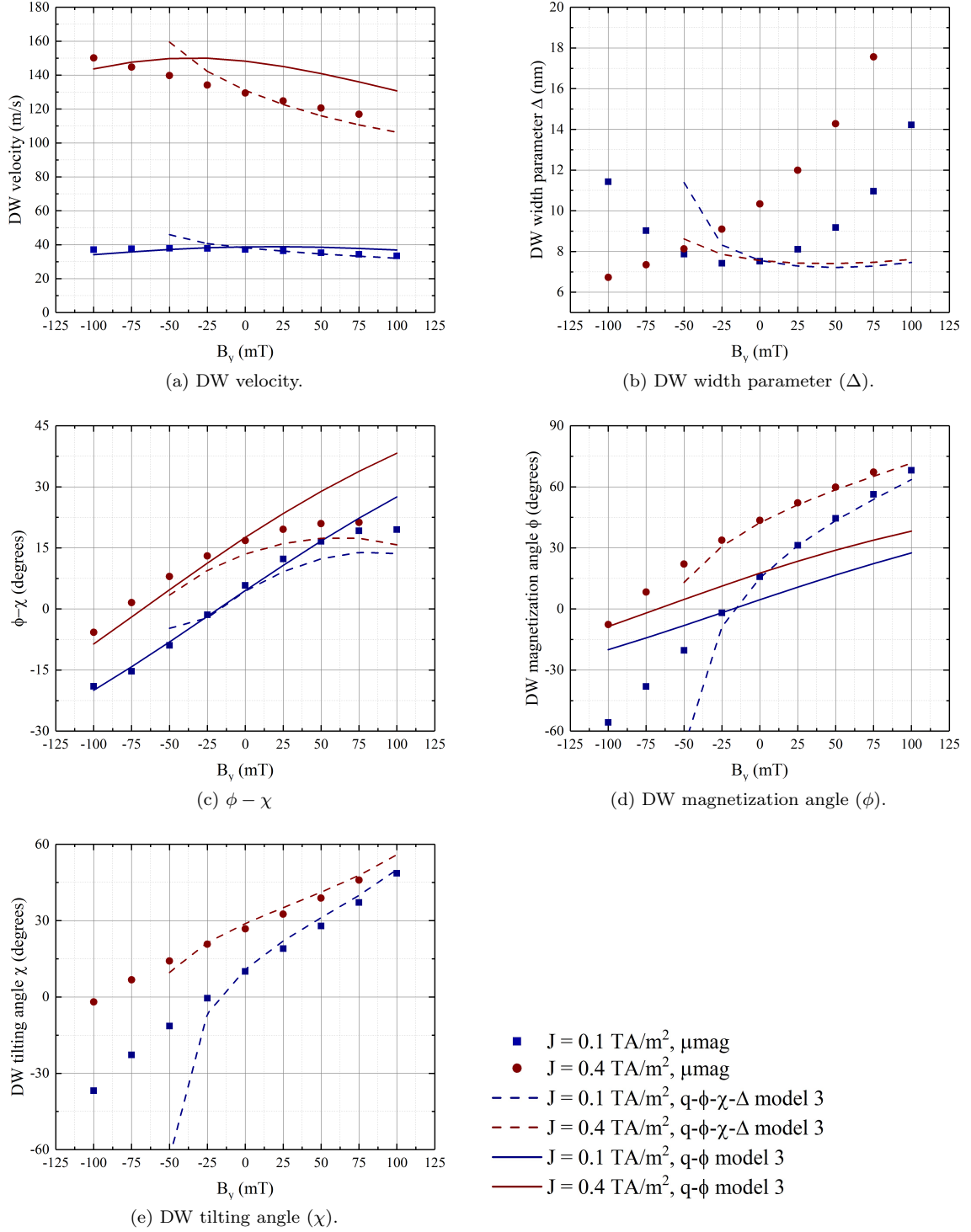
Figure 5.15: Instantaneous steady state DW characteristics for SHE-driven DW motion in Pt/CoFe/MgO with different currents and transverse fields applied. Only the collective coordinate models with highest accuracy in predicting the DW velocity are shown.

(a) DW velocity.

(b) DW width parameter (Δ).

(c) $\phi - \chi$

(d) DW magnetization angle (ϕ).
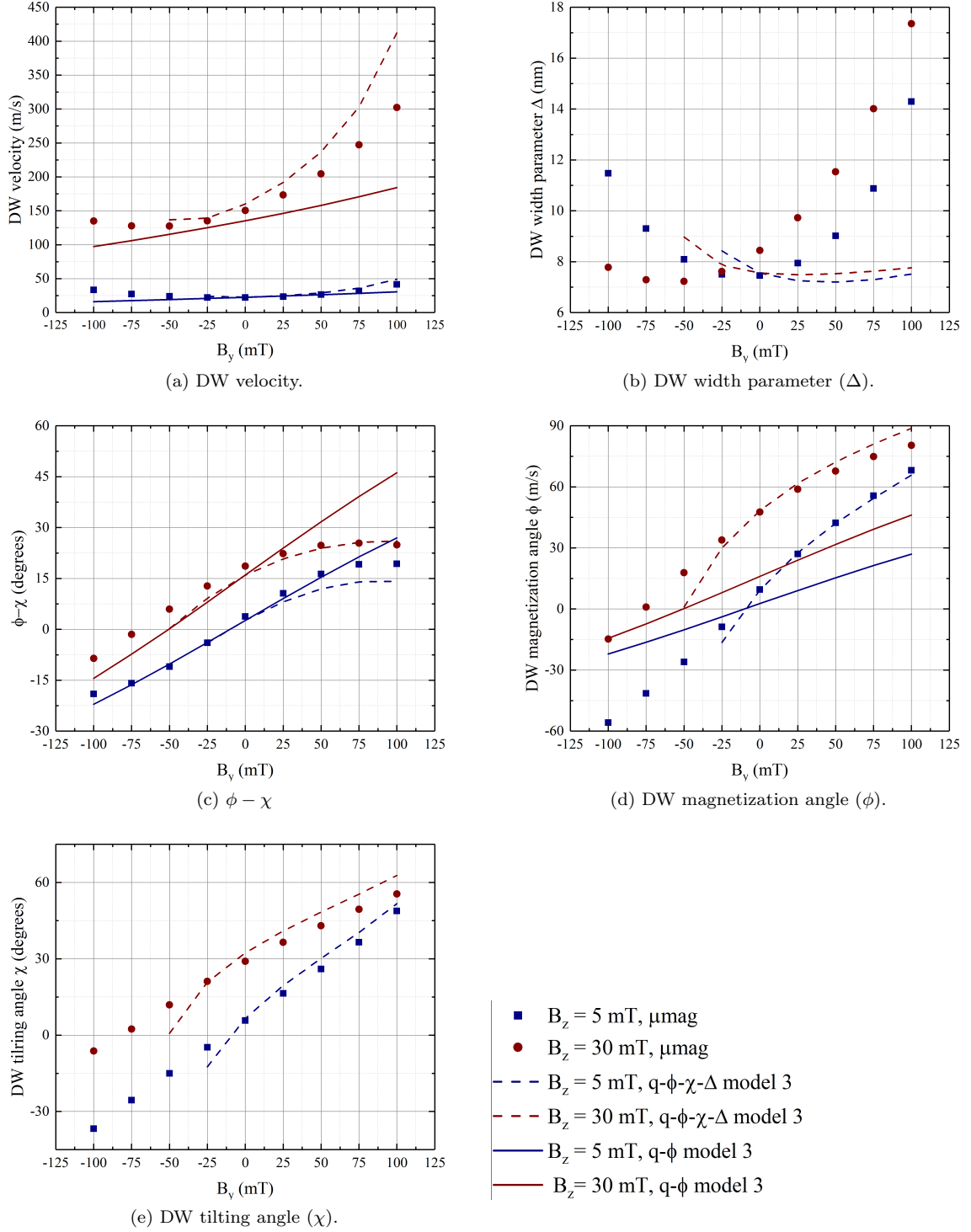
(e) DW tilting angle (χ).
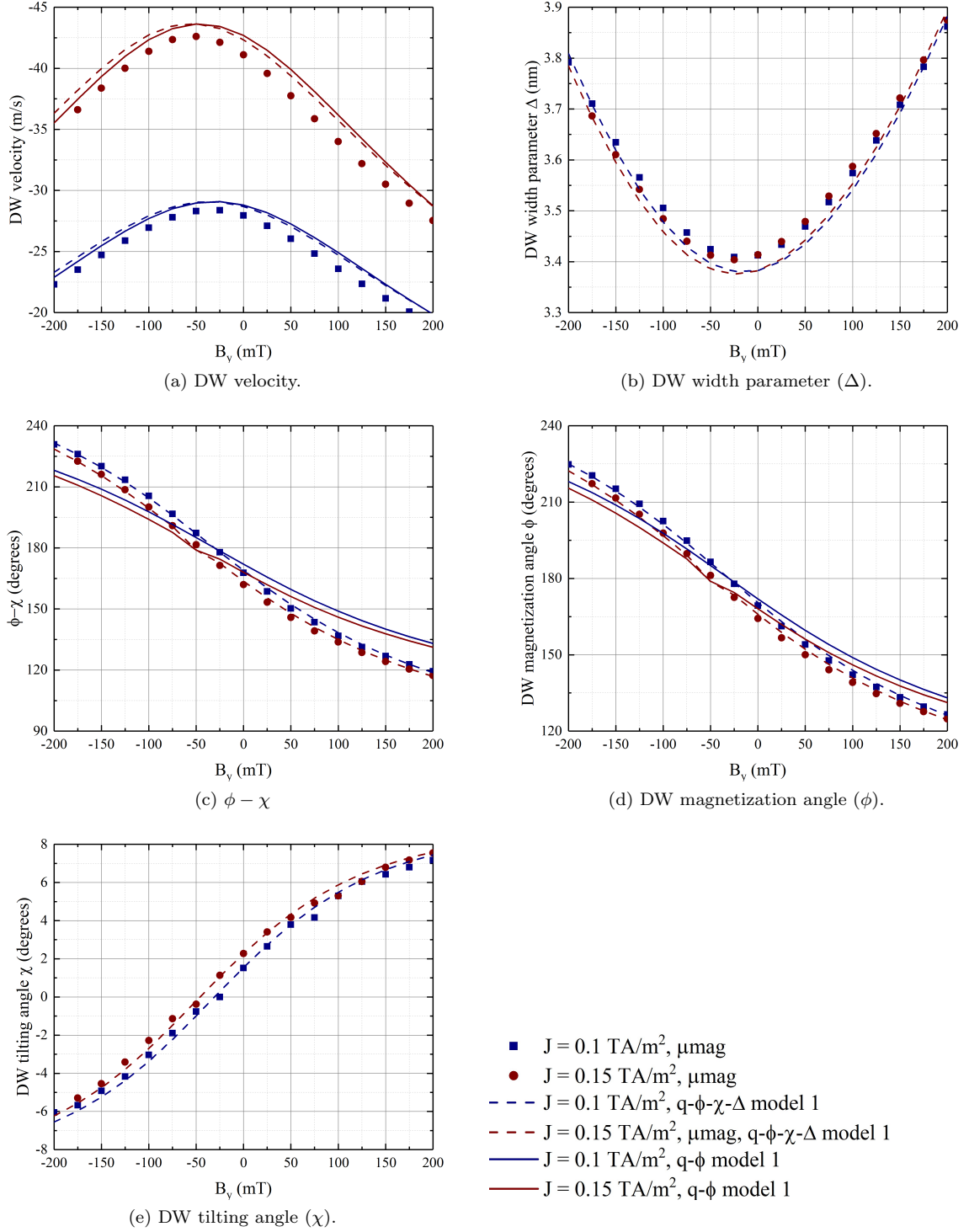
Figure 5.16: Instantaneous steady state DW characteristics for SHE-driven DW motion in Pt/Co/Ni/Co/MgO/Pt with different currents and transverse fields applied. Only the collective coordinate models with highest accuracy in predicting the DW velocity are shown.

5.4.5 Effect of Combinations of transverse and longitudinal fields

All our simulations involved addition of a transverse or longitudinal field in the absence of the other. To better understand the effect of combinations of these fields, we used the collective coordinate models to study the Pt/CoFe/MgO system for a current density of $J_x = 0.1TA/m^2$ when both longitudinal and transverse fields are applied simultaneously. Figure 5.17 shows the results of this study. Clearly, transverse fields can be used for fine tuning properties such as DW velocity with an almost linear effect, while longitudinal in-plane fields showcase a rather nonlinear effect on DW motion, and can be used to make major changes to the motion. This was also understandable from the micromagnetic simulations in the previous section, where a nonlinear effect is seen when longitudinal fields are used, with a more linear effect in the case of transverse fields.

(a) DW average velocity in m/s.

(b) DW tilting χ in degrees.

(c) DW width parameter

(d) DW magnetization angle

(e) $\phi - \chi$
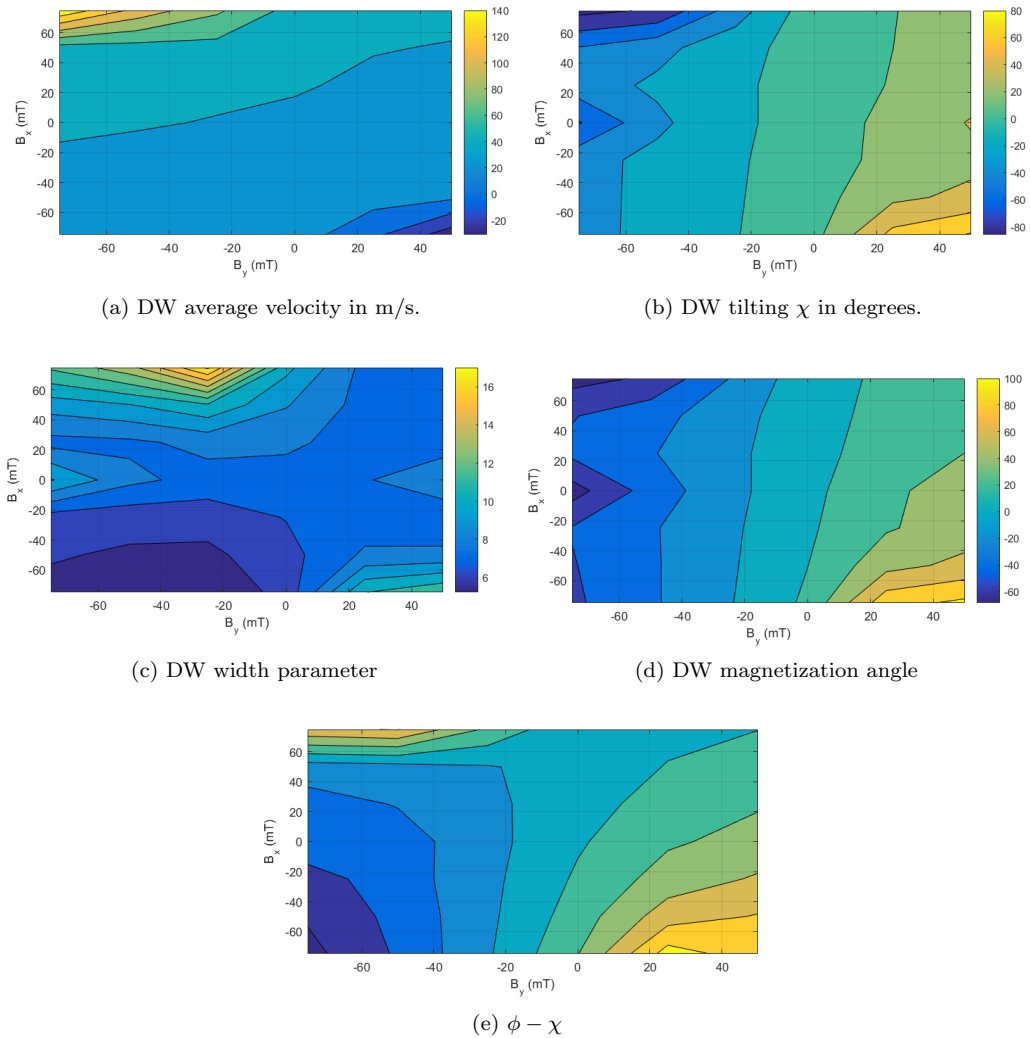
Figure 5.17: Effect of combinations of longitudinal and transverse fields on DW motion for a fixed current density of $J_x = 0.1TA/m^2$. The effect were modeled using the CCM with four collective coordinates and a canted ansatz.

5.4.6   Effect of Sample Width

The dimensions of the system also play a role on the motion of the DW. We studies the effect of increasing the dimensions of the wire on the motion of the DW. Figure 5.18 shows that doubling the width of the wire to 300 nm reduces the DW velocity only slightly, while the DW velocities drop dramatically when we reach a width of 500 nm for the wire at the same current density. This could be attributed to the structure of the DW. A larger width stabilizes domain walls with less Néel character, reducing the effect of the SHE torques on the DW and reducing the DW velocity. This fact was verified in Figure 5.18, where clearly the magnetization angle of the DW is much lower for a width of 500 nm compared to the other two cases. These effects can be attributed to the change in demagnetizing field within the system.

(a) DW velocity.

(b) DW magnetization angle.

(c) DW tilting angle.

(d) DW width parameter.
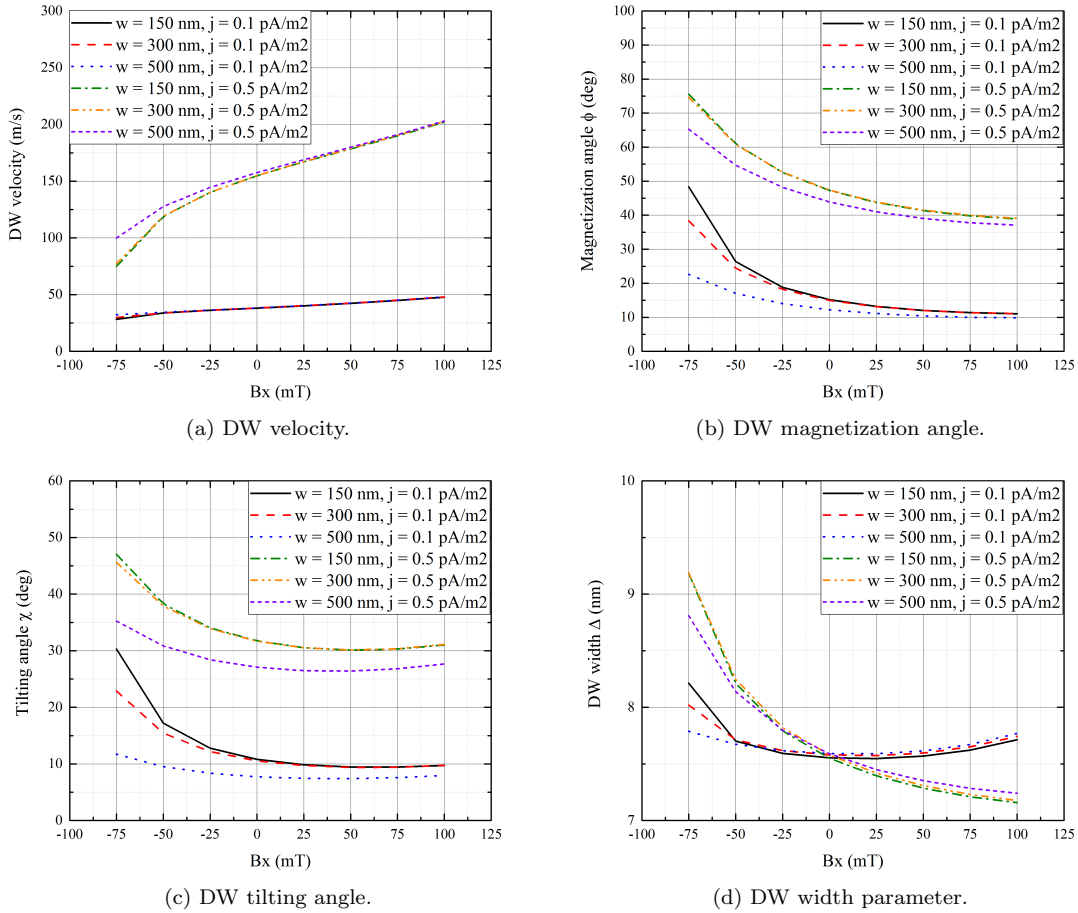
Figure 5.18: Effect of changing the width of the nanowire on DW motion.

5.5   Selecting the Right CCM

The results of the micromagnetic simulations presented in Figures 5.9-5.16 highlighted the importance of using the right CCM when studying different systems.

First, we found that canting in the domains should be included in the model only if canting in the domains is larger than about 10°; otherwise its inclusion does not add value to the models and can overcomplicate the study. Hence, we recommend using the canted models only when $\theta_c > 10°$ is expected.

We also found that model set 3 is more applicable without the Δ degree of freedom, as it does not predict this parameter correctly and seems to be of a more rigid nature than the Bloch profile. This is understandable from a modeling perspective, as Δ in a way determines the transition from DW to domain, and canting impacts the domain's structure.

Finally, most of our models are adept at predicting the right tilting and magnetization angles at the critical in-plane fields identified. As such, use of these critical points when trying to identify material properties from the collective coordinate models is recommended.

Overall, it seems that when studying the velocity of the domain wall under longitudinal fields, use of the $q - \phi$ form of model 3 is sufficient, while under transverse fields or other cases where predicting the DW tilting is of interest, the $q - \phi - \chi$ form of model 3 or the $q - \phi - \chi - \Delta$ form of model 2 should be used.

5.6   Conclusion

In this Chapter, we showed that the models developed in Chapter 4 fail when applied to DW motion under in-plane fields, and then presented two extended models which better replicated micromagnetic results in these cases. Through these models, we observed the important role played by canting in the domains on the motion of the domain walls. This showed that profile used to derive the DW is much more important that the number of collective coordinates and we were able to show that the best results are observed when a canted profile is used with only two collective coordinates.

We showed how the application of moderate in-plane fields could change the dynamics of domain walls by adjusting the internal structure of the DW (magnetization and DW width) along with the tilting of the DW. The collective coordinate models were used to describe certain critical points in the dynamics of the DW under in-plane fields, including points where the DW velocity reaches zero or the DW does not tilt. The collective coordinate description at these points may be used to measure the strength of different interactions in the system.

Chapter 6

Collective Coordinate Modeling of Magnetic Bubbles

In the previous Chapters we derived collective coordinate models for domain wall motion in PMA nanowires. Specifically, our results show the importance of canting when DW motion is studied under in-plane fields, showcasing that the impact of canting should always be included in collective coordinate descriptions when in-plane fields are applied [1, 4, 8].

Bubble memory sparked initial interest in studying magnetic bubbles in the 1970s [43, 44]. Many models of DW motion currently in use such as the Slonczewski [54] or Thiele models [56, 57] stem from bubble memory studies in the 1970s.

Today, behavior of a magnetic bubble is used both in devices to code information [34], and as a means to measure the strength of specific interactions including the DMI. The strength of the DMI is assessed using expansion of magnetic bubbles under the application of in-plane and out-of-plane fields [88–90]. This method assumes significant Néel character on the axis of the in-plane field applied, an assumption that can be debated. Moreover, the measurement relies on collective coordinate descriptions of DW motion.

In this Chapter, we study the applicability of collective coordinate models to the study of DW motion in expanding magnetic bubbles under in-plane and out-of-plane fields. We will present a method for extending models developed in the previous Chapter to magnetic bubbles, and assess the accuracy of these models.

6.1   Toy Model

Based on the principles presented in Chapter 2 and assuming that there is no interaction between different points on a bubble (an assumption valid for a static bubble), the energy of the domain wall along the local x and y coordinate systems defined in 6.1 along any radius of the bubble may
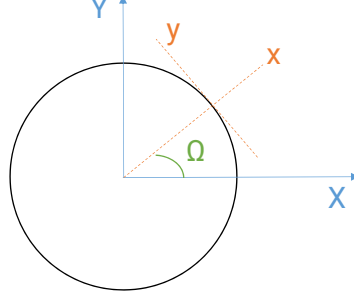
Figure 6.1: The local x,y coordinates and the global X,Y coordinates.

be written as:

$$
E_r = \overbrace{\frac{2I_1 A}{\Delta}}^{Exchange} + \overbrace{2I_3 D \cos\phi}^{DMI} + \overbrace{2I_4 \Delta K_U}^{Anisotropy}
$$
$$
+ \overbrace{2I_4 \frac{\mu_0 M_s^2}{2} \left(N_z l + 2\Delta \left[N_{x,\,eff} \cos^2\phi + N_{y,\,eff} \sin^2\phi - N_z \right] \right)}^{Magnetostatic}
$$
$$
\underbrace{-2\mu_0 M_s \left[I_6 \Delta \left(H_{x,\,eff} \cos\phi + H_{y,\,eff} \sin\phi \right) + I_2 H_z q \right]}_{Zeeman}
$$

$$(6.1)$$

Here we assumed the DW follows the profiles presented in Chapter 2 along each radius. ϕ is the angle with the radial axis at each point, and the I_i factors are the same factors defined in Chapter 5. The local x and y coordinate system is defined as a right handed coordinate system with the x-axis along the radius and the y-axis perpendicular to the radius (Figure 6.1).

In Equation 6.1, the effective applied fields in the x and y direction on the wall depend on the applied field and the position along the bubble. Assuming the radius of interest makes an angle Ω with the global X and Y coordinates, the effective local x and y field may be calculated as:

$$
\begin{aligned}
H_{x,\,eff} &= H_X \cos\Omega + H_Y \sin\Omega \\
H_{y,\,eff} &= -H_X \sin\Omega + H_Y \cos\Omega
\end{aligned}
$$

$$(6.2)$$

The same concept should be applied to demagnetizing factors, if the demagnetizing factors of the system are taken into account in the global coordinate system.

This energy description forms the basis of our toy model. In this model, we are assuming that each segment of the DW on the bubble is acting as if it was a DW moving in a nanowire pointing along the radius. Clearly, this means that the DW segments are unaware of the existence of other segments, and they are decoupled from each other; as such, this reduced model loses some realism but can provide some initial insights into the behavior of magnetic bubbles.

6.2   Static Structure of the DW

In the static case ($H_z = 0$), the energy equation simplifies to:

$$
E_r = \overbrace{\frac{2I_1A}{\Delta}}^{Exchange} + \overbrace{2I_3D\cos\phi}^{DMI} + \overbrace{2I_4\Delta K_U}^{Anisotropy}
$$
$$
+ \overbrace{\frac{\mu_0 M_s^2}{2}\left(N_z l + 2I_4\Delta\left[N_{x,eff}\cos^2\phi + N_{y,eff}\sin^2\phi - N_z\right]\right)}^{Magnetostatic} +
$$
$$
\overbrace{-2\mu_0 M_s\left[I_6\Delta\left(H_{x,eff}\cos\phi + H_{y,eff}\sin\phi\right)\right]}^{Zeeman}
$$

$$(6.3)$$

Minimizing this energy can give us the equilibrium structure of the DW. Figure 6.4 shows the magnetization angle of the a bubble DW in a Pt/CoFe/MgO sample under different applied in-plane fields as predicted by model 1 (the model without canting). The effect of in-plane fields can clearly be seen and seems to match what one would expect taking into account the interaction of local spins with the local in-plane field. We did not observe any major effect from canting when comparing models 1-3 in the static case. The in-plane fields also affect the DW width, as depicted in Figure 6.2; however, these changes are less than 0.13% of the DW width.

Figure 6.3 illustrates the local energy of the bubble DW, highlighting that the points of minimal energy occur for $\Omega = 0°$, $180°$ in the case of fields in the x-direction and $\Omega = 90°$, $270°$. This seems to be the evidence experimentalists provide for the way they measure DMI.

Energy minimization can also be done mathematically to find the equilibrium angle ϕ for the DW. Assuming a fixed DW width (which seems acceptable due to the negligible changes in DW width), we have:

$$
\frac{dE_r}{d\phi} = 0 \rightarrow -I_3 D\sin\phi + \mu_0 M_s^2 I_4\Delta\left(N_{y,eff} - N_{x,eff}\right)\sin 2\phi - \mu_0 M_s I_6\Delta\left(H_{y,eff}\cos\phi - H_{x,eff}\sin\phi\right) = 0
$$

$$(6.4)$$

which yields the equilibrium DW magnetization:

$$
\cos\phi_{eq} = \frac{I_3\frac{D}{\mu_0 M_s\Delta} - I_6 H_{x,eff} + I_6 H_{y,eff}\cot\phi}{2I_4 M_s(N_{y,eff} - N_{x,eff})} = \frac{I_3 H_{DMI} + I_6\left(H_{y,eff}\cot\phi - H_{x,eff}\right)}{2I_4 H_K}
$$
$$
= \frac{I_3}{2I_4}h_{DMI} + \frac{I_6}{2I_4}\left(h_{y,eff}\cot\phi - h_{x,eff}\right)
$$

$$(6.5)$$

with H_K denoting the shape anisotropy field, and the h_is being the relevant field normalized by the shape anisotropy field. It is clear that, in the absence of applied fields, the DW structure is determined by the competition between the DMI and in-plane fields normalized by the shape anisotropy. The equation above will only be valid when numerator is less than or equal to H_k; for all other cases, $\phi_{eq} = 0$ and the wall will be Néel. Interestingly, the same equation may be recovered from the dynamic equations developed in the previous section if no excitation is driving the wall. A solution taking into account the changes in the DW width may also be derived, but has a complex form.
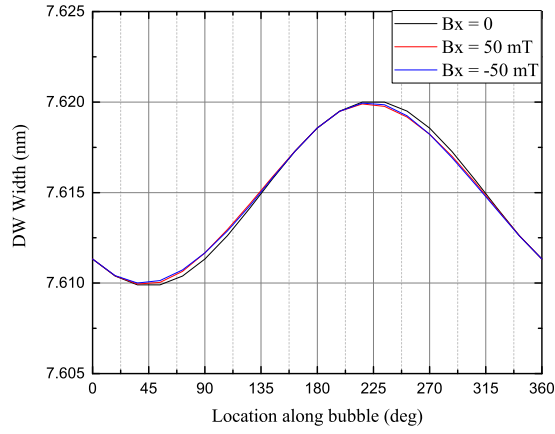
(a) Fields in the x-direction.
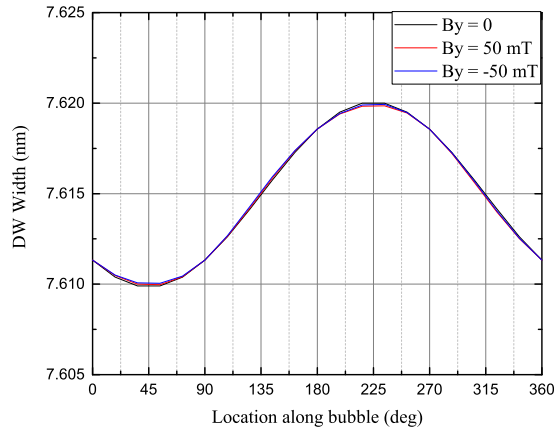
(b) Fields in the y-direction.

Figure 6.2: Variation of static DW width of the bubble at different points along the bubble in the presence of in-plane fields. Clearly, the width varies negligibility around the bubble and is only slightly affected by the in-plane fields applied.

(a) Fields in the x direction.

(b) Fields in the y-direction.
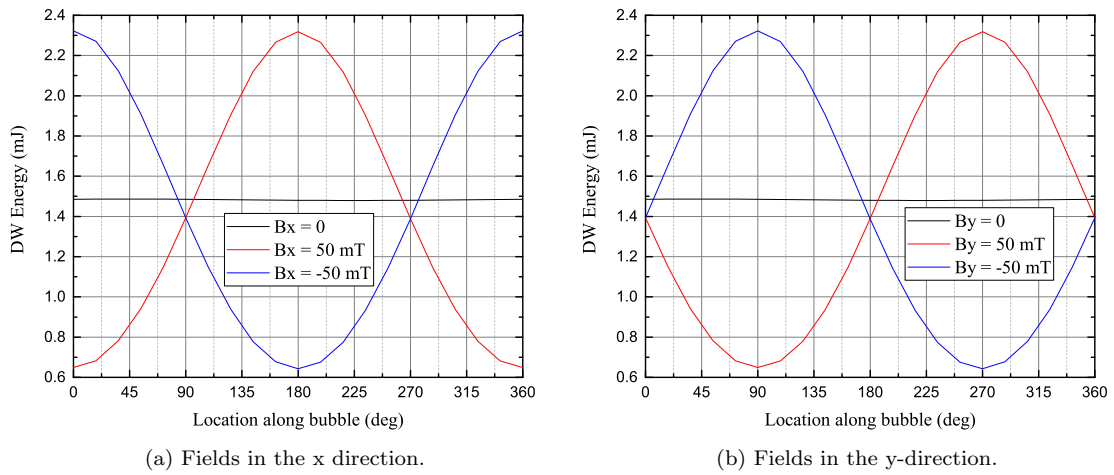
Figure 6.3: Variation of static DW energy of the bubble at different points along the bubble in the presence of in-plane fields.

(a) No inplane field.

(b) $B_x = 50\,\text{mT}$.

(c) $B_x = -50\,\text{mT}$.

(d) $B_y = 50\,\text{mT}$.

(e) $B_y = -50\,\text{mT}$.
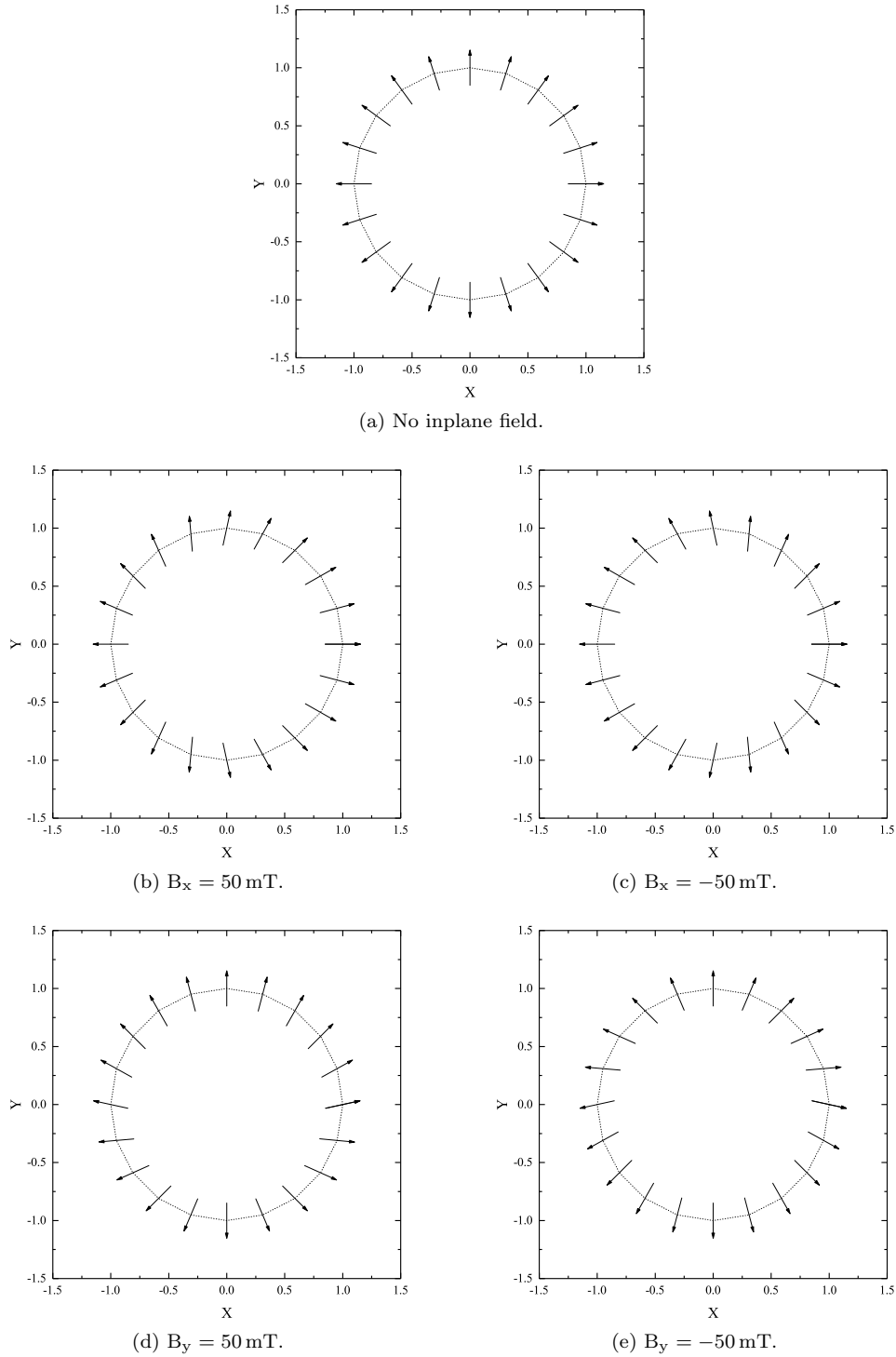
Figure 6.4: Internal structure of the static bubble under different in-plane fields. The material properties used are those of a Pt/CoFe/MgO system. The arrows show the local direction of magnetization at each position along the circular bubble.

6.3 Dynamics: Extension of CCMs to Bubbles

The equations of motion developed in the previous Chapter could be extended to a magnetic bubble. Specifically the $q - \phi$ and $q - \phi - \Delta$ equations could be extended to the bubble, by applying them at each point around the bubble. These equations could also be derived from the energy description highlighted earlier in this Chapter.

Simplifying the collective coordinate equations in the presence of an applied field (or minimizing the system energy in Equation 6.1 with $\frac{\partial E_r}{\partial \phi} \sim 0$), the steady state DW magnetization may be extracted as:

$$
\begin{aligned}
\cos \phi_{eq} &= \frac{I_3 \frac{D}{\mu_0 M_s \Delta} - I_6 H_{x,eff} + I_6 H_{y,eff} \cot \phi_{eq}}{2 I_4 M_s (N_{y,eff} - N_{x,eff})} + \frac{I_2 H_z}{\alpha I_4 M_s (N_{y,eff} - N_{x,eff}) \sin \phi_{eq}} \\
&= \frac{I_3}{2 I_4} \frac{H_{DMI}}{H_K} - \frac{I_6}{2 I_4} \frac{H_{x,eff}}{H_K} + \frac{I_6}{2 I_4} \frac{H_{y,eff}}{H_K} \cot \phi_{eq} + \frac{I_2}{I_4} \frac{H_z}{\alpha H_K \sin \phi_{eq}} \\
&= \frac{I_3}{2 I_4} h_{DMI} - \frac{I_6}{2 I_4} h_{x,eff} + \frac{I_6}{2 I_4} h_{y,eff} \cot \phi_{eq} + \frac{I_2}{I_4 \alpha} h_z \csc \phi_{eq}
\end{aligned}
\tag{6.6}
$$

with the velocity defined as $\dot{q} = \frac{\mu_0 \gamma}{\alpha} H_z \Delta^*$. A description for the steady state DW width (Δ^*) was already extracted in Chapter 3 and remains valid.

While we postulated that applying these equations without a constraint taking into account the fact that the points are connected would be unfruitful, preliminary results show that the model works for the bubble. As shown in Figure 6.5, the relevant strength of the in and out of plane fields seems to play a role in the evolution of the bubble. First, it is notable that the bubble is not of Néel character at time zero, as the in-plane fields disrupt the static structure of the bubble. Addition of the out-of-plane field clearly leads to additional changes in the magnetization. Even for the 10mT out-of-plane field, clearly under the application of in-plane fields the Néel point is no longer on the axis, being at $15°$ axis for $B_x = 150\,\text{mT}$, $B_z = 10\,\text{mT}$, and $-5°$ axis for $B_x = -150\,\text{mT}$, $B_z = 10\,\text{mT}$. Clearly, as the out-of-plane field increases, part of the DW reaches Walker breakdown, which in a real interface will give rise to Bloch lines at which point our model is invalid. This effect can be better visualized in Figure 6.6 which shows the location of the interface at each position along the bubble under in-plane fields. Clearly, there are always two points which are least deviating from the case without in-plane fields; however, these points move along the wire with time. For high drive field of $B_z = 90\,\text{mT}$ we can clearly see the deformation of the bubble as the interface shows breaking points.

In conclusion, in the dynamic case, B_z leads to a shift in the axis on which the DW maintains Néel structure. This shift will shed some doubt on whether the bubble expansion approach for DMI measurement [89] is accurate or not, specially since the amount of shift depends not only on the field applied, but the properties of the material system being studied. In addition, vertical Bloch lines may form and propagate along the bubble; the effects of these Bloch lines require a two dimensional description of the bubble and are not well predicted by our collective coordinate model.

6.4 Comparison to Micromagnetic Simulation

To assess the accuracy of the model presented for realistic systems, we performed micromagnetic simulations on a $2.048\,\mu\text{m} \times 2.048\,\mu\text{m} \times 0.6\,\text{nm}$ film. Material constants used were saturation magnetization $M_s = 1353\,\text{kA/m}$, uniaxial anisotropy constant $K_u = 1.5\,\text{MJ/m}^3$ along positive z-axis, exchange constant $A_{ex} = 13\,\text{pJ/m}$, and Gilbert damping $= 0.2$.

(a) $B_z = 10\,\text{mT}$, $B_x = -150\,\text{mT}$. (b) $B_z = 10\,\text{mT}$, $B_x = 0\,\text{mT}$. (c) $B_z = 10\,\text{mT}$, $B_x = 150\,\text{mT}$.

(d) $B_z = 90\,\text{mT}$, $B_x = -150\,\text{mT}$. (e) $B_z = 90\,\text{mT}$, $B_x = 0\,\text{mT}$. (f) $B_z = 90\,\text{mT}$, $B_x = 150\,\text{mT}$.

Figure 6.5: Evolution of the bubble magnetization under different combinations of in- and out-of-plane fields for a Pt/CoFe/MgO sample. The bubbles have been rescaled to the original bubble size to show the difference in magnetization. Clearly, addition of the B_z field disrupts the DW structure from the predicted static structure (shown as t = 0).

During deposition of realistic materials, disorders such as grain boundaries, dislocations, and lattice vacancies can be introduced into the material. To mimic a realistic system, disorders was introduced into the system following the method presented in reference [164] using randomly distributed grains of size 10 nm with exchange constant varied at the border of the grains by 43%.

In the simulations, a magnetic bubble of radius 256 nm was initialized in the system. Then an out-of-plane field and an in-plane field are applied simultaneously. The bubble was allowed to expand until it reaches the boundary of the system. An infinitely large system with one bubble was mimicked by replacing the dipolar energy of the film with that of an infinite system.

We compared the model presented in this Chapter to the results of micromagnetic simulations to assess whether these models are accurate especially considering the disorder included in the model. As depicted in Figure 6.7, we found that by reducing the exchange constant to 57% of the actual value (equivalent to reducing it by the amount of exchange constant variation at the grain boundaries) we are able to almost reproduce the micromagnetic results. As such, the toy model seems to be valid at least for cases with low drive field.

The micromagnetic simulations showed some rippling effects on the DW, which is the reason for the sudden drop in DW velocity in Figure 6.7.a. The CCM can be used to understand what happens at the ripple points. In the absence of the DMI and in-plane fields, the drive field determines whether Walker breakdown happens. However, in the presence of the in-plane field and DMI, there are two additional parameters that play a role in whether or not precession continues.

(a) $B_z = 10\,\mathrm{mT}$, $B_x = 150\,\mathrm{mT}$.

(b) $B_z = 10\,\mathrm{mT}$, $B_x = -150\,\mathrm{mT}$.

(c) $B_z = 90\,\mathrm{mT}$, $B_x = 150\,\mathrm{mT}$.

(d) $B_z = 90\,\mathrm{mT}$, $B_x = -150\,\mathrm{mT}$.
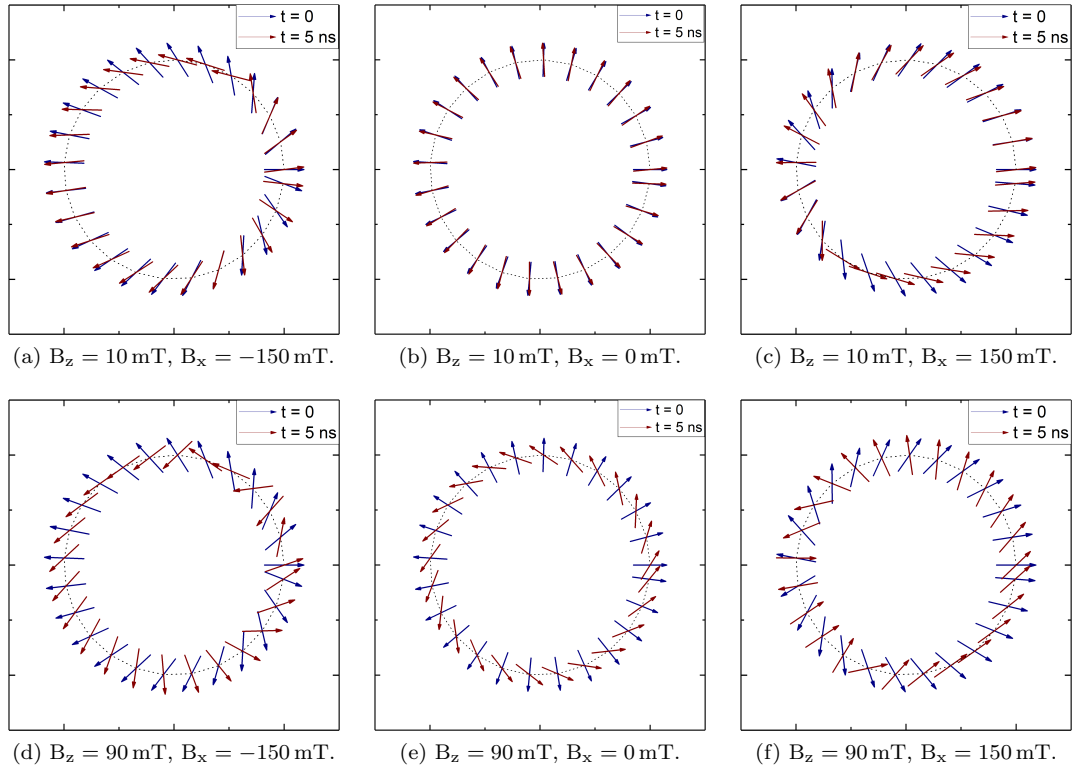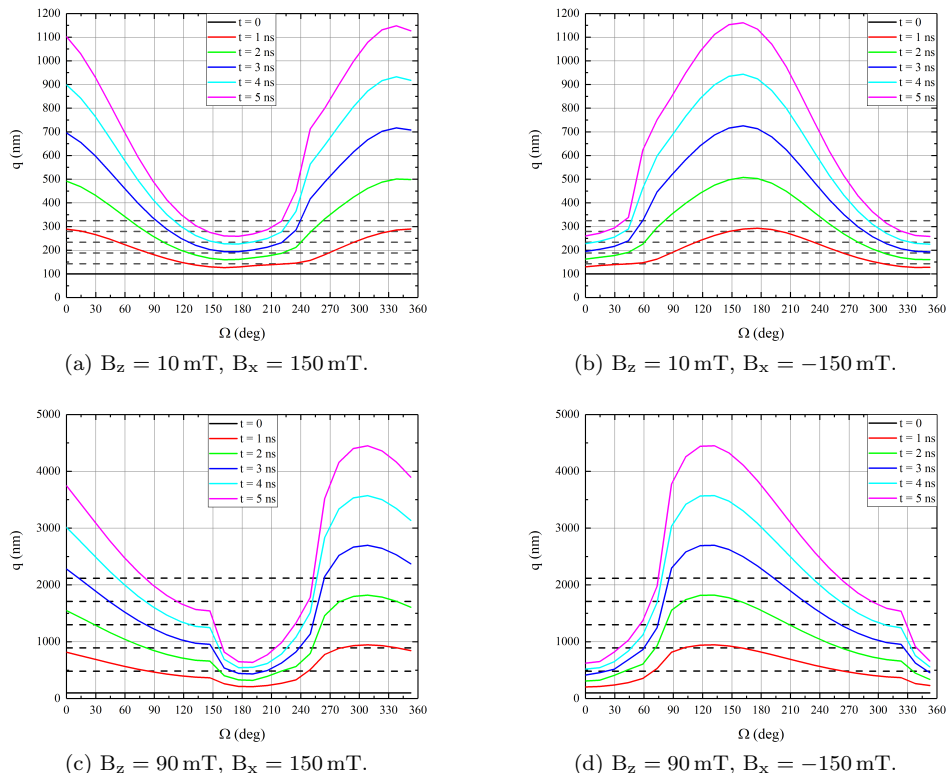
Figure 6.6: Evolution of the bubble radius under different combinations of in- and out-of-plane fields for a Pt/CoFe/MgO sample. The dashed lines show the position of the bubble in the absence of in-plane fields. Clearly, the in-plane fields make the bubbles look ellipsoidal, with some parts moving faster than in the absence of these fields and some parts of the bubble slower. At high out of plane fields, the formation of vertical Bloch lines along the bubble disrupts this motion, leading to a Walker breakdown like behavior which can be seen as non-smooth points in the graphs (for example $B_x = 150\,\mathrm{mT}$ in (c)) .

The fact that the in-plane fields are locally determined means that points of precession can nucleate within the bubble locally, showing local Walker breakdown behavior. Physically speaking, such precessional motion will lead to 2-D effects on the bubble, affecting the spin texture around that point and giving rise to the ripple like shape of the bubble. Even though the CCM is effectively a one-dimensional model, such ripples can be observed in the results as well.

6.5 Conclusion

We presented a toy model that can elucidate to the structure of magnetic bubbles to an extent. This model showed that the Néel points on a magnetic bubble depend on the relative strength of the DMI, applied in-plane fields and the out=of-plane field applied. Moreover, as previously mentioned, canting in the domains can play a role and our model took this effect into account. This casts some doubt on the assumptions used by experimental groups in measuring DMI [88–90]. Of course, these experiments are usually done in the creep regime where the assumptions could be

(a) DW velocity.

(b) DW width parameter.
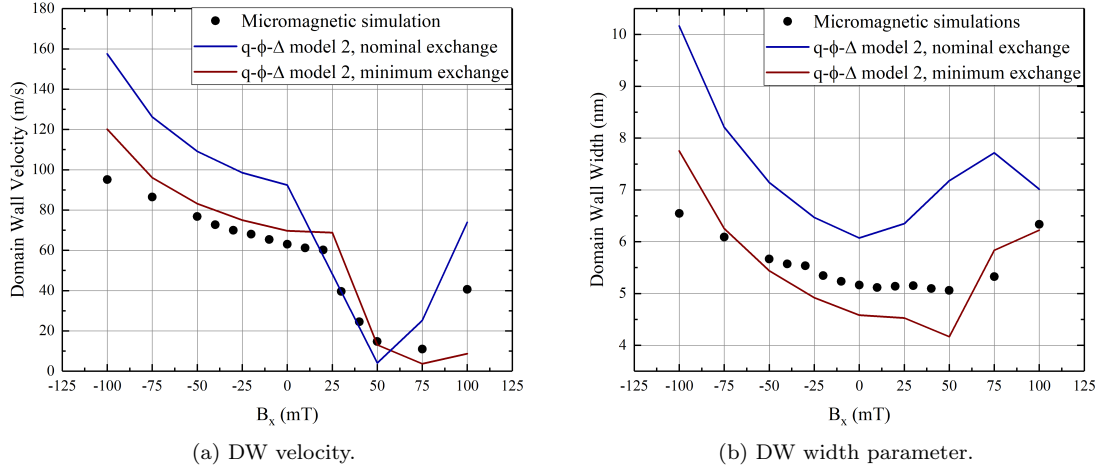
Figure 6.7: Comparison between the micromagnetic simulations and collective coordinate model for a drive field of $B_z = 17$mT. The velocity was calculated for the left side of the bubble along the axis of the in-plane field.

valid due to the very low value of the out-of-plane field; however, thresholds need to be identified based on material properties for when these assumptions are valid.

We also verified that these models fit micromagnetic simulations well and could account for the effects of disorder and pining in the system. The collective coordinate model and micromagnetic simulations both show ripelling effects in the bubble due to the formation of vertical Bloch lines. These effects are further studied in reference [2].

Chapter 7

Comparison with a Semi-analytical Model

In this Chapter, the collective coordinate models derived using the Euler-Lagrange equation in Chapter 4 are compared to a semi-analytical approach based on taking averages of the magnetization [3, 5, 160]. These semi-analytical approaches are effectively a method to post process micromagnetic simulation; yet they can also shed some light on shortcomings of the collective coordinate models presented in the previous Chapters, and the effect of the ansatz.

7.1 The semi-analytical approach

Based on the LLG-equation and using statistical averages, a semi-analytical collective coordinate model could be developed [3, 5, 160]. While in micromagnetic simulations the LLG-equation describes the local magnetization dynamics in each finite difference cell, the semi-analytical collective coordinate model developed using statistical averages describes DW dynamics in terms of the average value of magnetization along different axes. By performing a few simulations and identifying which combinations of these average magnetization values remain constant, one can develop a fingerprint of DW behavior in the system under study in the form of a few equations.

7.1.1 The Effective Field on the Domain Wall

To derive the semi-analytical model, the effective field presented in Chapter 2 should be properly averaged over the DW volume and substituted in the LLG equation. The effect field on the DW

will have the form:

$$\mathbf{H}_{eff,DW} = \mathbf{H}_{ext} + \mathbf{H}_R + \frac{1}{\frac{\langle(|m_{ip}|)^2}{\langle m_{ip}^2\rangle}} \left[\langle\mathbf{H}_{anis}\rangle + \langle\mathbf{H}_{ms}\rangle + \langle\mathbf{H}_{DMI}\rangle + \langle\mathbf{H}_{exch}\rangle + \langle\mathbf{H}_{SH}\rangle\right]$$

$$\cong H_{ext,x}\mathbf{e}_x + H_{ext,y}\mathbf{e}_y + H_{ext,z}\mathbf{e}_z + H_R\mathbf{e}_y + \frac{2K_u}{\mu_0 M_s}\frac{\langle m_{ip}^2\rangle}{\langle|m_{ip}^2|\rangle}\frac{\langle m_z m_{ip}^2\rangle}{\langle m_{ip}^2\rangle}\mathbf{e}_z$$

$$- \frac{M_s}{\langle m_{ip}^2\rangle}\left[N_{eff,x}\langle m_x m_{ip}^2\rangle\mathbf{e}_x + N_{eff,y}\langle m_y m_{ip}^2\rangle\mathbf{e}_y + N_{eff,z}\langle m_z m_{ip}^2\rangle\mathbf{e}_z\right]$$

$$+ \frac{2D}{\mu_0 M_s}\frac{\langle m_{ip}^2\rangle}{\langle|m_{ip}^2|\rangle}\left[\langle\partial_x m_z\rangle\mathbf{e}_x + \langle\partial_y m_z\rangle\mathbf{e}_y - \langle\partial_x m_x + \partial_y m_y\rangle\mathbf{e}_z\right] \qquad (7.1)$$

$$+ \frac{2A}{\mu_0 M_s}\frac{\langle m_{ip}^2\rangle}{\langle|m_{ip}^2|\rangle}\left[\langle\partial_{xx} m_x\rangle\mathbf{e}_x + \langle\partial_{yy} m_y\rangle\mathbf{e}_y + \langle\partial_{zz} m_z\rangle\mathbf{e}_z\right]$$

$$+ H_{SHE}\frac{\langle m_{ip}^2\rangle}{\langle|m_{ip}^2|\rangle}\left[-\langle m_z\rangle\mathbf{e}_x + \langle m_x\rangle\mathbf{e}_z\right]$$

with H_{ext} the external magnetic field, $H_R = \frac{\alpha_R P}{\mu_0\mu_B M_s}j_x$ the Rashba field strength, H_{anis} the anisotropy field, H_{ms} the magnetostatics field, H_{DMI} the DMI field, H_{exch} the exchange field, and $H_{SHE} = \frac{\hbar\theta_{SHE}}{2eM_s L_z\mu_0}j_x$ the SHE strength. Note that the demagnetizing factors in the equation above are effective and are calculated by diagonalizing the demagnetizing tensor along the x-, y-, and z-direction [3,5]. The vector $\mathbf{e}_i$ denotes the unit vector in the i direction.

The spatial averages used in the field definition above are calculated over the Dw volume; for example $\langle f\rangle$ denotes a spatial average of the function f over the domain wall volume V_{DW}

$$\langle f\rangle(t) = \frac{1}{V_{DW}}\int\int\int_{V_{DW}} f(\mathbf{r},t)\,dV. \qquad (7.2)$$

The DW volume V_{DW} is defined based on a parameter ϵ, with the left boundary of this volume defined so that $|\partial_x m_z| \geq \epsilon$, maintaining the changes in the z-component of magnetization larger than a threshold in the computational window. The right boundary of the volume is defined by fulfilling $\int_{DW} m_z(\mathbf{r},t)\,dx = 0$ along every row in y. A too large ϵ means that only part of the DE is taken into account. A value of $\epsilon = 0.002$ was found to work best based on experience [5].

In Equation 7.1, $\mathbf{m}_{ip}$ is the in-plane magnetization vector

$$\mathbf{m}_{ip} \equiv m_x\mathbf{e}_x + m_y\mathbf{e}_y. \qquad (7.3)$$

with the properties

$$\langle m_{ip}^2\rangle = \langle m_x^2 + m_y^2\rangle \qquad (7.4)$$

and

$$\langle|m_{ip}|\rangle \equiv \langle\sqrt{m_x^2 + m_y^2}\rangle. \qquad (7.5)$$

Note that $\frac{\langle m_{ip}^2\rangle}{\langle|m_{ip}^2|\rangle}$ in the first line of Equation 7.1 is a scaling factor to ensure that $\mathbf{H}_{eff}$ and $\mathbf{H}_{eff,DW}$ are physically equivalent when locally interacting with the DW magnetization from the perspective of the DW, despite one being defined over the Dw and the other at every point within the system. Due to their uniformity, the external field $\mathbf{H}_{ext}$ and the Rashba field $\mathbf{H}_R$ are not scaled.

7.1.2   The Collective Coordinates and Other Model Parameters

Equation 7.1 can be thought of as the ansatz for the semi-analytical model. In the context of this model, after substituting equation (7.1) in the LLG-equation different collective coordinated may be introduced. Here we first introduce the collective coordinate:

- The DW position may be defined as:

$$Q(t) = \frac{1}{-\langle \partial_x m_z(\mathbf{r}, t) \rangle} \langle m_z(\mathbf{r}, t) \rangle, \tag{7.6}$$

  from where we can derive the DW velocity as:

$$v(t) \equiv \frac{dQ(t)}{dt} = \frac{1}{-\langle \partial_x m_z(\mathbf{r}, t) \rangle} \frac{\mathrm{d}\langle m_z(\mathbf{r}, t) \rangle}{\mathrm{dt}}, \tag{7.7}$$

- The averaged DW magnetization angle may be defined as:

$$\Phi_{av} = \arctan \frac{\langle m_y \rangle}{\langle m_x \rangle} = \arctan \frac{\langle m_{ip} sin\phi \rangle}{\langle m_{ip} cos\phi \rangle} \tag{7.8}$$

  To define Φ_{av} unambiguously, we impose that $\Phi_{\mathrm{av}} = 0$ corresponds to a Néel wall characterized by $\langle \mathrm{m_y} \rangle = 0$ and $\langle \mathrm{m_x} \rangle > 0$ while $\Phi_{\mathrm{av}} = \pi$ corresponds to a Néel wall characterized by $\langle \mathrm{m_y} \rangle = 0$ and $\langle \mathrm{m_x} \rangle < 0$.

- The averaged DW width is defined as:

$$\Delta_{av} = 2 \frac{\langle m_{ip}^2 \rangle}{-\langle \partial_x m_z \rangle}, \tag{7.9}$$

- The averaged DW geometrical tilting is defined as:

$$X_{av} = \arctan \frac{\langle \partial_y m_z \rangle}{\langle \partial_x m_z \rangle}, \tag{7.10}$$

In the derived equations for DW motion in this system, several rescaling factors show up, including:

$$\kappa_{av} = \frac{\langle m_{ip}^2 \rangle}{\langle |m_{ip}| \rangle} \tag{7.11}$$

$$\kappa_{av,w} = \frac{\langle |m_{ip}|^3 \rangle}{\langle m_{ip}^2 \rangle} \tag{7.12}$$

$$g_{i,av} = \frac{\partial_{ii} m_i}{\langle |m_{ip}| \rangle} \forall i \in \{x, y, z\} \tag{7.13}$$

κ_{av} and $\kappa_{\mathrm{av,w}}$ characterize the DW shape, while $\mathrm{g_{i,av}}$ are related to effects from the exchange interaction.

7.1.3 Equations of Motion

Based on the descriptions above, the equation describing DW velocity will have the following form:

$$
\begin{aligned}
\frac{1+\alpha^2}{\gamma_0}\frac{2}{\Delta_{av}}v(\mathbf{H}_{ext}) =& \alpha H_z + \frac{2}{\Delta_{av}}\frac{1+\alpha\beta}{\gamma_0}u_x + \frac{1}{\kappa_{av}}\left[H_x\sin\Phi_{av} - H_y\cos\Phi_{av}\right]\\
&+ \alpha\kappa_{av}H_{SH}\cos\Phi_{av} + \frac{\kappa_{av,w}}{\kappa_{av}}H_{demag}\frac{\sin 2\Phi_{av}}{2}\\
&- 4\kappa_{av}H_{DMI}\left[\sin\Phi_{av} - \tan X_{av}\cos\Phi_{av}\right]\\
&+ H_{exch}\left[2\Delta_{av}^2\left(g_{x,av}\sin\Phi_{av} - g_{y,av}\cos\Phi_{av}\right)\right]\\
&+ asymetric \quad terms
\end{aligned}
\tag{7.14}
$$

The magnetization angle of the DW will be evolve according to the following equation:

$$
\begin{aligned}
\frac{1+\alpha^2}{\gamma_0}\frac{\langle m_{ip}^2\frac{\partial\phi}{\partial t}\rangle}{\langle m_{ip}^2\rangle}(\mathbf{H}_{ext}, j_x) =& H_z + \frac{2}{\Delta_{av}}\frac{\beta-\alpha}{\gamma_0}u_x - \frac{\alpha}{\kappa_{av}}\left[H_x\sin\Phi_{av} - (H_y + H_R)\cos\Phi_{av}\right]\\
&+ \kappa_{av}H_{SHE}\cos\Phi_{av} - \alpha\frac{\kappa_{av,w}}{\kappa_{av}}H_{demag}\frac{\sin 2\Phi_{av}}{2}\\
&+ \alpha 4\kappa_{av}H_{DMI}\left[\sin\Phi_{av} - \tan X_{av}\cos\Phi_{av}\right]\\
&- \alpha H_{exch}\left[2\Delta_{av}^2\left(g_{x,av}\sin\Phi_{av} - g_{y,av}\cos\Phi_{av}\right)\right]\\
&+ asymetric \quad terms
\end{aligned}
\tag{7.15}
$$

with ϕ the local magnetization angle, the shape anisotropy field $H_{demag} = M_s(N_{eff,y} - N_{eff,x})$, the DMI-field $H_{DMI} = \frac{D}{\mu_0 M_s \Delta_{av}}$ and the exchange field $H_{exch} = \frac{A}{\mu_0 M_s \Delta_{av}^2}$. The asymmetric terms may be found in reference [3]; they do not have an equivalent term in the Lagrangian based models as symmetry of the ansatz and assumptions on the DW structure lead to their removal from the equation.

7.1.4 Analytical Comparison of the Models

The velocity equation from the semi-analytical collective coordinate model can be written as:

$$
\begin{aligned}
\frac{1+\alpha^2}{\gamma_0}\frac{2}{\Delta_{av}}v =& \alpha H_z + \frac{2}{\Delta_{av}}\frac{1+\alpha\beta}{\gamma_0}u_x + \alpha\kappa\left(H_{SHE,y}\cos\Phi_{av} - H_{SHE,x}\sin\Phi_{av}\right)\\
&+ \frac{1}{\kappa}\left[(H_x + H_{R,x})\sin\Phi_{av} - (H_y + H_{R,y})\cos\Phi_{av}\right]\\
&+ M_s(N_{eff,y} - N_{eff,x})\cos\Phi_{av}\sin\Phi_{av}\\
&- 2\kappa\frac{D}{\mu_0 M_s}\frac{2}{\Delta_{av}}\left[\sin\Phi_{av} - \tan X_{av}\cos\Phi_{av}\right]\\
&+ \frac{A}{\mu_0 M_s\frac{\Delta_{av}^2}{4}}\left[\frac{\Delta_{av}^2}{2}\left(g_x\sin\Phi_{av} - g_y\cos\Phi_{av}\right)\right]
\end{aligned}
\tag{7.16}
$$

which can be directly compared to the equation for q̇ in the collective coordinate models presented in Chapter 5:

$$
\begin{aligned}
\frac{(I_2 + \frac{I_1 I_4}{I_2}\alpha^2)}{\gamma_0}\frac{\cos\chi}{p_w\Delta}\dot{q} =& \alpha I_4 H_z + \frac{\cos\chi}{\Delta}\frac{1+\alpha\beta}{\gamma_0}u + \alpha\kappa_{SH}\left[H_{SL}u_{SOT,y}\cos\phi - H_{SL}u_{SOT,x}\sin\phi\right] \\
&+ \frac{1}{\kappa_{field}}\left[(H_x + H_{FL}u_{SOT,x})\sin\phi - (H_y + H_{FL}u_{SOT,y})\cos\phi\right] \\
&+ M_{\mathrm{s}}(N_y - N_x)\sin(\phi-\chi)\cos(\phi-\chi) \\
&- 2\kappa_{DMI}\frac{D}{\mu_0 M_{\mathrm{s}}}\frac{\sin(\phi-\chi)}{\Delta},
\end{aligned}
\tag{7.17}
$$

Similarly, the change in averaged magnetization angle in the semi-analytical model can be written as

$$
\begin{aligned}
\frac{1+\alpha^2}{\gamma_0}\frac{\langle m_{ip}^2\frac{\partial\phi}{\partial t}\rangle}{\langle m_{ip}^2\rangle}(\mathbf{H}_{ext}, j_x) =& H_z + \frac{2}{\Delta_{av}}\frac{\beta-\alpha}{\gamma_0}u_x + \kappa\left(H_{SHE,\,y}\cos\Phi_{av} - H_{SHE,\,x}\sin\Phi_{av}\right) \\
&- \alpha\frac{1}{\kappa}\left[(H_x + H_{R,\,x})\sin\Phi_{av} - (H_y + H_{R,\,y})\cos\Phi_{av}\right] \\
&- \alpha M_{\mathrm{s}}(N_{eff,y} - N_{eff,x})\cos\Phi_{av}\sin\Phi_{av} \\
&+ \alpha 2\kappa\frac{D}{\mu_0 M_{\mathrm{s}}}\frac{2}{\Delta_{av}}\left[\sin\Phi_{av} - \tan X_{av}\cos\Phi_{av}\right] \\
&- \alpha\frac{A}{\mu_0 M_{\mathrm{s}}\frac{\Delta_{av}^2}{4}}\left[\frac{\Delta_{av}^2}{2}\left(g_x\sin\Phi_{av} - g_y\cos\Phi_{av}\right)\right]
\end{aligned}
\tag{7.18}
$$

which could be compared to the analytical equations for the evolution of the DW magnetization angle

$$
\begin{aligned}
\frac{(1+\alpha^2)}{\gamma_0}\dot{\phi} =& H_z + H_{FL}u_{SOT,z} + \frac{\cos\chi}{\Delta}\frac{\beta-\alpha}{\gamma_0}u \\
&+ \kappa_{SH}\left[H_{SL}u_{SOT,y}\cos\phi - H_{SL}u_{SOT,x}\sin\phi\right] \\
&- \alpha\frac{1}{\kappa_{field}}\left[(H_x + H_{FL}u_{SOT,x})\sin\phi - (H_y + H_{FL}u_{SOT,y})\cos\phi\right] \\
&- \alpha M_{\mathrm{s}}(N_y - N_x)\sin(\phi-\chi)\cos(\phi-\chi) \\
&+ \alpha 2\kappa_{DMI}\frac{D}{\mu_0 M_{\mathrm{s}}}\frac{\sin(\phi-\chi)}{\Delta}
\end{aligned}
\tag{7.19}
$$

While both models include almost equivalent terms for each interaction, the semi-analytical model has additional terms relating to the exchange interaction (in Brown in Equations 7.16 and 7.18) which do not exist in the Lagrangian-based models. Further studies revealed the sum of these terms to be relatively small compared to the other terms.

Table 7.1 outlines the results of comparing the equations for velocity (or magnetization angle) in the two types of models. The comparison shows that, while the terms related to the Zeeman energy are identical, there are slight differences in the two descriptions in terms of magnetostatic terms. In fact, the magnetostatic terms suggest that the semi-analytical model takes into account the effect of changes in the DW plane by varying the demagnetizing factors, while the Lagrangian based model takes this change into account by including it as an additional tilt in the magnetization. The DMI terms in the two models, while at first sight not identical, can be connected based

on the definitions for DW width, magnetization angle and geometrical tilting angle in the semi-analytical model. On the other hand, κ in the semi-analytical model (with values close to 2/3 in micromagnetic simulations) is equivalent to three different constants in the Lagrangian-based model.

	semi-analytical	$q - \phi - \chi - \Delta$
general	$\frac{\Delta_{\text{av}}}{2}$	$\frac{\Delta}{\cos \chi}$
DMI/field/Rashba/SHE	Φ_{av}	ϕ
ms		$\phi - \chi$
DMI		$\kappa_{\text{DMI}} = \pi/4$
field/Rashba	κ	$\kappa_{\text{field}} = 2/\pi$
SHE		$\kappa_{\text{SH}} = \pi/2$
DMI	X_{av}	χ
ms	$N_{\text{eff,y}} - N_{\text{eff,x}}$	$N_y - N_x$
exch	$g_x \sin \Phi_{\text{av}} - g_y \cos \Phi_{\text{av}}$	0
general	$\frac{\langle m_{\text{ip}}^2 \frac{\partial \phi}{\partial t} \rangle}{\langle m_{\text{ip}}^2 \rangle}$	$\dot{\phi}$

Table 7.1: Equivalent collective coordinates and factors in the Lagrangian-based and semi-analytical models based on comparison of the velocity/DW magnetization angle equations.

7.2 Numerical Comparison

To quantitatively understand the correspondence between the coordinates defined in the two models, a case of field-driven DW motion was studied. Simulations were performed using the micromagnetic software package Mumax[3] [143] on a nanostrip with the following properties: $M_s = 1090 \times 10^3 \, \text{A/m}$, $A = 1 \times 10^{-11} \, \text{J/m}$, $K_u = 1.25 \times 10^6 \, \text{J/m}^3$ in the z-direction, $\alpha = 0.2$, $D = -0.7 \, \text{mJ/m}^2$, width = 100 nm, thickness = 0.6 nm and infinite length. Discretization cells with dimensions $\Delta x \times \Delta y \times \Delta z = 1.5625 \times 1.5625 \times 0.6 \, \text{nm}^3$ were used.

Figure 7.1 summarizes the results of comparing the collective coordinates. Previous studies have highlighted that both models are able to predict DW velocity accurately, as such DW velocity results were omitted. While the two models seem to predict almost similar magnetization angles (ϕ and Φ_{av}), their predictions of tilting (χ and X_{av}) differ. In spite of this, the two models predict $\phi - \chi$ accurately.

As depicted in Figure 4.2, the definition of the DW width also differs in the two models. While the Lagrangian-based models are in agreement with the Thiele definition [62], Δ_{av} seems to follow the same trend but at almost twice the value. Detailed analysis showed that $\frac{\Delta_{\text{av}}}{\Delta_{\text{TH}}} \sim [1.903, 1.912]$ while $\frac{\Delta_{\text{av}}}{\Delta} \sim [1.910, 1.960]$.

Observations:

1. The velocity calculated from the semi-analytical model is lower than that of the Thiele definition.

2. Note that the $q - \phi - \chi$ and $q - \phi$ models predict early Walker Breakdowns.

3. The Thiele definition for velocity works perfectly with the analytical models.

4. Largest error in predicting velocity is about 3% which is acceptable for an analytical model.

5. The semi-analytical and Lagrangian-based definitions of the tilting angle and ϕ seem to be almost the same (except at very high fields).

6. The Lagrangian-based models predict higher values of tilting. The analytical moels that include tilting predict ϕ within 10% accuracy. However, all analytical models fail when $\phi = 45$degrees.

7. The DW width defined in the semi-analytical model is between 1.9 and 1.91 times the Thiele DW width.

7.3   Conclusion

The analysis presented in this Chapter showed that similar models for DW motion can be derived using two different approaches, namely the Lagrangian approach based on an ansatz, and a method based on statistical averages of the LLG equation. Introducing the ansatz clearly assumes some symmetries which remove some assymetric terms from the LLG. Moreover, the semi-analytical approach showed that some small terms based on exchange are removed when the ansatz is introduced in the Lagrangian approach.
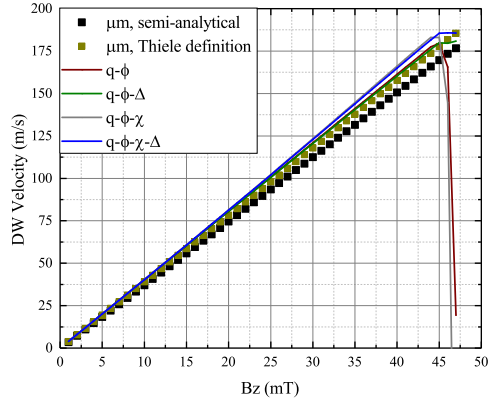
(a) DW velocity ($\dot{q}$).
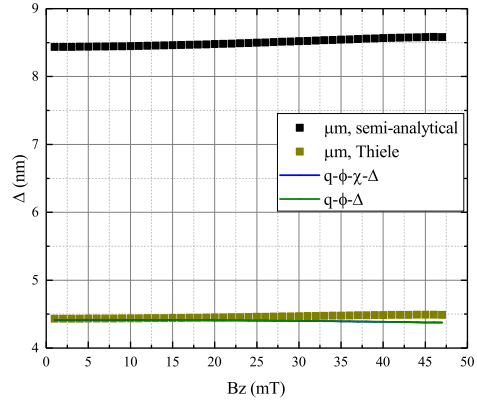
(b) DW width (Δ).
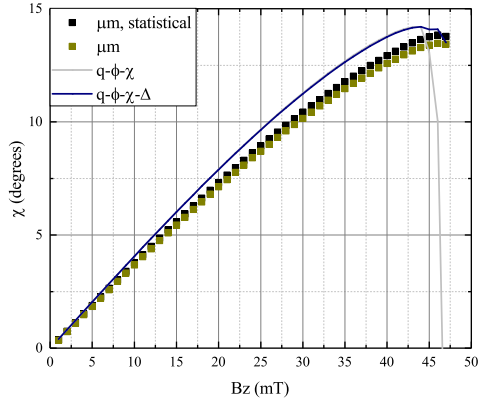
(c) DW tilting angle (χ).
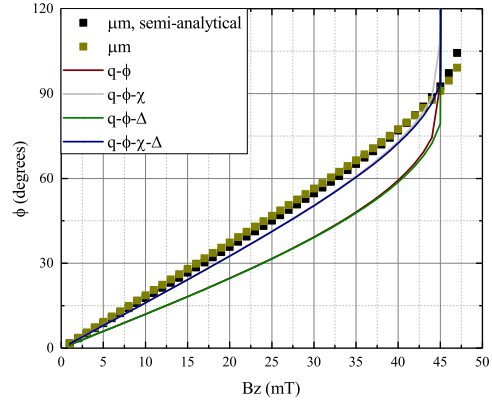
(d) DW magnetization angle (ϕ).
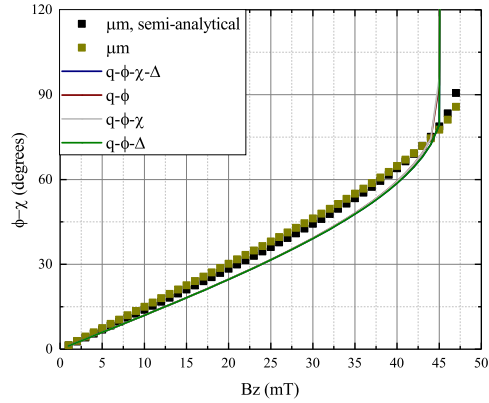
(e) $\phi - \chi$.

Figure 7.1: Comparison of the 1-D model predictions to micromagnetic simulations for field driven DW motion below Walker breakdown.

Chapter 8

Modeling Realistic Systems

Real devices differ from the ideal models presented in the previous Chapters. The working temperature of these devices is finite, as opposed to the T = 0 assumption of the LLG equation. In addition, the quality of material deposition can affect the performance of devices. In this Chapter, we comment on how these effects can be included in the models.

8.1   Pinning

The ability to control the motion of domain walls within a device is crucial to reaching the required levels of performance. As devices become smaller, the effects of material edges and the quality of material deposition become important in DW motion. These properties can lead to the pinning of magnetic domain walls. Pining of DWs can be used to control the location of data coded in the magnetic memories, while it can also affect switching of data bits in devices such as the MRAM.

Past studies on DW pinning in materials such as permalloy focused on pinning due to geometric constrictions. The strength of pinning was found to be related to the notch depth [165, 166] with minimal contributions from the notch shape [167–169] (although this is not the case in triangular notches [170, 171]). Square notches were found to be most suitable for transverse DWs [169]. The position of the notch was also a factor as the pinning strength at the notch is high when the spins in the wall oppose the direction of the magnetostatically determined spins around the notch showcasing a chirality dependence in the pinning potentials [27, 167, 171–175].Such studies found a pinning depth saturation effect when the notch size reaches 60-70% of the nanowire width or larger [167, 171] and a minimum depth of around 18% for pinning [165]. Studies on antinotches have suggested they might be more effective at pinning DWs [176]. A symmetric set of double notches was presented as the best technological solution [170]. The deppining for transverse DWs was characterized into three different categories [169] depending on notch size and geometry.

Other studies on permalloy have used the stray field from an external magnet or transverse fields as a means of pinning DWs [27, 177–179].

While study of notches in PMA is not common, one study found the pinned DW forms a circular arc when a field is applied before deppining [180], which was a feature we could reproduce in micromagnetic simulations as well. Bruno et al. analytically studied geometrically constrained magnetic DWs in such systems, proposing that such a configuration constitutes a new kind of DW, different from the Bloch and Néel walls [181]. Other features which may induce pinning include linear defects [93], structural defects [67, 68, 182, 183], and edge roughness [184–186].

102

8.1.1 Defects and Disorder in Micromagnetics

To model pinning arising from material property changes within the system due to imperfections in micromagnetic simulations, one can introduce grains in the material using 2D Voronoi tessellation [143, 164, 187]. This methods lets the user define regions within the material where material properties change, simulating grains with different material properties and is well accepted in the community. In Chapter 6, we presented some results from micromagnetic simulations on a bubble in which the effects of imperfections in the material were taken into account. When matching micromagnetic simulations to experimental results, the difficulty is determining the amount of material property changes from grain to grain to reproduce the experimental results.

Another way to model the effect of defects and disorder in the system is adding an additional damping term based on dry friction to the LLG equation of the form [67, 68]:

$$T_d = \zeta \vec{m} \times \frac{\dot{\vec{m}}}{|\dot{\vec{m}}|} \tag{8.1}$$

Where the phenomenological parameter ζ accounts for the average distribution of defects in the material and, for a nonhomogenous material, may be replaces by a tensor accounting for anisotropy.

8.1.2 Modeling Pinning in Collective Coordinate models

Previous attempts at characterizing pinning in collective coordinate models used a parabolic pinning potential of the following form in the equations [66, 141]:

$$V_{pin} = \begin{cases} -\frac{1}{2} K_N x^2 & \text{for} |x| \leq L_N \\ 0 & \text{for} |x| \geq L_N \end{cases} \tag{8.2}$$

Where x is the DW position, L_N denoted the spatial extension of the pinning potential, and K_N was the elastic constant of the pinning potential. This model was applied to pinning at notches where K_N was extracted from micromagnetic simulations.

By analogy with a mechanical oscillator, the DW in this approach is considered as a particle confined in a simple parabolic potential, the bottom of which is assumed to correspond to the physical center of the notch.Derivation of the collective coordinate models with this equation leads to an additional term linear with position in the equations for the evolution of q and ϕ.

8.1.3 Pinning due to Anisotropy Variation

Recent studies on magnetic domain wall motion have focused on the use ion irradiation to tailor material properties and modify DW motion by creating magnetic soft spots due to alloying effects [91–94]. This helps reduce pinning at areas of the material such as edges where the material growth is not perfect, and may also be used to create areas in the material to pin the DW.

In one such study, irradiation by He^+ ions reduced uniaxial anisotropy to 1/3 its original value, reducing saturation magnetization up to 30% and increasing the depinning field more than two fold [94]. These studies have revealed that the determining factors in DW pinning are the width of the nanowire and the irradiation fluence [92, 94].

We performed micromagnetic simulations to recreate these effects. A Pt/CoFe/MgO nanowire with dimensions $2.8\mu m \times 160nm \times 0.6nm$ was simulated with the uniaxial anisotropy changing 5, 10, 15 and 20 percent in it at 10, 20, 40, and 80 nm intervals. Figure 8.1 shows the results of anisotropy variation in the case of field driven DW motion. Micromagnetic simulations reveal a pinning effect due to the change in anisotropy, which is mildly effected by the size of the regions with fixed anisotropy. The mobility curves from micromagnetics make sense, taking into account

that the DW width calculated from simulations with anisotropy variation is 3 to 4 times that of no anisotropy variation. The full collective coordinate model based on four coordinates fails to reproduce the results. Further investigation in the micromagnetic simulations revealed a lack of tilting. However, the $q - \phi - \Delta$ model which does not include the tilting degree of freedom still fails to reproduce the micromagnetic results as well. In both cases, collective coordinate models predict faster DW motion likely due to inability to predict the increase in DW width.
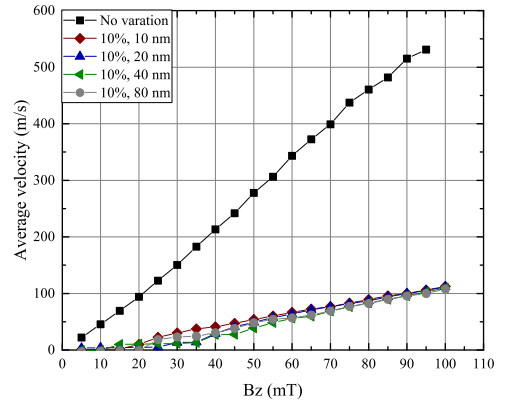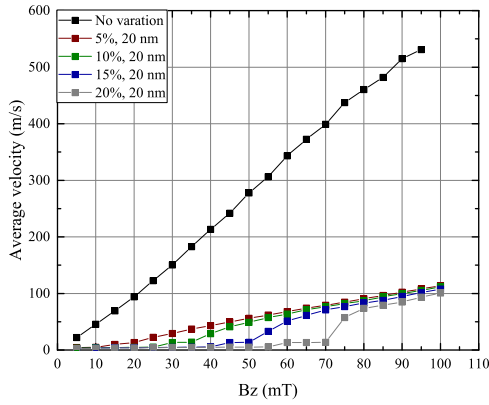
(a) Micromagnetic simulations for different anisotropy varia-tions.

(b) Micromagnetic simulations for different variation region sizes.
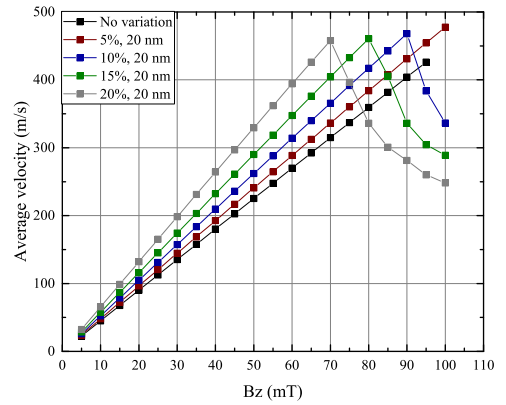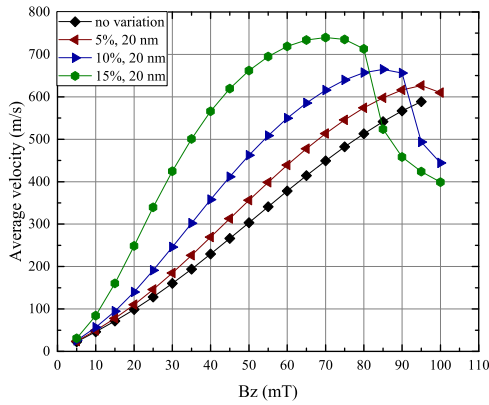
(c) Predictions of the $q - \phi - \chi - \Delta$ model.

(d) Predictions of the $q - \phi - \Delta$ model.

—

Figure 8.1: Effect of anisotropy variation on field driven DW motion.

After the initial study of adding anisotropy variation directly to the equations, we rederived

the equations, assuming anisotropy varies with the DW position.

$$\alpha \frac{\dot{q}}{\Delta} \cos \chi + \dot{\phi} = \mu_0 \gamma \left(H_z - \frac{\pi}{2} H_{SL} \left[\sin \phi u_{SOT,x} - \cos \phi u_{SOT,y} \right] \right) + \beta \frac{u}{\Delta} \cos \chi - K_{var} \frac{\gamma \Delta}{M_s \cos \chi} \quad (8.3)$$

$$\frac{\dot{q}}{\Delta} \cos \chi - \alpha \dot{\phi} = \frac{1}{2} \mu_0 \gamma M_s \left(N_y - N_x \right) \sin 2(\phi - \chi) - \frac{\pi}{2} \frac{\gamma D}{M_s \Delta} \sin(\phi - \chi)$$
$$+ \frac{u}{\Delta} \cos \chi + \frac{\pi}{2} \mu_0 \gamma \left[H_x \sin \phi - H_y \cos \phi \right] + \mu_0 \gamma H_{SL} u_{SOT,z} \quad (8.4)$$

$$\frac{\pi^2}{12} \alpha \left[\frac{\dot{\Delta}}{\Delta} + \frac{\dot{\chi}}{\cos \chi} \sin \chi \right] =$$
$$\frac{\gamma}{M_s} \left[\frac{A}{\Delta^2} - K_{eff} - \frac{\mu_0 M_s^2}{2} \left[N_x \cos^2 (\phi - \chi) + N_y \sin^2 (\phi - \chi) - N_z \right] \right]$$
$$+ \frac{\pi}{2} \mu_0 \gamma \left(H_x \cos \phi + H_y \sin \phi \right) \quad (8.5)$$

$$- \alpha \frac{\pi^2}{12} \left[\frac{\dot{\Delta}}{\Delta} \sin \chi + \frac{\dot{\chi}}{\cos \chi} \left[\left(\frac{w}{\pi \Delta} \right)^2 + \sin^2 \chi \right] \right] = \frac{\gamma}{M_s} \sin \chi \left[\frac{A}{\Delta^2} \right.$$
$$+ \left(K_{eff} + \frac{\mu_0 M_s^2}{2} \left[N_x \cos^2 (\phi - \chi) + N_y \sin^2 (\phi - \chi) - N_z \right] \right) \right]$$
$$+ \frac{1}{2} \gamma \mu_0 M_s \cos \chi (N_x - N_y) \sin 2 (\phi - \chi)$$
$$+ \frac{\pi}{2} \frac{\gamma D}{M_s \Delta} \sin \phi - \frac{\pi}{2} \mu_0 \gamma \left(H_x \cos \phi + H_y \sin \phi \right) sin\chi \quad (8.6)$$

In the above $K_{eff}(q) = (1 + \eta(q))K_u$ where $\eta(q)$ is a random variation defined for each region along the nanowire and K_{var} is defined as:

$$K_{var} = \frac{dK_{eff}}{dq} = \begin{cases} \frac{\eta K_u}{\Delta q}, & \text{if passed into new region} \\ 0, & \text{if in old region} \end{cases} \quad (8.7)$$

However, this model failed to reproduce the micromagnetic results as well.

8.2   Finite Temperature Effects

The LLG equation is valid only at zero temperature; however, real systems work at finite temperature. Thermal fluctuations can induce changes in DW motion, making it stochastic. More importantly, thermal fluctuations may depin a DW from a pinning point. Changes in temperature may also lead to changes in saturation magnetization. As such, it is important to include these effects in models, specially when low excitations are used to manipulate the DW. Thermal effects on DW motion have been investigated in PMA material [66, 188] and in permalloy [141, 189, 190].

The first attempts to include thermal fluctuations in the LLG equation were those of Brown, where he applies fluctuations in the effective field (modeled using a random white noise thermal

field) to single domain particles [191, 192]. Both the Fokker Planck equation and fluctuation-dissipation theorem may be used in this context to derive the right terms to be included in the stochastic form of the LLG. Brown's method is still the method used to date to include thermal effects in micromagnetics.

Fan et al. studied the effect of finite temperature on DW motion [193]. The results showed that the velocity of the DW is almost independent of temperature until the Walker breakdown. They also showed that the thermal field can suppress Walker breakdown and makes domain wall move faster.

Another important effect when currents are used is Joule heating, which can have additional consequences for DW motion [194]. While initial studies postulated that this effect is negligible, recent studies have confirmed that such high temperatures could be reached that the magnetic order is lost [195].

8.2.1 Stochastic LLG

Thermal fluctuations have traditionally been added to the LLG as a thermal field in the effective field [141, 191, 192] . This field had a Guassian distribution with zero mean value and uncorrelated in time and space [65]:

$$
\begin{aligned}
&< H_{th,i}(\vec{r}, t) >= 0 \\
&< H_{th,i}(\vec{r}, t) H_{th,j}(\vec{r\prime}, t\prime) >= 2D_{\mu m}\delta_{ij}\delta(\vec{r} - \vec{r\prime})\delta(t - t\prime)
\end{aligned}
\tag{8.8}
$$

Where $D_{\mu m}$ characterizes the strength of the fluctuation and may be calculated from the fluctuation dissipation function as:

$$
D_{\mu m} = \frac{\alpha K_B T}{\mu_0 \gamma_0 M_s \Delta x^3}
\tag{8.9}
$$

Where Δx is the cell size, K_B is the Boltzman constant and T is the temperature. Note that this formulation assumes that the saturation magnetization is unaffected by the temperature, which is valid at temperatures much lower than the Curie temperature. This method is already included in simulation tools such as Mumax [143].

8.2.2 Stochastic Collective Coordinate Models

The effect of the above thermal fluctuations has been introduced in the 1-D model as a thermal force [65] or a field of the following form [66]:

$$
\begin{aligned}
&< H_{th}(t) >= 0 \\
&< h_{th}(t) H_{th}(t') >= 2D_{an}\delta(t - t')
\end{aligned}
\tag{8.10}
$$

Where D_{an} characterizes the strength of the fluctuation and may be calculated from the fluctuation dissipation function as:

$$
D_{an} = \sqrt{\frac{\alpha K_B T}{\mu_0 \gamma_0 M_s V_{DW}}}
\tag{8.11}
$$

Where $V_{DW} = \Delta Lw$ is the DW volume, K_B is the Boltzman constant and T is the temperature. Note that this formulation assumes that the saturation magnetization is unaffected by the temperature, which is valid at temperatures much lower than the Curie temperature.

8.2.3   The LLB Equation

When high temperature closer to the Curie temperature are reached, the assumption of a fixed saturation magnetization is no longer valid. In such cases, the effects of enhanced damping and the change in saturation magnetization need to be taken into account [196]. Such a model should include both transverse and longitudinal relaxation terms and interpolate between the Landau-Lifshitz equation at low temperatures and the Bloch equation at high temperatures [197].

Torrey introduced diffusive terms in the LL equation to take into account the relaxation of magnetization LLB with diffusive terms [198]:

$$\frac{d\vec{M}}{dt} = -\gamma \vec{M} \times \vec{H}_{eff} - \frac{\vec{M}}{T_2} + \chi_0 \frac{\vec{H}_{eff}}{T_1} + \frac{\vec{M} \cdot \vec{H}_{eff} \vec{H}_{eff}}{H_{eff}^2}[\frac{1}{T_2} - \frac{1}{T_1}] + \nabla \cdot \nabla(\vec{M} - \vec{M}_0) \quad (8.12)$$

In case spin-exchange diffusion is not negligible, an additional term $\nabla \cdot \nabla(\tilde{M} - \tilde{M}_0) \cdot \tilde{H}_{eff} \tilde{H}_{eff}/H_{eff}^2$ needs to be added to the right side of the above equation.

One stochastic form of the LLB equation reads [199]:

$$\dot{m} = \gamma(\mathbf{m} \times (\mathbf{H_{eff}} + \zeta)) + \frac{\gamma \alpha_\parallel}{m^2}(\mathbf{m} \cdot (\mathbf{H_{eff}} + \zeta_\parallel))\mathbf{m} - \frac{\gamma \alpha_\perp}{m^2}\mathbf{m} \times (\mathbf{m} \times (\mathbf{H_{eff}} + \zeta_\perp)) \quad (8.13)$$

where $\mathbf{m} = \mathbf{M}/\mathrm{M_s(T)}$ and $\alpha_\parallel$ and $\alpha_\perp$ are dimensionless longitudinal and transverse damping coefficients. The stochastic fields in the LLB-Langevin equation above can be, in fact, introduced in many different ways.

$$\alpha_\parallel = \lambda \frac{2T}{3T_c}, \alpha_\perp = \lambda(1 - \frac{T}{3T_c}) for T < T_c \quad (8.14)$$

For $T > T_c$, $\alpha_\parallel = \alpha_\perp$. Here λ is the parameter describing the coupling of the spins to the heat bath on an atomistic level.

Perpendicular and longitudinal noise parameters have the following properties:

$$< \zeta^\mu >= 0$$
$$< \zeta_i^\mu(0)\zeta_j^\nu(t) >= \frac{2K_BT}{\gamma M_s^0 V \alpha_\mu}\delta_{ij}\delta\mu\nu\delta(t) \quad (8.15)$$

where $\mu, \nu = \parallel, \perp$, i and j denote x,y,z components and V is the particle volume.

Evans et al. proposed another stochastic form for the LLB equations [200], claiming it to be more proper than that proposed in [199] as it is consistent with the Boltzmann distribution at high temperatures. This equation has the form [200]:

$$\dot{m} = \gamma(\mathbf{m} \times \mathbf{H_eff}) + \frac{\gamma \alpha_\parallel}{m^2}(\mathbf{m} \cdot \mathbf{H_eff})\mathbf{m} - \frac{\gamma \alpha_\perp}{m^2}\mathbf{m} \times (\mathbf{m} \times (\mathbf{H_eff} + \eta_\perp)) + \eta_\parallel \quad (8.16)$$

$$< \eta^\mu >= 0$$
$$< \eta_i^\perp(0)\eta_j^\perp(t) >= \frac{2K_BT(\alpha_\perp - \alpha_\parallel)}{\gamma M_s^0 V \alpha_\perp^2}\delta_{ij}\delta(t)$$
$$< \eta_i^\parallel(0)\eta_j^\parallel(t) >= \frac{2K_BT\alpha_\parallel}{M_s^0 V}\delta_{ij}\delta(t) \quad (8.17)$$
$$< \eta_i^\parallel \eta_j^\perp >= 0$$

8.3   Conclusion

Pinning and temperature are rather important factors specially when low excitations are concerned. These effects can be studied using modified forms of the LLG equations as presented here, and are already available in micromagnetic codes. There are methods for including these effects in collective coordinate models; however, these methods will need further study and require extension to the four coordinate model.

Chapter 9

Conclusion and Future Work

This dissertation was initiated as part of the ITN-WALL project, with the aim of improving collective coordinate models for magnetic domain wall motion. In this Chapter, a summary of the main finding are provided, along with areas where improvements are needed.

9.1 Summary of Findings

This report summarized a study on the motion of magnetic domain walls in perpendicular magnetic anisotropy (PMA) materials with DMI using collective coordinate models developed using a Lagrangian approach. Specifically, we showed:

- Magnetic domain walls can be of Bloch, Néel or intermediate structure depending on the strength of the different interactions involved. While intermediate structures in between Bloch and Néel are not predicted using analytical models for systems without DMI, they were observed in micromagnetic simulations.

- The profile describing the change in the out-of-plane component of magnetization changes under in-plane fields. While the Bloch profile (Equations 3.4 and 3.9) is valid for systems with or without DMI, in systems under in-plane field a canted profile (Equation 3.18) should be used.

- The collective behavior of the domain wall may be characterized by four collective coordinates (position q, magnetization angle ϕ, tilting χ and domain wall width parameter Δ). Using an Euler Largrange equation the $q - \phi$, $q - \phi - \Delta$, $q - \phi - \chi$, and $q - \phi - \chi - \Delta$ models were derived based on the Bloch profile and compared to micromagnetic simulations.

- Models based on the Bloch profile cannot reproduce micromagnetic results of DW motion under in-plane fields for systems with high DMI and low anisotropy. In these systems canting plays an important role. We developed models based on canted profile (Equation 3.18) which better reproduce the micromagnetics. This shows that canting and the profile play a more important role in these models. We also functional form of the equations in terms of collective coordinates is unaffected by the profile used, and the profiles only affect prefactors in the equations.

- Several features of DW motion under in-plane fields in nanowires may be used to measure specific material properties. Critical points include a point of zero velocity under longitudinal fields for current driven DW motion, and a point of zero tilting under transverse fields. Closed

form equations were presented to describe the dynamics of these critical points. We also observed the formation of vertical Bloch lines in systems with low DMI and high anisotropy.

- The collective coordinate models were extended to magnetic bubbles. These models for bubbles may be used in the measurement of DMI using bubble expansion experiments. We showed that some of the assumptions of bubble expansion experiments are only valid at very low drive fields.

9.2 Future Work

While the models developed in this work helped improve accuracy of previous models, and shed light on the importance of canting in the domains, they had inherently complex equations. Simplification of these equations can help with the dissemination and use of these equations by experimental groups.

Additionally, there is much more work that could be done in including the effects of pinning and thermal fluctuations in the models. Models for magnetic bubbles which took into account the elliptical shape of the bubble were unsuccessfully attempted and could be an additional topic of study.

Some of the equations presented in this work presented potential for measurement of specific material properties. Experimental verification of these methods is the next step in verifying the applicability of the equations presented.

Finally, close form equations can be useful for the design of devices. While our current equations can be used to develop conceptual understanding, additional aspects of performance of real devices could be integrated in them to lead to more application focused models.

Bibliography

[1] S. A. Nasseri, E. Martinez, G. Durin, Collective coordinate descriptions of magnetic domain wall motion in perpendicularly magnetized nanostructures under the application of in-plane fields, ArXiv e-prints `arXiv:1804.00569`.

[2] B. Sarma, S. A. Nasseri, A. Casiraghi, F. Garcia-Sanchez, G. Durin, Dynamics and morphology of chiral magnetic bubbles in perpendicularly magnetized ultra-thin films, Journal of Magnetism and Magnetic Materials `doi:10.1016/j.jmmm.2018.01.075`.

[3] J. Vandermeulen, S. A. Nasseri, B. V. de Wiele, G. Durin, B. V. Waeyenberge, L. Dupre, Comparison between collective coordinate models for domain wall motion in PMA nanostrips in the presence of the Dzyaloshinskii-Moriya interaction, Journal of Magnetism and Magnetic Materials 449 (2018) 337 – 352. `doi:10.1016/j.jmmm.2017.10.008`.

[4] S. A. Nasseri, S. Moretti, E. Martinez, C. Serpico, G. Durin, Collective coordinate models of domain wall motion in perpendicularly magnetized systems under the spin Hall effect and longitudinal fields, Journal of Magnetism and Magnetic Materials 426 (2017) 195 – 201. `doi:10.1016/j.jmmm.2016.11.081`.

[5] J. Vandermeulen, S. A. Nasseri, B. V. de Wiele, G. Durin, B. V. Waeyenberge, L. Dupre, The effect of Dzyaloshinskii-Moriya interaction on field-driven domain wall dynamics analysed by a semi-analytical approach, Journal of Physics D: Applied Physics 49 (465003). `doi:10.1088/0022-3727/49/46/465003`.

[6] S. A. Nasseri, B. Sarma, G. Durin, C. Serpico, Analytical modelling of magnetic DW motion, Physics Procedia 75 (2015) 974 – 985, (Proceedings of the 20th International Conference on Magnetism - ICM 2015). `doi:10.1016/j.phpro.2015.12.133`.

[7] S. A. Nasseri, E. Martinez, G. Durin, Effect of canting on magnetic domain wall motion, in: IEEE International Magnetics Conference (INTERMAG), Dublin, 2017. `doi:10.1109/INTMAG.2017.8007942`.

[8] S. A. Nasseri, S. Moretti, E. Martinez, G. Durin, C. Serpico, Analytical modeling of domain wall dynamics in PMA materials under spin Hall effect and in-plane fields, in: 1st IEEE Conference Advances in Magnetics (AIM), Bormio, 2016.

[9] S. Bader, S. Parkin, Spintronics, Annual Review of Condensed Matter Physics 1 (1) (2010) 71–88. `doi:10.1146/annurev-conmatphys-070909-104123`.

[10] C. H. Marrows, B. J. Hickey, New directions in spintronics, Philosophical Transactions of the Royal Society A 369 (1948) (2011) 3027–3036. `doi:10.1098/rsta.2011.0156`.

[11] I. Žutić; J. Fabian; S. Das Sarma, Spintronics: Fundamentals and applications, Reviews of Modern Physics 76 (2004) 323–410. `doi:10.1103/RevModPhys.76.323`.

[12] J. Åkerman, Toward a universal memory, Science 308 (5721) (2005) 508–510. `doi:10.1126/science.1110549`.

[13] H. Zabel, Progress in spintronics, Superlattices and Microstructures 46 (4) (2009) 541–553. `doi:10.1016/j.spmi.2009.07.008`.

[14] H. Ohno, A window on the future of spintronics, Nature Materials 9 (2010) 952–954. `doi:10.1038/nmat2913`.

[15] G. Hrkac, J. Dean, D. A. Allwood, Nanowire spintronics for storage class memories and logic, Philosophical Transactions of the Royal Society A 369 (1948) (2011) 3214–3228. `doi: 10.1098/rsta.2011.0138`.

[16] G. Catalan, J. Seidel, R. Ramesh, J. F. Scott, Domain wall nanoelectronics, Reviews of Modern Physics 84 (2012) 119–156. `doi:10.1103/RevModPhys.84.119`.

[17] R. L. Stamps, S. Breitkreutz, J. Akerman, A. V. Chumak, Y. Otani, G. E. W. Bauer, J. U. Thiele, M. Bowen, S. A. Majetich, M. Kläui, I. L. Prejbeanu, B. Dieny, N. M. Dempsey, B. Hillebrands, The 2014 magnetism roadmap, Journal of Physics D: Applied Physics 47 (333001). `doi:10.1088/0022-3727/47/33/333001`.

[18] S. Urazhdin, V. E. Demidov, H. Ulrichs, T. Kendziorczyk, T. Kuhn, J. Leuthold, G. Wilde, S. O. Demokritov, Nanomagnonic devices based on the spin-transfer torque, Nature Nanotechnology 9 (2014) 509–513. `doi:10.1038/nnano.2014.88`.

[19] A. Hirohata, K. Takanashi, Future perspectives for spintronic devices, Journal of Physics D: Applied Physics 47 (193001). `doi:10.1088/0022-3727/47/19/193001`.

[20] A. V. Chumak, V. I. Vasyuchka, A. A. Serga, B. Hillebrands, Magnon spintronics, Nature Physics 11 (2015) 453–461. `doi:10.1038/nphys3347`.

[21] D. A. Allwood, G. Xiong, M. D. Cooke, C. C. Faulkner, D. Atkinson, N. Vernier, R. P. Cowburn, Submicrometer ferromagnetic NOT gate and shift register, Science 296 (5575) (2002) 2003–2006. `doi:10.1126/science.1070595`.

[22] D. A. Allwood, G. Xiong, C. C. Faulkner, D. Atkinson, D. Petit, R. P. Cowburn, Magnetic domain-wall logic, Science 309 (5741) (2005) 1688–1692. `doi:10.1126/science.1108813`.

[23] J. Jaworowicz, N. Vernier, J. Ferre, A. Maziewski, D. Stanescu, D. Ravelosona, A. S. Jacqueline, C. Chappert, B. Rodmacq, B. Dieny, Magnetic logic using nanowires with perpendicular anisotropy, Nanotechnology 20 (215401). `doi:10.1088/0957-4484/20/21/215401`.

[24] L. Thomas, M. Hayashi, R. Moriya, C. Rettner, S. Parkin, Topological repulsion between domain walls in magnetic nanowires leading to the formation of bound states, Nature Communications 3 (810). `doi:10.1038/ncomms1808`.

[25] J. A. Currivan-Incorvia, S. Siddiqui, S. Dutta, E. R. Evarts, J. Zhang, D. Bono, C. A. Ross, M. A. Baldo, Logic circuit prototypes for three-terminal magnetic tunnel junctions with mobile domain walls, Nature Communications 7 (10275). `doi:10.1038/ncomms10275`.

[26] C. Chappert, A. Fert, F. N. Van Dau, The emergence of spin electronics in data storage, Nature Materials 6 (11) (2007) 813–823. `doi:10.1038/nmat2024`.

[27] D. Atkinson, D. S. Eastwood, L. K. Bogart, Controlling domain wall pinning in planar nanowires by selecting domain wall type and its application in a memory concept, Applied Physics Letters 92 (022510). `doi:10.1063/1.2832771`.

[28] S. P. Parkin, M. Hayashi, L. Thomas, Magnetic domain-wall racetrack memory, Science 320 (5873) (2008) 190–194. `doi:10.1126/science.1145799`.

[29] S. Parkin, S. H. Yang, Memory on the racetrack, Nature Nanotechnology 10 (2015) 195–198. `doi:10.1038/nnano.2015.41`.

[30] J. A. King, D. S. Eastwood, L. K. Bogart, H. Armstrong, M. Bath, D. Atkinson, ChiralMEM: a novel concept for high density magnetic memory technology, in: Nanotech Conference and Expo 2009, 2009.

[31] W. S. Zhao, J. Duval, D. Ravelosona, J. O. Klein, J. V. Kim, C. Chappert, A compact model of domain wall propagation for logic and memory design, Journal of Applied Physics 109 (07D501). `doi:10.1063/1.3536793`.

[32] J. H. Franken, H. J. M. Swagten, B. Koopmans, Shift registers based on magnetic domain wall ratchets with perpendicular anisotropy, Nature Nanotechnology 7 (2012) 499–503. `doi: 10.1038/nnano.2012.111`.

[33] R. Lavrijsen, J. H. Lee, A. Fernandez-Pacheco, D. C. M. C. Petit, R. Mansell, R. P. Cowburn,

Magnetic ratchet for three-dimensional spintronic memory and logic, Nature 493 (2013) 647–650. `doi:10.1038/nature11733`.

[34] K. W. Moon, D. H. Kim, S. C. Yoo, S. G. Je, B. S. Chun, W. Kim, B. C. Min, C. Hwang, S. B. Choe, Magnetic bubblecade memory based on chiral domain walls, Scientific Reports 5 (9166). `doi:10.1038/srep09166`.

[35] J. Katine, E. E. Fullerton, Device implications of spin-transfer torques, Journal of Magnetism and Magnetic Materials 320 (2008) 1217–1226. `doi:10.1016/j.jmmm.2007.12.013`.

[36] How to substantially reduce encoder cost while gaining functionality with multi-turn rotary position sensors, White Paper.
URL `http://www.novotechnik.com/pdfs/MultiturnWhitePaperV4.pdf`

[37] M. N. Baibich, J. M. Broto, A. Fert, F. N. Van Dau, F. Petroff, P. Etienne, G. Creuzet, A. Friederich, J. Chazelas, Giant magnetoresistance of (001)Fe/(001)Cr magnetic superlattices, Physical Review Letters 61 (1988) 2472–2475. `doi:10.1103/PhysRevLett.61.2472`.

[38] G. Binasch, P. Grünberg, F. Saurenbach, W. Zinn, Enhanced magnetoresistance in layered magnetic structures with antiferromagnetic interlayer exchange, Physical Review B 39 (1989) 4828–4830. `doi:10.1103/PhysRevB.39.4828`.

[39] R. P. Cowburn, The future of universal memory, Materials Today 6 (7) (2003) 32–38. `doi:10.1016/S1369-7021(03)00730-2`.

[40] W. N. Papian, The MIT magnetic-core memory, in: Papers and Discussions Presented at the Dec. 8-10, 1953, Eastern Joint AIEE-IRE Computer Conference: Information Processing Systems-reliability and Requirements, AIEE-IRE '53 (Eastern), ACM, New York, NY, USA, 1953, pp. 37–42. `doi:10.1145/1434878.1434888`.

[41] J. A. Rajchman, A myriabit magnetic-core matrix memory, Proceedings of the IRE 41 (10) (1953) 1407–1421. `doi:10.1109/JRPROC.1953.274317`.

[42] P. Kuttner, The rope memory: A permanent storage device, in: Proceedings of the November 12-14, 1963, Fall Joint Computer Conference, AFIPS '63 (Fall), ACM, 1963, pp. 45–57. `doi:10.1145/1463822.1463829`.

[43] A. H. Bobeck, P. I. Bonyhard, J. E. Geusic, Magnetic bubbles: An emerging new memory technology, Proceedings of the IEEE 63 (8) (1975) 1176–1195. `doi:10.1109/PROC.1975.9912`.

[44] A. H. Bobeck, Magnetic bubble memory (7 1979).

[45] A. D. West, K. J. Weatherill, T. J. Hayward, P. W. Fry, T. Schrefl, M. R. J. Gibbs, C. Adams, D. A. Allwood, I. G. Hughes, Realization of the manipulation of ultracold atoms with a reconfigurable nanomagnetic system of domain walls, Nano Letters 12 (8) (2012) 4065–4069. `doi:10.1021/nl301491m`.

[46] M. T. Bryan, J. Dean, T. Schrefl, F. E. Thompson, J. Haycock, D. A. Allwood, The effect of trapping superparamagnetic beads on domain wall motion, Applied Physics Letters 96 (192503). `doi:10.1063/1.3428775`.

[47] A. Ehresmann, D. Lengemann, T. Weis, A. Albrecht, J. Langfahl-Klabes, F. Göllner, D. Engel, Asymmetric magnetization reversal of stripe-patterned exchange bias layer systems for controlled magnetic particle transport, Advanced Materials 23 (46) (2011) 5568–5573. `doi:10.1002/adma.201103264`.

[48] E. Rapoport, G. S. D. Beach, Dynamics of superparamagnetic microbead transport along magnetic nanotracks by magnetic domain walls, Applied Physics Letters 100 (082401). `doi:10.1063/1.3684972`.

[49] J. Grollier, D. Querlioz, M. D. Stiles, Spintronic nanodevices for bioinspired computing, Proceedings of the IEEE 104 (10) (2016) 2024–2039. `doi:10.1109/JPROC.2016.2597152`.

[50] M. I. Dyakonov, Spin Hall effect, ArXiv e-prints`arXiv:1210.3200`.

[51] J. Ferré, P. J. Metaxas, A. Mougin, J.-P. Jamet, J. Gorchon, V. Jeudy, Universal magnetic domain wall dynamics in the presence of weak disorder, Comptes Rendus Physique 14 (2013)

651–666. `doi:10.1016/j.crhy.2013.08.001`.

[52] S. Emori, G. S. D. Beach, Roles of the magnetic field and electric current in thermally activated domain wall motion in a submicrometer magnetic strip with perpendicular magnetic anisotropy, Journal of Physics: Condensed Matter 24 (024214). `doi:10.1088/0953-8984/24/2/024214`.

[53] N. L. Schryer, L. R. Walker, The motion of 180º domain walls in uniform dc magnetic fields, Journal of Applied Physics 45 (1974) 5406–5421. `doi:10.1063/1.1663252`.

[54] J. C. Slonczewski, Dynamics of magnetic domains, AIP Conference Proceedings 5 (1972) 170–174. `doi:10.1063/1.3699416`.

[55] A. P. Malozemoff, J. C. Slonczewski, Magnetic Domain Walls in Bubble Materials, Academic Press, 1979. `doi:10.1016/C2013-0-06998-8`.

[56] A. A. Thiele, Steady-state motion of magnetic domains, Physical Review Letters 30 (1973) 230–233. `doi:10.1103/PhysRevLett.30.230`.

[57] A. A. Thiele, F. B. Hagedorn, G. P. Vella-Coleiro, Dynamic spin configuration for hard magnetic bubbles in translational motion, Physical Review B 8 (1973) 241–245. `doi:10.1103/PhysRevB.8.241`.

[58] V. L. Sobolev, S. C. Chen, H. L. Huang, Equations of domain wall motion in ferromagnetic medium with q > 1, IEEE Transactions on Magnetics 29 (1993) 2542–2544. `doi:10.1109/20.280960`.

[59] V. L. Sobolev, H. L. Huang, S. C. Chen, Generalized equations for domain wall dynamics, Journal of Applied Physics 75 (1994) 5797–5799. `doi:10.1063/1.355566`.

[60] V. L. Sobolev, H. L. Huang, S. C. Chen, Domain wall dynamics in the presence of an external magnetic field normal to the anisotropy axis, Journal of Magnetism and Magnetic Materials 147 (1995) 284–298. `doi:10.1016/0304-8853(95)00065-8`.

[61] V. L. Sobolev, H. L. Huang, New equations for the domain wall dynamics, Journal of Magnetism and Magnetic Materials 140-144 (1995) 1849–1850. `doi:10.1016/0304-8853(94)01602-x`.

[62] A. Thiaville, Y. Nakatani, Spin Dynamics in Confined Magnetic Structures III, Vol. Volume 101/2006 of Topics in Applied Physics, Springer, 2006, Ch. Domain-Wall Dynamics in Nanowires and Nanostrips, pp. 161–205. `doi:10.1007/10938171_5`.

[63] A. Thiaville, Y. Nakatani, J. Miltat, N. Vernier, Domain wall motion by spin-polarized current: a micromagnetic study, Journal of Applied Physics 95 (2004) 7049–7051. `doi:10.1063/1.1667804`.

[64] A. Thiaville, Y. Nakatani, J. Miltat, Y. Suzuki, Micromagnetic understanding of current-driven domain wall motion in patterned nanowires, Europhysics Letters 69 (2005) 990–996. `doi:10.1209/epl/i2004-10452-6`.

[65] E. Martinez, L. Lopez-Diaz, L. Torres, C. Tristan, O. Alejos, Thermal effects in domain wall motion: Micromagnetic simulations and analytical model, Physical Review B 75 (174409). `doi:10.1103/PhysRevB.75.174409`.

[66] E. Martinez, L. Lopez-Diaz, O. Alejos, L. Torres, Thermally activated domain wall depinning in thin strips with high perpendicular magnetocrystalline anisotropy, Journal of Applied Physics 106 (043914). `doi:10.1063/1.3204496`.

[67] G. Consolo, E. Martinez, The effect of dry friction on domain wall dynamics: A micromagnetic study, Journal of Applied Physics 111 (07D312). `doi:10.1063/1.3679007`.

[68] G. Consolo, C. Currò, E. Martinez, G. Valenti, Mathematical modeling and numerical simulation of domain wall motion in magnetic nanostrips with crystallographic defects, Applied Mathematical Modelling 36 (2012) 4876–4886. `doi:10.1016/j.apm.2011.12.024`.

[69] M. Bode, M. Heide, K. von Bergmann, P. Ferriani, S. Heinze, G. Bihlmayer, A. Kubetzka, O. Pietzsch, S. Blügel, R. Wiesendanger, Chiral magnetic order at surfaces driven by inversion asymmetry, Nature 447 (2007) 190–193. `doi:10.1038/nature05802`.

[70] E. Y. Vedmedenko, L. Udvardi, P. Weinberger, R. Wiesendanger, Chiral magnetic ordering in two-dimensional ferromagnets with competing Dzyaloshinsky-Moriya interactions, Physical Review B 75 (104431). `doi:10.1103/PhysRevB.75.104431`.

[71] M. Heide, G. Bihlmayer, S. Blügel, Dzyaloshinskii-Moriya interaction accounting for the orientation of magnetic domains in ultrathin films: Fe/W(110), Physical Review B 78 (140403). `doi:10.1103/PhysRevB.78.140403`.

[72] I. Dzyaloshinsky, A thermodynamic theory of "weak" ferromagnetism of antiferromagnetics, Journal of Physics and Chemistry of Solids 4 (1958) 241–255. `doi:10.1016/0022-3697(58)90076-3`.

[73] T. Moriya, Anisotropic superexchange interaction and weak ferromagnetism, Physical Review 120 (1960) 91–98. `doi:10.1103/PhysRev.120.91`.

[74] A. Thiaville, S. Rohart, E. Jué, V. Cros, A. Fert, Dynamics of dzyaloshinskii domain walls in ultrathin magnetic films, Europhysics Letters 100 (57002). `doi:10.1209/0295-5075/100/57002`.

[75] P. P. J. Haazen, E. Muré, J. H. Franken, R. Lavrijsen, H. J. M. Swagten, B. Koopmans, Domain wall depinning governed by the spinhalleffect, Nature Materials 12 (2013) 299–303. `doi:10.1038/nmat3553`.

[76] K. S. Ryu, L. Thomas, S. H. Yang, S. Parkin, Chiral spin torque at magnetic domain walls, Nature Nanotechnology 8 (2013) 527–533. `doi:10.1038/nnano.2013.102`.

[77] I. M. Miron, T. Moore, H. Szambolics, L. D. Buda-Prejbeanu, S. Auffret, B. Rodmacq, S. Pizzini, J. Vogel, M. Bonfim, A. Schuhl, G. Gaudin, Fast current-induced domain-wall motion controlled by the rashba effect, Nature Materials 10 (2011) 419–423. `doi:10.1038/nmat3020`.

[78] A. Manchon, H. C. Koo, J. Nitta, S. M. Frolov, R. A. Duine, New perspectives for Rashba spin-orbit coupling, Nature Materials 14 (2015) 871–882. `doi:10.1038/nmat4360`.

[79] E. van der Bijl, R. A. Duine, Current-induced torques in textured Rashba ferromagnets, Physical Review B 86 (094406). `doi:10.1103/PhysRevB.86.094406`.

[80] K. Garello, I. M. Miron, C. O. Avci, F. Freimuth, Y. Mokrousov, S. Bluegel, S. Auffret, O. Boulle, G. Gaudin, P. Gambardella, Symmetry and magnitude of spin-orbit torques in ferromagnetic heterostructures, Nature Nanotechnology 8 (2013) 587–593. `doi:10.1038/NNANO.2013.145`.

[81] A. V. Khvalkovskiy, V. Cros, D. Apalkov, V. Nikitin, M. Krounbi, K. A. Zvezdin, A. Anane, J. Grollier, A. Fert, Matching domain-wall configuration and spin-orbit torques for efficient domain-wall motion, Physical Review B 87 (020402). `doi:10.1103/PhysRevB.87.020402`.

[82] O. Boulle, S. Rohart, L. D. Buda-Prejbeanu, E. Jué, I. M. Miron, S. Pizzini, J. Vogel, G. Gaudin, A. Thiaville, Domain wall tilting in the presence of the Dzyaloshinskii-Moriya interaction in out-of-plane magnetized magnetic nanotracks, Physical Review Letters 111 (217203). `doi:10.1103/PhysRevLett.111.217203`.

[83] O. Boulle, L. D. Buda-Prejbeanu, E. Jué, I. M. Miron, G. Gaudin, Current induced domain wall dynamics in the presence of spin orbit torques, Journal of Applied Physics 115 (17D502). `doi:10.1063/1.4860946`.

[84] E. Martinez, S. Emori, G. S. D. Beach, Current-driven domain wall motion along high perpendicular anisotropy multilayers: The role of the rashba field, the spin Hall effect, and the Dzyaloshinskii-Moriya interaction, Applied Physics Letters 103. `doi:10.1063/1.4818723`.

[85] E. Martinez, S. Emori, N. Perez, L. Torres, G. S. D. Beach, Current-driven dynamics of Dzyaloshinskii domain walls in the presence of in-plane fields: Full micromagnetic and one-dimensional analysis, Journal of Applied Physics 115 (213909). `doi:10.1063/1.4881778`.

[86] S. Emori, U. Bauer, S.-M. Ahn, E. Martinez, G. S. D. Beach, Current-driven dynamics of chiral ferromagnetic domain walls, Nature Materials 12 (2013) 611–616. `doi:10.1038/nmat3675`.

[87] S. Emori, E. Martinez, K.-J. Lee, H.-W. Lee, U. Bauer, S.-M. Ahn, P. Agrawal, D. C. Bono, G. S. D. Beach, Spin Hall torque magnetometry of Dzyaloshinskii domain walls, Physical Review B 90 (184427). `doi:10.1103/PhysRevB.90.184427`.

[88] S.-G. Je, D.-H. Kim, S.-C. Yoo, B.-C. Min, K.-J. Lee, S.-B. Choe, Asymmetric magnetic domain-wall motion by the Dzyaloshinskii-Moriya interaction, Physical Review B 88 (214401). `doi:10.1103/PhysRevB.88.214401`.

[89] A. Hrabec, N. A. Porter, A. Wells, M. J. Benitez, G. Burnell, S. McVitie, D. McGrouther, T. A. Moore, C. H. Marrows, Measuring and tailoring the Dzyaloshinskii-Moriya interaction in perpendicularly magnetized thin films, Physical Review B 90 (020402). `doi:10.1103/PhysRevB.90.020402`.

[90] R. Lavrijsen, D. M. F. Hartmann, A. van den Brink, Y. Yin, B. Barcones, R. A. Duine, M. A. Verheijen, H. J. M. Swagten, B. Koopmans, Asymmetric magnetic bubble expansion under in-plane field in Pt/Co/Pt: Effect of interface engineering, Physical Review B 91 (104414). `doi:10.1103/PhysRevB.91.104414`.

[91] J. Fassbender, D. Ravelosona, Y. Samson, Tailoring magnetism by light-ion irradiation, Journal of Physics D: Applied Physics 37 (R179). `doi:10.1088/0022-3727/37/16/r01`.

[92] A. Vogel, S. Wintz, J. Kimling, M. Bolte, T. Strache, M. Fritzsche, M.-Y. Im, P. Fischer, G. Meier, J. Fassbender, Domain-wall pinning and depinning at soft spots in magnetic nanowires, IEEE Transactions on Magnetics 46 (2010) 1708–1710. `doi:10.1109/TMAG.2010.2042285`.

[93] M. A. Basith, S. McVitie, D. McGrouther, J. N. Chapman, Reproducible domain wall pinning by linear non-topographic features in a ferromagnetic nanowire, Applied Physics Letters 100 (232402). `doi:10.1063/1.4724210`.

[94] L. Herrera Diez, F. García-Sánchez, J.-P. Adam, T. Devolder, S. Eimer, M. S. El Hadri, A. Lamperti, R. Mantovan, B. Ocker, D. Ravelosona, Controlling magnetic domain wall motion in the creep regime in He+-irradiated CoFeB/MgO films with perpendicular anisotropy, Applied Physics Letters 107 (032401). `doi:10.1063/1.4927204`.

[95] A. N. Bogdanov, D. A. Yablonskiĭ, Thermodynamically stable "vortices" in magnetically ordered crystals. the mixed state of magnets, Soviet Physics JETP 68.

[96] A. N. Bogdanov, U. K. Rößler, Chiral symmetry breaking in magnetic thin films and multilayers, Physical Review Letters 87. `doi:10.1103/physrevlett.87.037203`.

[97] S. Zhang, Z. Li, Roles of nonequilibrium conduction electrons on the magnetization dynamics of ferromagnets, Physical Review Letters 93 (127204). `doi:10.1103/physrevlett.93.127204`.

[98] G. Bertotti, Hysteresis in Magnetism: For Physicists, Materials Scientists, and Engineers, Academic Press, 1998. `doi:10.1016/B978-0-12-093270-2.X5048-X`.

[99] A. Aharoni, Introduction to the Theory of Ferromagnetism, 2000.

[100] R. Skomski, Simple Models of Magnetism, 2008. `doi:10.1093/acprof:oso/9780198570752.001.0001`.

[101] A. Hubert, Theorie der Domanenwande in geordneten Medien, Springer-Verlag, 1974. `doi:10.1007/3-540-06680-2`.

[102] A. Hubert, R. Schafer, Magnetic Domains: The Analysis of Magnetic Microstructures, Springer, 2009. `doi:10.1007/978-3-540-85054-0`.

[103] W. F. Brown, Magnetostatic Principles in Ferromagnetism, North-Holland Publishing Company, 1962.

[104] W. F. Brown, Micromagnetics, Interscience Publishers, 1963.

[105] M. T. Johnson, P. J. H. Bloemen, F. J. A. den Broeder, J. J. de Vries, Magnetic anisotropy in metallic multilayers, Reports on Progress in Physics 59 (1409). `doi:10.1088/0034-4885/59/11/002`.

[106] J. A. Osborn, Demagnetizing factors of the generalized ellipsoid, Physical Review 67 (1945) 351–357. `doi:10.1103/physrev.67.351`.

[107] A. Aharoni, Demagnetizing factors for rectangular ferromagnetic prisms, Journal of Applied Physics 83 (1998) 3432–3434. `doi:10.1063/1.367113`.

[108] D.-X. Chen, J. A. Brug, R. B. Goldfarb, Demagnetizing factors for cylinders, IEEE Transactions on Magnetics 27 (1991) 3601–3619. `doi:10.1109/20.102932`.

[109] M. Sato, Y. Ishii, Simple and approximate expressions of demagnetizing factors of uniformly magnetized rectangular rod and cylinder, Journal of Applied Physics 66 (1989) 983–985. `doi:10.1063/1.343481`.

[110] D. C. Cronemeyer, Demagnetization factors for general ellipsoids, Journal of Applied Physics 70 (1991) 2911–2914. `doi:10.1063/1.349315`.

[111] T. L. Gilbert, A phenomenological theory of damping in ferromagnetic materials, IEEE Transactions on Magnetics 40 (2004) 3443–3449. `doi:10.1109/TMAG.2004.836740`.

[112] L. D. Landau, E. M. Lifshitz, Electrodynamics of Continuous Media, Pergamon Press, 1960.

[113] G. Tatara, H. Kohno, J. Shibata, Microscopic approach to current-driven domain wall dynamics, Physics Reports 468 (2008) 213–301. `doi:10.1016/j.physrep.2008.07.003`.

[114] A. Brataas, A. D. Kent, H. Ohno, Current-induced torques in magnetic materials, Nature Materials 11 (2012) 372–381. `doi:10.1038/nmat3311`.

[115] L. Berger, Emission of spin waves by a magnetic multilayer traversed by a current, Physical Review B 54 (1996) 9353–9358. `doi:10.1103/PhysRevB.54.9353`.

[116] J. C. Slonczewski, Current-driven excitation of magnetic multilayers, Journal of Magnetism and Magnetic Materials 159 (1996) L1–L7. `doi:http://dx.doi.org/10.1016/0304-8853(96)00062-5`.

[117] M. Tsoi, A. G. M. Jansen, J. Bass, W. C. Chiang, M. Seck, V. Tsoi, P. Wyder, Excitation of a magnetic multilayer by an electric current, Physical Review Letters 80 (1998) 4281–4284. `doi:10.1103/PhysRevLett.80.4281`.

[118] E. B. Myers, D. C. Ralph, J. A. Katine, R. N. Louie, R. A. Buhrman, Current-induced switching of domains in magnetic multilayer devices, Science 285 (1999) 867–870. `doi:10.1126/science.285.5429.867`.

[119] J. C. Slonczewski, Excitation of spin waves by an electric current, Journal of Magnetism and Magnetic Materials 195 (1999) 261–268. `doi:10.1016/s0304-8853(99)00043-8`.

[120] G. Tatara, H. Kohno, Theory of current-driven domain wall motion: Spin transfer versus momentum transfer, Physical Review Letters 92 (086601). `doi:10.1103/physrevlett.92.086601`.

[121] A. K. Nguyen, H. J. Skadsem, A. Brataas, Giant current-driven domain wall mobility in (Ga,Mn)As, Physical Review Letters 98 (146602). `doi:10.1103/PhysRevLett.98.146602`.

[122] A. Manchon, S. Zhang, Theory of nonequilibrium intrinsic spin torque in a single nanomagnet, Physical Review B 78 (212405). `doi:10.1103/physrevb.78.212405`.

[123] A. Matos-Abiague, R. L. Rodriguez-Suarez, Spin-orbit coupling mediated spin torque in a single ferromagnetic layer, Physical Review B 80 (094424). `doi:10.1103/PhysRevB.80.094424`.

[124] A. Chernyshov, M. Overby, X. Liu, J. K. Furdyna, Y. Lyanda-Geller, L. P. Rokhinson, Evidence for reversible control of magnetization in a ferromagnetic material by means of spin-orbit magnetic field, Nature Physics 5 (2009) 656–659. `doi:10.1038/nphys1362`.

[125] L. Liu, O. J. Lee, T. J. Gudmundsen, D. C. Ralph, R. A. Buhrman, Current-induced switching of perpendicularly magnetized magnetic layers using spin torque from the spin Hall effect, Physical Review Letters 109 (096602). `doi:10.1103/PhysRevLett.109.096602`.

[126] M. I. Dyakonov, V. I. Perel, Current-induced spin orientation of electrons in semiconductors, Physics Letters A 35 (1971) 459–460. `doi:10.1016/0375-9601(71)90196-4`.

[127] M. I. D'yakonov, V. I. Perel, Possibility of orienting electron spins with current, JETP Letters 13 (1971) 467.

[128] C. O. Avci, K. Garello, C. Nistor, S. Godey, B. Ballesteros, A. Mugarza, A. Barla, M. Valvidares, E. Pellegrin, A. Ghosh, I. M. Miron, O. Boulle, S. Auffret, G. Gaudin, P. Gambardella, Field-like and antidamping spin-orbit torques in as-grown and annealed Ta/CoFeB/MgO layers, Physical Review B 89 (214419). `doi:10.1103/PhysRevB.89.214419`.

[129] J. Kim, J. Sinha, M. Hayashi, M. Yamanouchi, S. Fukami, T. Suzuki, S. Mitani, H. Ohno, Layer thickness dependence of the current-induced effective field vector in Ta—CoFeB—MgO, Nature Materials 12 (2013) 240–245. `doi:10.1038/nmat3522`.

[130] X. Wang, A. Manchon, Diffusive spin dynamics in ferromagnetic thin films with a Rashba interaction, Physical Review Letters 108 (117201). `doi:10.1103/PhysRevLett.108.117201`.

[131] A. V. Khvalkovskiy, K. A. Zvezdin, Y. V. Gorbunov, V. Cros, J. Grollier, A. Fert, A. K. Zvezdin, High domain wall velocities due to spin currents perpendicular to the plane, Physical Review Letters 102 (067206). `doi:10.1103/PhysRevLett.102.067206`.

[132] J. Torrejon, M. Hayashi, Spin Hall torque driven chiral domain walls in magnetic heterostructures, ArXiv e-prints`arXiv:1503.07250`.

[133] H. Yang, A. Thiaville, S. Rohart, A. Fert, M. Chshiev, Anatomy of Dzyaloshinskii-Moriya Interaction at Co/Pt Interfaces, ArXiv e-prints`arXiv:1501.05511`.

[134] A. P. Pyatakov, A. S. Sergeev, D. A. Sechin, G. A. Meshkov, E. P. Nikolaeva, A. V. Nikolaev, A. S. Logginov, A. K. Zvezdin, Magnetic domain wall motion triggered by electric field, Journal of Physics: Conference Series 200. `doi:10.1088/1742-6596/200/3/032059`.

[135] B. Van de Wiele, L. Laurson, K. J. A. Franke, S. van Dijken, Electric field driven magnetic domain wall motion in ferromagnetic-ferroelectric heterostructures, Applied Physics Letters 104 (012401). `doi:10.1063/1.4860963`.

[136] K. J. A. Franke, B. Van de Wiele, Y. Shirahata, S. J. Hämäläinen, T. Taniyama, S. van Dijken, Reversible electric-field-driven magnetic domain-wall motion, Physical Review X 5 (011010). `doi:10.1103/PhysRevX.5.011010`.

[137] M. T. Bryan, J. Dean, D. A. Allwood, Dynamics of stress-induced domain wall motion, Physical Review B 85 (144411). `doi:10.1103/PhysRevB.85.144411`.

[138] E. Martinez, L. Lopez-Diaz, O. Alejos, L. Torres, Resonant domain wall depinning induced by oscillating spin-polarized currents in thin ferromagnetic strips, Physical Review B 77 (144417). `doi:10.1103/PhysRevB.77.144417`.

[139] G. Tatara, E. Saitoh, M. Ichimura, H. Kohno, Domain-wall displacement triggered by an ac current below threshold, Applied Physics Letters 86 (232504). `doi:10.1063/1.1944902`.

[140] R. A. Duine, A. S. Núnez, J. Sinova, A. H. MacDonald, Functional Keldysh theory of spin torques, Physical Review B 75 (214420). `doi:10.1103/PhysRevB.75.214420`.

[141] E. Martinez, L. Lopez-Diaz, O. Alejos, L. Torres, C. Tristan, Thermal effects on domain wall depinning from a single notch, Physical Review Letters 98 (267202). `doi:10.1103/PhysRevLett.98.267202`.

[142] M. J. Donahue, D. G. Porter, OOMMF User's Guide, Version 1.0, National Institute of Standards and Technology (1999). `doi:10.6028/NIST.IR.6376`.

[143] A. Vansteenkiste, J. Leliaert, M. Dvornik, M. Helsen, F. Garcia-Sanchez, B. Van Waeyenberge, The design and verification of MuMax3, AIP Advances 4 (107133). `doi:10.1063/1.4899186`.

[144] J. Sinha, M. Hayashi, A. J. Kellock, S. Fukami, M. Yamanouchi, H. Sato, S. Ikeda, S. Mitani, S.-h. Yang, S. S. P. Parkin, H. Ohno, Enhanced interface perpendicular magnetic anisotropy in Ta—CoFeB—MgO using nitrogen doped Ta underlayers, Applied Physics Letters 102 (242405). `doi:10.1063/1.4811269`.

[145] L. Liu, R. A. Buhrman, D. C. Ralph, Review and analysis of measurements of the spin Hall effect in platinum, ArXiv e-prints`arXiv:1111.3702`.

[146] Y. H. Choi, Y. Yoshimura, K.-J. Kim, K. Lee, T. W. Kim, T. Ono, C.-Y. You, M. H. Jung, Field-driven domain wall motion under a bias current in the creep and flow regimes in Pt/[CoSiB/Pt]N nanowires, Scientific Reports 6 (23933). `doi:10.1038/srep23933`.

[147] N. Mikuszeit, O. Boulle, I. M. Miron, K. Garello, P. Gambardella, G. Gaudin, L. D. Buda-Prejbeanu, Spin-orbit torque driven chiral magnetization reversal in ultrathin nanostructures, Physical Review B 92 (144424). `doi:10.1103/PhysRevB.92.144424`.

[148] E. Jué, A. Thiaville, S. Pizzini, J. Miltat, J. Sampaio, L. D. Buda-Prejbeanu, S. Rohart, J. Vogel, M. Bonfim, O. Boulle, S. Auffret, I. M. Miron, G. Gaudin, Domain wall dynamics in ultrathin Pt/Co/AlOx microstrips under large combined magnetic fields, Physical Review B 93 (014403). `doi:10.1103/PhysRevB.93.014403`.

[149] T. H. Pham, J. Vogel, J. Sampaio, M. Vanatka, J.-C. Rojas-Snchez, M. Bonfim, D. S. Chaves, F. Choueikani, P. Ohresser, E. Otero, A. Thiaville, S. Pizzini, Very large domain wall velocities in Pt/Co/GdOx and Pt/Co/Gd trilayers with Dzyaloshinskii-Moriya interaction, Europhysics Letters 113 (67001). `doi:10.1209/0295-5075/113/67001`.

[150] B. Boehm, A. Bisig, A. Bischof, G. Stefanou, B. J. Hickey, R. Allenspach, Achiral tilted domain walls in perpendicularly magnetized nanowires, Physical Review B 95 (180406). `doi:10.1103/PhysRevB.95.180406`.

[151] Y. Yoshimura, K.-J. Kim, T. Taniguchi, T. Tono, K. Ueda, R. Hiramatsu, T. Moriyama, K. Yamada, Y. Nakatani, T. Ono, Soliton-like magnetic domain wall motioninducedby the interfacial dzyaloshinskii-moriyainteraction, Nature Physics 12 (2016) 157–161. `doi:10.1038/nphys3535`.

[152] K.-S. Ryu, S.-H. Yang, L. Thomas, S. S. P. Parkin, Chiral spin torque arising from proximity-induced magnetization, Nature Communications 5 (3910). `doi:10.1038/ncomms4910`.

[153] S. Rohart, A. Thiaville, Skyrmion confinement in ultrathin film nanostructures in the presence of Dzyaloshinskii-Moriya interaction, Physical Review B 88 (184422). `doi:10.1103/PhysRevB.88.184422`.

[154] M. D. DeJong, K. L. Livesey, Analytic theory for the switch from Bloch to Néel domain wall in nanowires with perpendicular anisotropy, Physical Review B 92 (214420). `doi:10.1103/PhysRevB.92.214420`.

[155] E. Martinez, L. Torres, L. Lopez-Diaz, Oscillator based on pinned domain walls driven by direct current, Physical Review B 83 (174444). `doi:10.1103/PhysRevB.83.174444`.

[156] O. Boulle, L. D. Buda-Prejbeanu, M. Miron, G. Gaudin, Current induced domain wall dynamics in the presence of a transverse magnetic field in out-of-plane magnetized materials, Journal of Applied Physics 112 (053901). `doi:10.1063/1.4747907`.

[157] J. C. Slonczewski, Theory of domain-wall motion in magnetic films and platelets, Journal of Applied Physics 44 (4) (1973) 1759–1770. `doi:10.1063/1.1662444`.

[158] W. Döring, Über die trägheit der wände zwischen weißschen bezirken, Zeitschrift für Naturforschung A 3 (1948) 373–379.

[159] D. G. Porter, M. J. Donahue, Velocity of transverse domain wall motion along thin, narrow strips, Journal of Applied Physics 95 (2004) 6729–6731. `doi:10.1063/1.1688673`.

[160] J. Vandermeulen, B. V. de Wiele, A. Vansteenkiste, B. V. Waeyenberge, L. Dupré, A collective coordinate approach to describe magnetic domain wall dynamics applied to nanowires with high perpendicular anisotropy, Journal of Physics D: Applied Physics 48 (035001). `doi:10.1088/0022-3727/48/3/035001`.

[161] M. Vanatka, J.-C. Rojas-Sánchez, J. Vogel, M. Bonfim, M. Belmeguenai, Y. Roussigné, A. Stashkevich, A. Thiaville, S. Pizzini, Velocity asymmetry of Dzyaloshinskii domain walls in the creep and flow regimes, Journal of Physics: Condensed Matter 27 (326002). `doi:10.1088/0953-8984/27/32/326002`.

[162] T. Tono, T. Taniguchi, K.-J. Kim, T. Moriyama, A. Tsukamoto, T. Ono, Chiral magnetic domain wall in ferrimagnetic GdFeCo wires, Applied Physics Express 8 (073001). `doi:`

10.7567/apex.8.073001.

[163] J. Yun, D. Li, B. Cui, X. Guo, K. Wu, X. Zhang, Y. Wang, J. Mao, Y. Zuo, L. Xi, Current induced domain wall motion and tilting in ptcota structures with perpendicular magnetic anisotropy in the presence of the Dyzaloshinskii-Moriya interaction, Journal of Physics D: Applied Physics 51 (155001). `doi:10.1088/1361-6463/aab419`.

[164] J. Leliaert, B. Van de Wiele, A. Vansteenkiste, L. Laurson, G. Durin, L. Dupré, B. Van Waeyenberge, A numerical approach to incorporate intrinsic material defects in micromagnetic simulations, Journal of Applied Physics 115 (17D102). `doi:10.1063/1.4854956`.

[165] C. C. Faulkner, M. D. Cooke, D. A. Allwood, D. Petit, D. Atkinson, R. P. Cowburn, Artificial domain wall nanotraps in Ni81Fe19 wires, Journal of Applied Physics 95 (2004) 6717–6719. `doi:10.1063/1.1652391`.

[166] S.-M. Ahn, D.-H. Kim, S.-B. Choe, Kinetic and static domain-wall pinning at notches on ferromagnetic nanowires, IEEE Transactions on Magnetics 45 (2009) 2478–2480. `doi:10.1109/TMAG.2009.2018662`.

[167] L. K. Bogart, D. S. Eastwood, D. Atkinson, The effect of geometrical confinement and chirality on domain wall pinning behavior in planar nanowires, Journal of Applied Physics 104 (033904). `doi:10.1063/1.2961313`.

[168] L. K. Bogart, D. Atkinson, K. O'Shea, D. McGrouther, S. McVitie, Dependence of domain wall pinning potential landscapes on domain wall chirality and pinning site geometry in planar nanowires, Physical Review B 79 (054414). `doi:10.1103/PhysRevB.79.054414`.

[169] J. Akerman, M. Muñoz, M. Maicas, J. L. Prieto, Stochastic nature of the domain wall depinning in permalloy magnetic nanowires, Physical Review B 82 (064426). `doi:10.1103/PhysRevB.82.064426`.

[170] S.-B. Choe, Unique depinning fields at symmetric double notches in a ferromagnetic permalloy nanowire, Journal of Magnetism and Magnetic Materials 320 (2008) 1112–1114. `doi:10.1016/j.jmmm.2007.10.023`.

[171] S. Goolaup, S. C. Low, M. C. Sekhar, W. S. Lew, Dependence of pinning on domain wall spin structure and notch geometry, Journal of Physics: Conference Series 266 (012079). `doi:10.1088/1742-6596/266/1/012079`.

[172] K. He, D. J. Smith, M. R. McCartney, Observation of asymmetrical pinning of domain walls in notched permalloy nanowires using electron holography, Applied Physics Letters 95 (182507). `doi:10.1063/1.3261753`.

[173] S.-H. Huang, C.-H. Lai, Domain-wall depinning by controlling its configuration at notch, Applied Physics Letters 95 (032505). `doi:10.1063/1.3187530`.

[174] D. Petit, A.-V. Jausovec, D. Read, R. P. Cowburn, Domain wall pinning and potential landscapes created by constrictions and protrusions in ferromagnetic nanowires, Journal of Applied Physics 103 (114307). `doi:10.1063/1.2936981`.

[175] D. Petit, A.-V. Jausovec, H. T. Zeng, E. Lewis, L. O'Brien, D. Read, R. P. Cowburn, Mechanism for domain wall pinning and potential landscape modification by artificially patterned traps in ferromagnetic nanowires, Physical Review B 79 (214405). `doi:10.1103/PhysRevB.79.214405`.

[176] L. J. Chang, Y. D. Yao, P. Lin, S. F. Lee, Magnetic interaction in domain wall depinning at square notch and antinotch traps, IEEE Transactions on Magnetics 47 (2011) 2519–2521. `doi:10.1109/TMAG.2011.2157114`.

[177] C. Blanco-Roldán, C. Quirós, G. Rodriguez-Rodriguez, M. Vélez, J. I. Martin, J. M. Alameda, Switchable field-tuned control of magnetic domain wall pinning along co microwires by 3D e-beam lithographed structures, Journal of Magnetism and Magnetic Materials 400 (2016) 213–218, proceedings of the 20th International Conference on Magnetism (Barcelona) 5-10 July 2015. `doi:10.1016/j.jmmm.2015.07.056`.

[178] M. Hara, J. Shibata, T. Kimura, Y. Otani, Control of domain wall pinning by a switchable magnetic gate, Applied Physics Letters 89 (192504). `doi:10.1063/1.2385224`.

[179] M. Vázquez, G. A. Basheed, G. Infante, R. P. Del Real, Trapping and injecting single domain walls in magnetic wire by local fields, Physical Review Letters 108 (037201). `doi:10.1103/PhysRevLett.108.037201`.

[180] K.-J. Kim, S.-B. Choe, Analytic theory of wall configuration and depinning mechanism in magnetic nanostructure with perpendicular magnetic anisotropy, Journal of Magnetism and Magnetic Materials 321 (2009) 2197–2199. `doi:10.1016/j.jmmm.2009.01.031`.

[181] P. Bruno, Geometrically constrained magnetic wall, Physical Review Letters 83 (1999) 2425–2428. `doi:10.1103/PhysRevLett.83.2425`.

[182] F. Garcia-Sanchez, H. Szambolics, A. P. Mihai, L. Vila, A. Marty, J.-P. Attané, J.-C. Toussaint, L. D. Buda-Prejbeanu, Effect of crystalline defects on domain wall motion under field and current in nanowires with perpendicular magnetization, Physical Review B 81 (134408). `doi:10.1103/PhysRevB.81.134408`.

[183] C.-L. Hu, L. Liao, R.-Q. Zhao, Transition of domain walls induced by current in defect permalloy nanowires, Journal of Magnetism and Magnetic Materials 399 (2016) 94–96. `doi:10.1016/j.jmmm.2015.09.070`.

[184] T. Y. Chen, M. J. Erickson, P. A. Crowell, C. Leighton, Surface roughness dominated pinning mechanism of magnetic vortices in soft ferromagnetic films, Physical Review Letters 109 (097202). `doi:10.1103/PhysRevLett.109.097202`.

[185] M. Albert, M. Franchin, T. Fischbacher, G. Meier, H. Fangohr, Domain wall motion in perpendicular anisotropy nanowires with edge roughness, Journal of Physics: Condensed Matter 24 (024219). `doi:10.1088/0953-8984/24/2/024219`.

[186] E. Martinez, The stochastic nature of the domain wall motion along high perpendicular anisotropy strips with surface roughness, Journal of Physics: Condensed Matter 24 (024206). `doi:10.1088/0953-8984/24/2/024206`.

[187] J. Leliaert, Magnetic disorder and thermal fluctuations in domain wall motion and nanoparticle dynamics, Ph.D. thesis, Ghent University (2016).

[188] J. P. Attane, D. Ravelosona, A. Marty, Y. Samson, C. Chappert, Thermally activated depinning of a narrow domain wall from a single defect, Physical Review Letters 96 (147204). `doi:10.1103/physrevlett.96.147204`.

[189] P. Lendecke, R. Eiselt, G. Meier, U. Merkt, Temperature dependence of domain-wall depinning fields in constricted permalloy nanowires, Journal of Applied Physics 103 (073909). `doi:10.1063/1.2903932`.

[190] M.-Y. Im, L. Bocklage, P. Fischer, G. Meier, Direct observation of stochastic domain-wall depinning in magnetic nanowires, Physical Review Letters 102 (147204). `doi:10.1103/PhysRevLett.102.147204`.

[191] W. F. Brown, Thermal fluctuations of a single-domain particle, Journal of Applied Physics 34 (1963) 1319–1320. `doi:10.1063/1.1729489`.

[192] W. Brown, Thermal fluctuation of fine ferromagnetic particles, IEEE Transactions on Magnetics 15 (1979) 1196–1208. `doi:10.1109/TMAG.1979.1060329`.

[193] L. Fan, J. Hu, Y. Su, J. Zhu, Influence of temperature on current-induced domain wall motion and its Walker breakdown, Journal of Magnetism and Magnetic Materials 401 (2016) 484–487. `doi:10.1016/j.jmmm.2015.10.090`.

[194] D. Ilgaz, M. Kläui, L. Heyne, O. Boulle, F. Zinser, S. Krzyk, M. Fonin, U. Rüdiger, D. Backes, L. J. Heyderman, Selective domain wall depinning by localized oersted fields and joule heating, Applied Physics Letters 93 (132503). `doi:10.1063/1.2990629`.

[195] S. Moretti, V. Raposo, E. Martinez, Influence of joule heating on current-induced domain wall depinning, Journal of Applied Physics 119 (213902). `doi:10.1063/1.4953008`.

[196] O. Chubykalo-Fesenko, U. Nowak, R. W. Chantrell, D. Garanin, Dynamic approach for micromagnetics close to the Curie temperature, Physical Review B 74 (094436). `doi:10.1103/PhysRevB.74.094436`.

[197] D. A. Garanin, Fokker-Planck and Landau-Lifshitz-Bloch equations for classical ferromagnets, Physical Review B 55 (1997) 3050–3057. `doi:10.1103/PhysRevB.55.3050`.

[198] H. C. Torrey, Bloch equations with diffusion terms, Physical Review 104 (1956) 563–565. `doi:10.1103/PhysRev.104.563`.

[199] C. J. Garcia-Cervera, One-dimensional magnetic domain walls, European Journal of Applied Mathematics 15 (2004) 451–486. `doi:10.1017/S0956792504005595`.

[200] R. F. L. Evans, D. Hinzke, U. Atxitia, U. Nowak, R. W. Chantrell, O. Chubykalo-Fesenko, Stochastic form of the Landau-Lifshitz-Bloch equation, Physical Review B 85 (014433). `doi:10.1103/PhysRevB.85.014433`.